JAERI-M
91-121

CONCEPTUAL DESIGN OF SC MAGNET SYSTEM FOR ITER (II)

— STRESS ANALYSIS —

August 1991

Koichi KOIZUMI, Mitsuru HASEGAWA and Kiyoshi YOSHIDA

日本原子力研究所
Japan Atomic Energy Research Institute

JAERI-Mレポートは，日本原子力研究所が不定期に公刊している研究報告書です。
入手の問合わせは，日本原子力研究所技術情報部情報資料課（〒319-11茨城県那珂郡東海村）あて，お申しこしください。なお，このほかに財団法人原子力弘済会資料センター（〒319-11 茨城県那珂郡東海村日本原子力研究所内）で複写による実費頒布をおこなっております。

JAERI-M reports are issued irregularly.
Inquiries about availability of the reports should be addressed to Information Division, Department of Technical Information, Japan Atomic Energy Research Institute, Tokai-mura, Naka-gun, Ibaraki-ken 319-11, Japan.

編集兼発行　日本原子力研究所
印　　刷　㈱原子力資料サービス

JAERI-M 91-121

Conceptual Design of SC Magnet System for ITER (II)
- Stress Analysis -

Koichi KOIZUMI, Mitsuru HASEGAWA+ and Kiyoshi YOSHIDA

Department Fusion Engineering Research
Naka Fusion Research Establishment
Japan Atomic Energy Research Institute
Naka-machi, Naka-gun, Ibaraki-ken

(Receivd July 8, 1991)

The International Thermonuclear Experimetnal Reactor (ITER) is an experimental tokamak machine testing the basic plasma performance and technologies required for future tokamak reactor. The joint work of the conceptual design activities for ITER was carried out at the Max Planck Institute for Plasma Physics in Garching, West Germany, from 1988 to 1990, under the auspices of the International Atomic Energy Agency (IAEA) according to the quadripartite agreement reached between the European Community (EC), the Soviet Union, the United State and Japan.

The Superconducting (SC) Magnet System is the most critical design unit, because its design dominates the plasma confinement and machine size. The design proposals for the SC magnet system from Japan were summarized by the Fusion Experimental Reactor (FER) Design Team and the Superconducting Magnet Laboratory of the Japan Atomic Energy Research Institute (JAERI). This report is one of the series reports on "Conceptual Design of Superconducting Magnet System For ITER", and describes the major results of the stress analysis regarding the Toroidal Field (TF) coil, the Center Solenoid (CS) coil and the Equilibrium Field (EF) coil and their support structures.

Among the design issues, the mechanical design of the coil system

---

+ Fusion Experimental Reactor Team

was one of the most critical items, not only because of the huge electromagnetic loads due to large size and high magnetic field, but also because of the demand of high reliability under neutron irradiation. In order to satisfy both the coil performance and the mechanical reliability, different types of conductors were employed for each coils. The mechanical behaviors and the safety margin of each coil were analyzed by using finite element method (FEM) of MSC/NASTRAN. The procedure to obtain the equivalent winding stiffness employed for the each FEM analysis is also described in this report. The details on the coil specifications, conductor design and mechanical design for each coils are described in other report of the series reports.

Keywords: ITER, SC Magnet, TF Coil, CS Coil, EF Coil, Support, FEM Analysis, Toresca Stress, Winding, Coil Case

JAERI－M 91－121

ITER用超電導マグネット・システム概念設計（II）
－応力解析－

日本原子力研究所那珂研究所核融合工学部
小泉 興一・長谷川 満＋・吉田 清

（1991年7月8日受理）

国際核融合実験炉（ITER）は，将来のトカマク型核融合炉に要求される基本的なプラズマ性能と工学技術の総合的実証試験を行うトカマク実験装置である。本装置の概念設計活動は，国際原子力エネルギー機関（IAEA）の協定に基づいて，ヨーロッパ共同体（EC），ソ連，米国，及び日本の四極による共同作業として，1988年から1990年までの3年間，西独のガルヒンにあるマックスプランク・プラズマ物理学研究所において実施された。

プラズマの閉じ込め性能と装置寸法を左右する最も重要な構成機器である超電導コイルに関する概念設計は，原研那珂研究所の核融合実験炉特別チーム及び超電導磁石研究室が中心となり，日本案の取りまとめを行った。本報告は，ITER用超電導コイル・システムの概念設計を取りまとめた一連の報告書の一分冊であり，トロイダル磁場（TF）コイル，中心ソレノイド（CS）コイル，平衡磁場（EF）コイル，並びに支持構造に関する応力解析の主要結果を報告するものである。

コイルの大型化，高磁界化及び高電流密度化に伴って増大する巨大な電磁力の支持と発生する応力の低減は，コイルの最も重要な設計課題の1つである。このため，各コイルに発生する電磁力と要求される性能に応じて異なる導体設計，構造設計を採用して機械的信頼性の確保を計るとともに，詳細な有限要素法（FEM）解析を行って各コイルに発生する機械的特性と機械的安全率を評価した。本報告では，各コイルの応力解析結果の他，FEM解析に使用した巻線部の等価剛性値の算出手順についても併せて報告する。各コイルの設計仕様，並びに導体設計，構造設計の詳細については，他の分冊を参照されたい。

那珂研究所：〒311－01 茨城県那珂郡那珂町大字向山801－1
＋ 核融合実験炉特別チーム

Contents

目　　次

PREFACE

All of technical design reports from Japanese contributors to ITER magnet design are listed below:

JAERI-M 91-120
CONCEPTUAL DESIGN OF SC MAGNET SYSTEM FOR ITER (I)
- OVERVIEW -

(1) Design Basis
(2) Toroidal Field Coils
(3) Central Solenoid Coils
(4) Outer Ring Coils
(5) Mechanical Design Guideline

JAERI-M 91-121
CONCEPTUAL DESIGN OF SC MAGNET SYSTEM FOR ITER (II)
- STRESS ANALYSIS -

(1) Toroidal Field Coils at End of Burn
(2) Toroidal Field Coils at Fault Conditions
(3) Center Solenoid Coils
(4) PF Coil Support Structure and Outer Ring Coil
(5) Winding Rigidity Analysis

JAERI-M 91-122
CONCEPTUAL DESIGN OF SC MAGNET SYSTEM FOR ITER (III)
- AC LOSS -

(1) Analysis and Measurement of AC Losses in Large Superconducting Coil
(2) AC Loss Analysis
(3) AC Loss in Cryogenic Structure

JAERI-M 91-123
CONCEPTUAL DESIGN OF SC MAGNET SYSTEM FOR ITER (IV)
- POWER SUPPLY AND CRYOGENIC SYSTEM -

(1) Power Supply System for Magnet System
(2) Fault Analysis of TF Power Supply System
(3) Cryogenic System

JAERI-M 91-124

CONCEPTUAL DESIGN OF SC MAGNET SYSTEM FOR ITER (V)

- MATERIAL -

(1) Superconducting Material

(2) Steels

(3) Insulator

JAERI-M 91-125

CONCEPTUAL DESIGN OF SC MAGNET SYSTEM FOR ITER (VI)

- R&D PROPOSALS -

(1) Requirements of Scalable Model Coil Test

(2) TF Scalable Model Coil

1. Introduction

The Superconducting (SC) Magnet System for International Thermonuclear Experimental Reactor (ITER) is composed of 16 Toroidal Field (TF) coils, 8 Center Solenoid (CS) coils, 6 Equilibrium Field (EF) coils and their support structures. The SC Magnet System is the key component of ITER, because its performances dominate the plasma confinement and machine size. In order to achieve the testing of high plasma performance with large plasma current, the SC Magnet System of ITER have to satisfy large coil sizes, high magnetic field and high operating currents. In addition to these requirements, some components such as the TF coil and the CS coil have to fulfill the inherent demand for extremely high reliability under huge electromagnetic loads and neutron irradiation. Since the allowable space for coil design is limited by the compatibility with the other design units, the mechanical reliability of coil system under huge electromagnetic loads is the most critical design issue of SC magnets. For these reasons, the extensive stress analyses were performed by using finite element method (FEM) models of MSC/NASTRAN.

Regarding the TF coil system, the mechanical behaviors of TF coil and TF coil system were analyzed under the normal loading condition at End of Burn (EOB) and the 4 abnormal loading conditions at the fault modes. The major results of these analysis are described in Chapter 2 and Chapter 3. For the CS coils, which have the function to provide magnetic flux to induce the plasma current with the high magnetic field of 13.5 T, the detail stress analysis of conduits were performed to specify the allowable limit of magnetic flux from the view point of allowable stress limit of fatigue cycles. The results are reported in Chapter 4. In Chapter 5 and 6, the results on the stress analysis of EF coil and the detailed procedure to obtain the equivalent winding stiffness are also reported.

2. Stress Analysis of Toroidal Field Coils at End of Burn

2.1 Introduction

The mechanical behaviors of the Toroidal Field (TF) coils have been analyzed under the normal loading condition at the End of Burn (EOB) by the 3-dimensional finite element model of the MSC/NASTRAN. By using the toroidally symmetric features of the machine geometry and loading under normal operating conditions, 1/16 sector of 16 TF coil system was modeled and analyzed. This report describes the finite element model, loading condition, boundary condition, and major results of the analysis.

2.2 FEM model for the analysis

Based on the toroidally symmetric features of the machine geometry and loading, a finite element model of a 22.5 degree sector of 16 TF coil system has been employed for the analysis. The FEM model, which includes the outer intercoil structure, is shown in Fig. 2.1 and Fig. 2.2. The basic dimensions of the FEM model are shown in Fig. 2.3 and Fig. 2.4.
The modeling detail are summarized as follows ;

(1) Winding Pack

The winding pack of the TF coil is modeled by using 432 solid elements (HEXA8) with an orthotropic and linear-elastic material properties. The cross section of the winding is assumed to be a rectangular shape, and it is divided into 12 rectangular sections.

(2) Winding Insulation

The insulators installed between the winding pack and the outer ring, between the winding and the side plates, are modeled by using simple truss elements (ROD). There is no connection between the winding pack and the inner ring in order not to avoid the deformation of winding. It is also assumed that the insulator between the winding and the coil case is effec-

tive only for compressive forces.

(3) Coil Case

The coil case is modeled by using solid elements (HEXA8) closely to the actual dimensions. In the region of outer ring, coil case is modeled by the two layers of solid elements. On the part of the inner leg, the inner ring (back plate) is omitted as shown in Fig. 2.5.

(4) Top and Bottom of Inner Leg

At the top and bottom of the inner leg, supporting structures of solid type elements (HEXA8) are attached to the coil case. The dimensions of this parts are shown in Fig. 2.6.

(5) Outer Intercoil Structure

The supporting structure at the outer radius of TF coil and the outer intercoil structure are modeled by shell type (QUAD4) elements which have a thickness of 200 mm. As shown in Fig. 2.1, a box structure is employed for this part. However, the front plate is "removed" by adjusting its thickness and stiffness down to negligible small values.

(6) Support Leg

The support leg is employed only for the stabilization of cyclic symmetry analysis. Instead of modeling explicitly the actual structure, the support leg is modeled by using a simple beam element. The stiffness similar to that of conventional Fiber Reinforced Plastic (FRP), Young's Modulus of 20 GPa and Poisson's Ratio of 0.1, are employed for beam elements.

2.3 Material Properties employed for the analysis

The winding pack are modeled with orthotropic, linear-elastic material properties. In order to obtain a realistic deformation and stress level, a set of equivalent stiffness, which was calculated for the Japanese TMC-FF type conductor, was employed for the analysis. For the coil case, supporting structures, and outer intercoil structure, the stiffness of the

Japanese Cryogenic Steel (JCS) at 4 K, was used. The material properties used for the analysis are summarized in Table 2.1.

2.4 Loading Condition

The electromagnetic loads occurs at the End of Burn of the normal operation was selected for the analysis. A computer program "FORCE" in JAERI was employed to calculate the distributed forces along the winding. The detail distributions of the electromagnetic loads along the coil perimeter are presented in Ref. 2.1. Total loads obtained by integrating distributed body force are calculated as follows:

Centering Load	FX :	- 475.8 MN/Coil
Hoop Load	FH :	1024.0 MN/Coil
Over-turning Moment	FX :	196.0 MN*m
Vertical Load	FV :	185.4 MN/Upper and Lower Half

For the actual analysis, equivalent nodal loads are calculated and inputted according to the each element shape and volume.

2.5 Boundary Conditions

Because of the toroidally symmetric feature of TF coil system and the coil loading which is repetitively symmetric around the machine axis, the cyclic symmetry analysis (SOL47 of MSC/NASTRAN) was employed to obtain the mechanical behavior of 16 TF coil system. To satisfy the conditions required for cyclic symmetry, the boundary conditions of cyclic symmetry are applied to the all nodes located on the two vertical planes at the toroidal angles of +/- 11.25 degree from vertical symmetry plane of TF coil (Fig. 2.2). The components of the TF coil cut by these two planes are, the contact surfaces in the inner leg for the wedging, shear key regions at the top and bottom of the inner leg, and the outer intercoil structures. Therefore, the Components located on the interfaces between TF coils are assumed to be idealized welded structure.

2.6 Analysis Results

2.6.1 Displacements

The deformation of the ITER TF coil under the normal loading condition at the End of Burn, is presented by a series of figures (Fig. 2.7 - Fig. 2.14). Regarding the displacement in the out-of-plane direction, it can be seen from these figures that there is no opposite sign. The maximum displacement of the winding pack in the out-of-plane direction is -26.5 mm, at the location shown in Fig. 2.11. The maximum displacement of the model is also occurs at this location. It can be seen that there is very small deformation due to twisting in the region of inner leg. In the radial direction, it is seen from Fig. 2.8 that there is the displacement of -4.6 mm and 10.9 mm, at the midplane of inner leg and the outer leg, respectively.

The maximum displacement of the model in the radial, the out-of-plane, and the vertical direction, are summarized as follows:

(1) Radial direction	:	13.5 mm	(Coil case in the mid plane of outer leg)
(2) Out-of-plane direction	:	-26.5 mm	(Winding)
(3) Vertical direction	:	16.5 mm	(Coil case at the top of D-shape)

2.6.2 Winding Pack Stresses

Figure 2.15 shows the contour of constant Tresca Stress in the winding pack calculated by using equivalent winding stiffness. It is seen that there are two high stress region in the inner leg. The maximum Tresca Stress calculated is 302 MPa in the region of inner leg.

The distribution of the Principal Stress (σ_1), the Medium Stress (σ_2), and the Minimum Stress (σ_3) in the winding pack, are presented in Fig. 2.16, Fig. 2.17, and Fig. 2.18. From these figures, it can be seen that the compressive stress component generated by the wedging has the major contribution on the stress peaking in the region of inner leg. The peaking

of compressive stress component is highly localized due to the simple modeling of the insulator (ROD elements) between the winding and coil case. Therefore, it is an artificial peaking, to a certain extent. The maximum compressive stress of the insulator between the winding and coil case is 127 MPa.

The distribution of Tresca Stress, the Principal Stress (σ_1), the Medium Stress (σ_2), and the Minimum Stress (σ_3), in the winding cross section at the midplane of the inner leg, are presented in a series of figures (Fig. 2.19 - Fig. 2.22).

The peak value of 6 stress components, appears in the winding cross section at the midplane of inner leg and the outer leg, are summarized in Table 2.2. Note that the direction of "X" and "Y" in the element coordinate system for the winding agrees with the radial and the out-of-plane direction defined by the global coordinate system. The Z-direction in the element coordinate system corresponds to the circumferential direction of the winding pack.

2.6.3 Coil Case Stresses

Figure 2.23 - Fig. 2.26 shows the global distribution of the Tresca Stress (σ_T), the Principal Stress (σ_1), the Medium Stress (σ_2), and the Minimum Stress (σ_3) in the TF coil case at the End of Burn. The detail distribution of these stresses, for the inner ring and the outer ring, are also presented in Fig. 2.27 - Fig. 2.30, and Fig. 2.31 - Fig. 2.34, respectively. It can be seen from Fig. 2.23 and Fig. 2.31 that the maximum Tresca Stress of 655 MPa occurs in the outer ring at the lower part of inner leg. This is the same location in which the maximum Tresca stress of the winding is calculated. Also, the location of the outer ring corresponds to the part of most thin section in the cross section connected to the side plate. The maximum Tresca stress calculated for the inner ring is 339 MPa.

The detail distribution of Tresca Stress (σ_T), the Principal Stress (σ_1), the Medium Stress (σ_2), and the Minimum Stress (σ_3) in the cross sections of inner leg and the outer leg, are presented in a series of figures (Fig. 2.35 - Fig. 2.42). In the cross section of the inner leg, the maximum

Tresca stress more than 600 Mpa is calculated around the contact surface for the wedging. Also, high stress region of more than 500 MPa is observed at the most thin section of the coil case.

The peak values of Tresca Stress (SIGE-T), von Mises Stress (SIGE-VM), SIG-X (which corresponds to the direct stress component in X-direction of global coordinate system), SIG-Y (which corresponds to the stress component in Y-direction), SIG-Z (corresponds to the stress component in Z-direction), and SIG-XY (the shear stress in the contact surface for the wedging), calculated in the cross section at the midplane of inner leg and the outer leg, are summarized in Table 2.3.

2.6.4 Stresses and Forces in the Outer Intercoil Structure

Regarding the four outer intercoil structures, the peak value of the Tresca stress (SIGE-T), the von Mises stress (SIGE-VM), the stress component in the out-of-plane direction (SIG-Y), and the in-plane shear stress (SIG-XY) are carefully checked. The results are summarized in Table 2.4.

The resultant forces act on the boundary of intercoil structure are calculated as shown in Table 2.5. Note that the component FX, FY, and FZ corresponds to the total force calculated in the global coordinate system of the TF coil. From these forces, the total force on the boundary in the radial direction (FR) and in the toroidal direction (FT), are calculated by using the following methods:

(1) For the boundary located in the plane of - 11.25 Deg.

$$FR = FX*\cos(11.25\ ) + FY*\sin(11.25\ )$$
$$FT = -FX*\cos(11.25\ ) + FY*\cos(11.15\ )$$

(2) For the boundary located in the plane of + 11.25 Deg.

$$FR = FX*\cos(11.25\ ) - FY*\sin(11.25\ )$$
$$FT = -FX*\cos(11.25\ ) - FY*\cos(11.15\ )$$

2.7 Summary

The stress analysis of ITER TF coil under normal loading condition at the End of Burn was performed by using idealized boundary condition specified by cyclic symmetry. The major results are summarized as follows ;

(1) The maximum displacements of the TF coil in the radial, the vertical and the out-of-plane direction are, - 13.5 mm, 16.5 mm and -26.5 mm, respectively.

(2) The maximum Tresca stress of 302 MPa is calculated in the winding by using the equivalent stiffness. Because of the simple modeling of insulator between the winding and the coil case, this value is considered as a result of artificial peaking to a certain extent.

(3) The maximum Tresca stress of 655 MPa is appeared in the inner leg of TF coil case. Compared with the allowable stress value of 800 MPa specified for the static loading conditions, stress of the coil case is within the allowable limit.

(4) However, compared with 600 MPa, which was tentatively specified for the stress limit on fatigue cycles, the stress in the outer ring over this limit. Further investigation and the detailed stress analysis are required to specify the mechanical safety margin of TF coil.

Table 2.1 Material Properties employed for the FEM analysis

Component	Winding	Insulator	Coil Case	Supporting Structure and Outer Intercoil Structure
Material		FRP Block	Japanese Cryogenic Steel (JCS)	JCS
Character	Orthotropic, linear-elastic	Isotropic, Linear-elastic	Isotropic, Linear-elastic	Isotropic, Linear-elastic
Young's Modulus				
E_r	73.2 GPa	19.6 GPa	196.0 GPa	196.0 GPa
E_θ	75.6 GPa	19.6 GPa	196.0 GPa	196.0 GPa
E_z	84.8 GPa	19.6 GPa	196.0 GPa	196.0 GPa
Poisson's Ratio				
$U_{r\theta}$	0.150	0.100	0.300	0.300
$U_{\theta r}$	0.155	0.100	0.300	0.300
U_{rz}	0.149	0.100	0.300	0.300
U_{zr}	0.173	0.100	0.300	0.300
$U_{\theta z}$	0.154	0.100	0.300	0.300
$U_{z\theta}$	0.173	0.100	0.300	0.300
Shear Modulus				
$G_{r\theta}$	31.8 GPa	8.9 GPa	75.4 GPa	75.4 GPa
$G_{\theta z}$	32.5 GPa	8.9 GPa	75.4 Gpa	75.4 GPa
G_{zr}	36.5 GPa	8.9 GPa	75.4 GPa	75.4 GPa

Table 2.2 Stresses in the Winding Pack

Stress Component	Maximum Value (MPa) Inner Leg	Outer Leg
SIG-X	- 75.9	- 32.4
SIG-Y	-129.4	- 45.5
SIG-Z	63.7	104.9
SIG-XY	6.5	3.2
SIG-YZ	- 1.8	14.0
SIG-XZ	- 2.9	- 5.7

Table 2.3 Stresses in the TF Coil Case

Stress Component	Maximum Value (MPa) Inner Leg	Outer Leg
SIGE-T (Tresca)	654.6	341.0
SIGE-VM (von Mises)	572.3	324.8
SIG-X	173.5	218.5
SIG-Y	- 392.0	113.7
SIG-Z	302.8	173.5
SIG-XY	- 83.2	- 80.9

Table 2.4 Stresses in the Outer Intercoil Structure

Stress Component	Maximum Value (MPa)			
	Upper(-)	Upper(+)	Lower(-)	Lower(+)
SIGE-T	276.4	351.8	351.8	277.3
SIGE-VM	261.7	346.9	345.9	261.7
SIG-Y	196.0	263.6	262.6	196.0
SIG-XY	35.2	- 50.1	50.1	- 35.2

Table 2.5 Forces acts on the Outer Intercoil Structure

Force Component	Force Sums for the Boundaries of the Outer Intercoil Structure			
	Upper(-)	Upper(+)	Lower(-)	Lower(+)
FX (MN)	8.12	- 8.12	- 8.12	8.12
FY (MN)	91.86	- 92.00	91.91	- 91.91
FZ (MN)	- 32.90	- 32.90	32.90	32.90
FR (MN)	25.88	9.98	9.97	25.89
FT (MN)	88.51	91.81	91.72	88.56

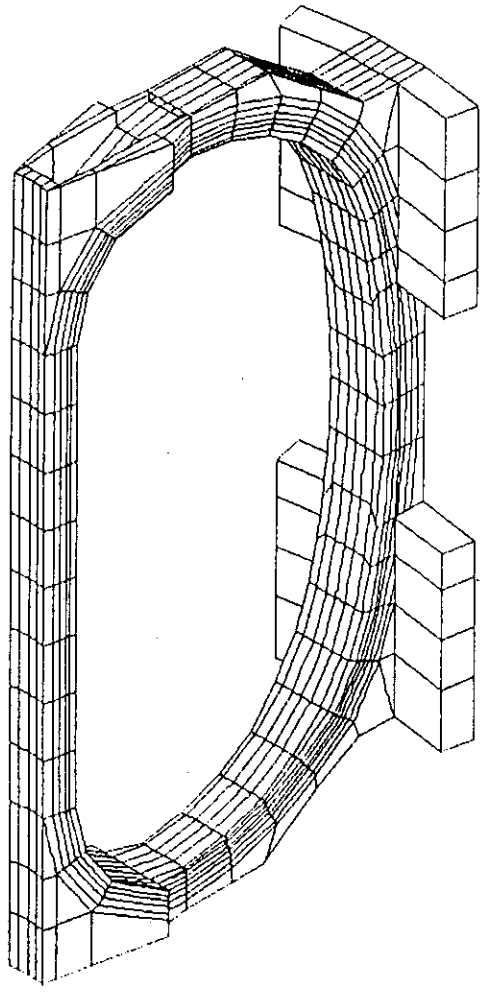

Fig. 2.1 FEM model of ITER TF coil and outer intercoil structure (1/16 sector of TF coil system)

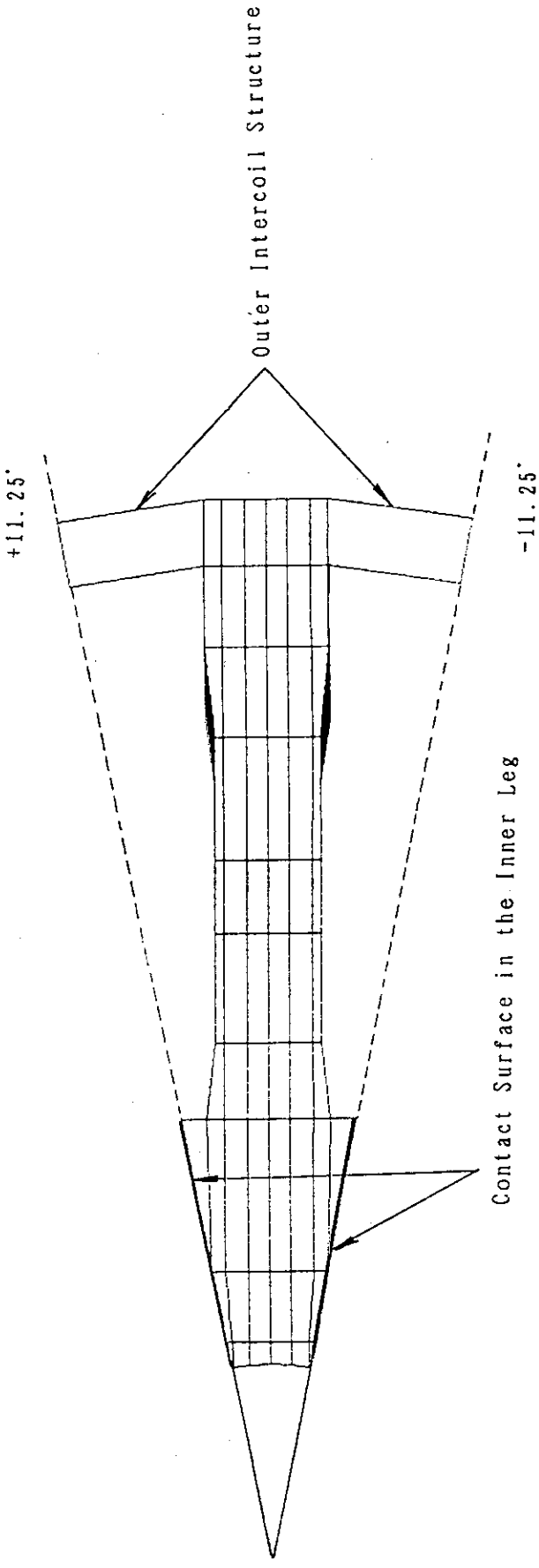

Fig. 2.2 FEM model of ITER TF coil and outer intercoil structure (1/16 sector of TF coil system, view from the top)

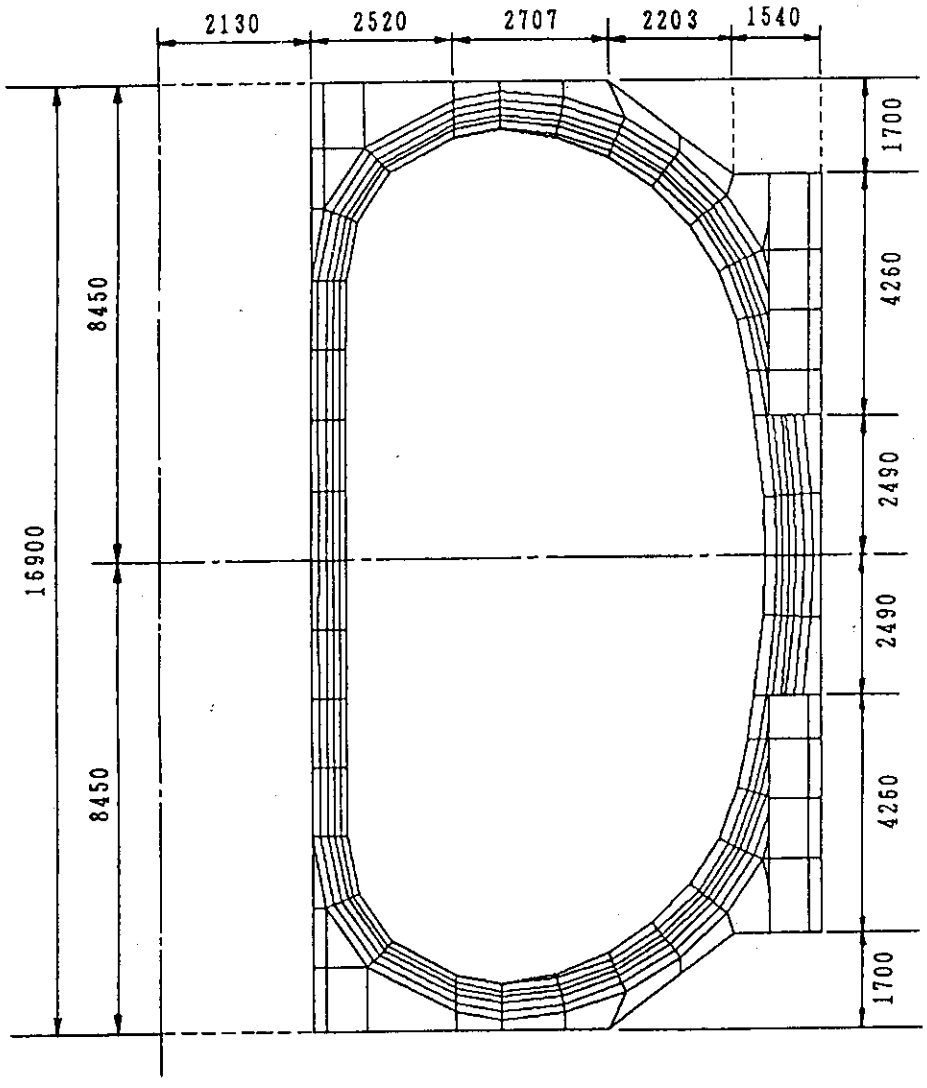

Fig. 2.3 Dimensions of the FEM model : side view

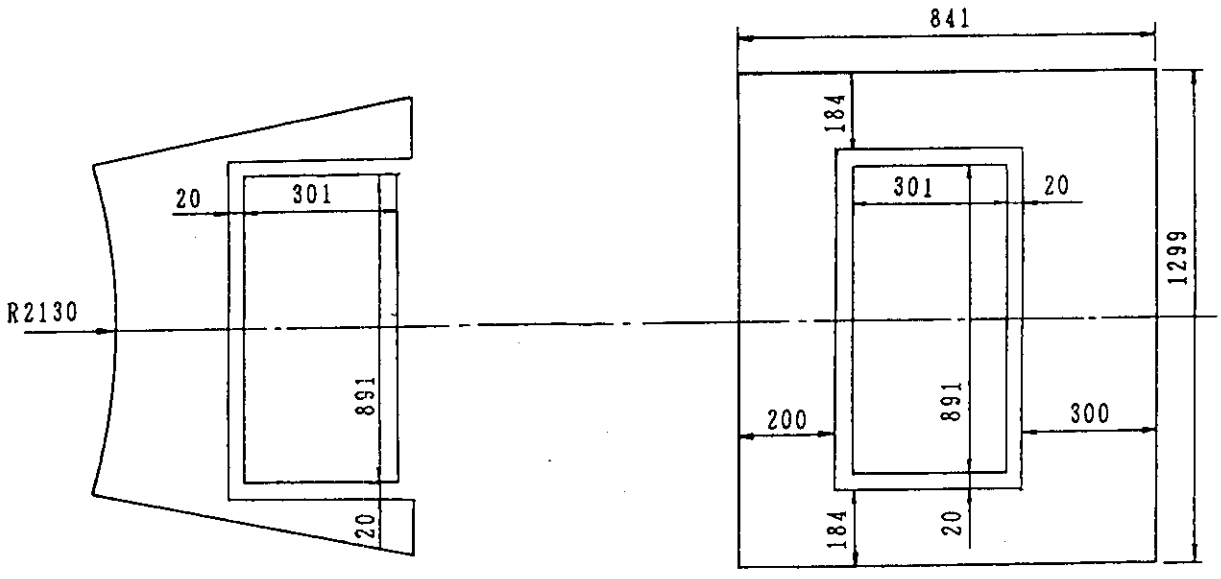

Fig. 2.4 Dimensions of the FEM model : cross section at the midplane

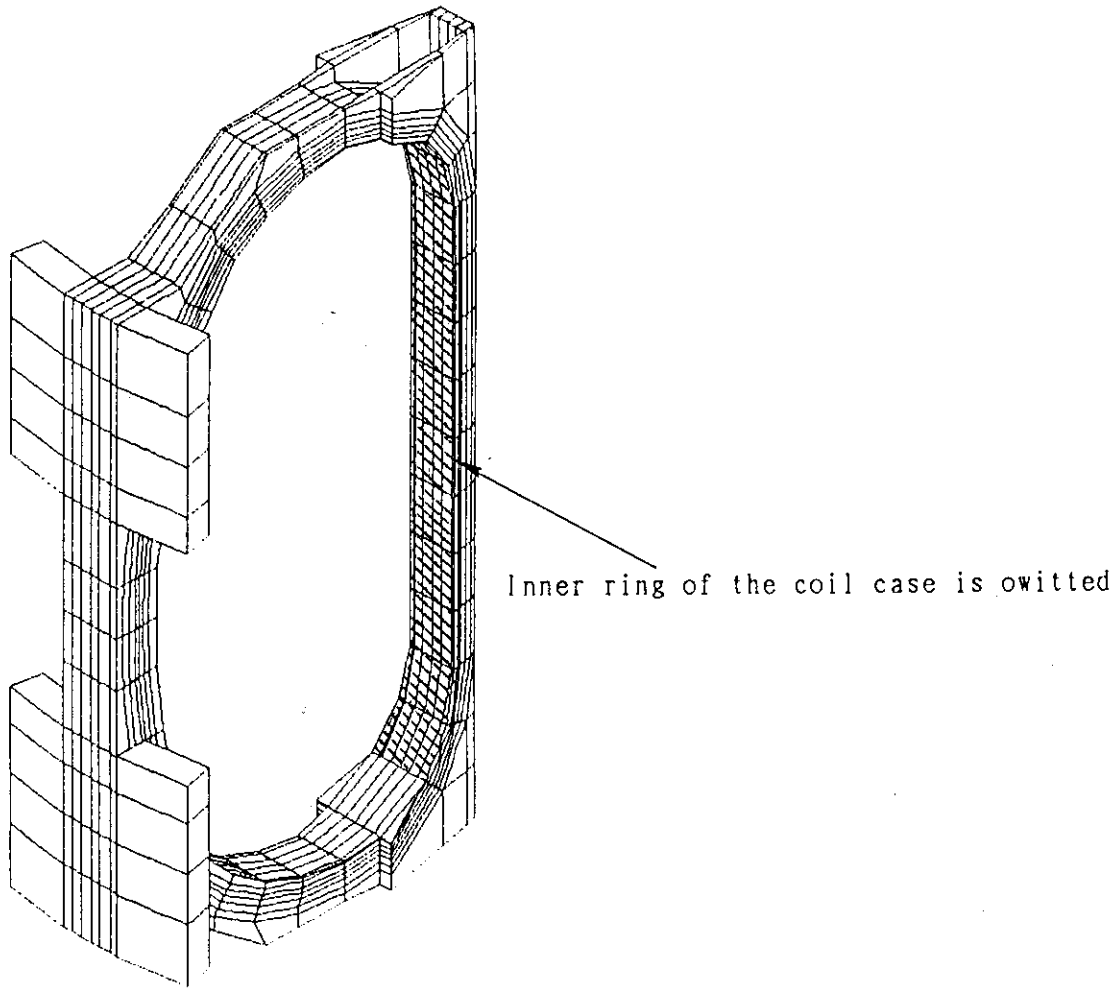

Fig. 2.5 Coil case at the region of inner Leg, the inner ring is omitted

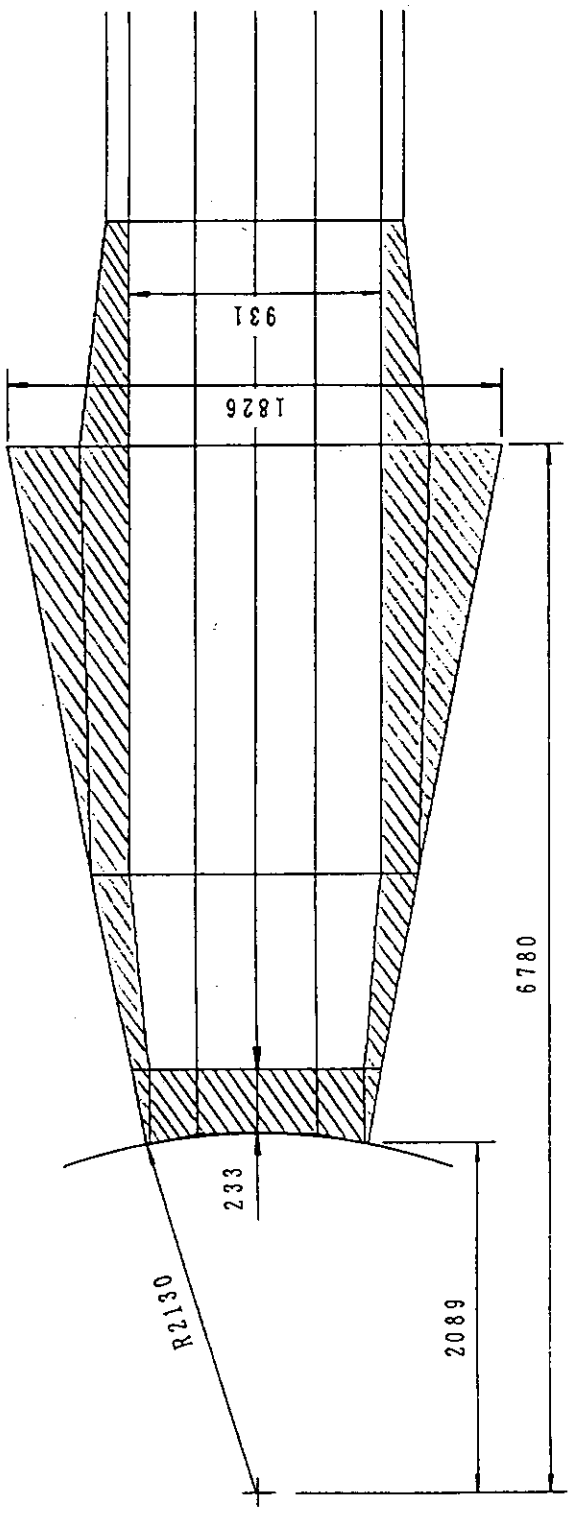

Fig. 2.6 Dimensions of the inner leg : view from the top

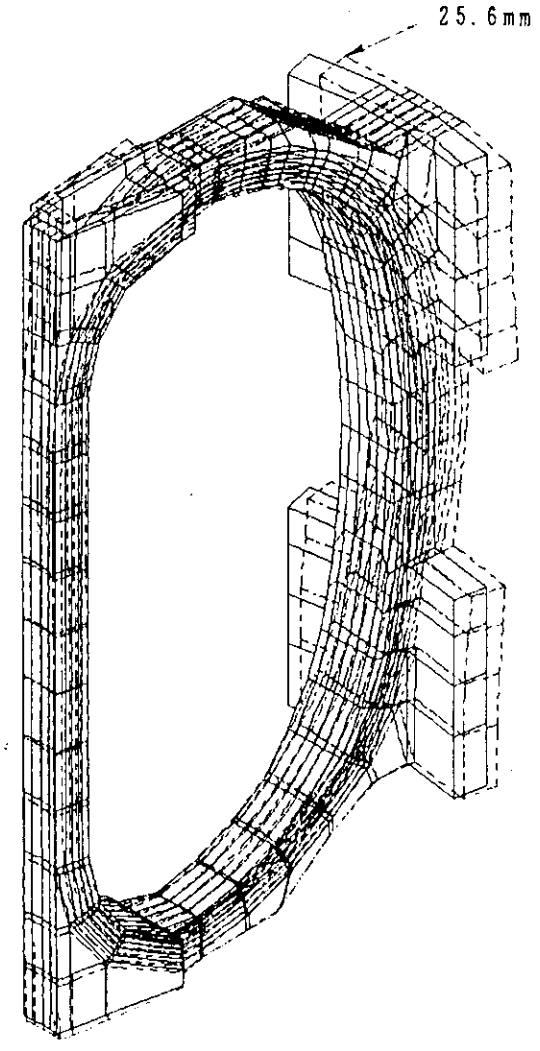

Fig. 2.7 Deformation of the ITER TF Coil at the End of Burn

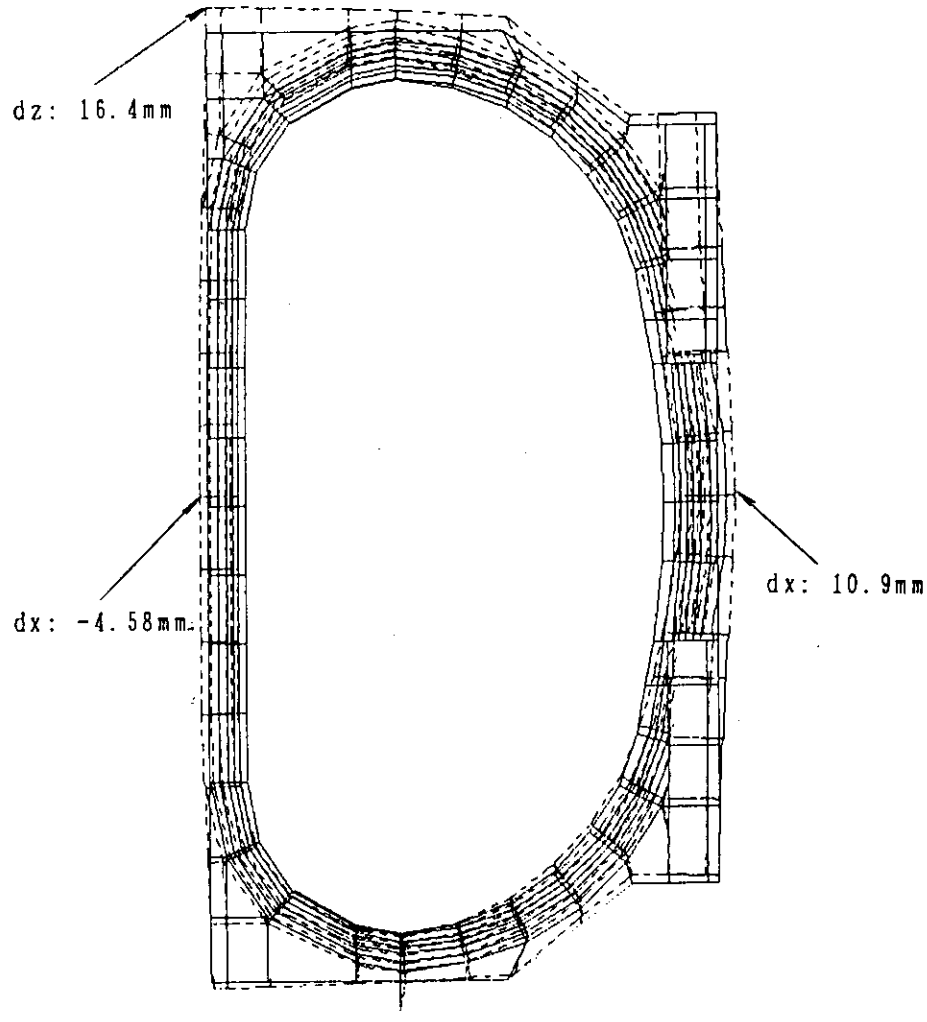

Fig. 2.8 Deformation of the ITER TF Coil at the End of Burn : side view

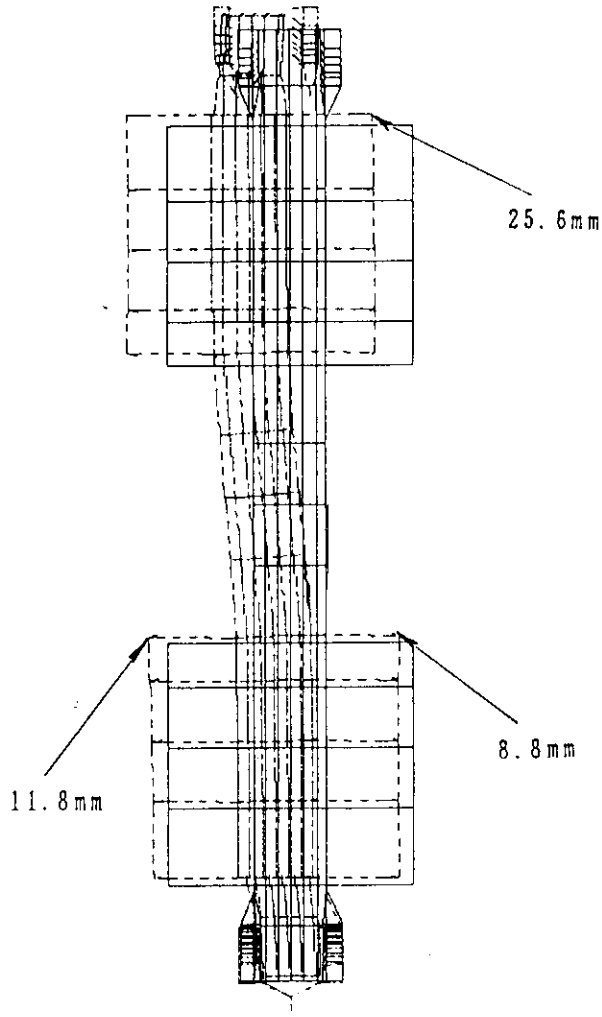

Fig. 2.9 Deformation of the ITER TF Coil at the End of Burn
: view from the back

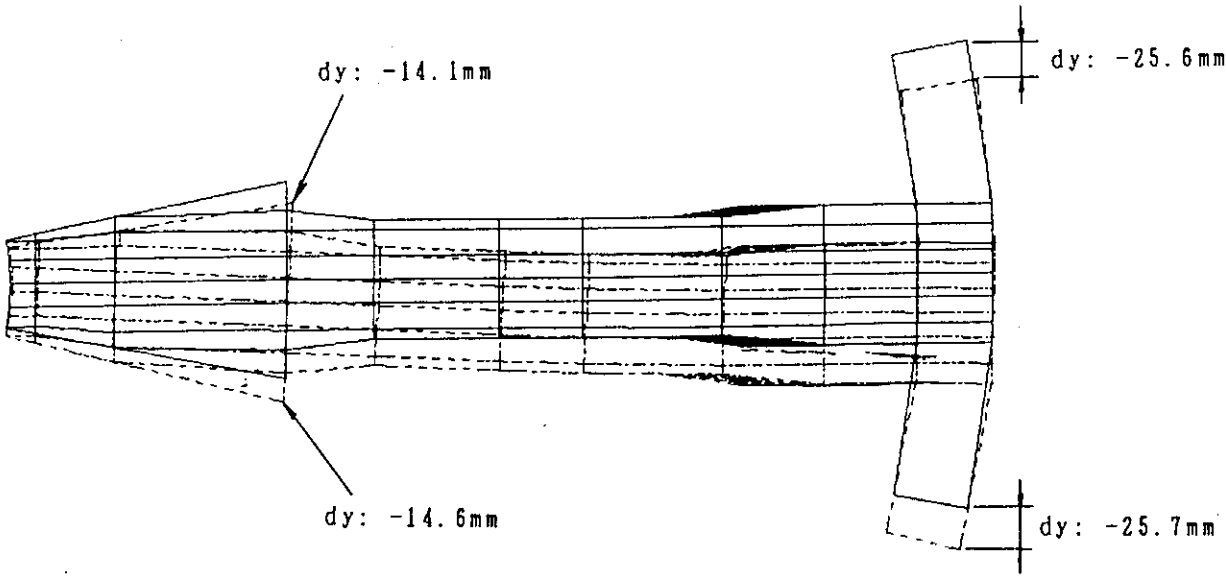

Fig. 2.10 Deformation of the ITER TF Coil at the End of Burn
: view from the top

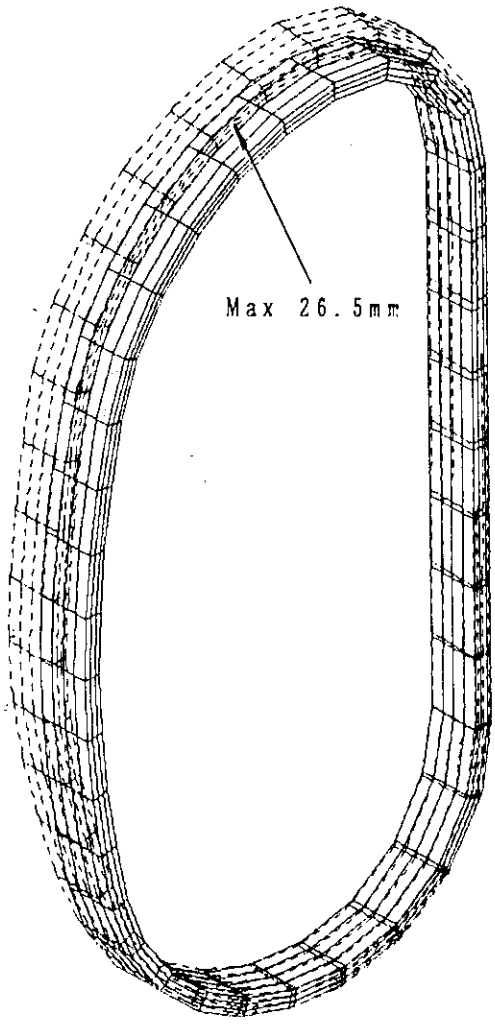

Fig. 2.11 Displacement of the winding pack at the End of Burn

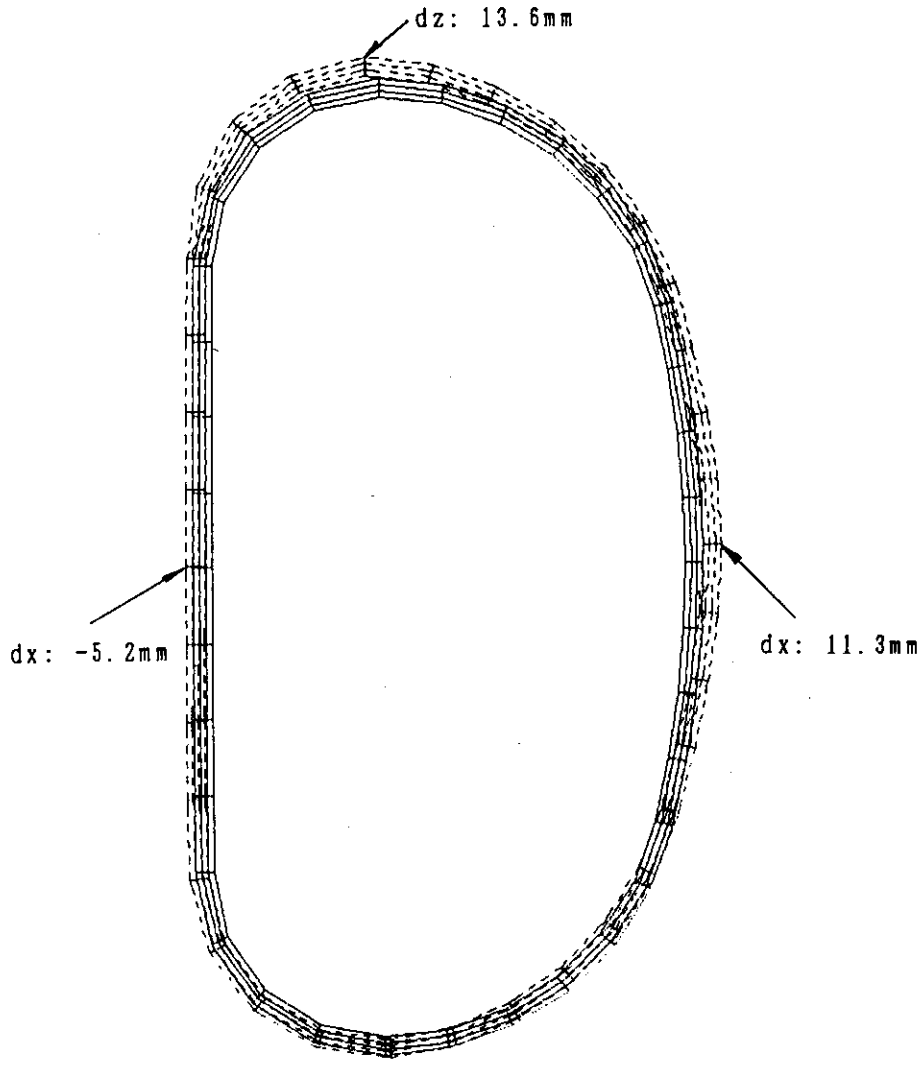

Fig. 2.12 Displacement of the winding pack at the End of Burn : side view

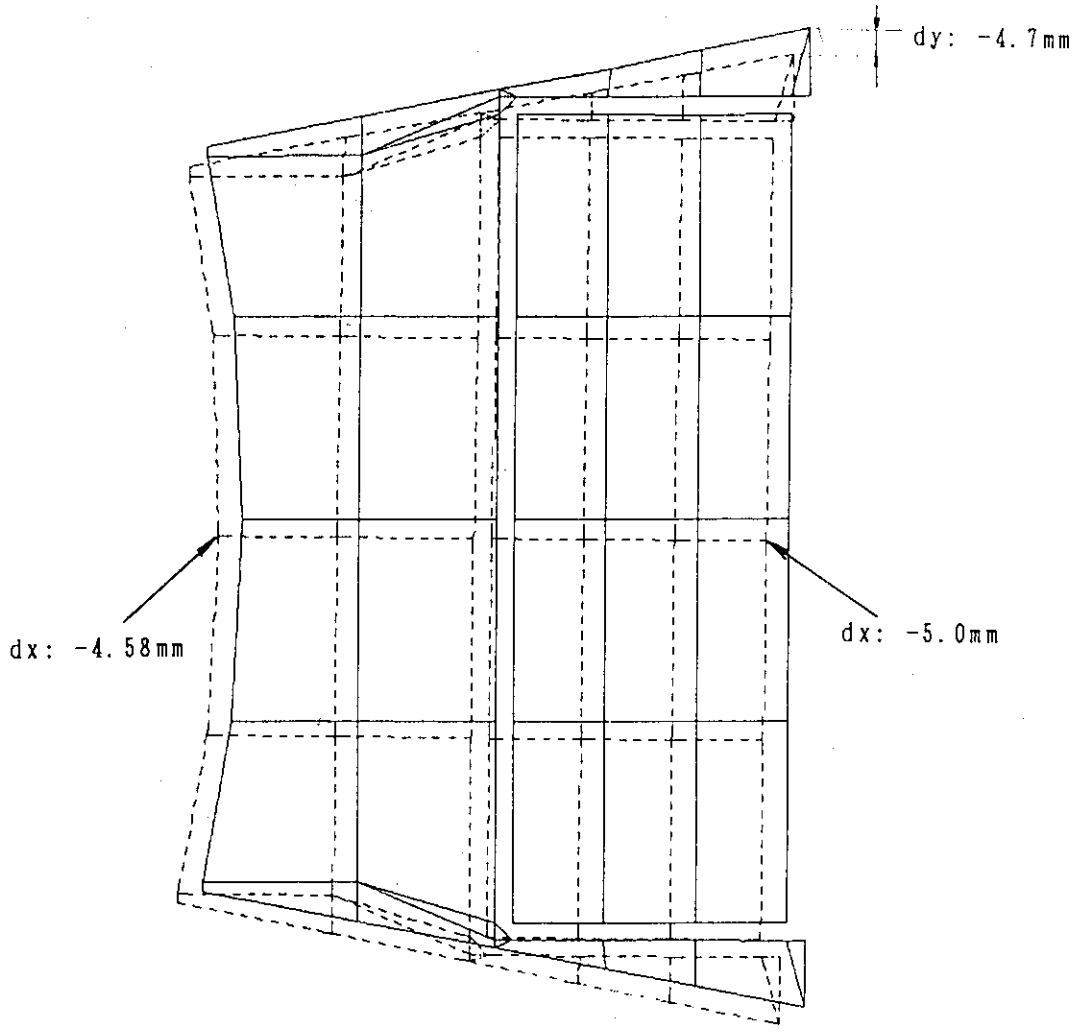

Fig. 2.13 Displacement of the coil case and winding at the End of Burn : midplane of the inner leg

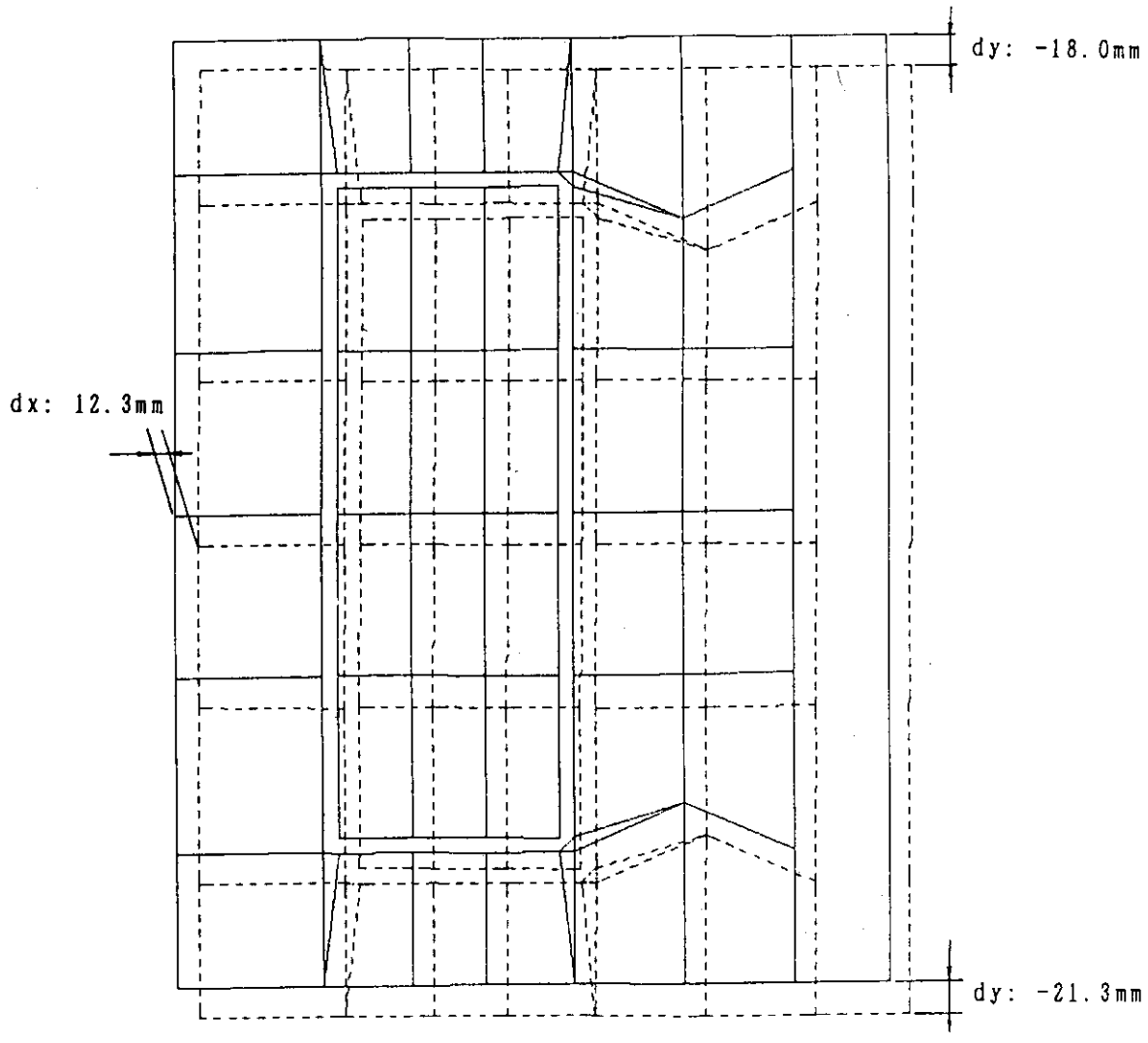

Fig. 2.14 Displacement of the coil case and winding at the End of Burn : midplane of the outer leg

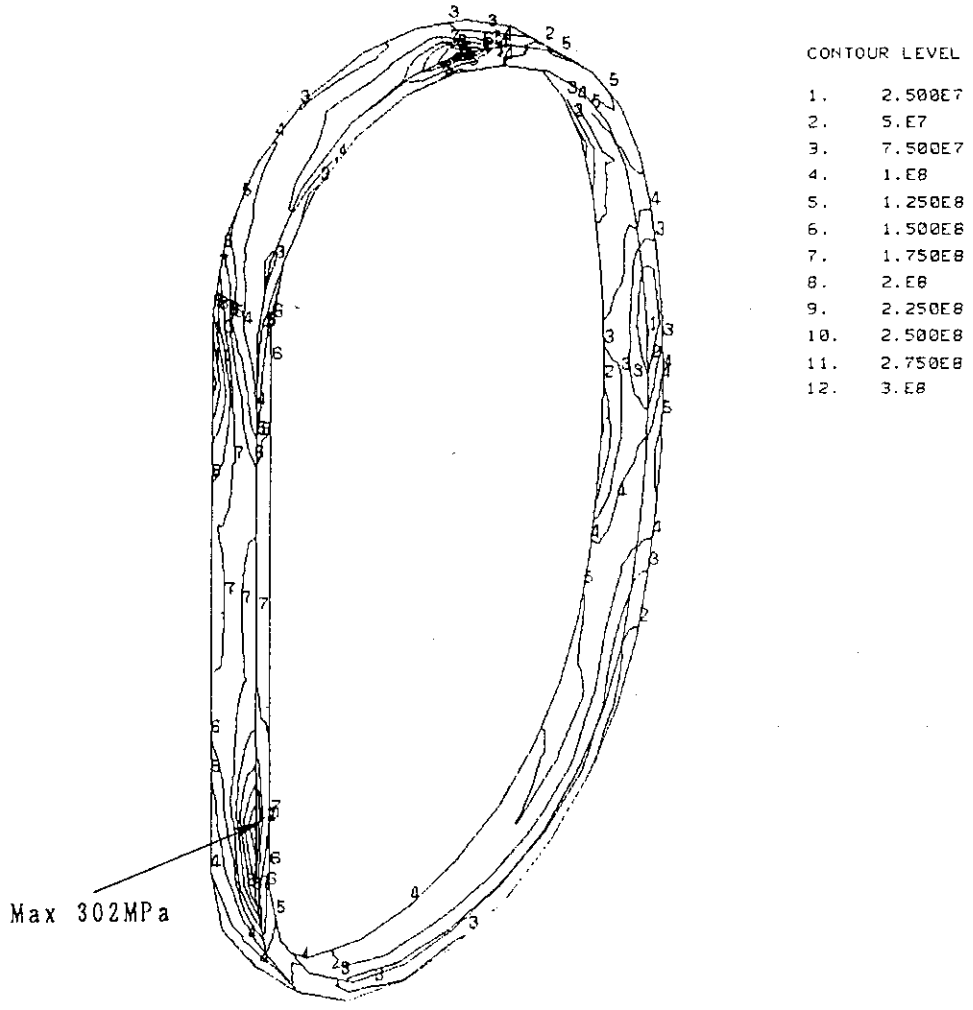

Fig. 2.15 Contour of the constant Tresca Stress (σ_T) of the winding at the End of Burn

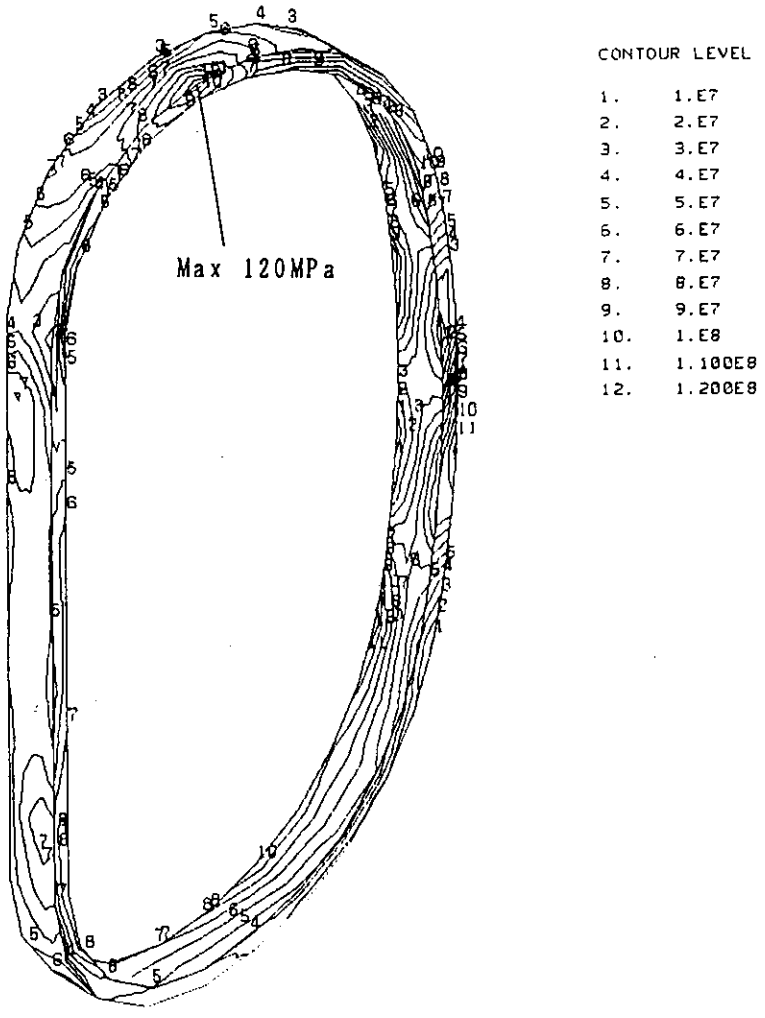

Fig. 2.16 Contour of the constant Principal Stress (σ_1) of the winding at the End of Burn

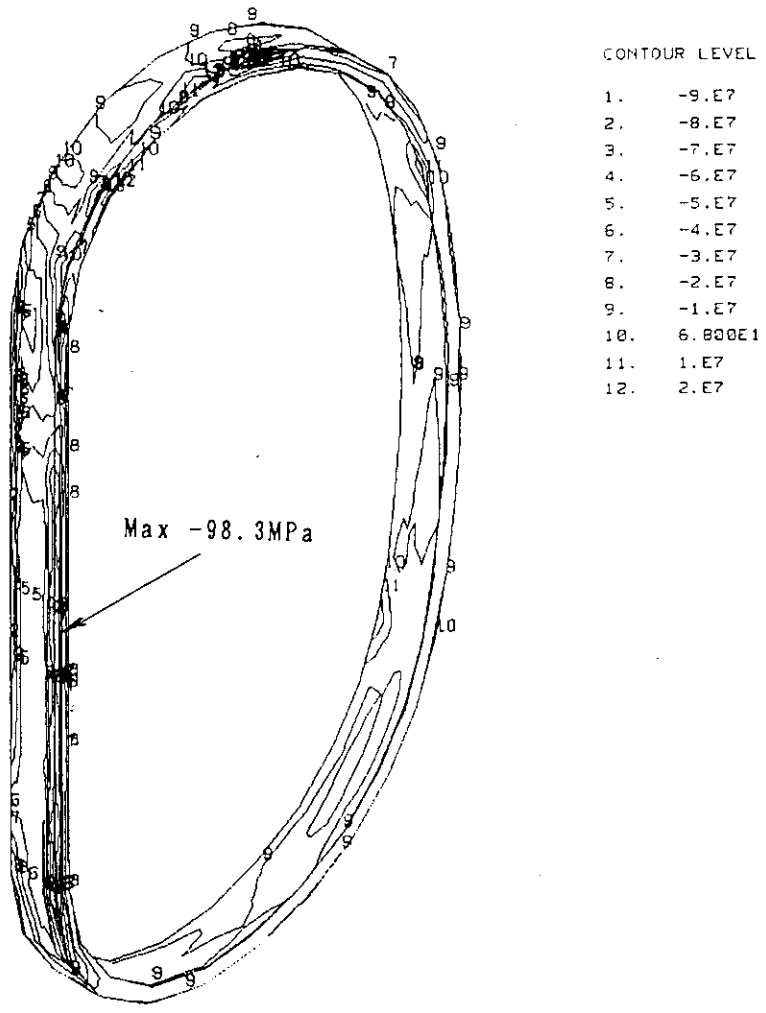

Fig. 2.17 Contour of the constant Medium Stress (σ_2) of the winding at the End of Burn

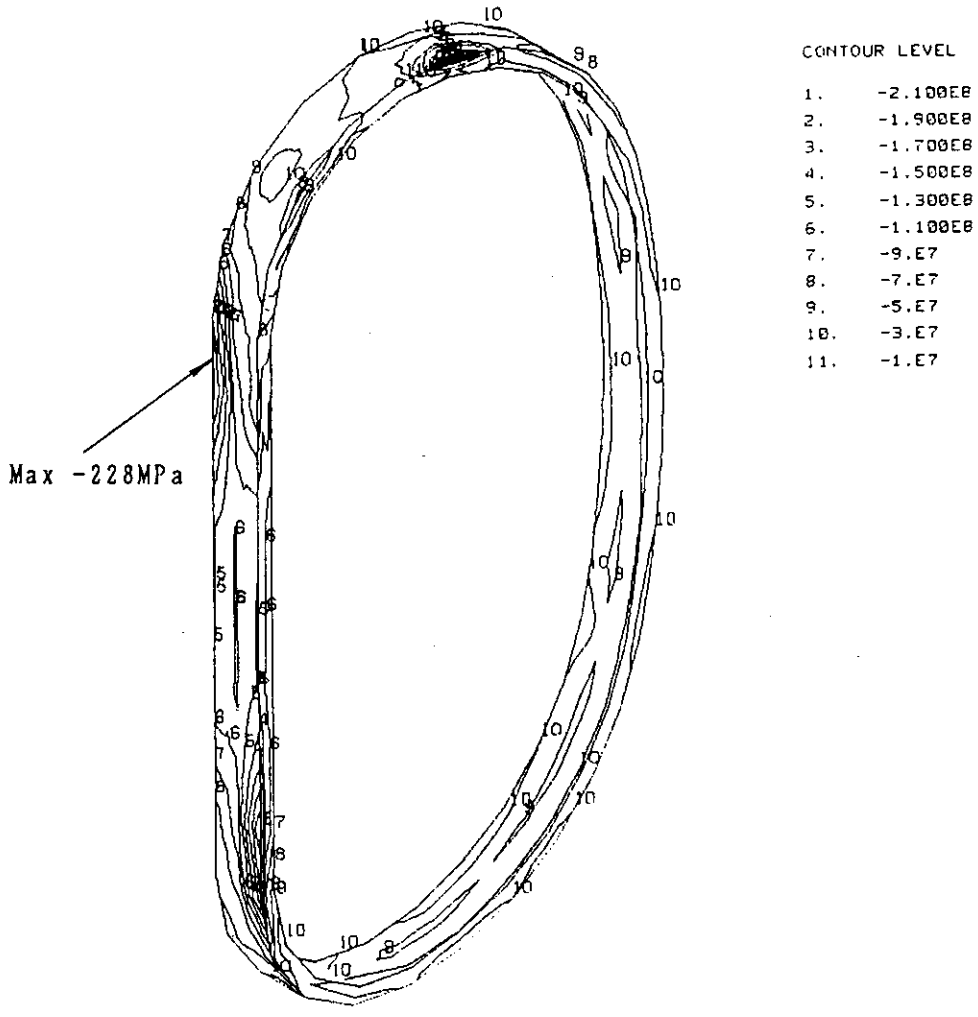

Fig. 2.18 Contour of the constant Minimum Stress (σ_3) of the winding at the End of Burn

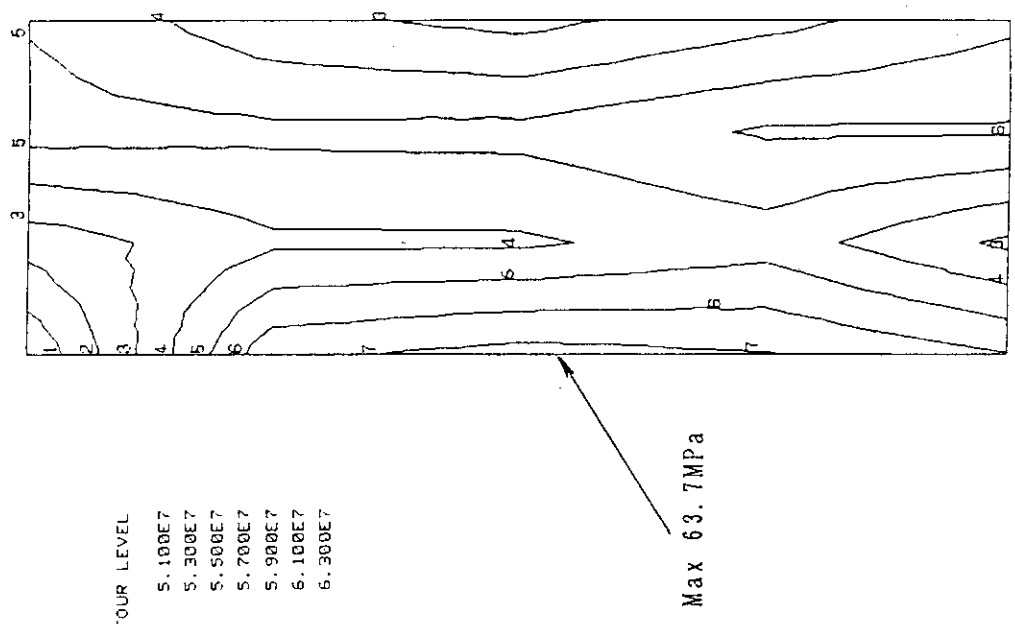

Fig. 2.20 Contour of the constant Principal Stress (σ_1) in the winding cross section of the inner leg at the End of Burn

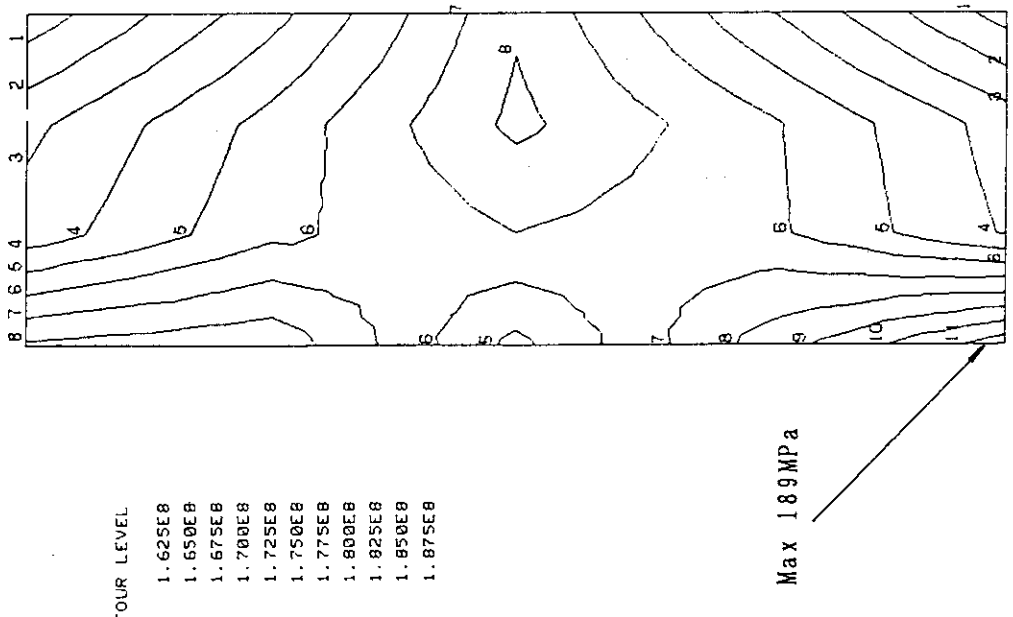

Fig. 2.19 Contour of the constant Tesca Stress (σ_T) in the winding cross section of the inner leg at the End of Burn

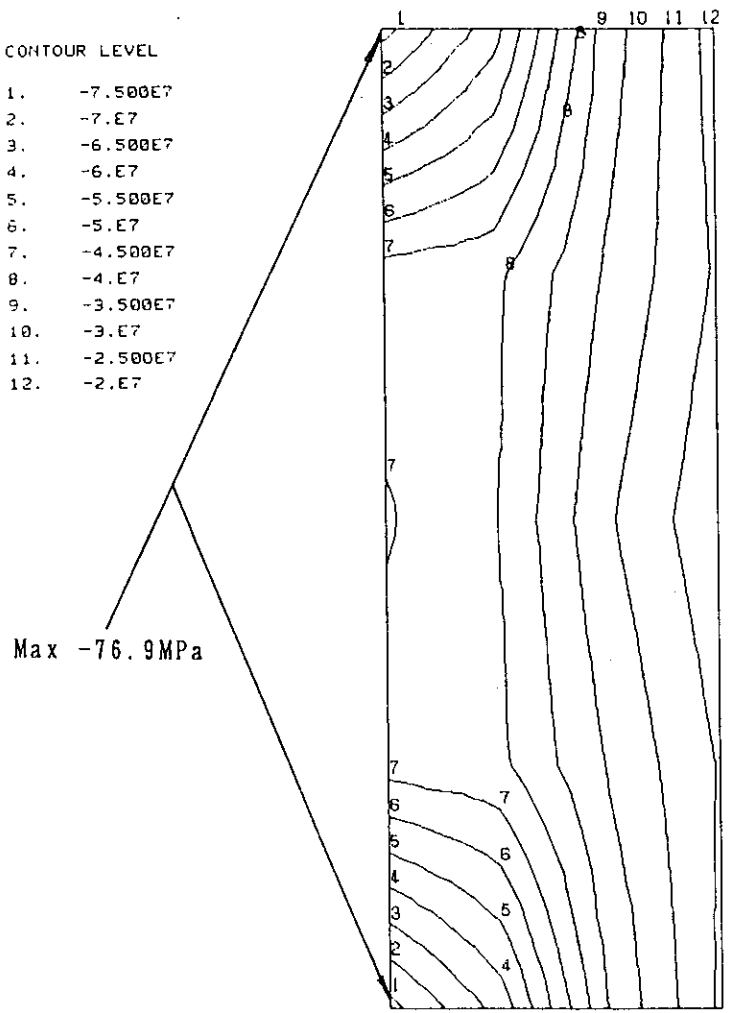

Fig. 2.21 Contour of the constant Medium Stress (σ_2) in the winding cross section of the inner leg at the End of Burn

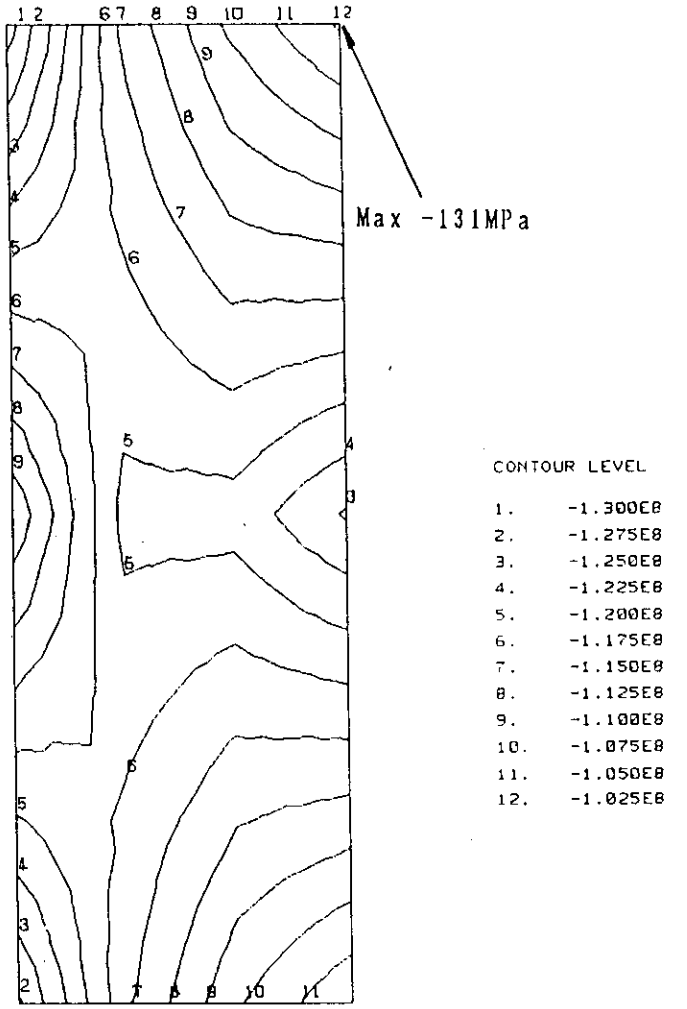

Fig. 2.22 Contour of the constant Minimum Stress (σ_3) in the winding cross section of the inner leg at the End of Burn

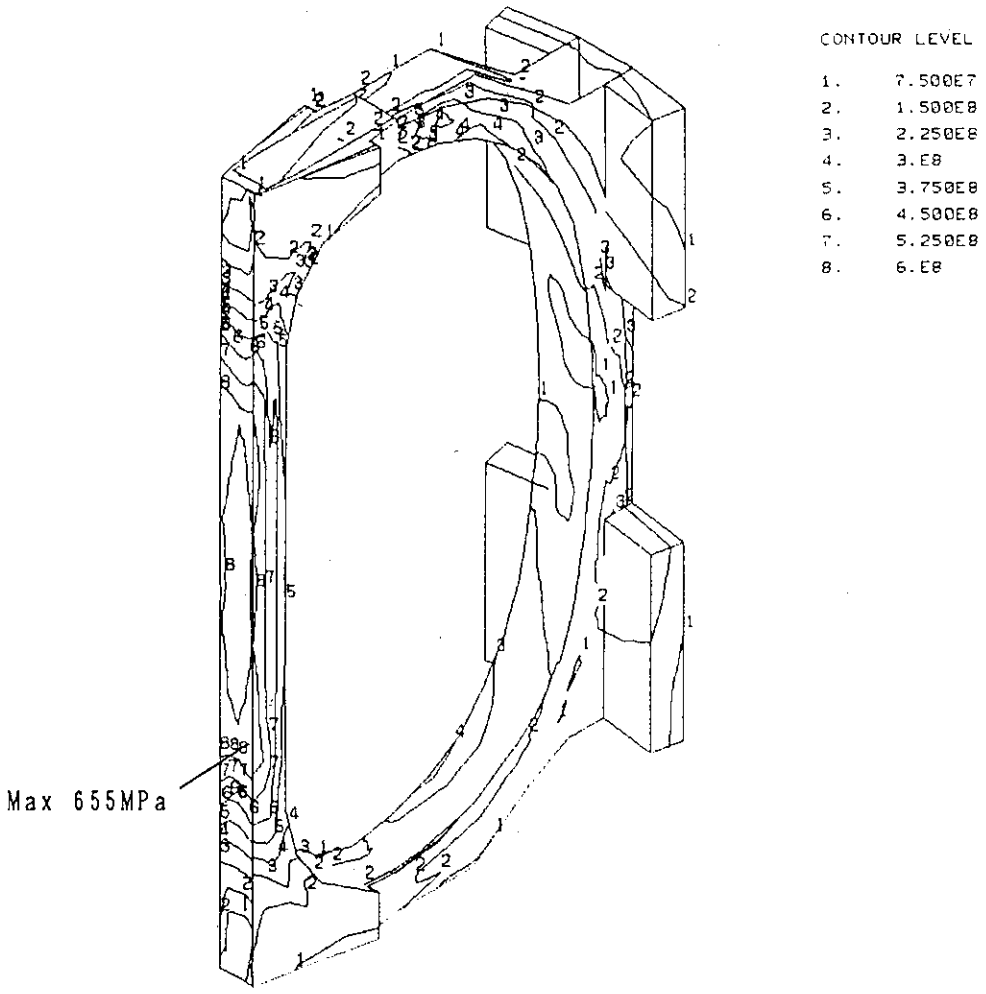

Fig. 2.23 Contour of the constant Tesca Stress (σ_T) of the TF coil case at the End of Burn

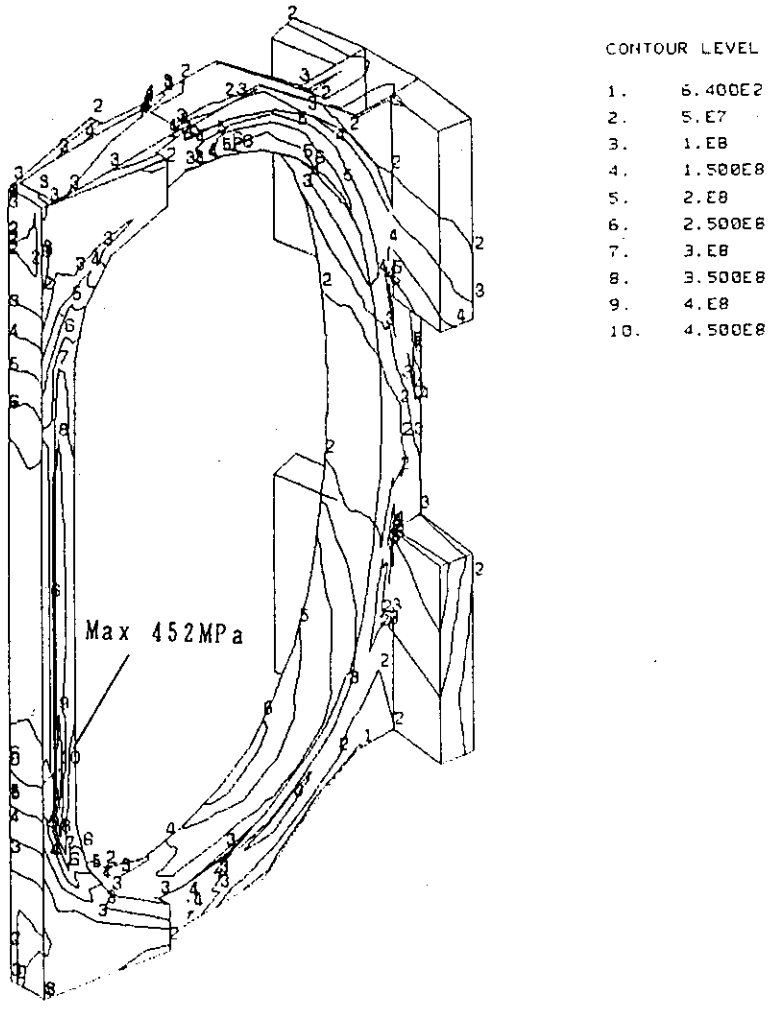

Fig. 2.24 Contour of the constant Principal Stress (σ_1) of the TF coil case at the End of Burn

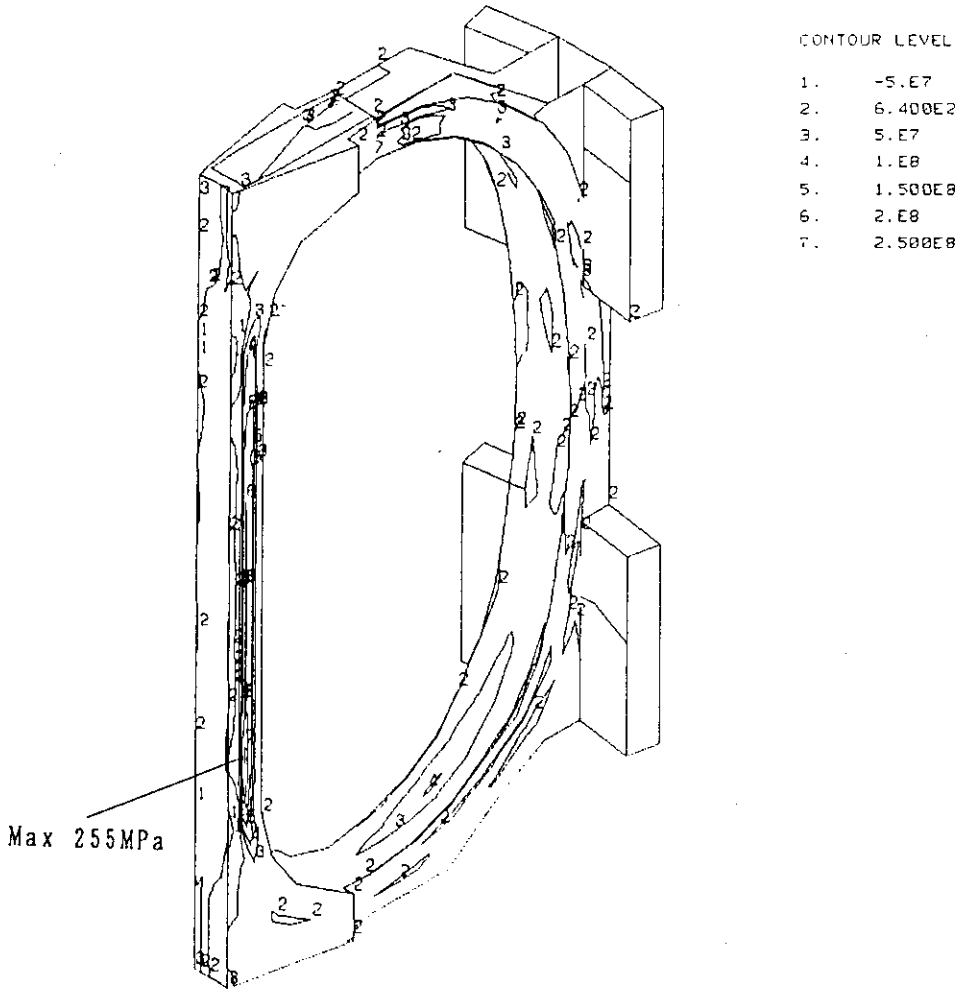

Fig. 2.25 Contour of the constant Medium Stress (σ_2) of the TF coil case at the End of Burn

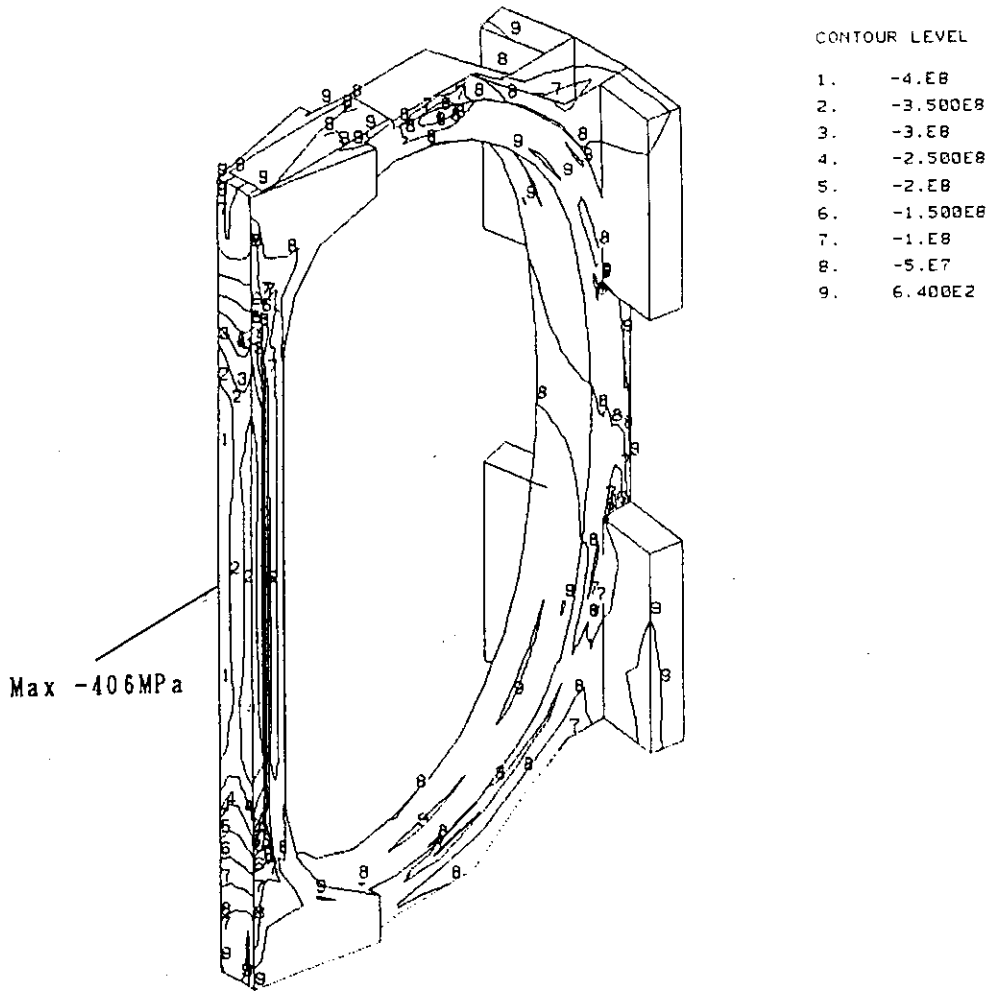

Fig. 2.26 Contour of the constant Minimum Stress (σ_3) of the TF coil case at the End of Burn

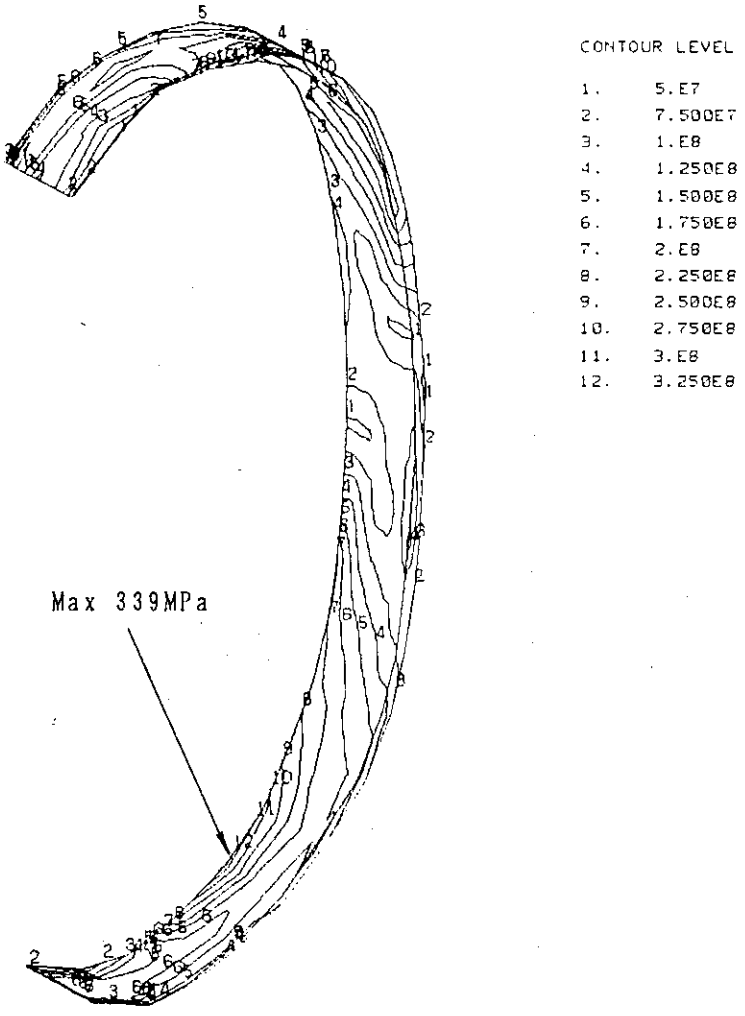

Fig. 2.27 Contour of the constant Tesca Stress (σ_T) of the inner ring at the End of Burn

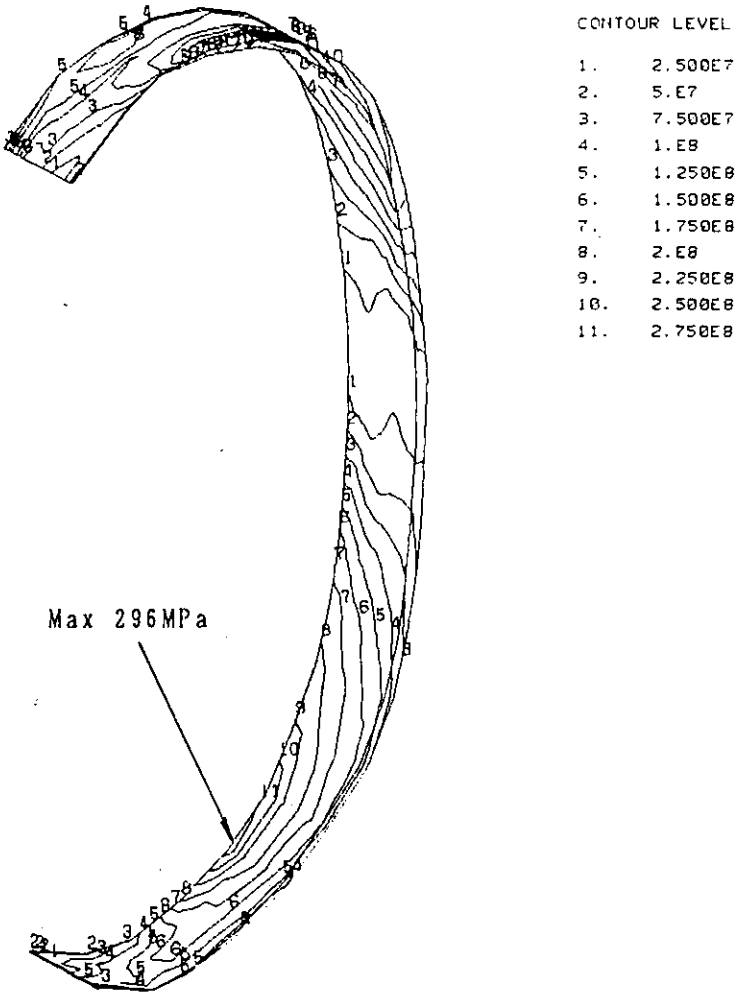

Fig. 2.28 Contour of the constant Principal Stress (σ_1) of the inner ring coil case at the End of Burn

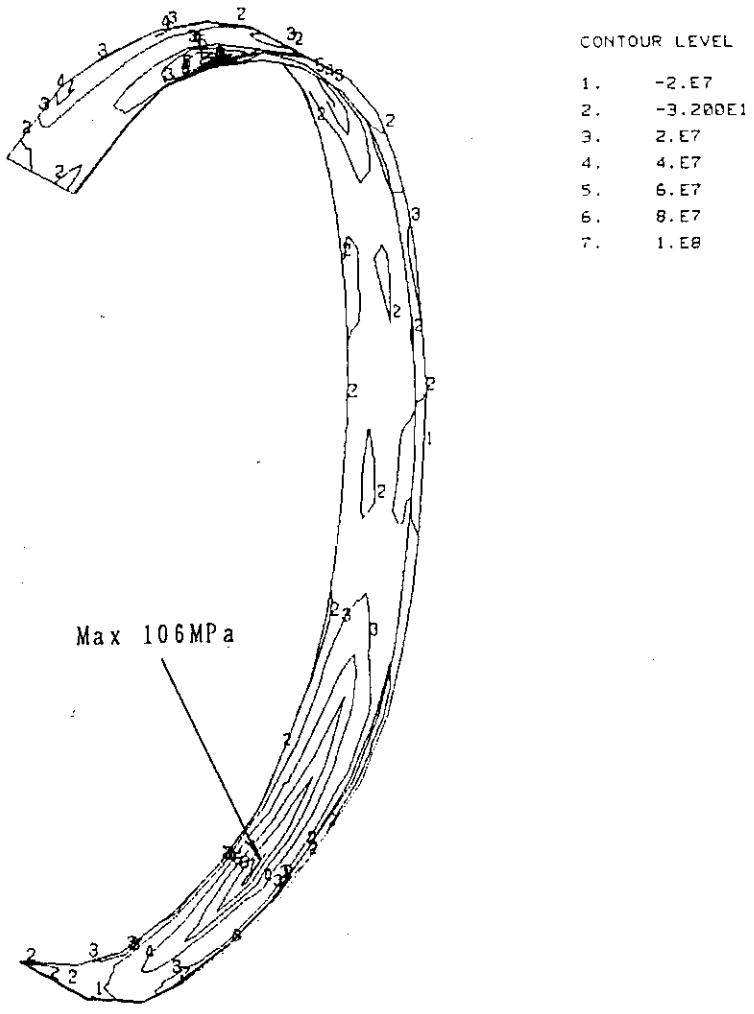

Fig. 2.29 Contour of the constant Medium Stress (σ_2) of the inner ring at the End of Burn

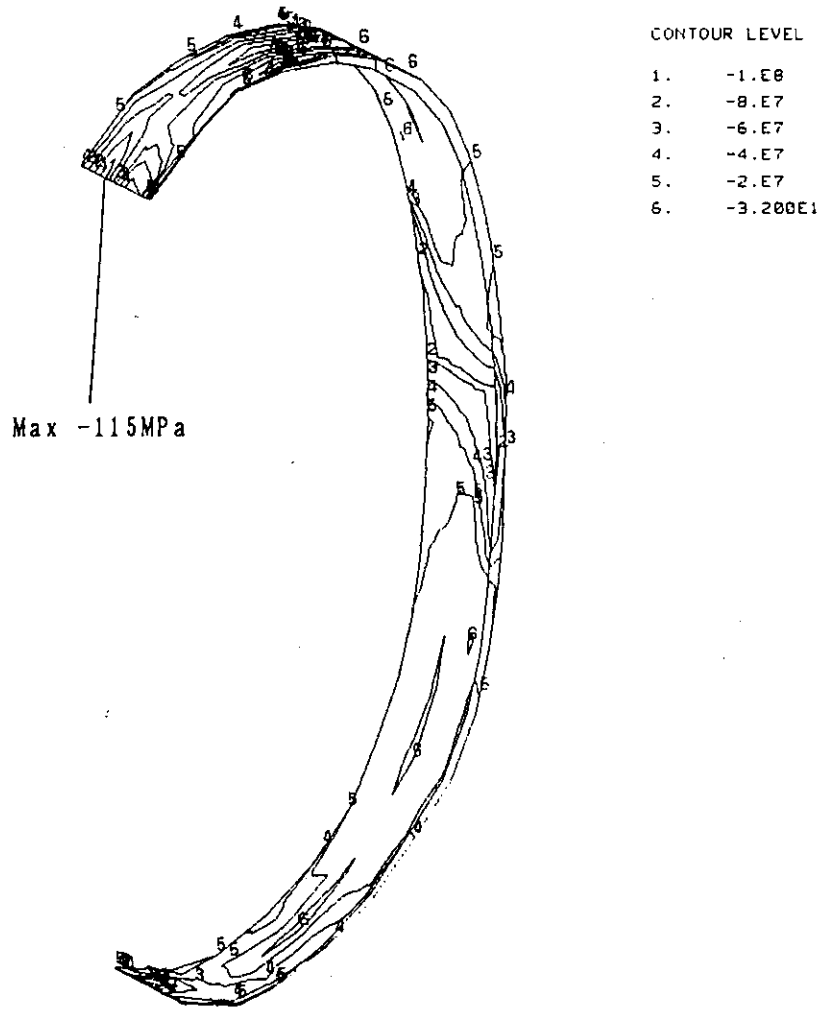

Fig. 2.30 Contour of the constant Minimum Stress (σ_3) of the inner ring at the End of Burn

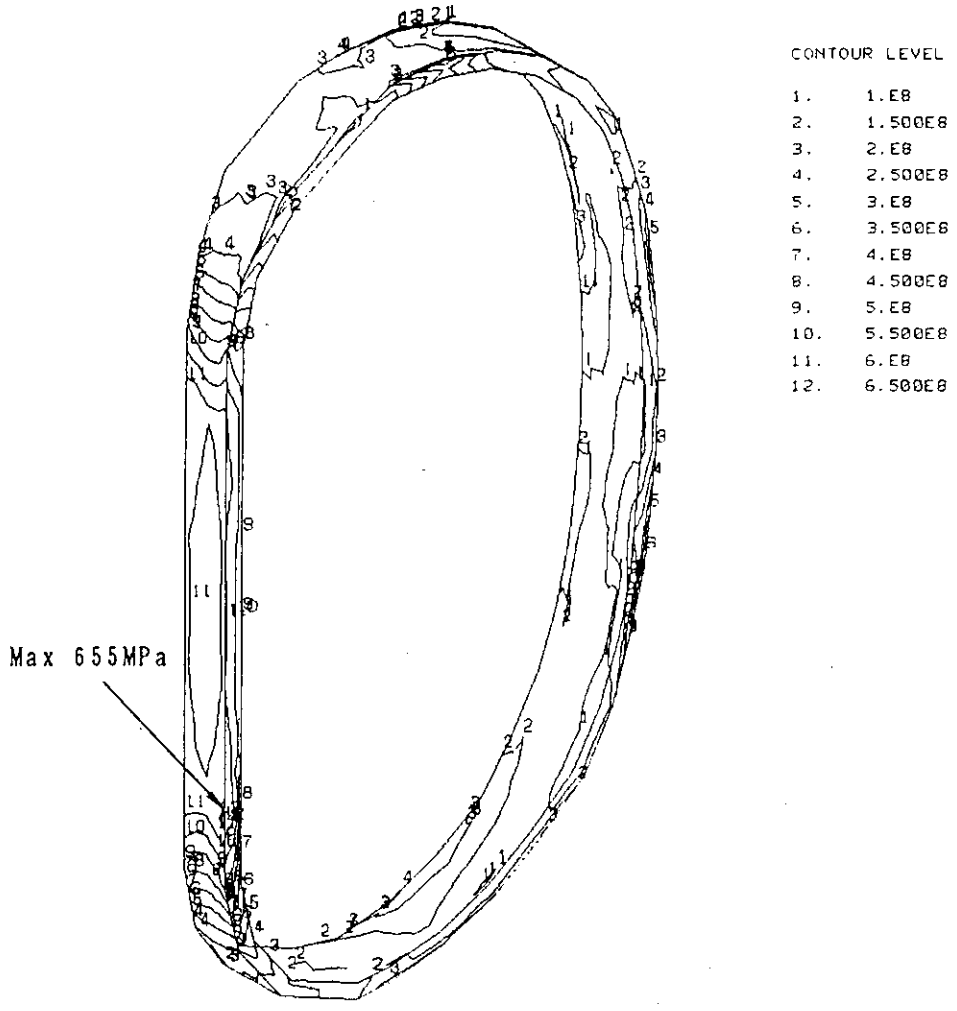

Fig. 2.31 Contour of the constant Tesca Stress (σ_T) of the outer ring at the End of Burn

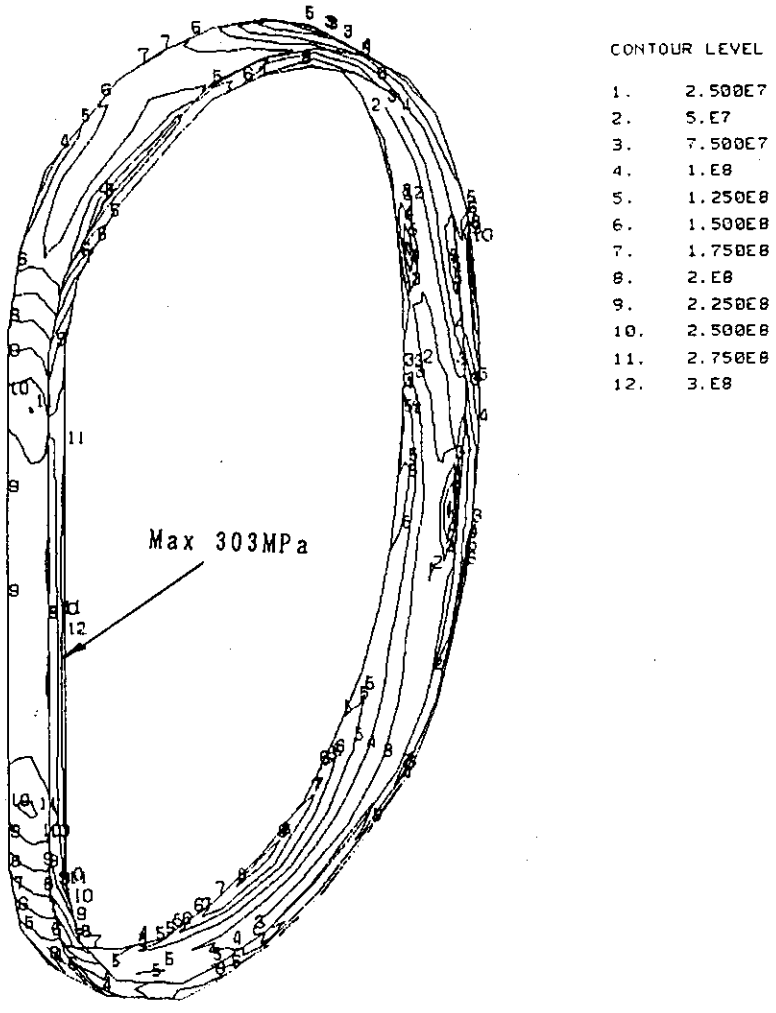

Fig. 2.32 Contour of the constant Principal Stress (σ_1) of the outer ring at the End of Burn

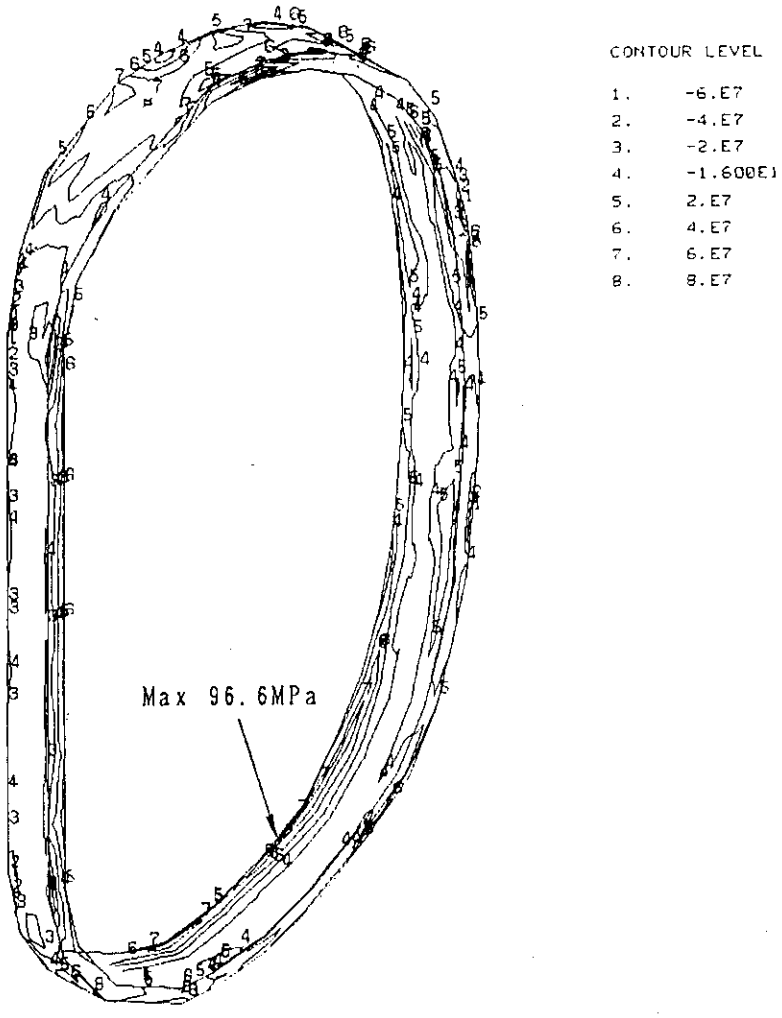

Fig. 2.33 Contour of the constant Medium Stress (σ_2) of the outer ring at the End of Burn

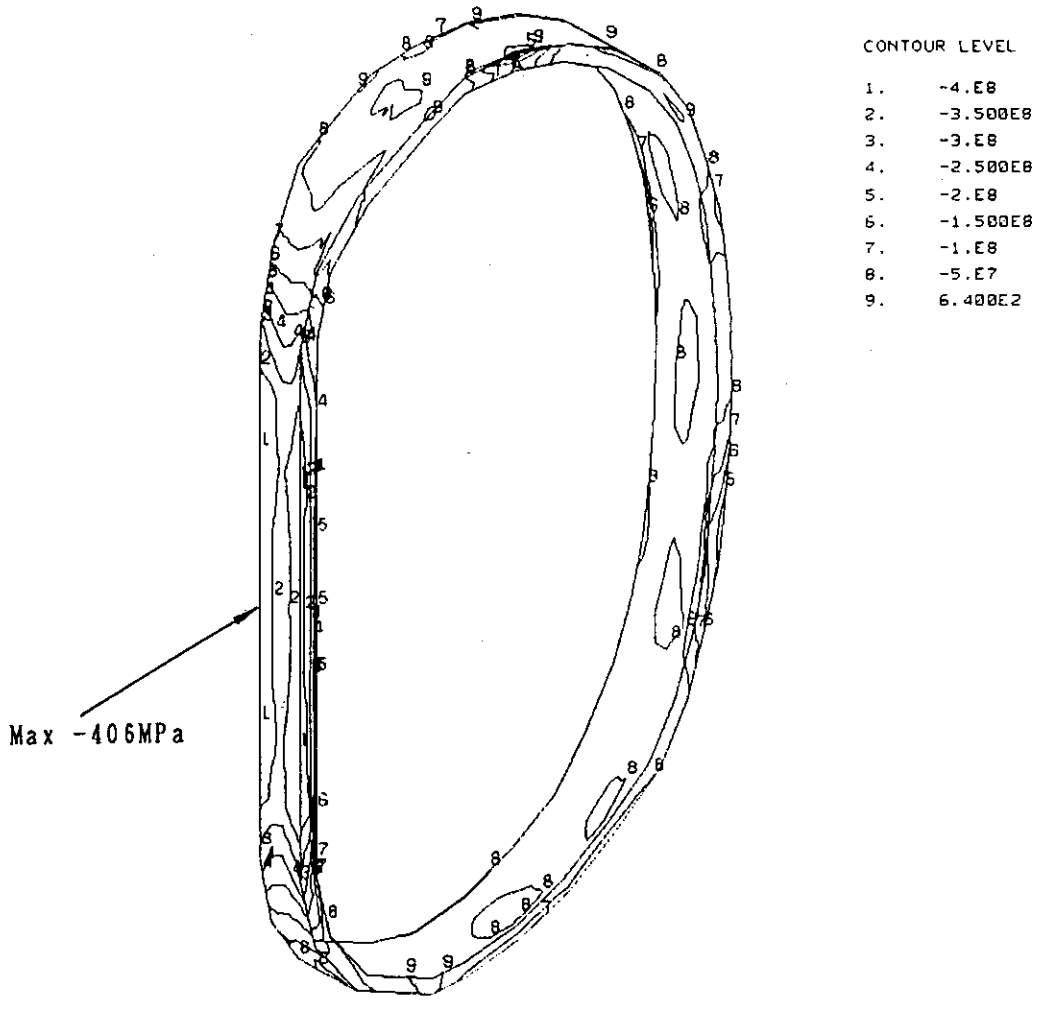

Fig. 2.34 Contour of the constant Minimum Stress (σ_3) of the outer ring at the End of Burn

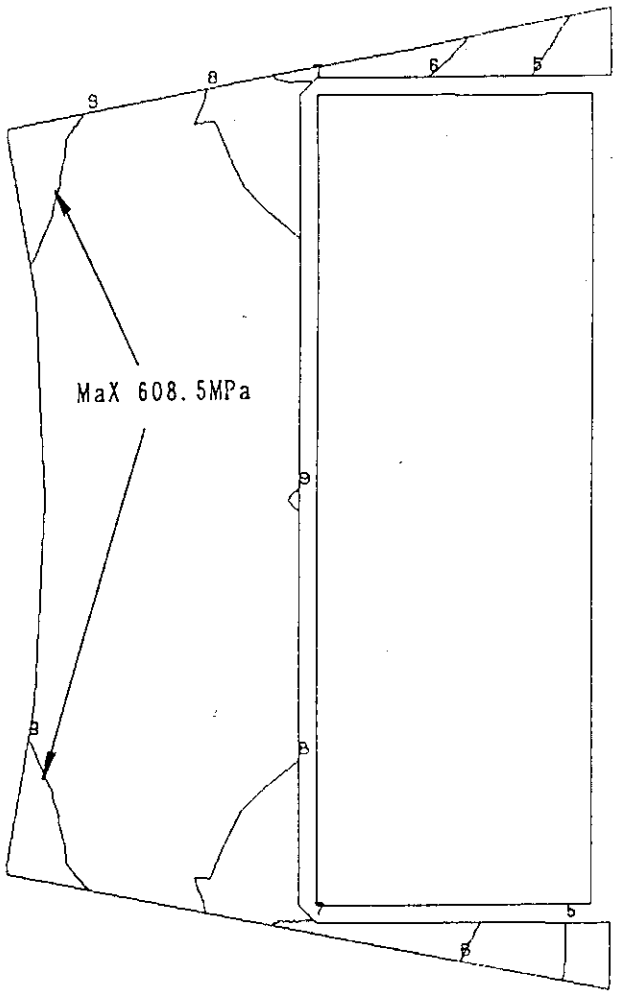

CONTOUR LEVEL (MPa)

1. 1.96E2
2. 2.45E2
3. 2.94E2
4. 3.43E2
5. 3.92E2
6. 4.41E2
7. 4.90E2
8. 5.39E2
9. 5.88E2

Fig. 2.35 Contour of the constant Tesca Stress (σ_T) in the cross section of TF coil in the inner leg at the End of Burn

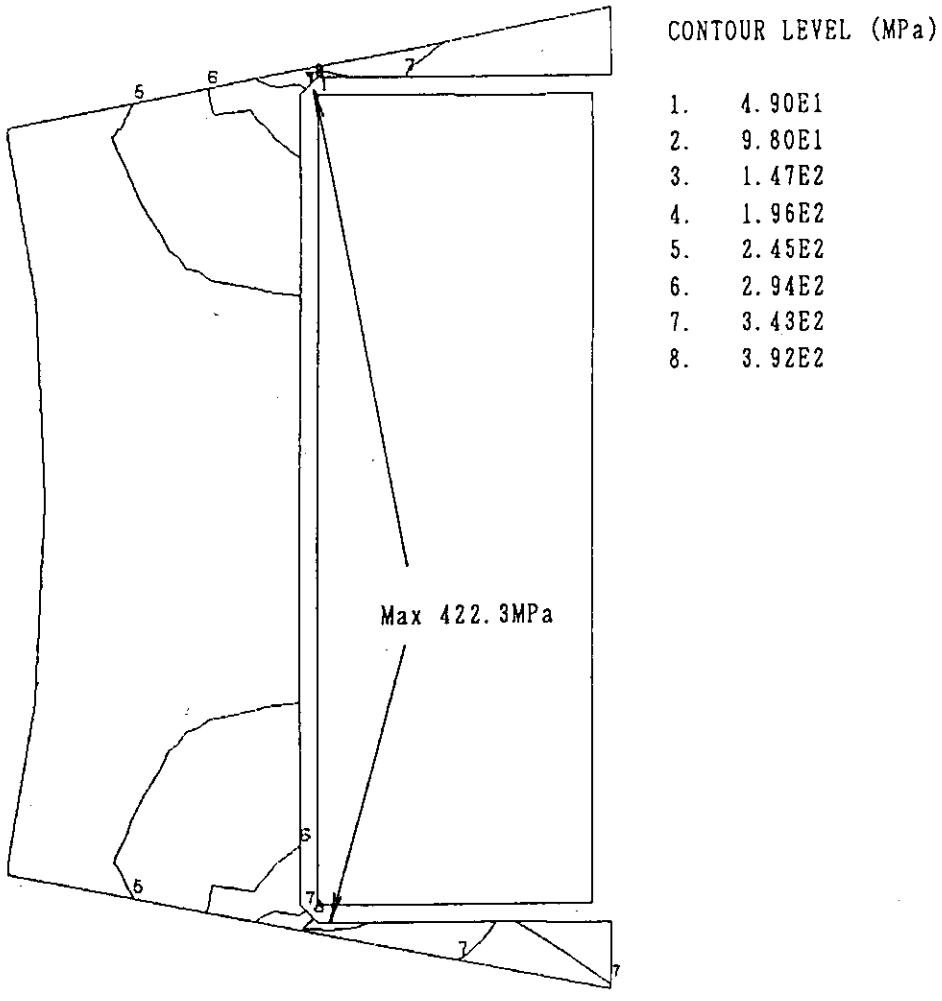

Fig. 2.36 Contour of the constant Principal Stress (σ_1) in the cross section of the TF coil in the inner leg at the End of Burn

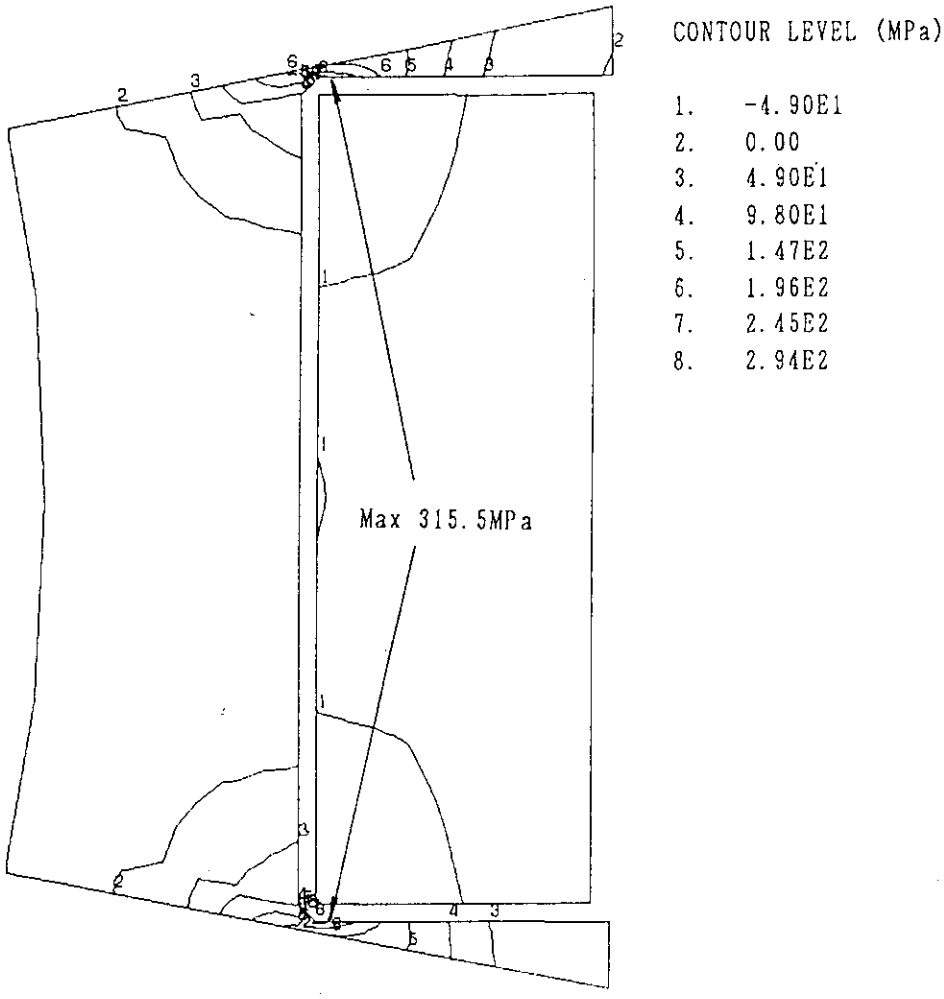

Fig. 2.37 Contour of the constant Medium Stress (σ_2) in the cross section of the TF coil in the inner leg at the End of Burn

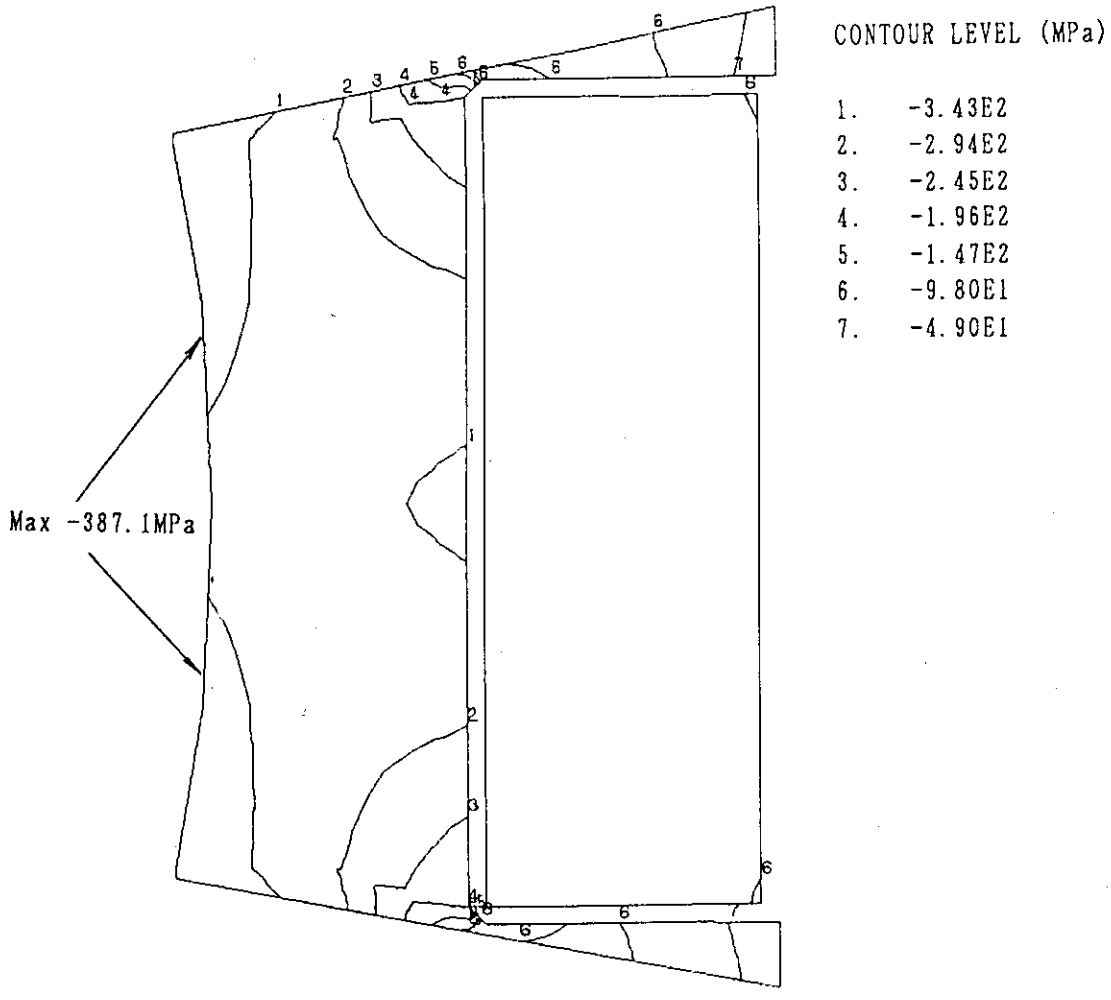

Fig. 2.38 Contour of the constant Minimum Stress (σ_3) in the cross section of the TF coil in the inner leg at the End of Burn

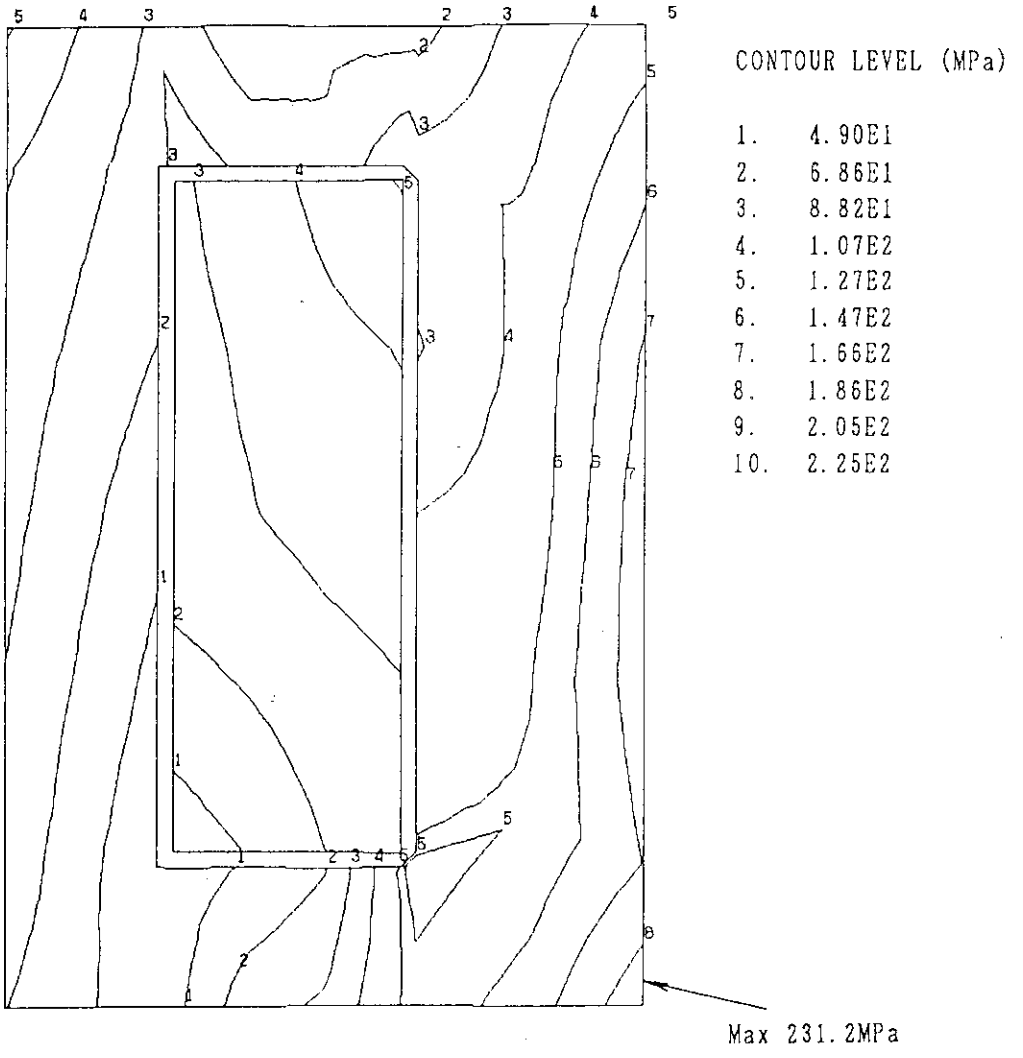

Fig. 2.39 Contour of the constant Tesca Stress (σ_T) in the cross section of TF coil in the outer leg at the End of Burn

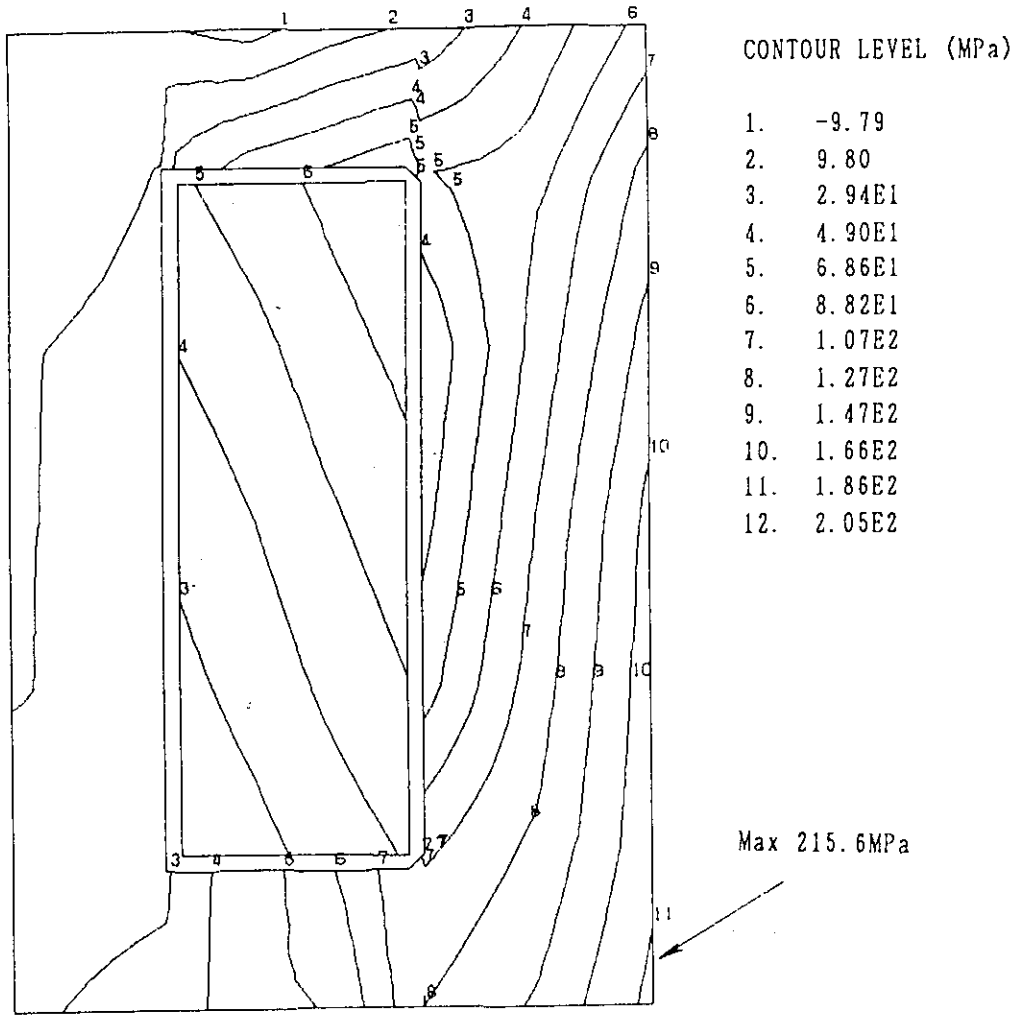

Fig. 2.40 Contour of the constant Principal Stress (σ_1) in the cross section of the TF coil in the outer leg at the End of Burn

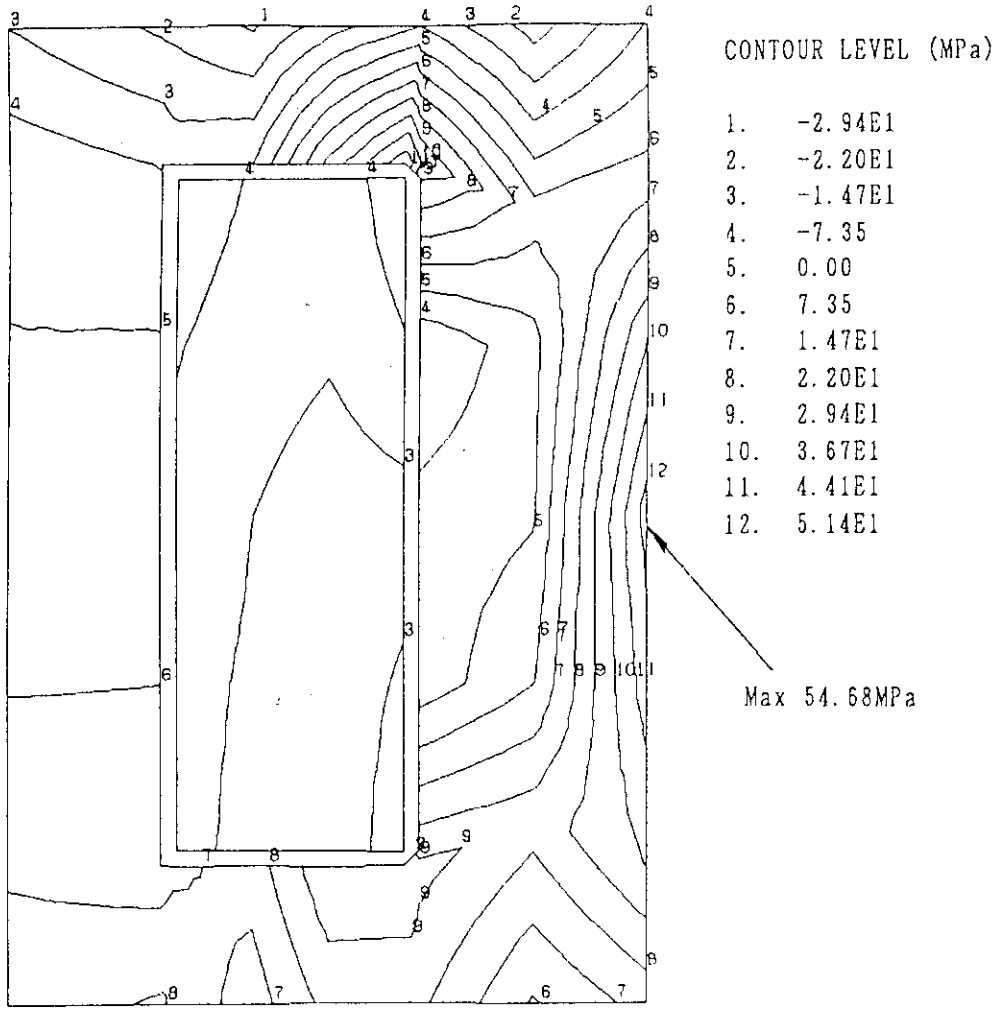

Fig. 2.41 Contour of the constant Medium Stress (σ_2) in the cross section of the TF coil in the outer leg at the End of Burn

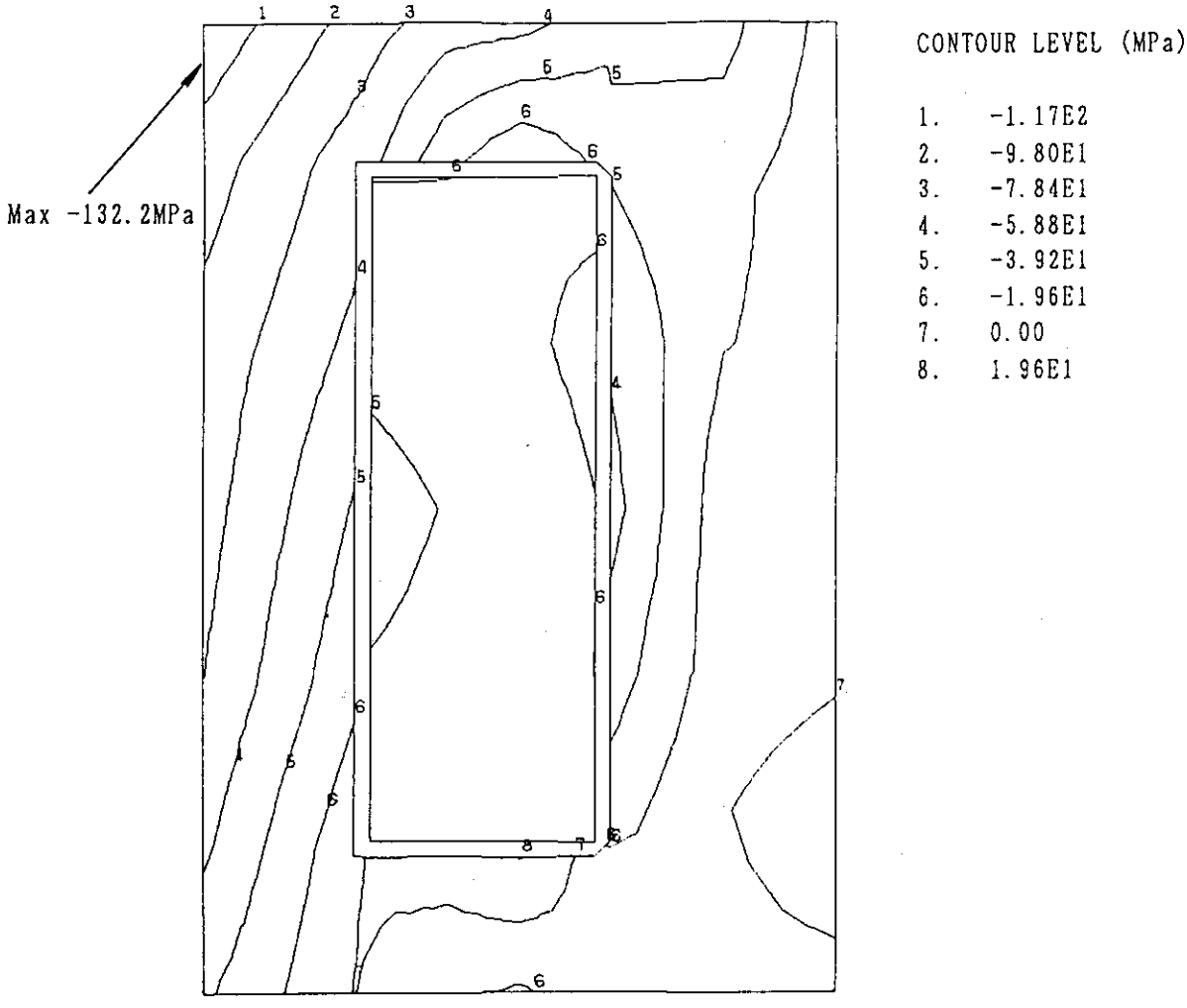

Fig. 2.42 Contour of the constant Minimum Stress (σ_3) in the cross section of the TF coil in the outer leg at the End of Burn

3. Stress Analysis of Toroidal Field Coils under Fault Conditions

3.1 Introduction

The mechanical behaviors of the ITER TF coil system under fault operating conditions have been analyzed by using 3-dimensional FEM model of MSC/NASTRAN. Based on the results obtained by the fault mode analysis [1], four abnormal loading conditions of the TF coil system, named "Short Circuit", "Open Circuit", "Breaker Failure", and "Ground Fault", were employed for the analysis. This analysis must be confirmed with the final power supply configuration since this may prevent some of these fault conditions. The FEM model, material properties, boundary conditions, loading conditions, magnetic field distributions, and the major results obtained by the stress analysis are described in this chapter.

3.2 FEM Model for the Analysis

3.2.1 FEM Model

The major objectives of a series of analysis were to obtain a) the relative displacement between the fault coil and the adjacent coil, and b) the stress level in the fault coil and the adjacent coils. For these purposes, it is not necessary to include all structures of TF coil system into the FEM model. Therefore, upper half of the 16 TF coil system was modeled and analyzed. The FEM model employed for the analysis is shown in Fig. 3.1. The upper-half of 16 TF coils and outer intercoil structures are included in the FEM model. The basic dimensions and the modeling methods employed for each components are the same described in Chapter 2. Because of the large number of components, relatively rough meshing is employed for each TF coil. Since the key structures to keep the integrity of wedging is designed based on the results obtained by a preliminary analysis [2], the contact surfaces of the wedging were assumed to be idealized welded structures. Also the same idealized structures were assumed on the interface of outer intercoil structure. The total number of nodes and the

elements are 4948 and 4209, respectively.

3.2.2 Material Properties

The material properties employed for the analysis is shown in Table 3.1. The material properties of each component are equal to the values which were employed for the analysis with cyclic symmetry model, except the equivalent stiffness of the winding pack. As shown in the table, the winding pack was assumed to have an isotropic, linear-elastic material properties. An averaged Young's Modulus of 77.8 GPa, and the Poisson's ratio of 0.3, were used for the equivalent stiffness.

3.2.3 Boundary Conditions

Because of the symmetrical geometry of TF coil and the symmetrical distribution of the magnetic loads with respect to the horizontal plane, the boundary condition was set on the horizontal plane of TF coil system. However, in the toroidal direction, the loading conditions in some fault modes are not symmetrical with respect to the fault coil. For these cases, bar elements, which represent the radial stiffness of center solenoid coils, are connected to the strait portion of inner leg from the torus center.

3.3 Loading Conditions

3.3.1 Definitions of Fault Mode

Based on the fault mode analysis [1], the following 4 abnormal operating conditions of the coil system were defined:

(1) Short Circuit Mode

This mode corresponds to a over-charging operation of one TF coil in the coil system. Because of the over-charging (225 %) without external field, the distribution of hoop load along the coil perimeter becomes nearly uniform. Then D-shaped TF coil tried to become circular. The operating currents of other 15 coils are less than 1 % of their rated current.

(2) Open Circuit Mode

This fault mode corresponds to the electrical failure of one TF coil in the coil system. Operating current of one TF coil goes down to nearly zero. The coil currents of the adjacent two coils increase more than 120 % of rated current due to mutual inductance coupling. The adjacent coils try to move away from the fault coil in the toroidal direction.

(3) Breaker Failure Mode

TF coil No.5 is connected to the two failed current breakers in the power supply system. The coil current of TF No.5 is 74.1 % of its rated current. The imbalance of operating currents in the coil system is rather small in the previous two fault modes. The difference of coil current of the fault coil and two adjacent coils is less than 1.5 %.

(4) Ground Fault Mode

This notation means the ground fault of coil current through the resistance in the coil protection circuit. TF No.5 coil is the fault mode. The current distribution in the coil system is not symmetric with respect to the fault coil. The maximum difference of coil current, which occurs between No.5 coil and No.6 coil, is 7 %.

The operating currents in the TF coil system calculated by the fault mode analysis are summarized in Table 3.2.

3.3.2 Distribution of Magnetic Field and Electromagnetic Loads

(1) Short Circuit Mode

The distribution of magnetic field in the midplane of inner leg is shown in Fig. 3.2. The distribution of magnetic field along the coil perimeter of fault coil is shown in Fig. 3.3. Because of the over-charging, the maximum field of fault coil (TF coil No. 5) reaches 14 T. The distribution of hoop load along the coil perimeter of TF coil No.5 is shown in Fig. 3.4. Total hoop load of 1177.2 MN corresponds to the 115 % of hoop load in the normal operating condition.

(2) Open Circuit Mode

The distribution of magnetic field in the midplane of inner leg is shown in Fig. 3.5. TF coil No.5 is the coil in the fault condition. It can be seen that the large field change of more than 7 T in the cross section of adjacent coils. The operating current of TF No.6, No.7, and No.8 coil are, 121.8 %, 104.4 %, and 101.7 %, respectively. Because of these imbalance of magnetic field and coil currents, the large out-of-plane load of 419 MN acts on the adjacent coils (TF coil No.4 and No.6).

(3) Breaker Failure Mode

The distribution of magnetic field in the midplane of inner leg is shown in Fig. 3.6. TF coil No.5 is the coil connected to the two current breakers in failure. The coil current of TF No.5 is 74.1 % of its rated current. The imbalance of the coil current in the TF coil system is rater small compared with the Short Circuit Mode or the Open Circuit Mode, the difference of coil current of the fault coil and two adjacent coils is less than 1.5 %.

(4) Ground Fault Mode

The distribution of magnetic field in the midplane of inner leg is shown in Fig. 3.7. Ground fault of coil current through the protection resistance also generates the imbalance of operating currents. The current distribution in the coil system is not symmetrical regarding the fault coil. The maximum difference of coil current, which occurs between No.5 coil and No.6 coil, is 7 %.

The maximum magnetic field of TF coils and the total magnetic loads calculated in each fault conditions are summarized in Table 3.3 and Table 3.4.

3.4. Analysis Results

3.4.1 Results under Normal Loading Conditions

In order to check the difference caused by the relatively rough meshing of TF coil, the mechanical behaviors under the normal loading conditions were also calculated and compared

with the results obtained by the FEM model described in Chapter 2. The displacements and the maximum Tresca stress of the TF coil obtained under the normal loading operating conditions are summarized in Table 3.5 and Table 3.6, respectively.

3.4.2 Results under Fault Loading Conditions

Since the magnetic load and its imbalance in the Breaker Failure and Ground Fault Mode are much smaller than those of the normal operation, the stress analysis was focused on the Short Circuit and Open Circuit Mode.

The deformation of the coil system under the Short Circuit Mode of TF No.5 is shown in Fig. 3.8. The deformation of the fault coil (TF No. 5) is also shown in Fig. 3.9. Because the hoop load try to make the D-shape to circular, the maximum displacement of 22.6 mm appears in the fault coil at the mid-plane of outer leg.

The distribution of the Tresca stress in the fault coil and the adjacent coils is shown in Fig. 3.10. It is seen from the figure that the maximum Tresca stress of 811 MPa is calculated in the inner ring of fault coil at the top of D-shape. The distribution of Tresca stress in the outer ring and side plate of the fault coil is shown in Fig. 3.11. The maximum stress of 431 MPa, appeared in the side plate, is more than 2 times larger than that in normal loading condition. The stress distribution of the winding pack of fault coil is shown in Fig. 3.12. The maximum Tresca stress of 218 MPa is calculated at the top of the D-shape. This value calculated by using equivalent winding stiffness in Table 3.1 corresponds to the conduit stress of about 600 MPa. The distribution of Tresca stress in the adjacent coil (TF No.4) is also shown in Fig. 3.13. As shown in the figure, the stress level of the adjacent coil is much smaller the fault coil, local stress concentration is calculated at the contact surface of wedging where the idealized condition was assumed. Detailed analysis of this section will be required in the next design phase.

The deformation of the coil system under the Open Circuit Mode is shown in Fig. 3.14. Around the fault coil (TF No. 5), it is seen that the adjacent coils move to the opposite side due to out-of-plane force. Although the large imbalance of radial load and the out-of-plane loads exist around the fault coil, the deformation of the coil system is not so serious. This means that the key structures at the contact surface of wedging and outer intercoil structure, which are modeled by welded interfaces, are effective to keep the integrity of coil system. The deformation of fault coil is shown in Fig. 3.15. It is seen from the figure that the inner leg and outer leg move to opposite directions and the horizontal bore is shorten by 17 mm. This means that the adjacent coils is pushing the inner leg of fault coil to outside.

The distributions of Tresca stress in the fault coil (TF No.5) and the adjacent coil (TF No.6) are shown in Fig. 3.16 and Fig. 3.17, respectively. It is shown in Fig. 3.16 that the stress concentration of 751 MPa is appeared in the fault coil around the contact surface of the wedging. Also in Fig. 3.17, the maximum Tresca stress of 575 MPa appears in the contact surface of wedging. Since the maximum stress in the contact surface between the fault coil and the adjacent coil is serious compared with the allowable limit of 800 MPa, the detailed analysis and evaluation should be done in the next design phase. The displacements in the radial direction and the maximum Tresca stresses calculated in the Short Circuit Mode and Open Circuit Mode are summarized in Table 3.7 and Table 3.8, respectively.

3.5 Summary

Based on the fault mode analysis, the electromagnetic loads and mechanical behaviors of the ITER TF coil system under 4 loading conditions, named "Short Circuit", "Open Circuit", "Breaker Failure" and "Ground Fault", were analyzed.
The major results are summarized as follows:

(1) The imbalance of magnetic load under "Breaker Failure" and

"Ground Fault" mode are not serious. The electromagnetic loads of TF coils are about 50 % of those in the normal operating conditions.

(2) The mechanical behaviors in the Short Circuit and the Open Circuit mode largely depend on the mechanical reliability of the wedging and the interface of the outer intercoil structure.

(3) In the Short Circuit mode, the maximum Tresca stress of 811 MPa is appeared in the inner ring of fault coil. In order to avoid the serious damage, investigation of coil protection system will be required. The effects on the adjacent coils are not so serious in this mode.

(4) The imbalance of the centering loads and out-of-plane loads caused by Open Circuit Mode also generate high stress of 751 MPa at the contact surface of the wedging.

(5) Because the two fault modes, Coil Short and Melt Down, have some possibilities to generate much influence to the TF coil system and the other components around the TF coil system, more careful analysis and detail investigation should be done in the next design phase.

References

[1] H. Hiue and K. Yoshida, "Fault Analysis of TF Power Supply System", (ITER-IL-MG-256)

[2] K. Koizumi, "Stress Analysis of Toroidal Field Coils at Fault Conditions" (ITER-IL-MG-246)

Table 3.1 Material Properties employed for the FEM Analysis in the Fault Loading Conditions

Component	Winding	Insulator	Coil Case	Supporting Structure Outer Intercoil Structure
Material	Isotropic, and linear-elastic	Isotropic, linear-elastic	Isotropic, linear-elastic	Isotropic, linear-elastic
Young's Modulus				
E_r	77.8 GPa	19.6 GPa	196.0 GPa	196.0 GPa
E_θ	77.8 GPa	19.6 GPa	196.0 GPa	196.0 GPa
E_z	77.8 GPa	19.6 GPa	196.0 GPa	196.0 GPa
Poisson's Ratio				
$U_{r\theta}$	0.3	0.1	0.3	0.3
$U_{\theta z}$	0.3	0.1	0.3	0.3
U_{rz}	0.3	0.1	0.3	0.3
Shear Modulus				
$G_{r\theta}$	30.0 GPa	8.9 GPa	75.4 GPa	75.4 GPa
$G_{\theta z}$	30.0 GPa	8.9 GPa	75.4 GPa	75.4 GPa
G_{rz}	30.0 GPa	8.9 GPa	75.4 GPa	75.4 GPa

Table 3.2 Operating Current of TF Coil System in the Fault Loading Conditions

Fault Mode Name	Coil Current (%) Short Circuit	Open Circuit	Breaker Failure	Ground Fault
TF Coil No. 1	0.54	100.79	68.63	67.98
No. 2	0.51	101.68	69.38	68.31
No. 3	0.46	104.45	70.63	68.87
No. 4	0.39	121.84	72.77	69.83
@ No. 5	225.45	1.13	74.12	71.58
No. 6	0.39	121.84	72.77	64.11
No. 7	0.46	104.45	70.63	65.57
No. 8	0.51	101.68	69.38	66.37
No. 9	0.54	100.79	68.63	66.83
No.10	0.57	100.42	68.19	67.10
No.11	0.59	100.32	67.93	67.27
No.12	0.60	100.25	67.80	67.38
No.13	0.60	100.25	67.76	67.47
No.14	0.60	100.25	67.80	67.55
No.15	0.59	100.32	67.93	67.65
No.16	0.57	100.42	68.19	67.78

@ : Coil in Fault mode

Table 3.3 Maximum Magnetic Field of the TF Coil System in the Fault Loading Conditions

Fault Mode Name	Maximum Magnetic Field (T) Short Circuit	Open Circuit	Breaker Failure	Ground Fault
TF Coil No. 3	0.0	11.0	7.7	7.5
No. 4	0.0	11.6	7.9	7.6
@ No. 5	14.0	6.0	7.9	7.6
No. 6	0.0	11.6	7.9	7.2
No. 7	0.0	11.0	7.7	7.3
No. 8	0.0	10.9	7.6	7.3

@ Coil in Fault Mode

Table 3.4 Electromagnetic Load of TF coils in the Fault Loading Conditions

Fault Mode Name	Electromagnetic Load (MN) Short Circuit	Open Circuit	Breaker Failure	Ground Fault
TF Coil No. 3				
FR (MN/Coil)	-----	-481.6	-239.2	-226.0
FY (MN/Coil)	-----	36.0	- 15.6	4.8
FZ (MN/Half)	-----	193.9	93.8	88.8
FH (MN/Coil)	-----	1187.2	580.8	549.4
TF Coil No. 4				
FR (MN/Coil)	-----	-521.0	-246.8	-228.6
FY (MN/Coil)	-----	419.2	- 13.2	2.0
FZ (MN/Half)	-----	221.2	97.7	90.3
FH (MN/Coil)	-----	1338.0	603.0	557.6
TF Coil No. 5 (Fault Coil)				
FR (MN/Coil)	- 5.0	- 5.8	-251.2	-232.2
FY (MN/Coil)	0.0	0.0	0.0	- 18.6
FZ (MN/Half)	290.1	1.6	100.1	92.5
FH (MN/Coil)	1177.2	11.6	616.2	569.4
TF Coil No. 6				
FR (MN/Coil)	-----	-521.0	-246.8	-208.4
FY (MN/Coil)	-----	419.2	- 13.2	- 16.4
FZ (MN/Half)	-----	221.2	97.7	80.2
FH (MN/Coil)	-----	1338.0	603.0	498.2
TF Coil No. 7				
FR (MN/Coil)	-----	-481.6	-239.2	-213.2
FY (MN/Coil)	-----	36.0	- 15.6	0.2
FZ (MN/Half)	-----	193.9	93.8	82.5
FH (MN/Coil)	-----	1187.2	580.8	513.4
TF Coil No. 8				
FR (MN/Coil)	-----	-477.2	-233.8	-215.2
FY (MN/Coil)	-----	8.0	- 12.4	3.2
FZ (MN/Half)	-----	189.9	91.2	83.6
FH (MN/Coil)	-----	1168.8	565.8	519.6

FR : Centering Load, FY : Out-of-plane Load,
FZ : Vertical Load, FH : Hoop Load

Note: in normal operation FR:-475 MN,FZ:185 MN,FH:1024 MN

Table 3.5 Displacements of TF Coil in the Radial and Vertical Direction in the Normal Loading Conditions

Displacement	Radial Direction Inner Leg (mm)	Radial Direction Outer Leg (mm)	Vertical Direction (mm)
<Normal Conditions>			
1. Normal Operation without PF Coil Operation	- 4.5	8.6	7.0
2. Normal Operation at End of Burn	- 4.3	7.2	7.5
(Cyclic Symmetry FEM Model for EOB)	(-4.6)	(10.9)	(16.4)

Table 3.6 Maximum Tresca Stress of TF Coil System in the Normal Loading Conditions

	Maximum Tresca Stress)
<Normal Conditions>	
1. Normal Operation without PF Coil Operation	580 MPa
2. Normal Operation at End of Burn	616 MPa
(Cyclic Symmetry FEM Model)	655 MPa

Table 3.7 Radial Displacement of the TF Coil No. 4 and No. 5 in the Short Circuit Mode and Open Circuit Mode.

Coil No.	TF Coil No. 4		TF Coil No. 5	
	Inner Leg (mm)	Outer Leg (mm)	Inner Leg (mm)	Outer Leg (mm)
1. Short Circuit Mode of TF No.5 coil	- 6.9	3.3	- 9.2	22.6
2. Open Circuit Mode of TF No.5 coil	3.6	9.2	7.0	-10.0

Table 3.8 The maximum Tresca stress of TF Coil No. 4 and TF Coil No. 5 in the Short Circuit Mode and Open Circuit MOde

Coil No.	Maximum Tresca Stress (MPa)	
	TF Coil No. 4 (Adjacent Coil)	TF Coil No. 5 (Fault Coil)
1. Short Circuit Mode of TF No.5 coil	157.8 MPa	811.4 MPa
2. Open Circuit Mode of TF No.5 coil	575.3 MPa	750.7 MPa

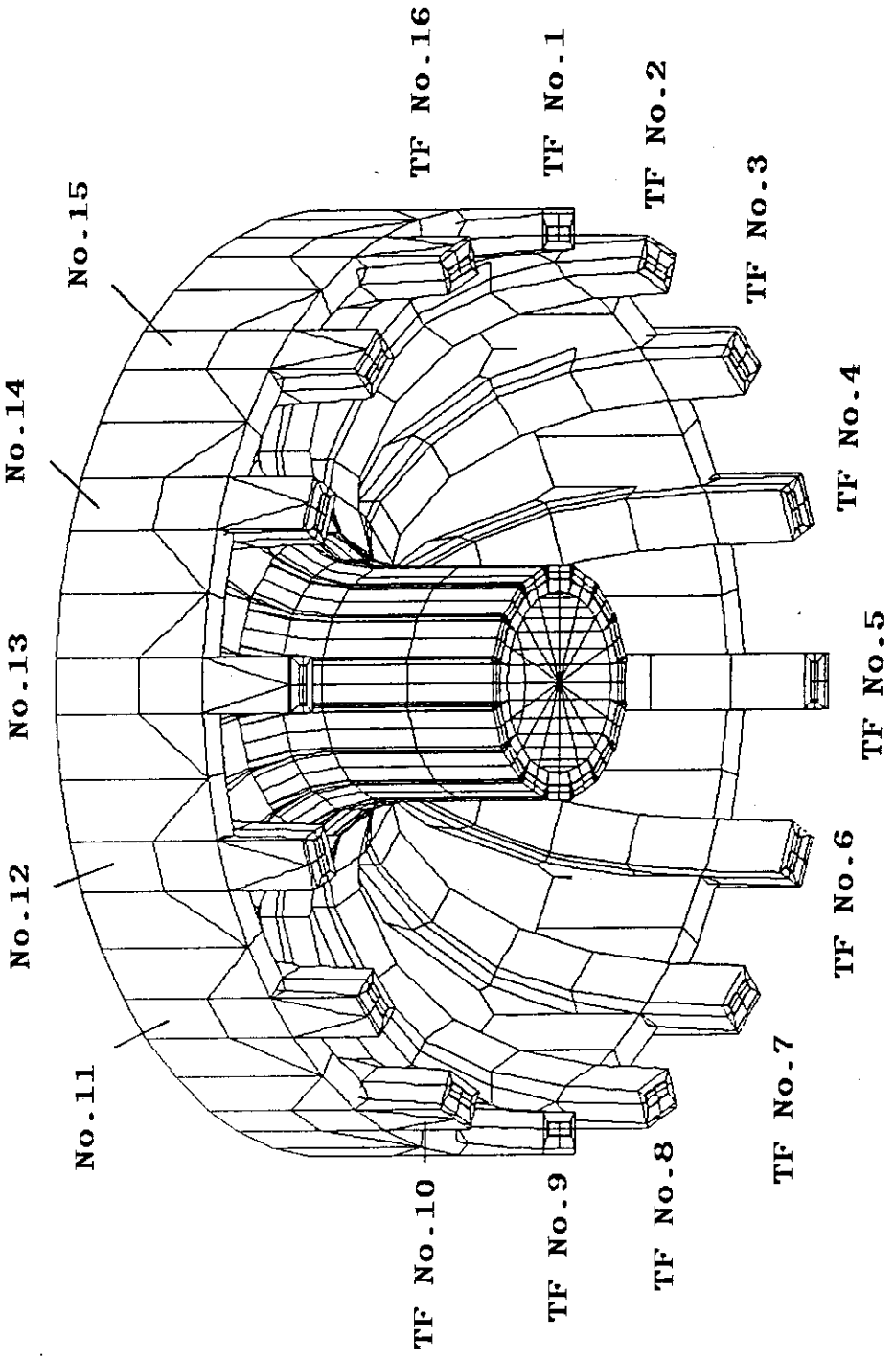

Fig. 3.1 3-dimensional FEM model of ITER TF coil system for the analysis under fault loading conditions. (Upper-half of the 16 TF coils is modeled)

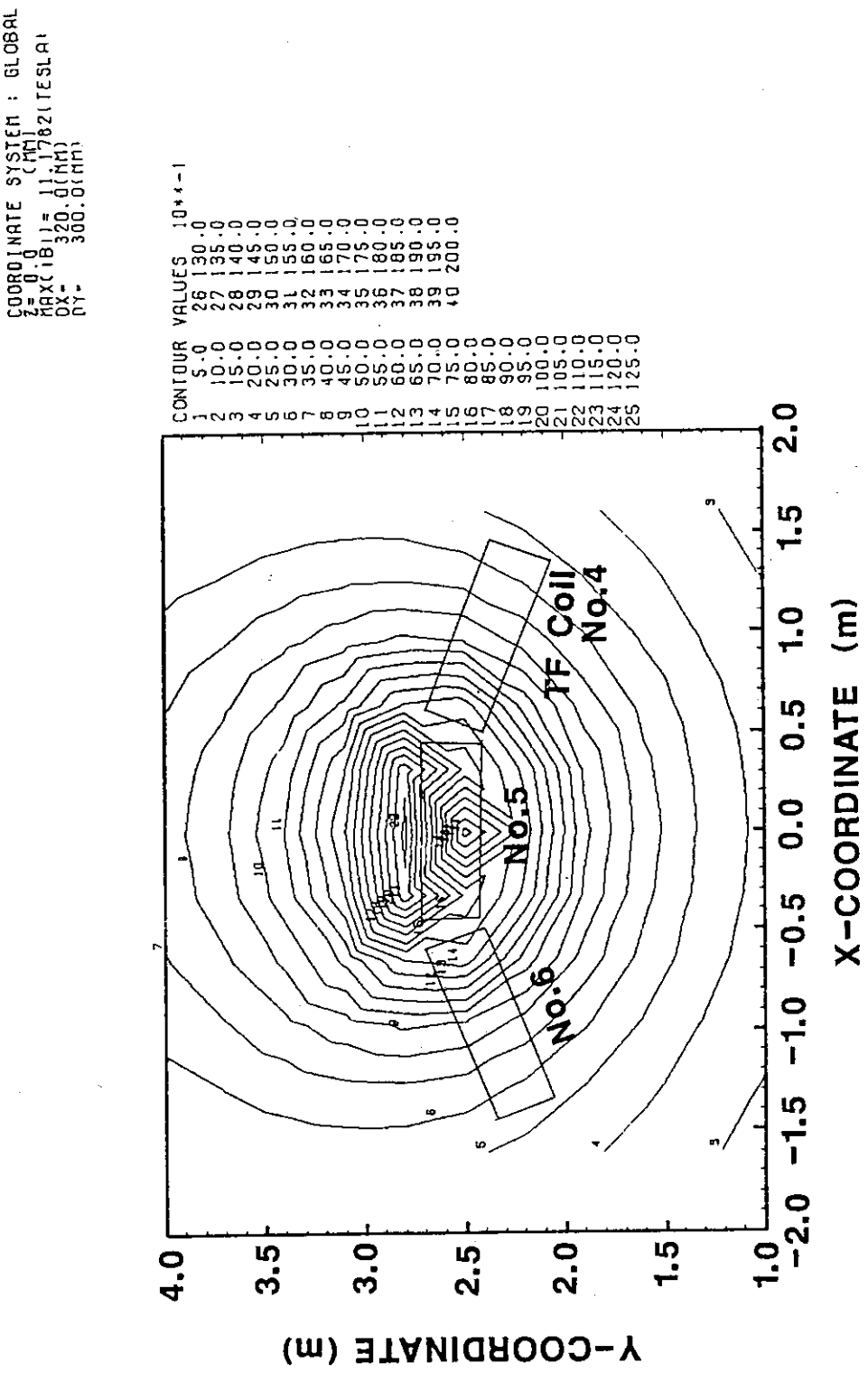

Fig. 3.2 Distribution of Magnetic Field in the midplane of Inner Leg in the Short Circuit Mode of TF coil No. 5

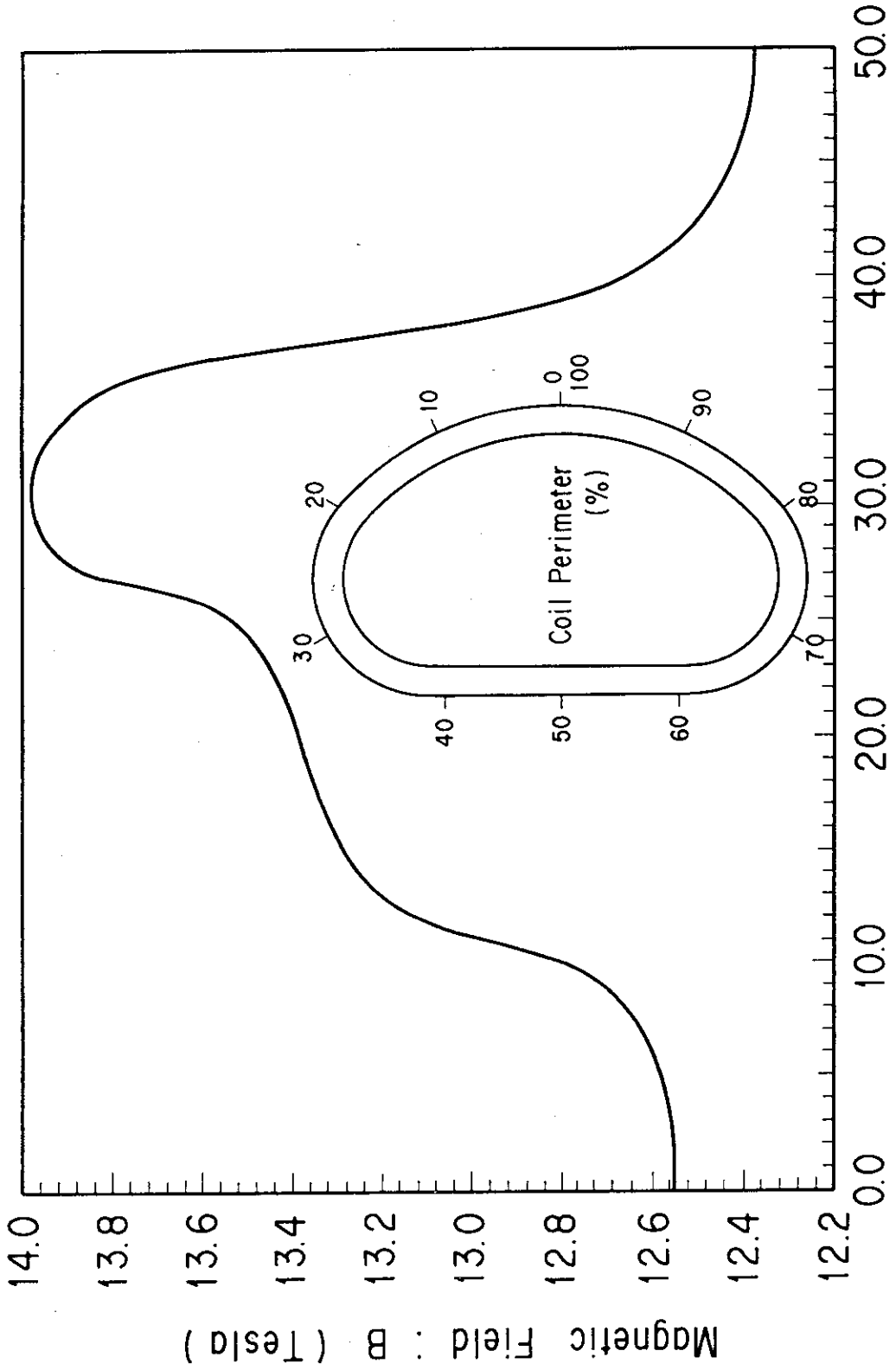

Fig. 3.3 Distribution of Magnetic Field along the coil perimeter of fault coil in the Short Circuit Mode.

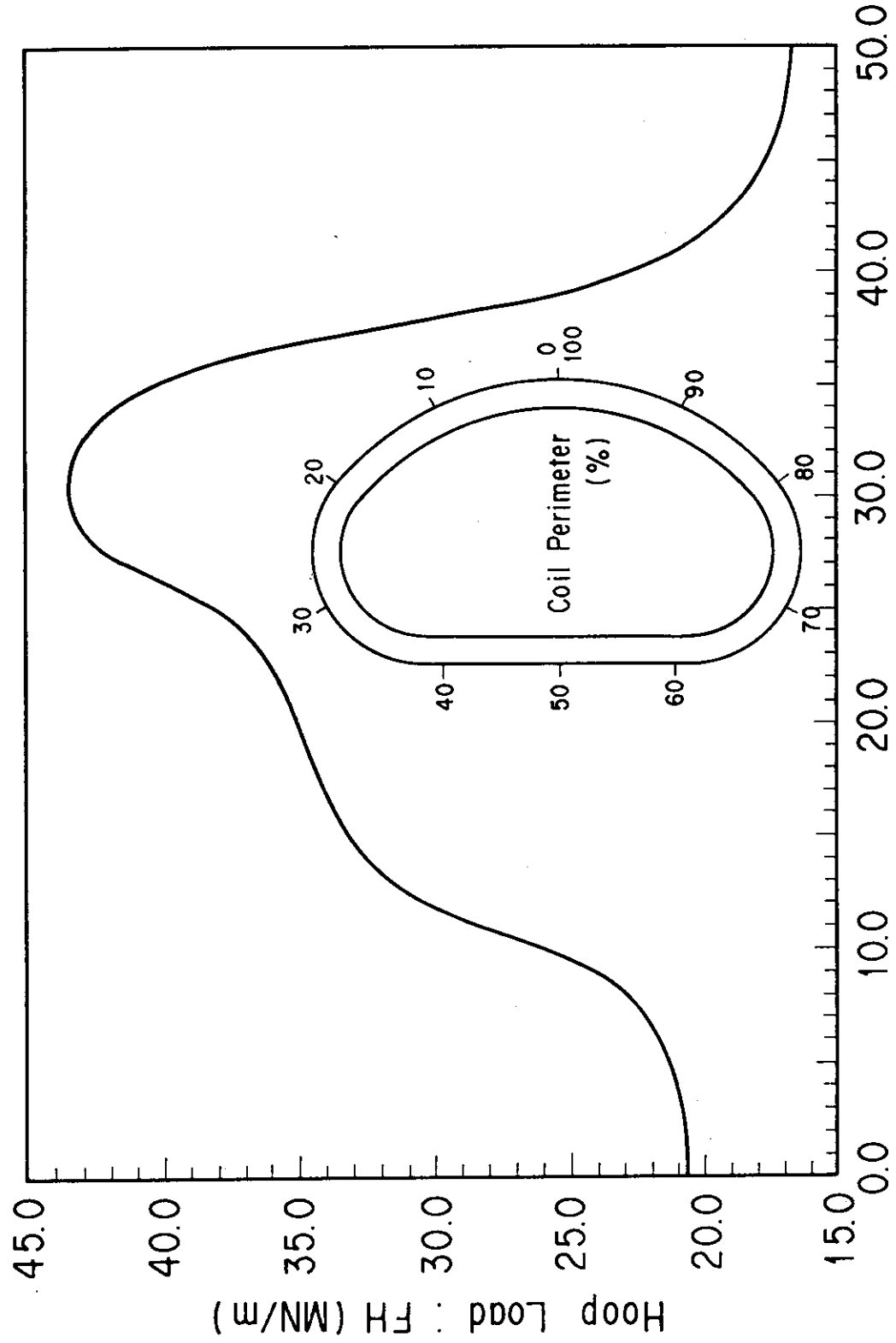

Fig. 3.4 Distribution of Hoop Load along the coil perimeter of the fault coil in the Short Circuit Mode.

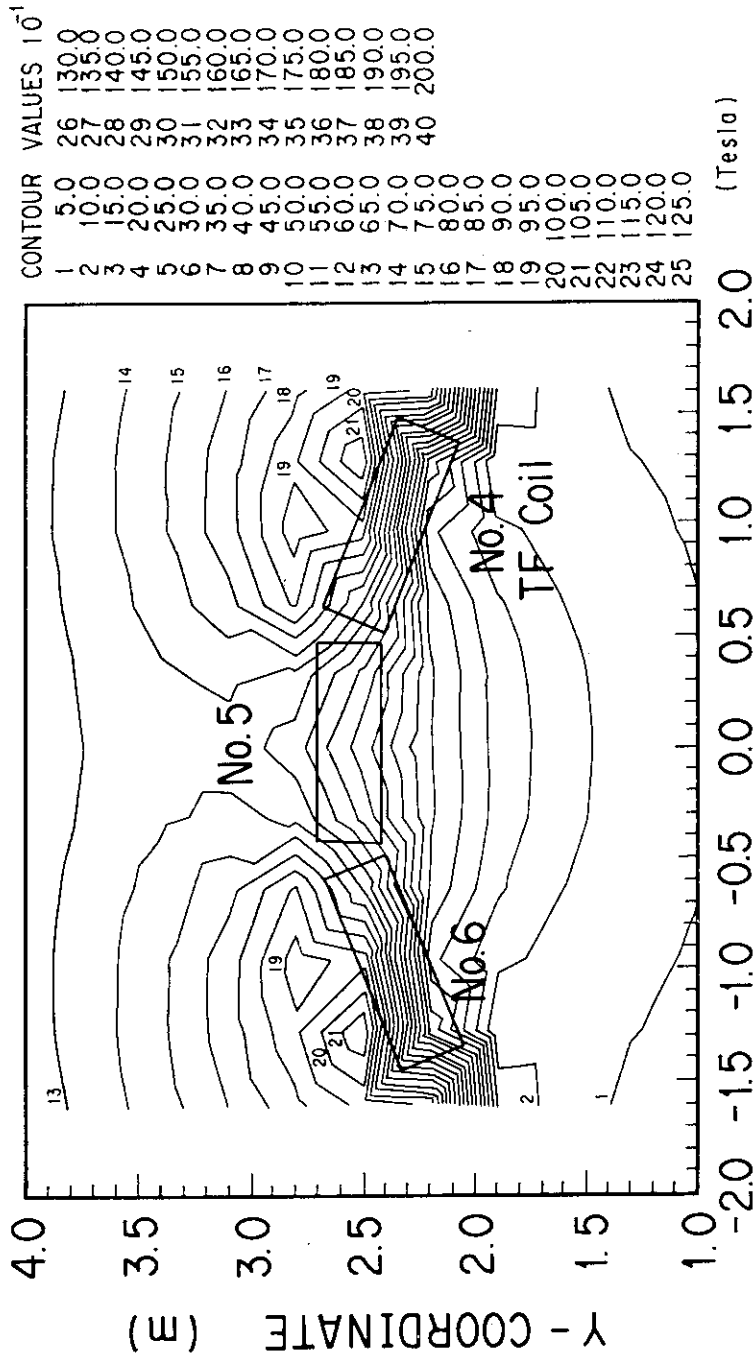

Fig. 3.5 Distribution of Magnetic Field in the midplane of Inner Leg in the Open Circuit Mode of TF No.5

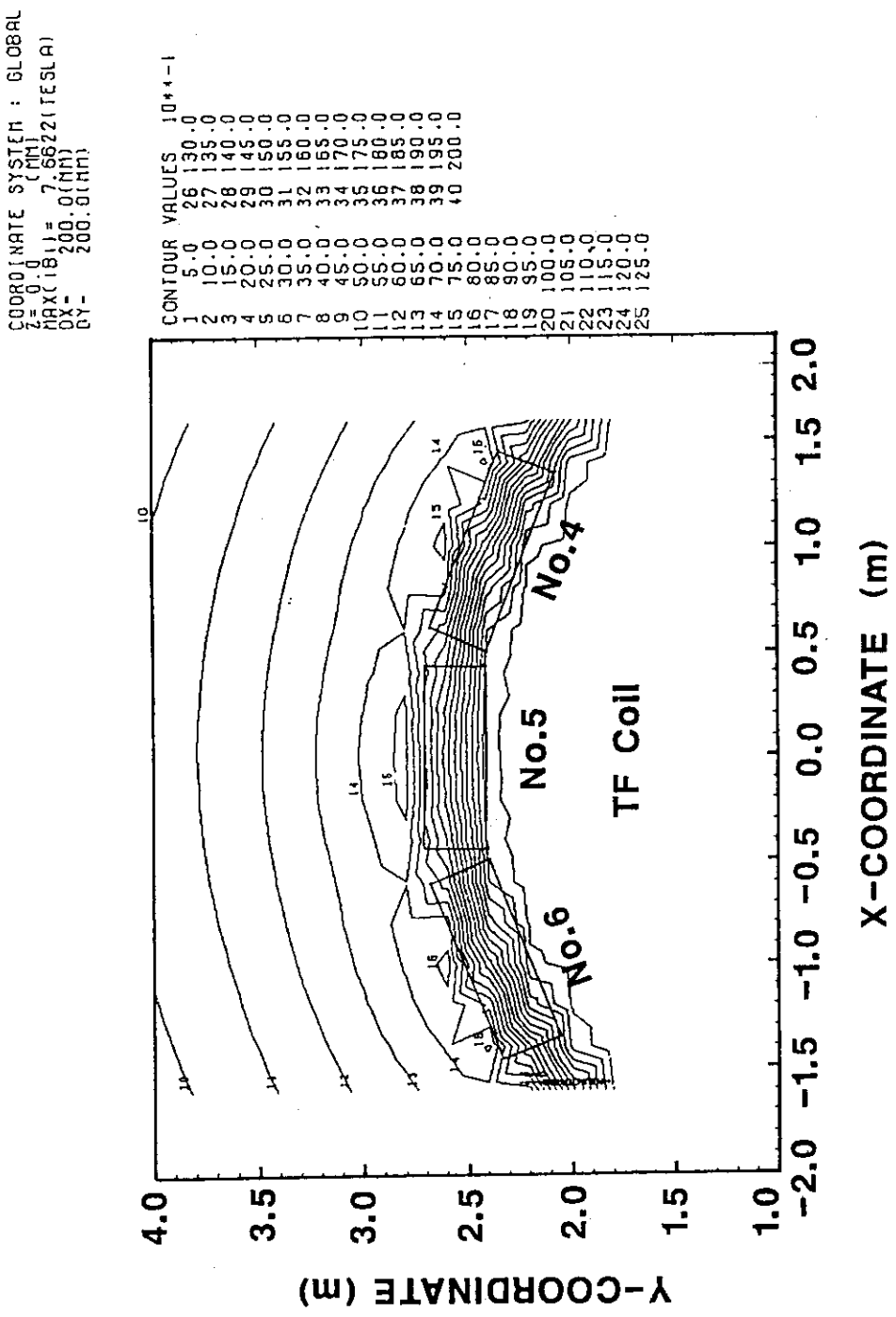

Fig. 3.6 Distribution of Magnetic Field in the midplane of Inner Leg in the Breaker Failure Mode of TF No.5

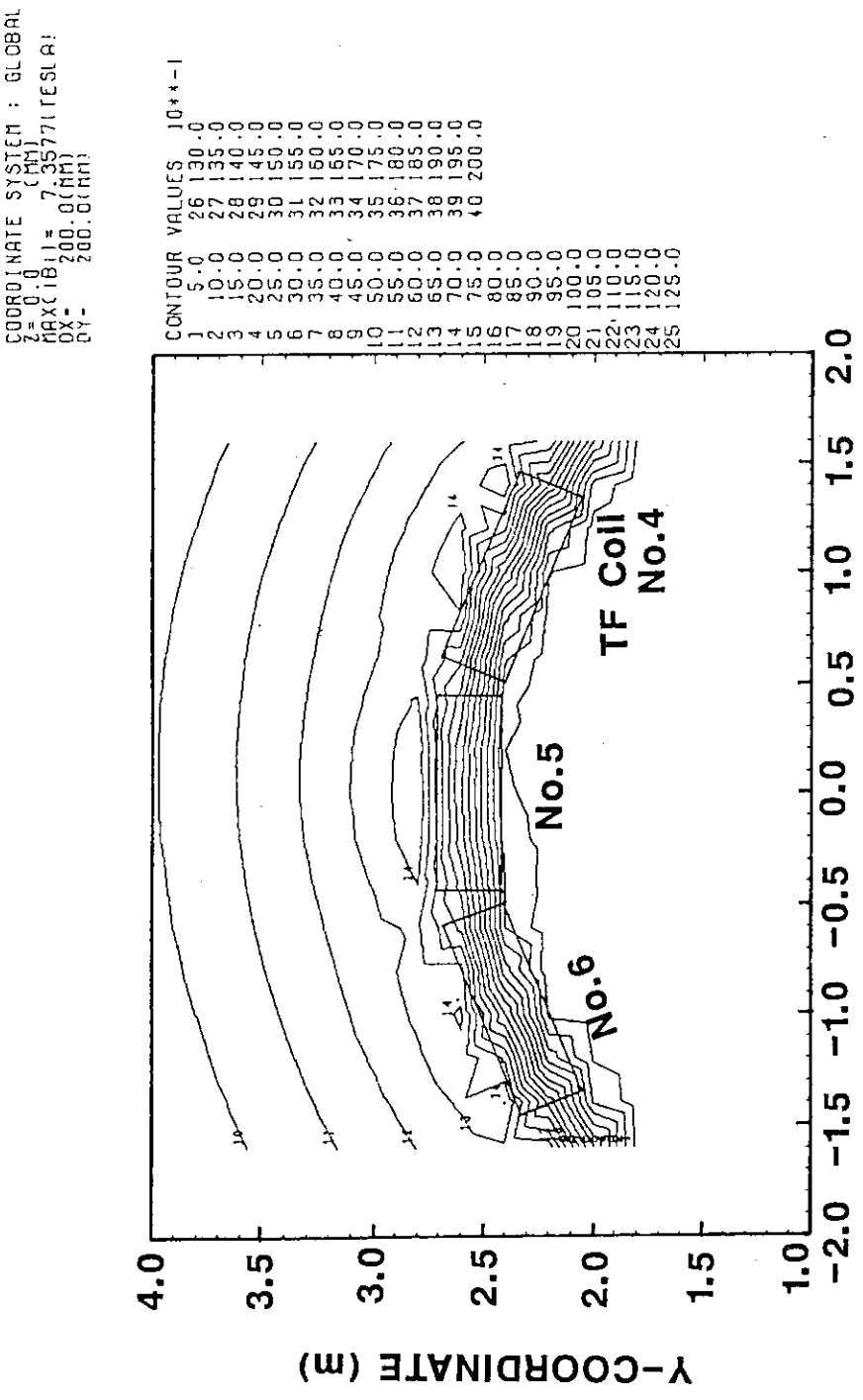

Fig. 3.7 Distribution of Magnetic Field in the midplane of Inner Leg in the Ground Fault Mode of TF No. 5.

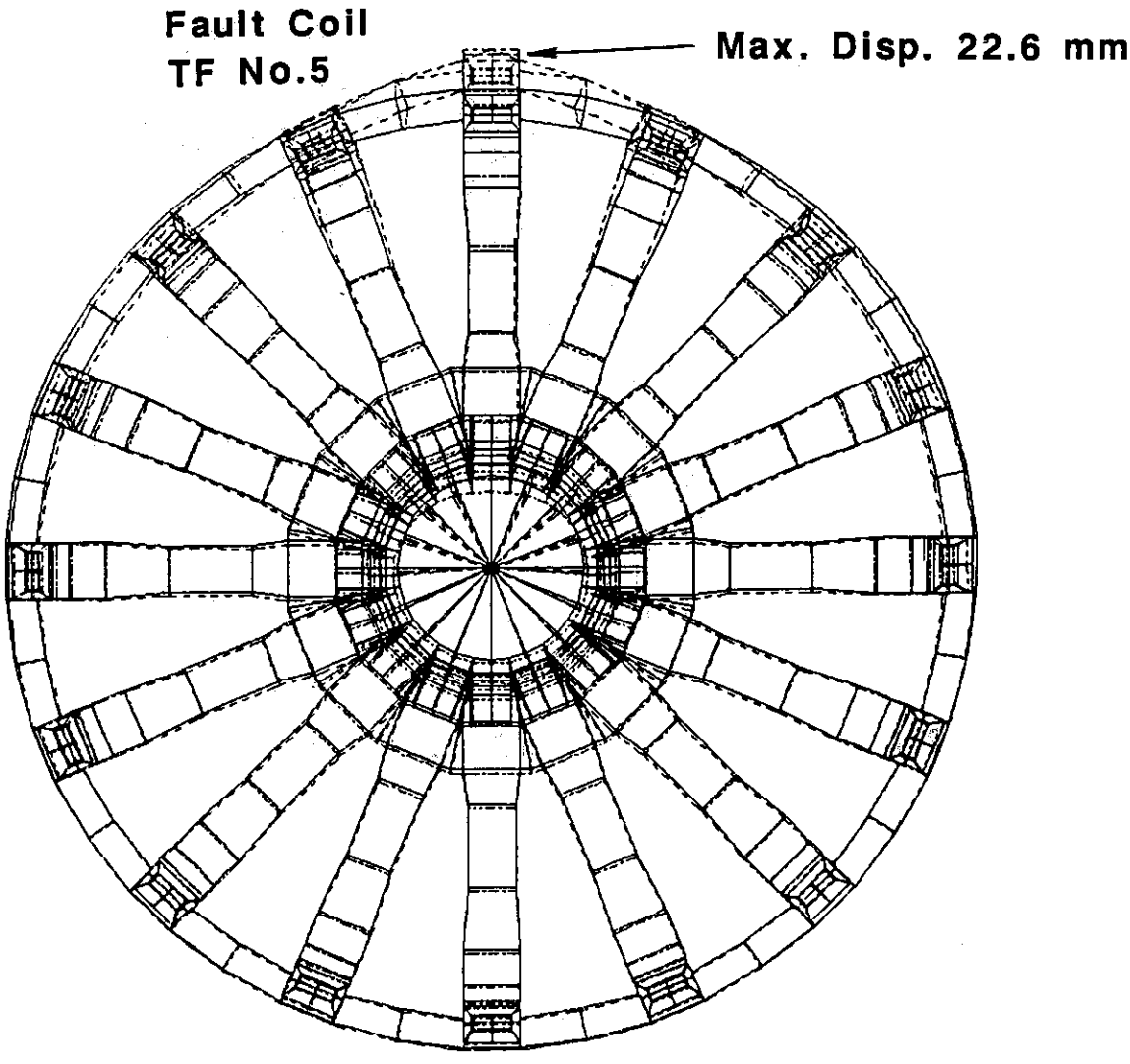

Fig. 3.8 Deformation of ITER TF Coil System in the Short Circuit Mode of TF Coil No. 5.

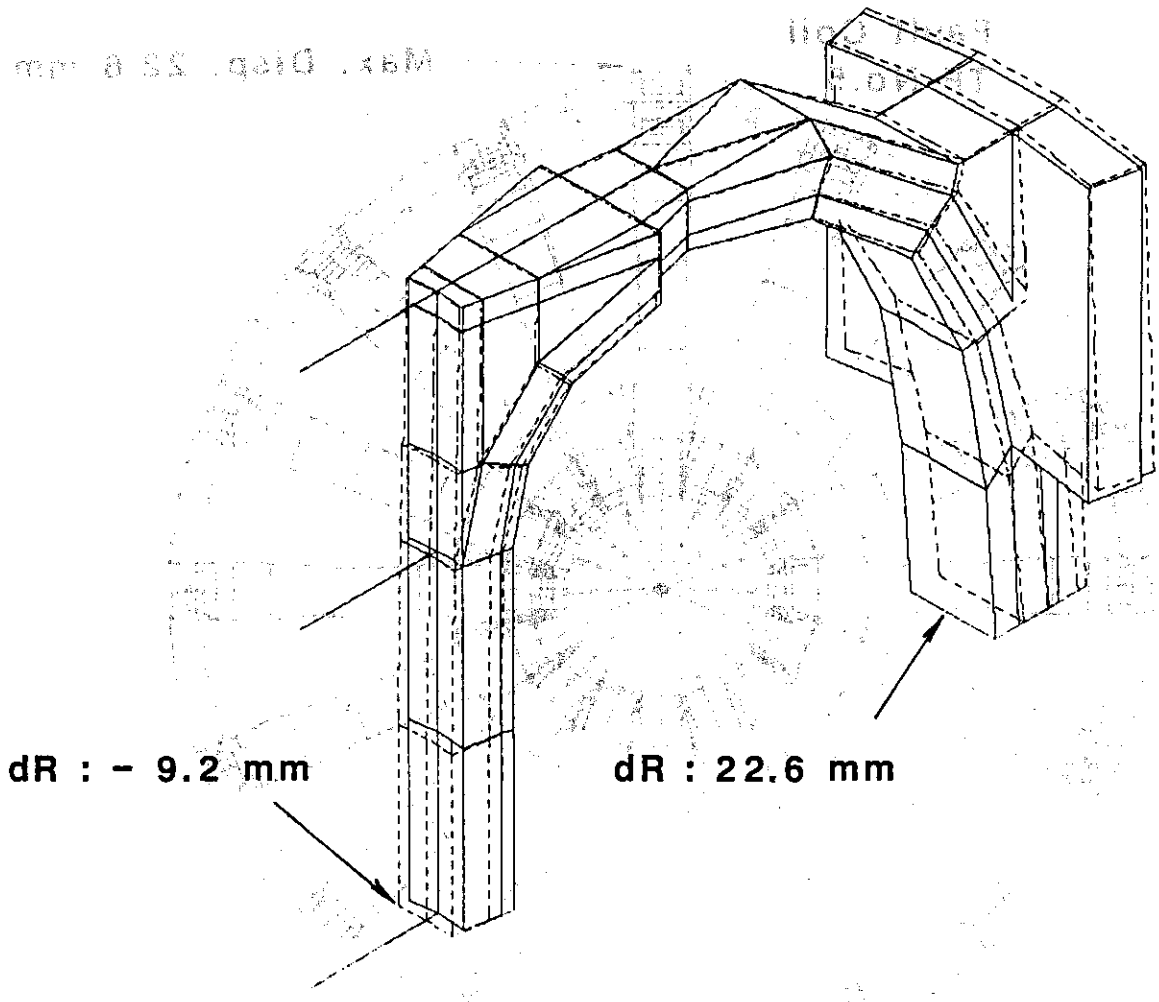

Fig. 3.9 Deformation of the fault coil in the Short Circuit Mode.

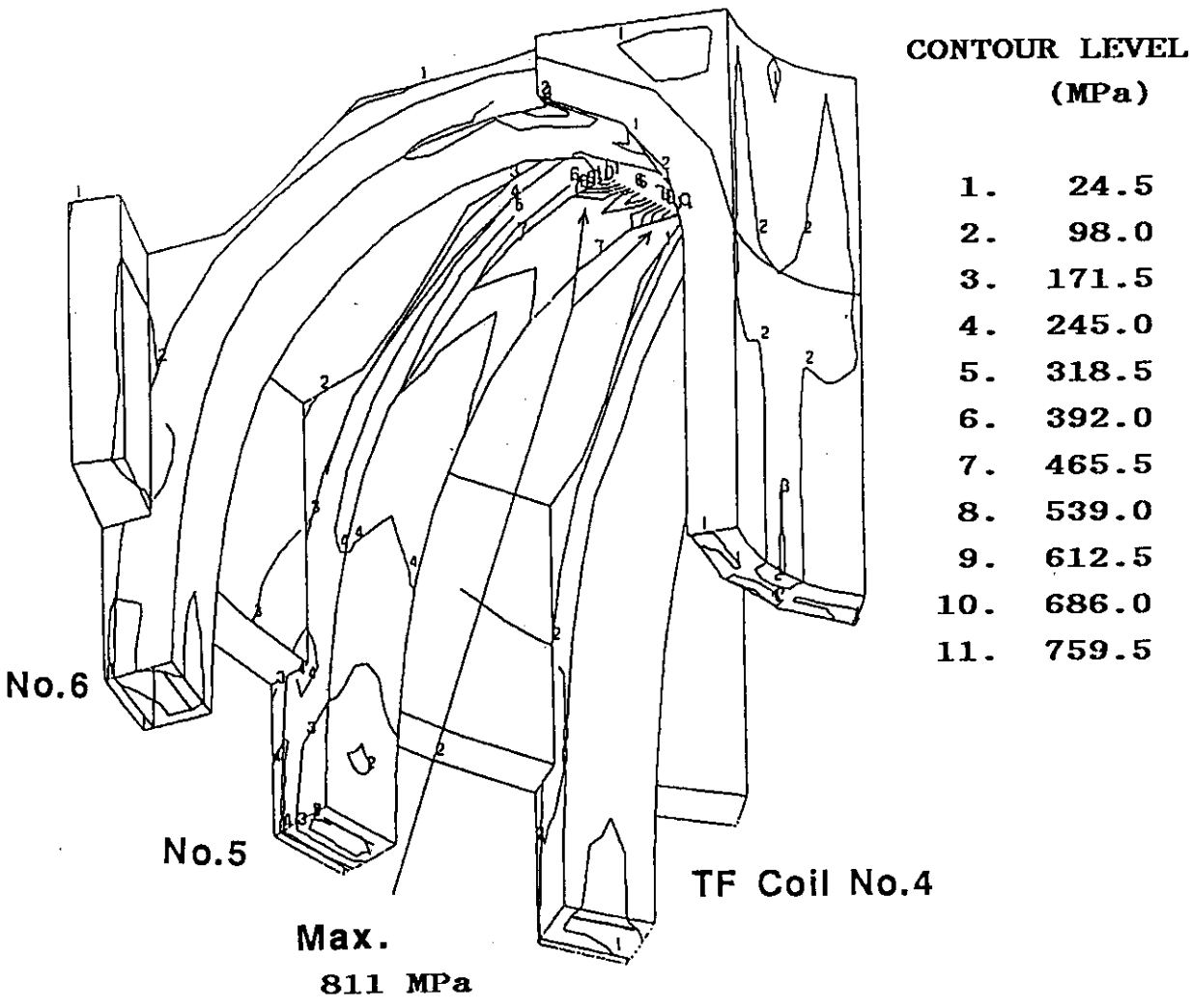

Fig. 3.10 Stress Distribution of TF coil No.4, No.5, and No.6, in the Short Circuit Mode of TF No.5.

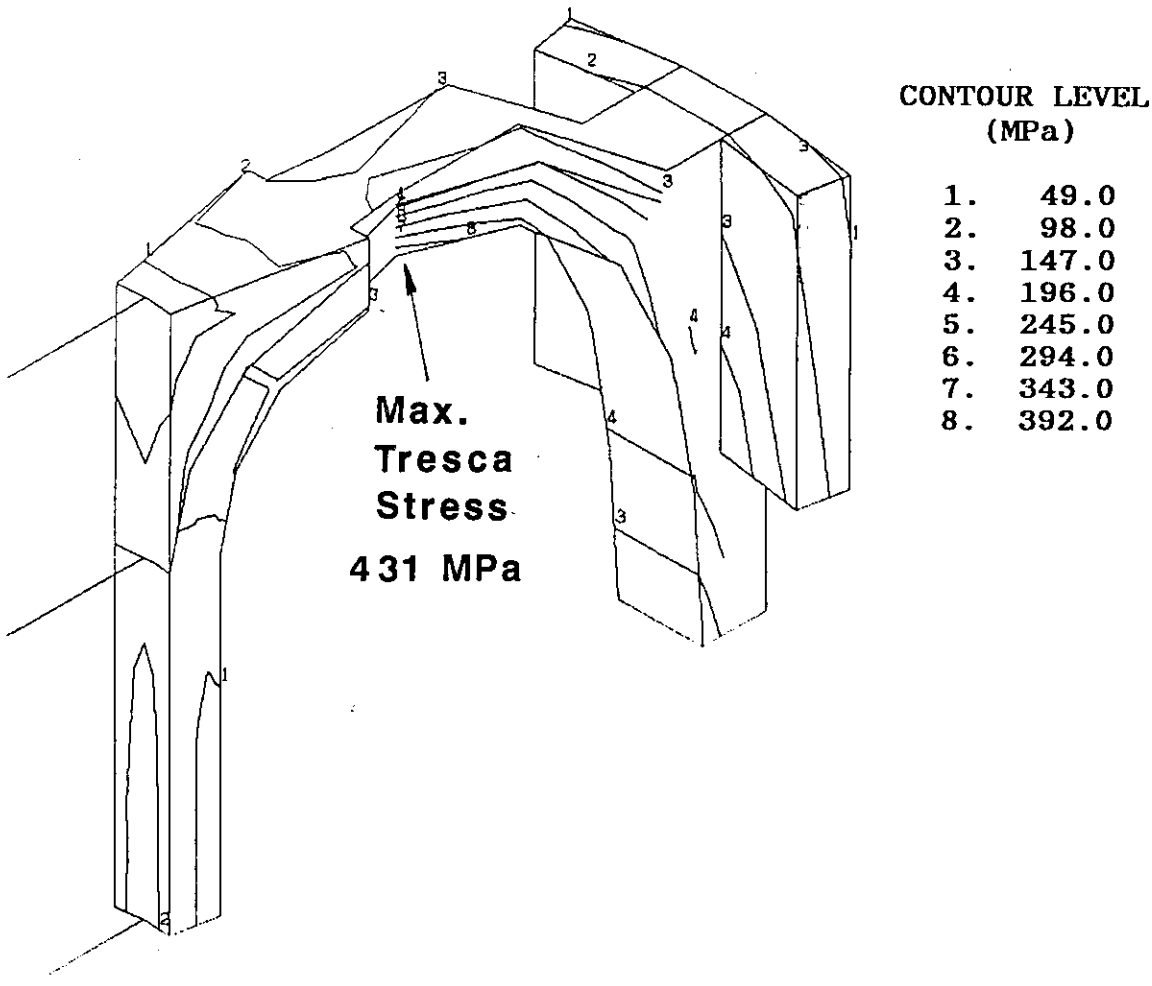

Fig. 3.11 Stress Distribution in the Outer Ring and Side Plate of fault coil in the Short Circuit Mode.

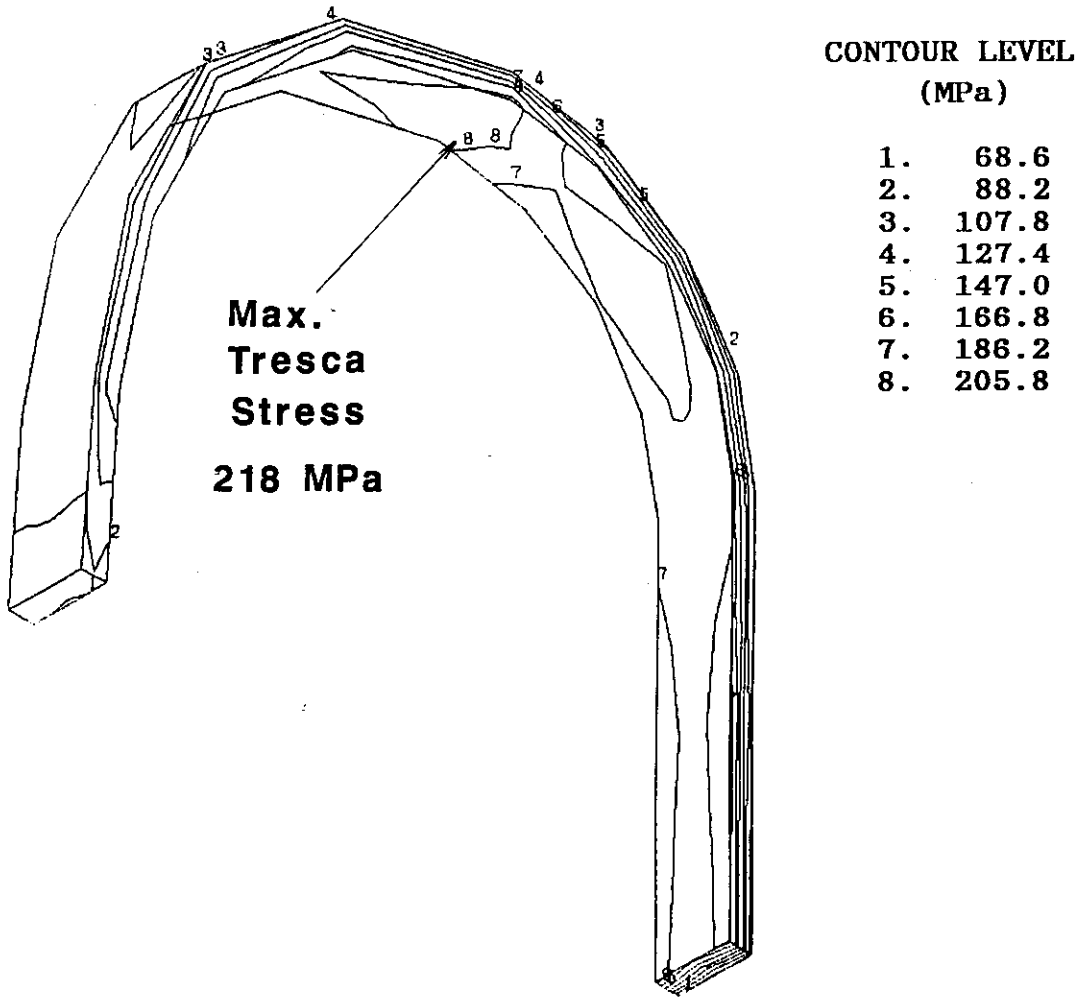

Fig. 3.12 Stress Distribution in the Winding of Fault Coil in the Short Circuit Mode.

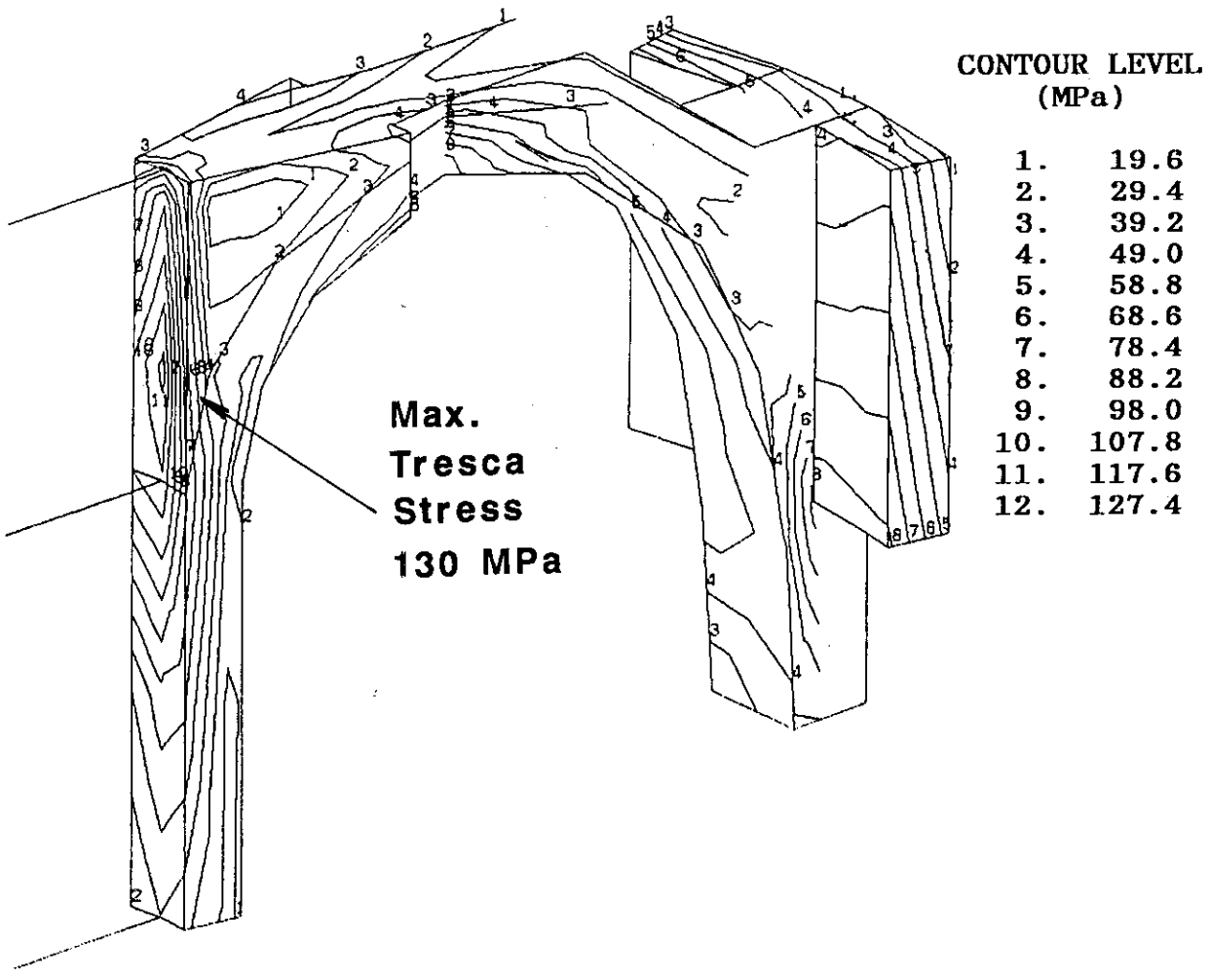

Fig. 3.13 Stress Distribution of TF Coil No.4 in the Short Circuit Mode of TF No.5.

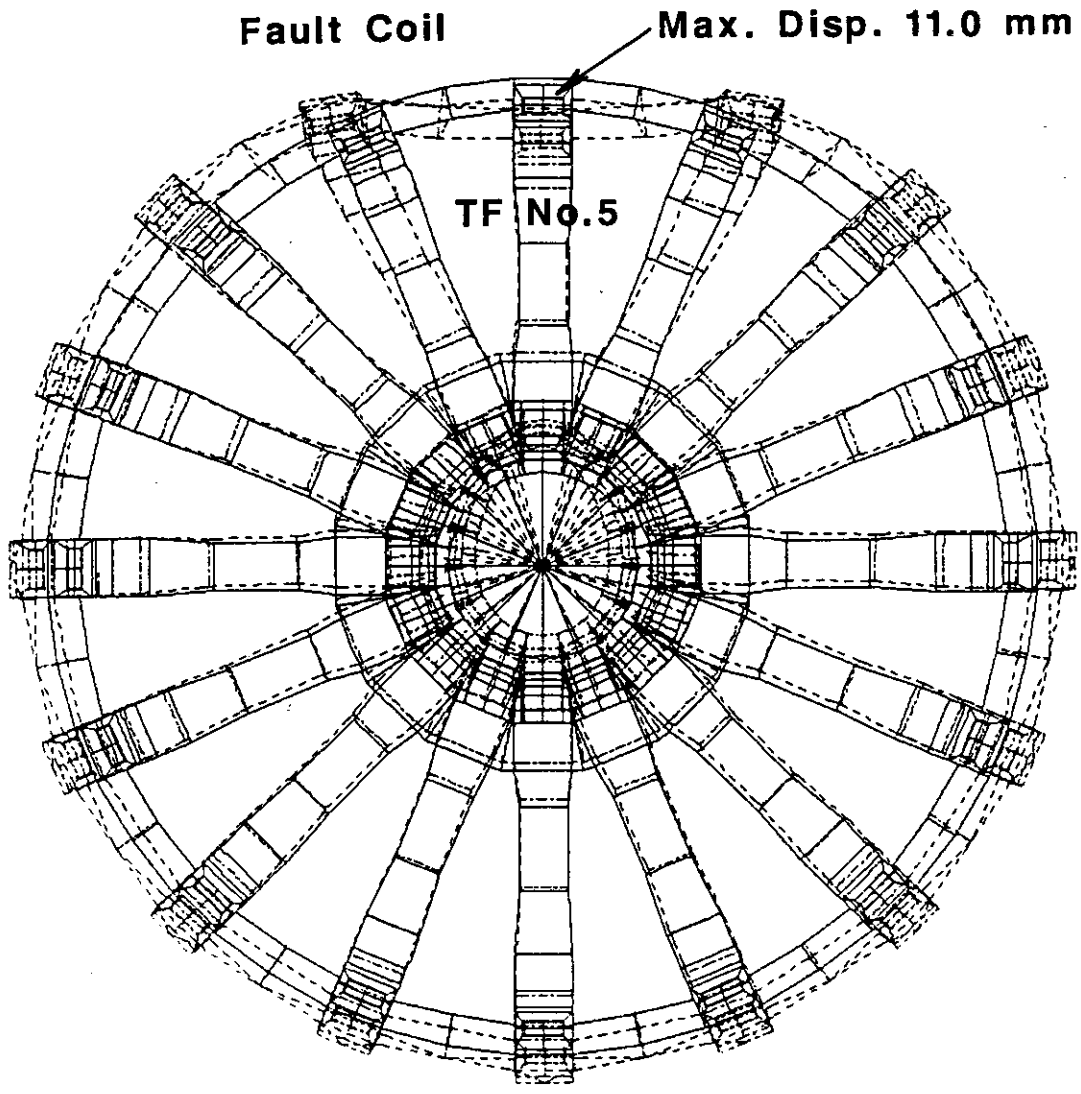

Fig. 3.14 Deformation of ITER TF Coil System in the Open Circuit Mode of TF No.5.

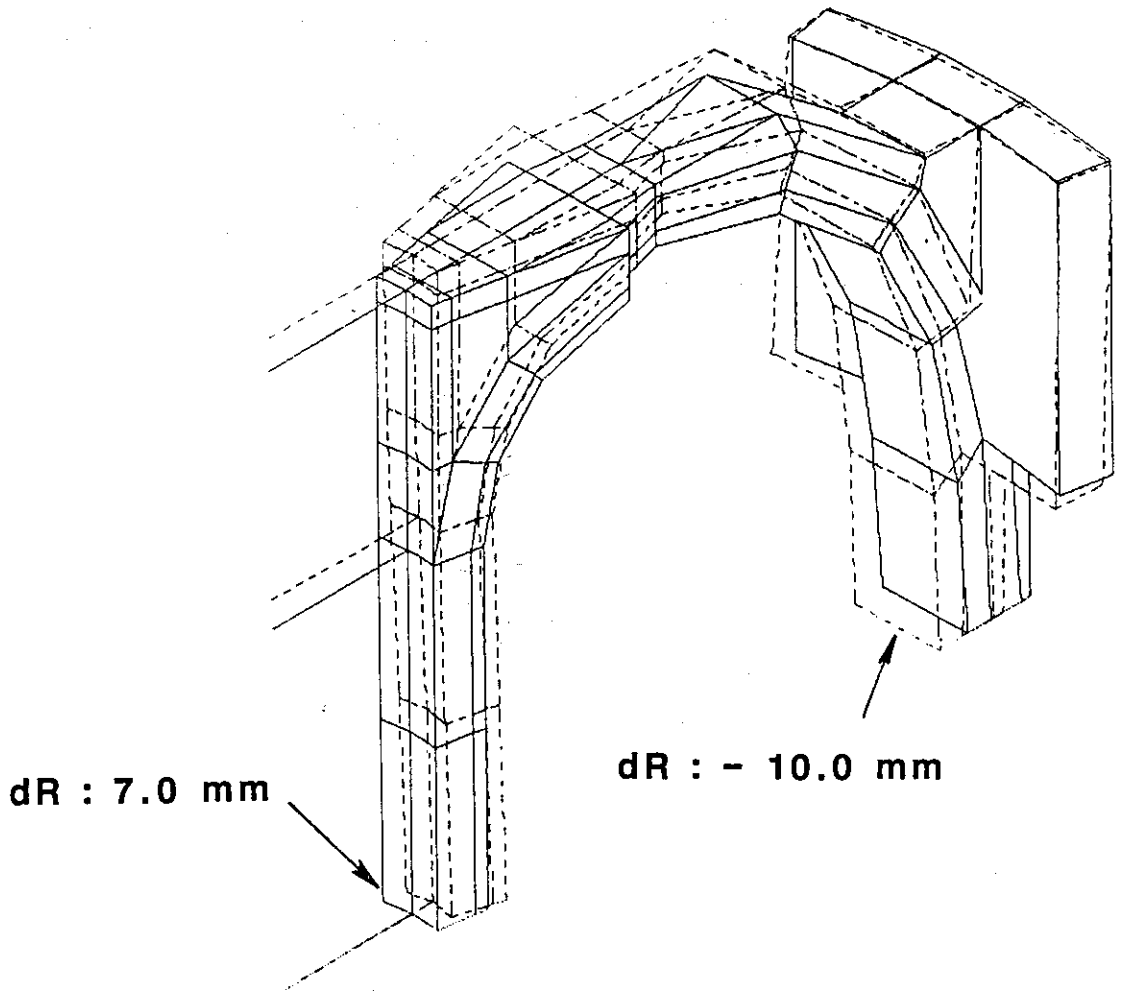

Fig. 3.15 Deformation of the Fault Coil (TF coil No.5) in the Open Circuit Mode.

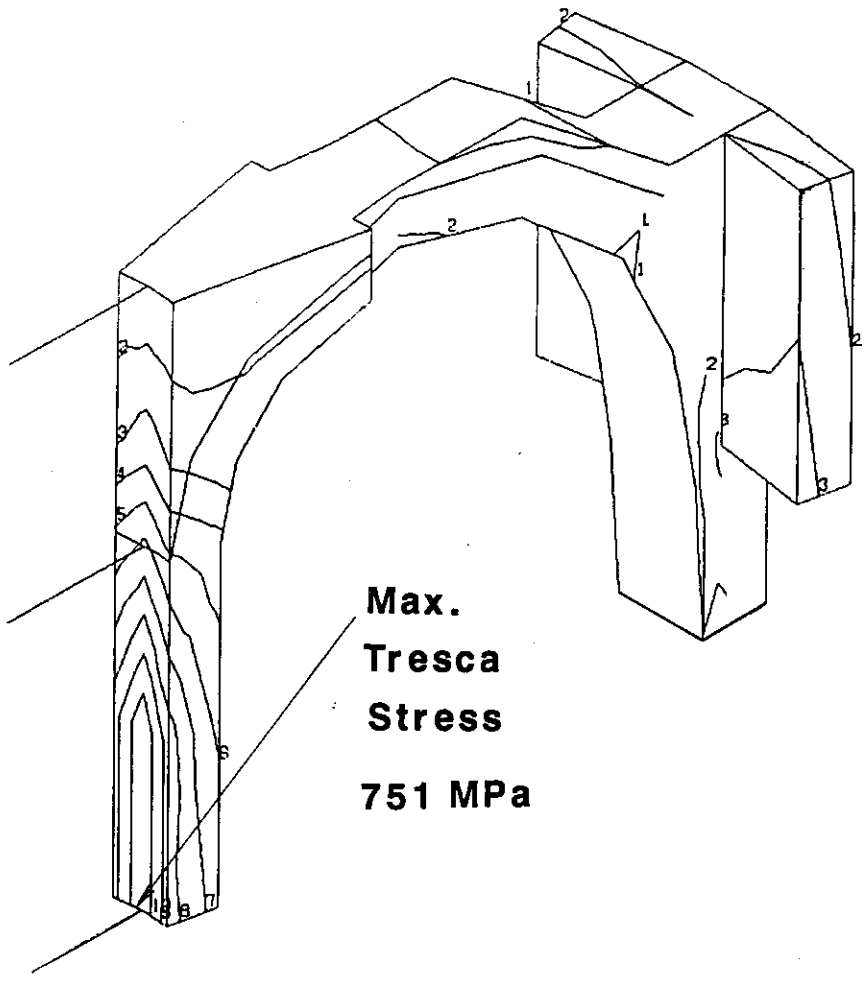

CONTOUR LEVEL (MPa)

1.	24.5
2.	98.0
3.	171.5
4.	245.0
5.	318.5
6.	392.0
7.	465.5
8.	539.0
9.	612.5
10.	686.0

Fig. 3.16 Stress Distribution in the TF Coil No.5 in the Open Circuit Mode of TF No.5.

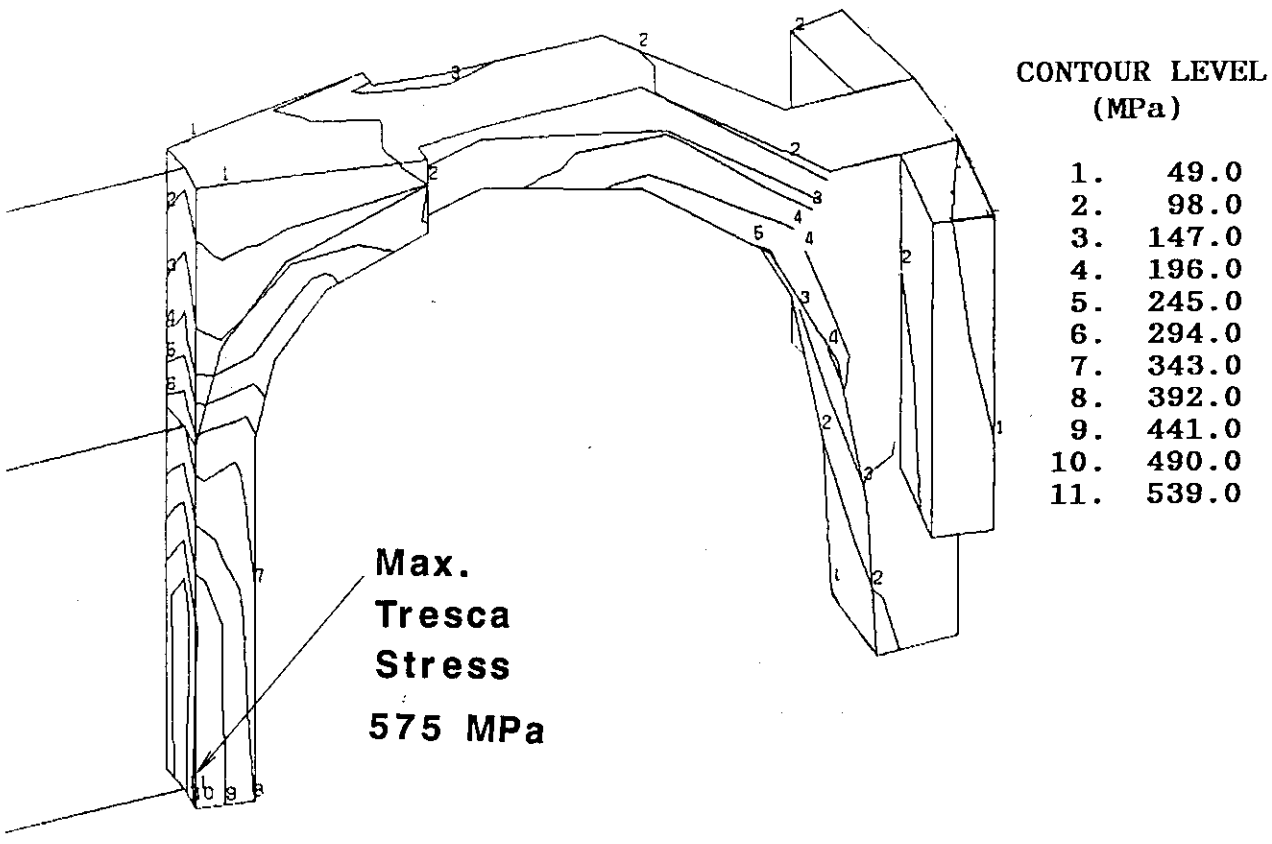

Fig. 3.17 Stress Distribution of TF Coil No.4 in the Open Circuit Mode of TF No.5.

4. Stress Analysis of Center Solenoid Coils

4.1 Introduction

The center solenoid (CS) coils have to support their own hoop forces without metal cases. Also, they have to sustain the vertical forces that include both their own magnetic force and the compressive force from neighboring coils. Hence, the net vertical force is applied to the coil located on the equatorial plane, i.e. PF-1 coil shown in Fig. 4.1. Therefore, the maximum stress appears in the PF-1 coil which has the highest magnetic field and suffer the largest electromagnetic forces in the CS coils.

Since the CS coils will be energized 100,000 times, there is a possibility that their operating life is limited by mechanical fatigue limit of the stainless steel conduits.

From these reasons, the stress analysis of the PF-1 coil's conduits was carried out. Since the preliminary stress analysis showed that the stress becomes largest at 'End of Burn (EOB)' during the operation [1], the stress analysis was performed using the loading condition at EOB for two operation scenarios. One is the EOB in the reference operation scenario (l_i=0.65, β_p=0.61). The other is the EOB in the operation scenario [1] (l_i=0.55, β_p=0.0), which can be considered to give the most severe stresses. These cases are named EOB1 and EOB2, respectively, in the analysis.

4.2 Procedure

The procedure to obtain the stress of the conduits is summarized as follows :

(1) Obtain the equivalent Young's modulus of CS coil.
(2) Obtain the distribution of vertical pressure on the equatorial plane.
(3) Obtain the distribution of radial pressure inside of each conduit.
(4) Obtain stress distribution of the conduits.

4.2.1 Equivalent Young's modulus of CS coil

The equivalent Young's modulus of the CS coil winding was calculated using a finite element method (FEM). The procedure is elucidated in Chapter 6 in detail. In this calculation, the effect of the structural grading is not considered and the FEM model was built for non-grading type conductor in Fig. 4.2.

The results are summarized as follows :

$$E_R = 51 \text{ GPa}$$
$$E_Z = 55 \text{ GPa}$$
$$E_\theta = 103 \text{ GPa}$$

$$\nu_{RZ} = 0.21$$
$$\nu_{ZR} = 0.23$$

$$\nu_{Z\theta} = 0.14$$
$$\nu_{\theta Z} = 0.26$$

$$\nu_{R\theta} = 0.14$$
$$\nu_{\theta R} = 0.28$$

4.2.2 Vertical pressure distribution

In the CS coils, the PF-1 coil located near the equatorial plane receives the most largest vertical pressure from adjacent coils. Also, in the PF-1 coil, the conduits near the equatorial plane receive the most largest vertical pressure. For these reasons, the pressure distribution on the equatorial plane was calculated by using FEM model.

The size of winding and the ampere-turn of each CS coil are listed in Table 4.1. The electromagnetic forces applied to each CS coil at EOB1 and EOB2 are shown in Table 4.2. The values at the initial magnetization (IMAG) are also shown in the same table as a reference.

The 2-dimensional FEM model of whole CS coils modeled by using axial symmetrical elements is shown in Fig. 4.3. The dimensions, the structure and the material properties are shown

in Fig. 4.4 (a) and (b). In this calculation, nodal displacement in the vertical direction was constrained on the equatorial plane. The maximum displacements calculated at the loading conditions listed in Table 4.2 are summarized below :

	R(mm)	Z(mm)
Initial Magnetization	3.9	10.8
EOB1 (Reference)	3.3	7.4
EOB2 (l_i=0.55, β_p=0)	3.2	8.6

The vertical pressure distributions near the equatorial plane, which was obtained by the distribution of vertical stress component, is shown in Fig. 4.5. The distribution is rather flat and the averaged values is about 65 MPa, 85 MPa and 95 MPa at Initial Magnetization, EOB1 and EOB2, respectively.

4.2.3 Radial pressure distribution

For the purpose of estimating the radial pressure inside of the conduits, the magnetic field distribution inside of the coil was calculated.

The distribution of the vertical component of magnetic field (Bz) on the inner surface of CS coil in the vertical direction is shown in Fig. 4.6 (a), (b) and (c). The maximum magnetic field is 13.6 T at Initial Magnetization and 12.5 T at both EOB1 and EOB2. The magnetic field on the equatorial plane is not maximum since the insulation gap of 50 mm exist between the coils. In order not to underestimate the radial pressure, the distribution of the vertical field in radial direction was plotted by using the maximum values at Z = 900.0 mm instead of those values on equatorial plane. The distributions are shown in Fig. 4.7 (a), (b) and (c). For these calculations, the grading model of 3 stages (3 grading) shown in Fig. 4.2 was employed. By using the conductor current (-40kA) and the vertical field component, the radial force applied on each conduit was obtained and transformed to the radial pressure. The distribution of radial pressure at Initial Magnetization,

EOB1, and EOB2, is shown in Fig. 4.8. The maximum pressures of three cases are about 15 MPa and nearly the same value. The negative values, which mean the inward pressure, arise at EOB phase.

4.2.4 Stress distribution in the conduits

For the calculation of stress distribution in the conduit, the three pancakes of PF-1 coil were modeled by using 2-dimensional axial symmetric elements. The FEM model for the analysis is shown in Fig. 4.9. In order to avoid the effects of local displacement and the boundary conditions, the stresses in the middle pancake were used for the stress evaluation.

In this analysis, the structural grading of 3 stages (3 grading) shown in Fig. 4.2 was modeled and analyzed. The displacement of the bottom surface was constrained in the vertical direction.

The conduits are surrounded by the insulation tape. The room between the corners of conduits are filled with the insulator. The material properties employed for the analysis is shown in Fig. 4.10.

The loading condition of the conduits are schematically shown in Fig. 4.11. The radial and vertical forces, which were obtained by the previous steps, were applied as a internal and external pressure.

Since a double pancake has a splice or traverse section in the innermost turn, there is a cross-section in which the upper pancake piles up on lower one with the displacement of half (or less than half) width of conduit as shown in Fig. 4.12. In this chapter, the names of 'extraordinary part' is used to distinguish such a part from 'ordinary' part. Although there exist both parts in one double pancake, the stress distribution of the extraordinary part was also analyzed by using corresponding FEM model.

4.3 Results

4.3.1 The stress of the conduits in the ordinary part

The global displacement of ordinary part calculated at EOB1 is shown in Fig. 4.13. The Tresca stress of the elements in the middle pancake is plotted along the radial direction. The distribution is shown in Fig. 4.14. The distributions of radial stress component (σ_R), circumferential stress component (σ_β, and vertical stress component (σ_Z) in the innermost conduit is shown in Fig. 15 (a), (b) and (c). The distribution of Tresca stress in the innermost conduit is also shown in Fig. 4.15 (d). The maximum values of each stress component, σ_R, σ_θ, σ_Z and σ_T, in the 1st, 5th and 9th conduits are summarized in Table. 4.3. The global displacement calculated at EOB2 is shown in Fig. 4.16. The distribution of Tresca stress in the elements of middle pancake at EOB2, which corresponds to Fig. 4.14, is shown in Fig. 4.17. The distributions of stress component at EOB2 are also shown in Fig. 4.18 (a), (b), (c) and (d). From Fig. 4.14 and Fig. 4.17, it can be recognized that the structural grading of 3 stages is feasible to flatten the stress distribution. The maximum Tresca stress is about 610 MPa at EOB2 and the stress region larger than 600 MPa is very small compared with the whole region. The maximum tensile stress (σ_θ) in the circumferential direction is about 440 MPa.

4.3.2 The stress of the conduits in the extraordinary part

The calculation was carried out for the 2 cases. Case 1 is the structural model without stainless steel filler in the empty space between the top and bottom pancakes. Case 2 is the case that the steel filler is installed in the empty space. Both structural models composed of three pancakes are shown in Fig. 4.19 (a) and (b). The loading condition at EOB2 was adopted for the analysis, because this condition gives the most sever stress.

The global displacements of both structural models at EOB2 are shown in Fig. 4.20 (a) and (b). The maximum values of each stress component, σ_R, σ_θ, σ_Z and σ_T, calculated at 1st, 5th,

and 9th conduit, are summarized in Table 4.4. In the model without the filler, the maximum Tresca stress is larger than 900 MPa and the tensile stress is 510 MPa.

On the other hand, in the model with the steel filler, the maximum Tresca stress is reduced to 650 Mpa and the region greater than 600 MPa is just a little fraction. The distributions of each stress component in the innermost conduits of middle pancake, which has the filler, are shown in Fig. 4.21 (a), (b), (c) and (d). The corresponding figures in the innermost conduit of bottom pancake are also shown in Fig. 4.22 (a), (b), (c) and (d). The maximum Tresca stress is about 650 MPa and the region greater than 600 MPa is a little larger than that calculated in the middle pancake. The maximum tensile stress is about 450 MPa.

It should be noticed that the stress in the extraordinary part is larger than that in the ordinary part. And the filler is required to reduce the stress to the allowable limit which are mentioned in next section.

4.4 Discussion

The maximum allowable Tresca stress (without any design margin) under static loading condition can be considered as ,

Primary stress : S_m

Local stress : $1.5\ S_m$,

where,

$S_m = \max (2/3\sigma_y, 1/2\sigma_u)$, σ_y : yield strength,

σ_u : ultimate strength

The value S_m is about 825 MPa for the newly developed cryogenic steels recommended by JAERI.

Since there is no assured data for the fatigue strength, ~70 % of the above values was assumed temporally as an allowable limit for the cyclic load of 30,000 times (i.e. about 600 MPa for the Primary stress). This assumption is roughly equivalent to the assumption that the allowable flaw size on the surface is less than 0.25 mm [2] (i.e. The 0.25 mm initial flaw

grows to the failure with 30,000 cycles of 600 MPa stress). In any way since it is very difficult to measure the initial flaw on the inner surface of the conduits after welding, it is required to confirm the fatigue stiffness experimentally and to determine the targets of the material developments.

If the above criteria can be used, the Japanese design can satisfy the requirements from the reference scenario operation. For the flexible operation, the design may be also available with the constraints of the number of such an operation, since the stress region larger than 600 MPa is not so large.

However, it should be noticed that these designs have no technological design margin and are very dangerous in technological sense. Therefore, such a margin should be included in the design of the next phase.

4.5 Summary

The stress analyses of the CS coil conduits were performed with considering the operational flexibility of the CS coil system. In the ordinary part, in which the conduits are piled up regularly in the vertical direction, the maximum Tresca stress in the innermost conduit was about 600 - 615 MPa at the EOB. In the extraordinary part, where the empty space to adjust the conductor splice exists, the maximum Tresca stress in the innermost conduit reaches 650 MPa. The filler of stainless steel, which is packed into the empty space between pancakes in the extraordinary part, is required to reduce the stress level to the allowable limit.

References

[1] M. Hasegawa, K. Yoshida, et al., "Conceptual design and Analysis of the Center Solenoid Coils" (ITER-IL-MG-247).

[2] N. Miki, F. Iida, Y. Wachi, K. Toyoda, et al., Conceptual Design Study of Fusion Experimental Reactor (FY87 FER) - Magnet Design - , JAERI-M 88-110

Table 4.1 Winding size and ampere-turns of each coil

	R (mm)	Z (mm)	D_R(mm)	D_Z(mm)	IMAG(MA)	EOB1(MA)	EOB2(MA)
PF-1U, L	1755	± 950	590	1848	20.41	- 22.30	- 22.42
PF-2U, L	1755	± 2850	590	1848	20.41	- 22.30	- 22.42
PF-3U, L	1755	± 4750	590	1848	20.41	- 9.14	- 11.45
PF-4U, L	1755	± 6650	590	1848	20.41	0.0	2.61
PF-5U, L	3900	± 9000	900	900	14.53	6.25	11.71
PF-6U, L	11500	± 6000	500	1500	0.25	- 6.49	- 13.61
PF-7U, L	11500	± 3000	500	900	0.25	- 5.25	0.36
PLASMA	6000	0	2150	4773	----	22.00	22.00

Table 4.2 Electromagnetic force of each CS coil

	IMAG		EOB1(βp=0.61, 1i=0.65)		EOB2 (βp=0.0, 1i=0.55)	
	F_R(MN)	F_Z(MN)	F_R(MN)	F_Z(MN)	F_R(MN)	F_Z(MN)
PF - 4U	1333.1	- 362.9	0.0	0.0	- 4.0	46.8
PF - 3U	1422.2	- 36.8	264.7	- 216.8	326.2	- 308.5
PF - 2U	1436.6	- 4.9	1069.0	- 313.9	1069.1	- 284.2
PF - 1U	1438.9	- 0.6	1163.1	- 26.3	1154.6	- 23.2

Table 4.3 Maximum values of stress component, σ_R, σ_θ, σ_Z and σ_T, in the 1st, 5th and 9th conduit in the ordinary part at IMAG, EOB1 and EOB2.

Stress in 1st Conduit (MPa)

	Max. σ_R	Max σ_θ	Max σ_Z	Max σ_T
IMAG	73.5	502.7	-183.3	615.4
EOB1	82.3	434.1	-256.8	594.9
EOB2	89.2	437.1	-283.2	614.5

Stress in 5th Conduit (MPa)

	Max. σ_R	Max σ_θ	Max σ_Z	Max σ_T
IMAG	50.0	421.4	-188.2	539.0
EOB1	-84.3	360.6	-251.9	524.3
EOB2	-91.1	363.6	-278.3	544.9

Stress in 9th Conduit (MPa)

	Max. σ_R	Max σ_θ	Max σ_Z	Max σ_T
IMAG	-57.8	369.5	-228.3	516.5
EOB1	-82.3	315.6	-307.7	525.3
EOB2	-89.2	320.5	-341.0	550.8

Table 4.4 Maximum values of stress component, σ_R, σ_θ, σ_Z and σ_T, in the 1st, 5th and 9th conduit in the extraordinary part at EOB2.

Stress in 1st Conduit (MPa)

	Max. σ_R	Max σ_θ	Max σ_Z	Max σ_T
CASE1	-437.1	506.7	-697.8	933.0
CASE2	207.8	446.9	-327.3	653.7

Stress in 5th Conduit (MPa)

	Max. σ_R	Max σ_θ	Max σ_Z	Max σ_T
CASE1	-177.4	386.1	-353.8	622.3
CASE2	-175.4	378.3	-351.8	603.7

Stress in 9th Conduit (MPa)

	Max. σ_R	Max σ_θ	Max σ_Z	Max σ_T
CASE1	159.7	350.0	-407.7	609.6
CASE2	160.7	342.0	-407.7	599.8

CASE1 : Stress without Steel Filler
CASE2 : Stress with Steel Filler

	DR (mm)	DZ (mm)
PF1U	590	1846
PF2U	590	1846
PF3U	590	1846
PF4U	590	1846
PF5U	752	850
PF6U	466	1522
PF7U	466	950

	DR (mm)	DZ (mm)
PF1L	590	1846
PF2L	590	1846
PF3L	590	1846
PF4L	590	1846
PF5L	752	850
PF6L	466	1522
PF7L	466	950

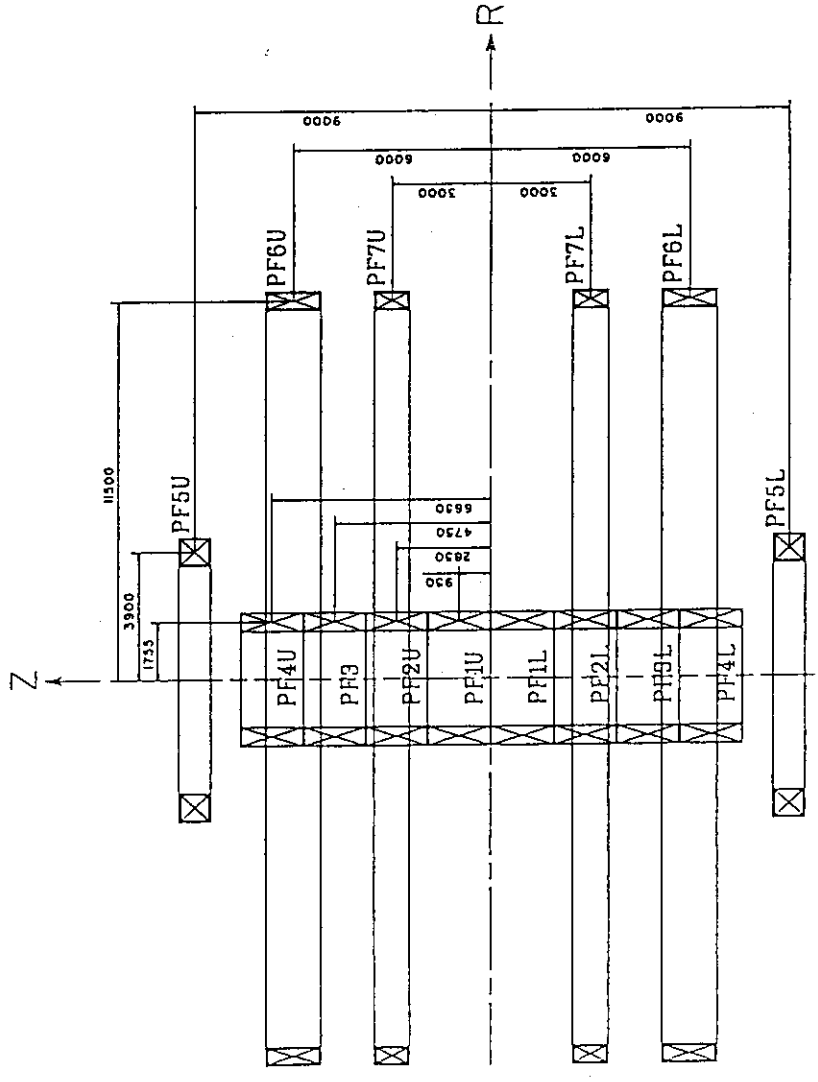

Fig. 4.1 Configuration and size of poloidal field coils.

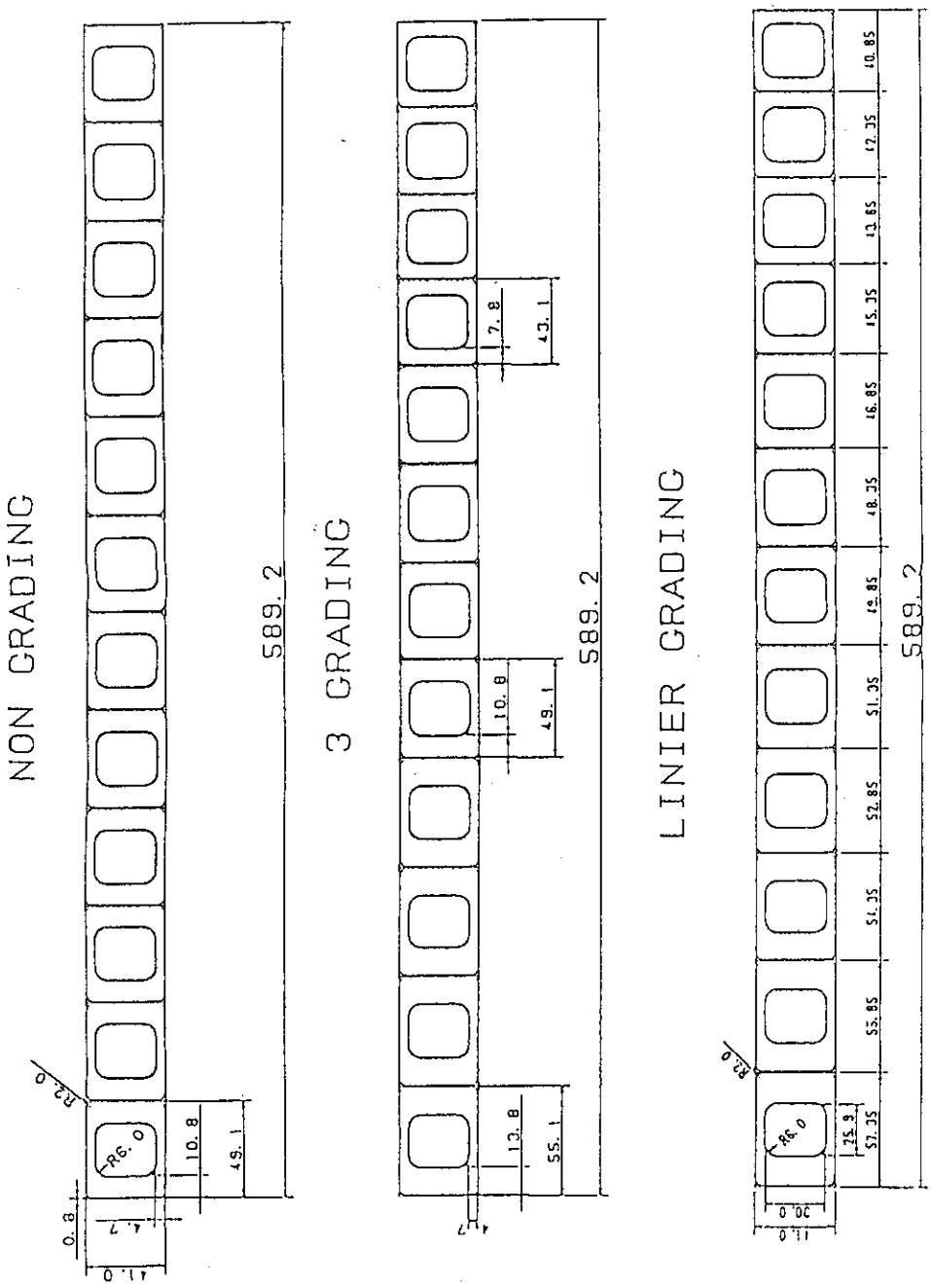

Fig. 4.2 Three types of structural grading for CS coil..

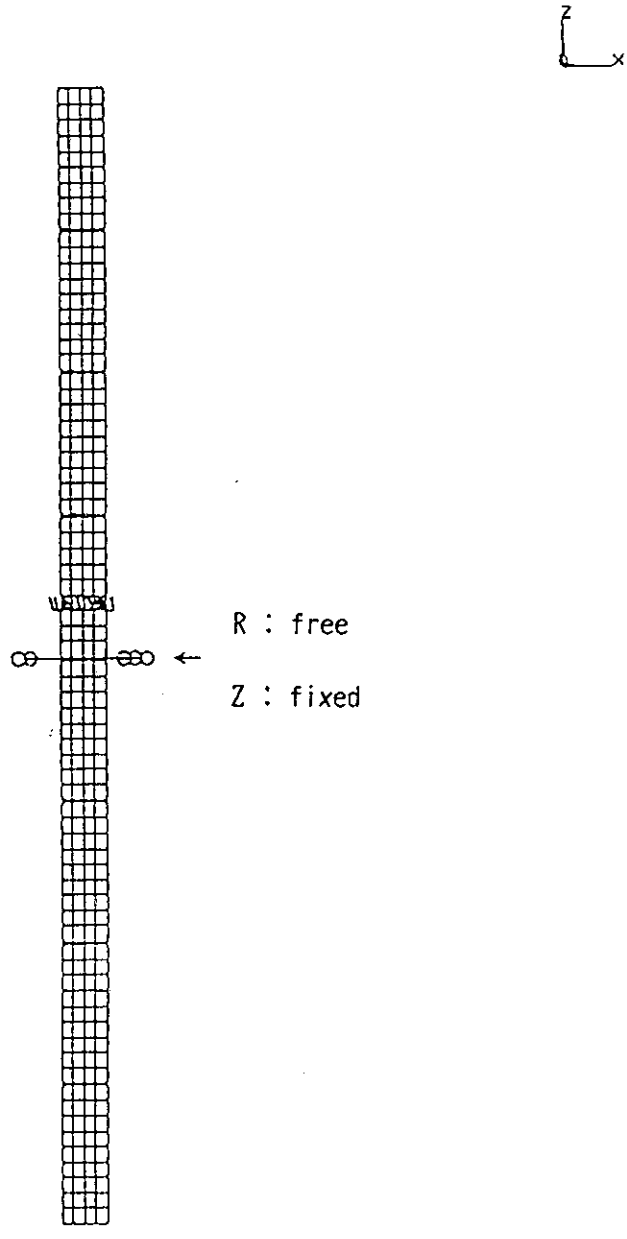

Fig. 4.3 The axial symmetrical FEM model and boundary condition for the analysis of whole CS coils.

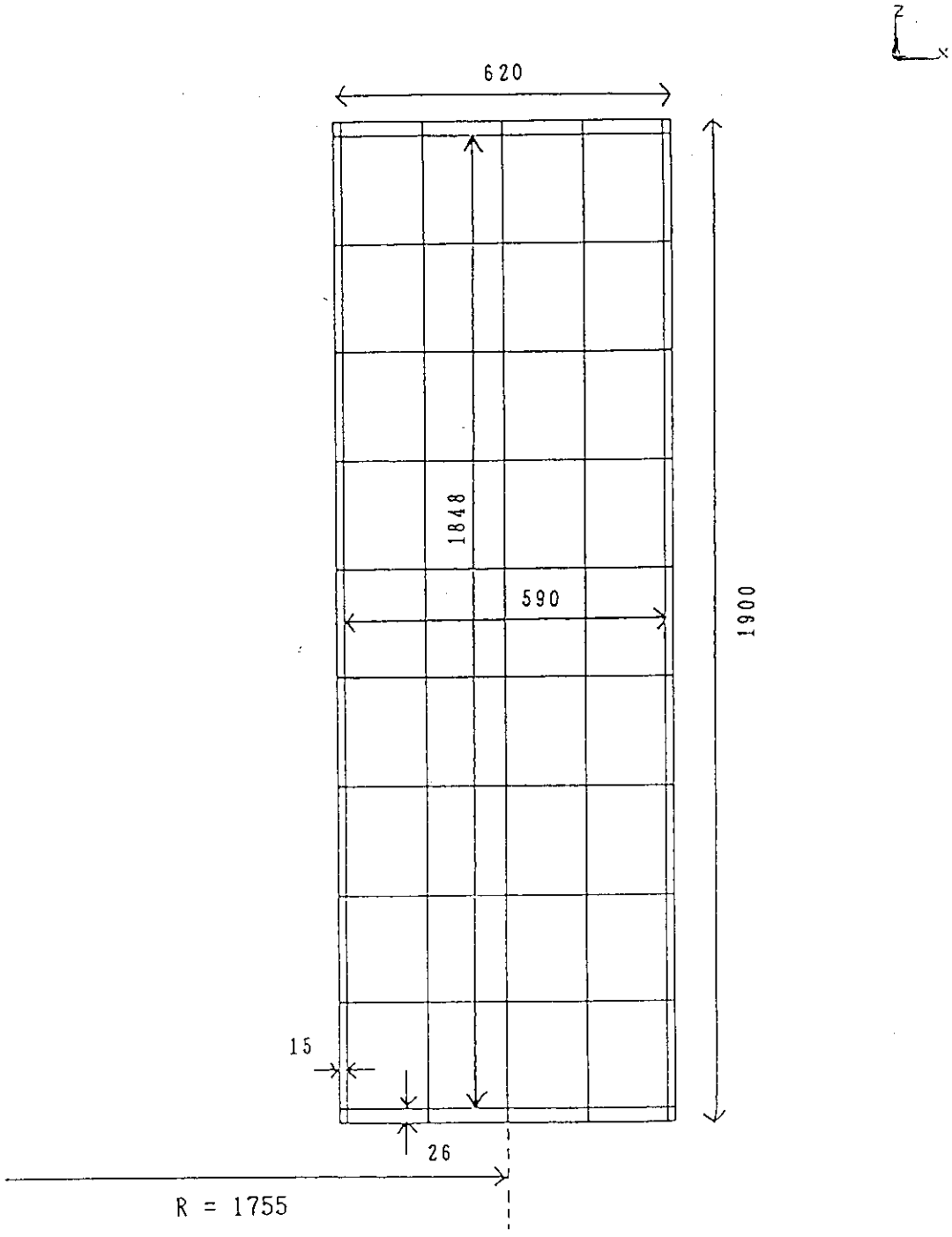

Fig. 4.4 (a) The dimensions of the CS coils

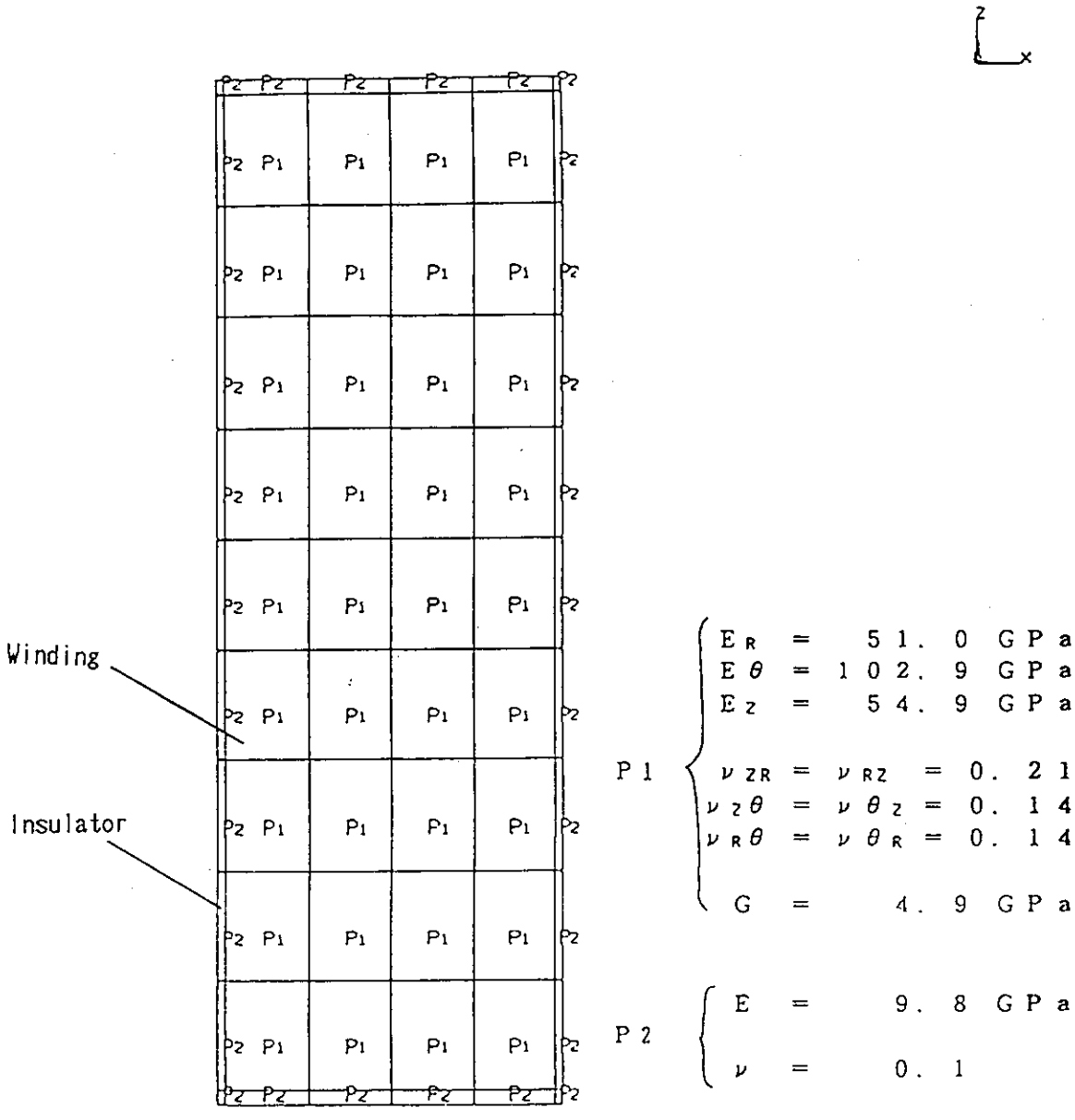

Fig. 4.4 (b) The structure and material properties of the CS coil.

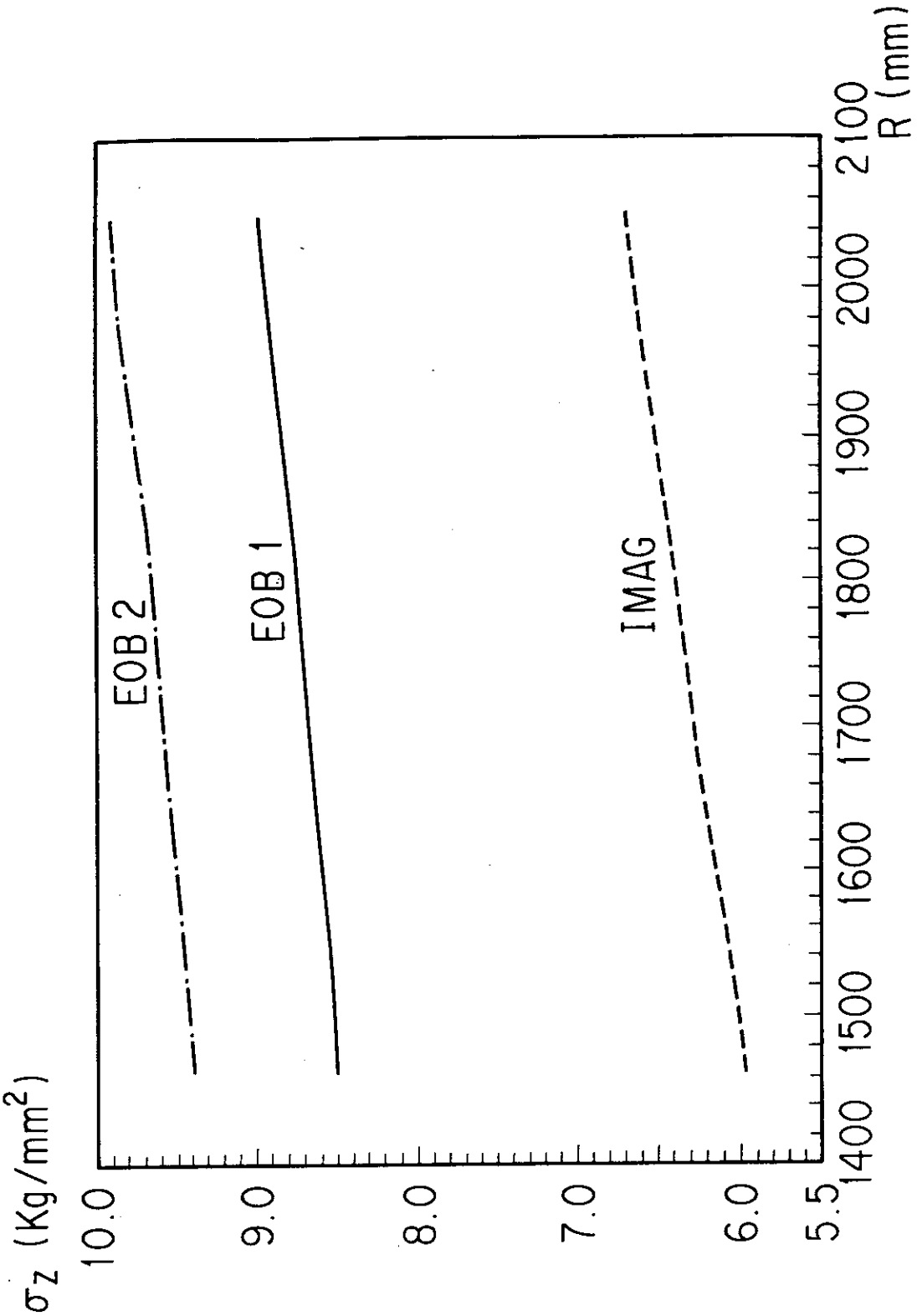

Fig. 4.5 The distribution of vertical pressure (or vertical stress) in the CS coil near the equatorial plane.

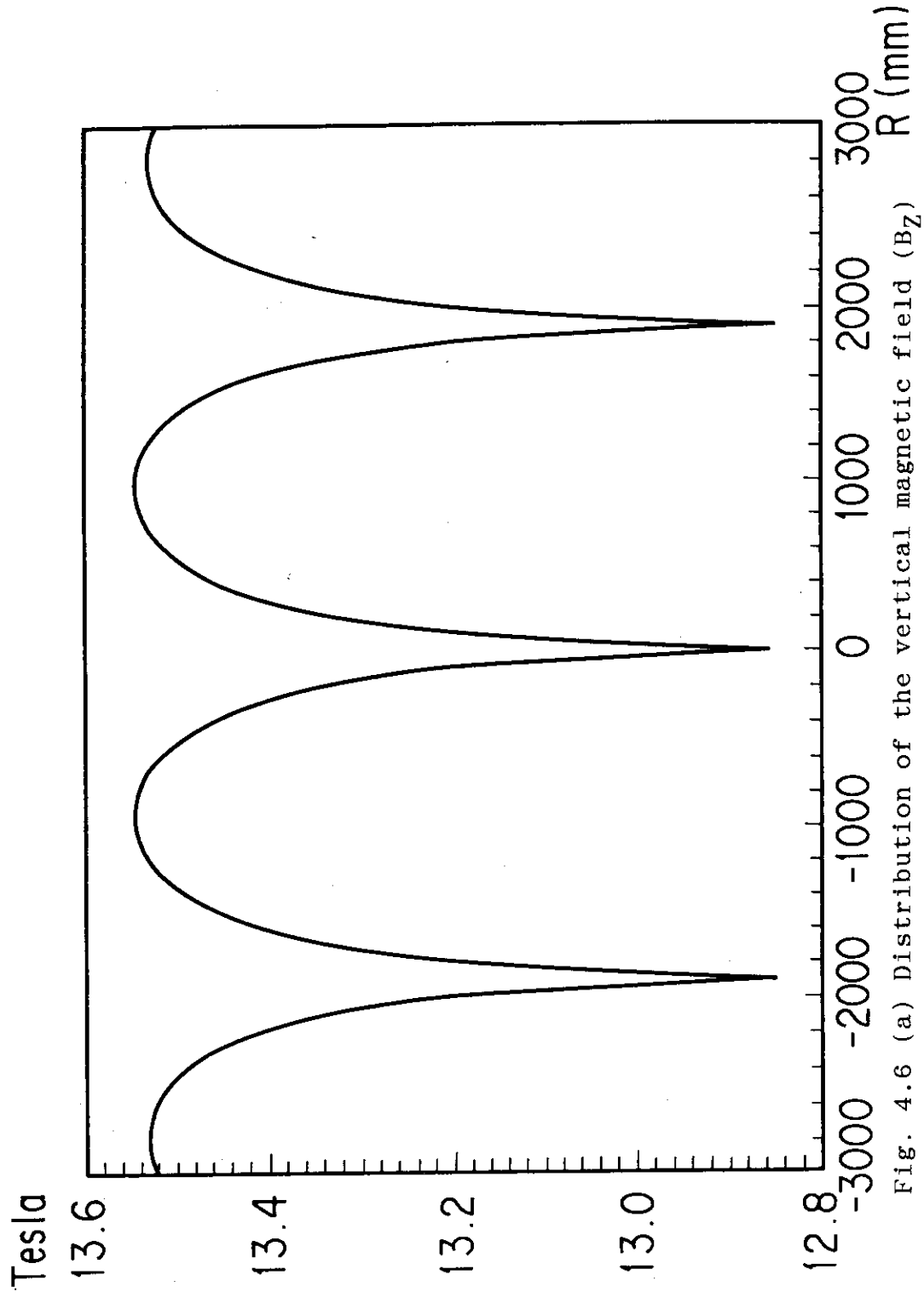

Fig. 4.6 (a) Distribution of the vertical magnetic field (B_Z) on the inner surface of CS coil in vertical direction at Initial Magnetization.

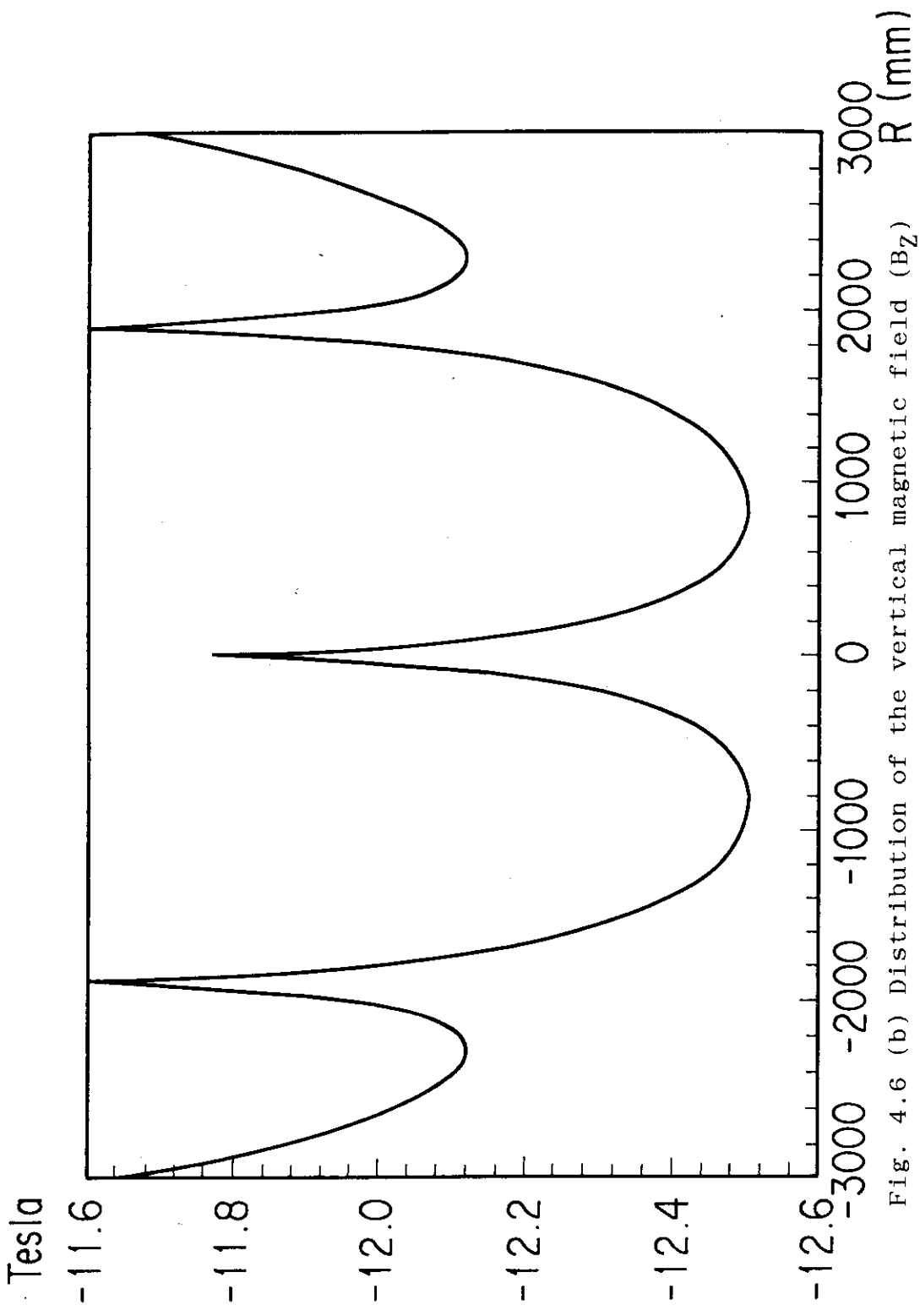

Fig. 4.6 (b) Distribution of the vertical magnetic field (B_Z) on the inner surface of CS coil in vertical direction at EOB1.

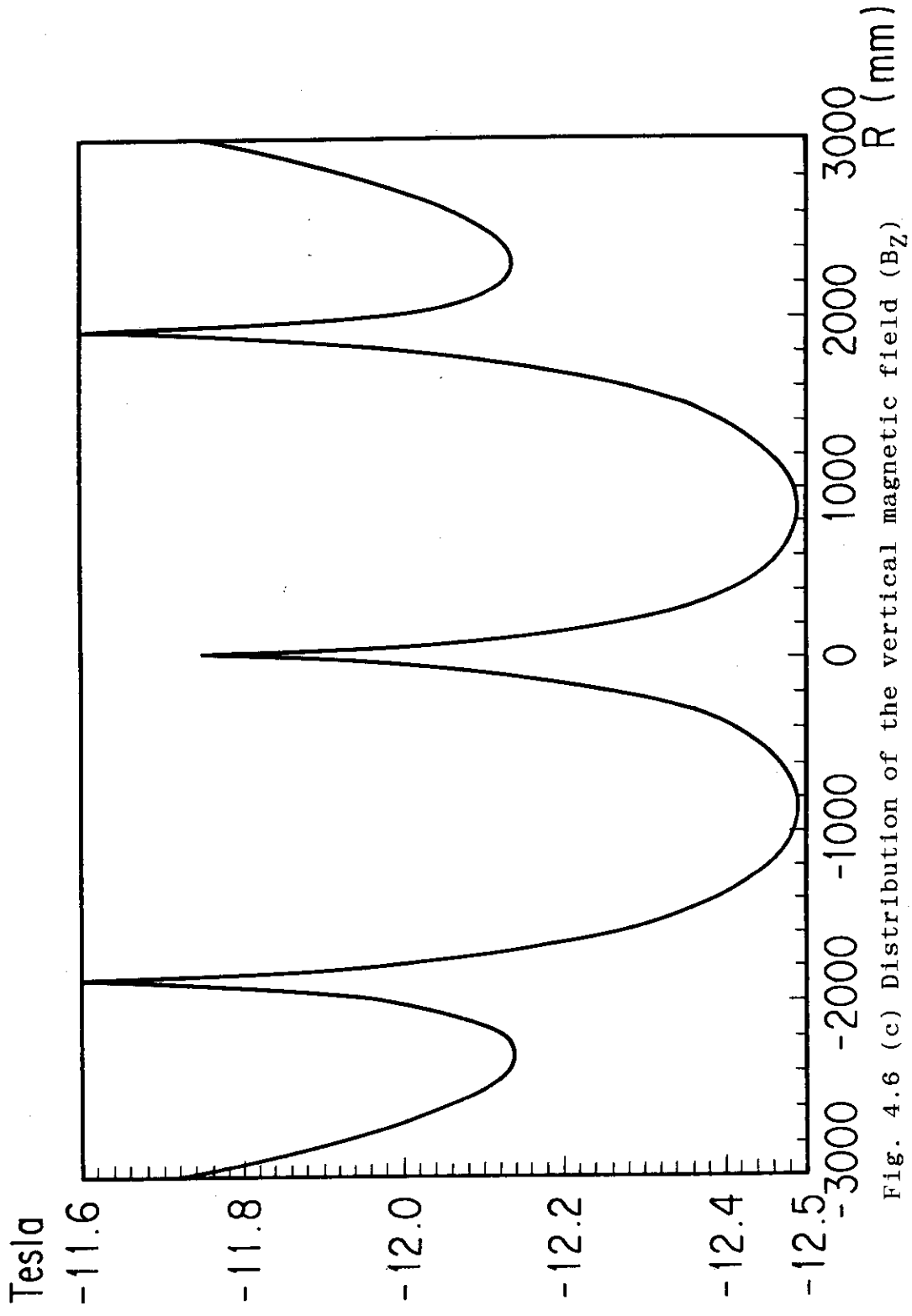

Fig. 4.6 (c) Distribution of the vertical magnetic field (B_Z) on the inner surface of CS coil in vertical direction at EOB2.

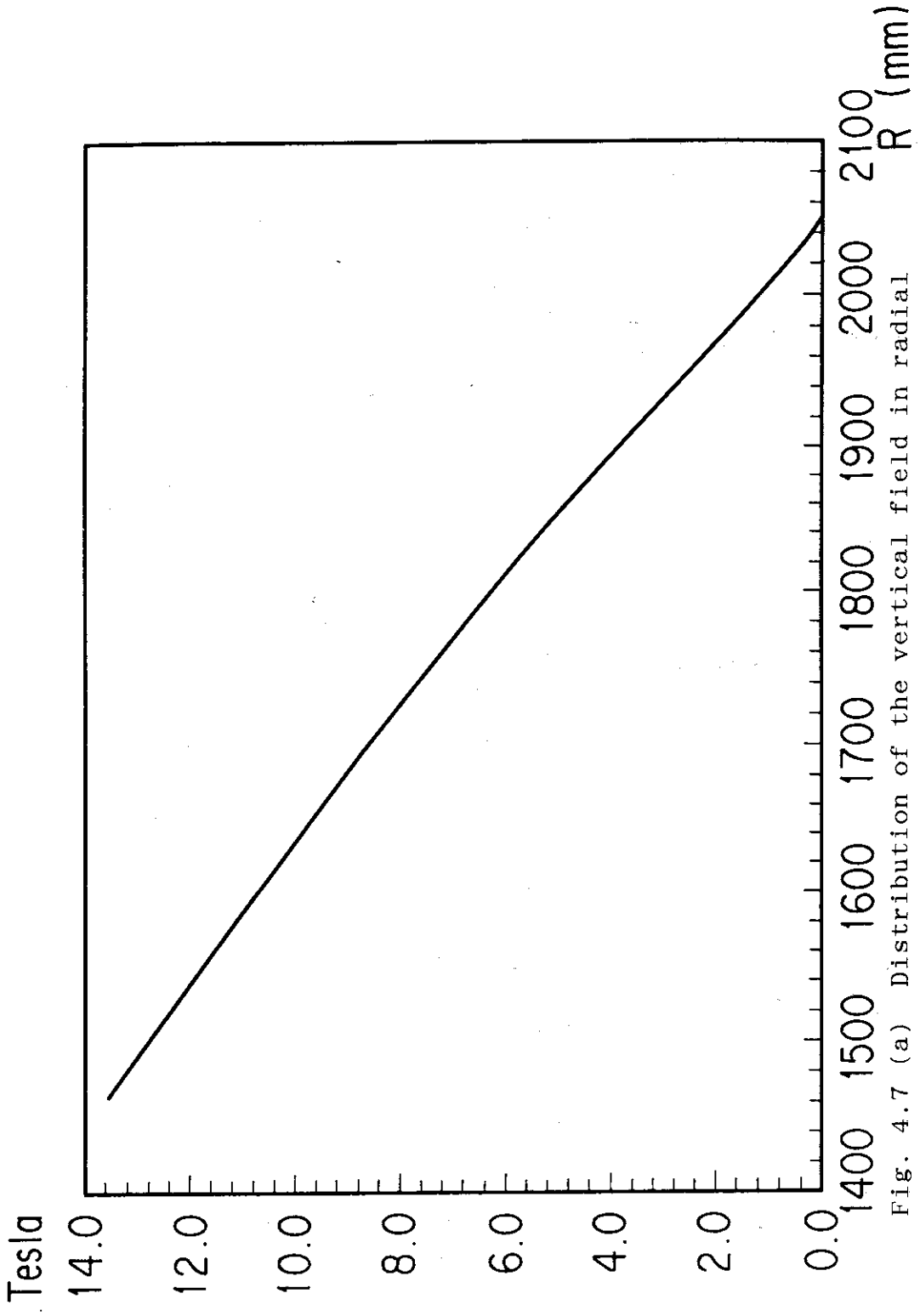

Fig. 4.7 (a) Distribution of the vertical field in radial direction on the horizontal plane at the maximum value point at Initial Magnetization.

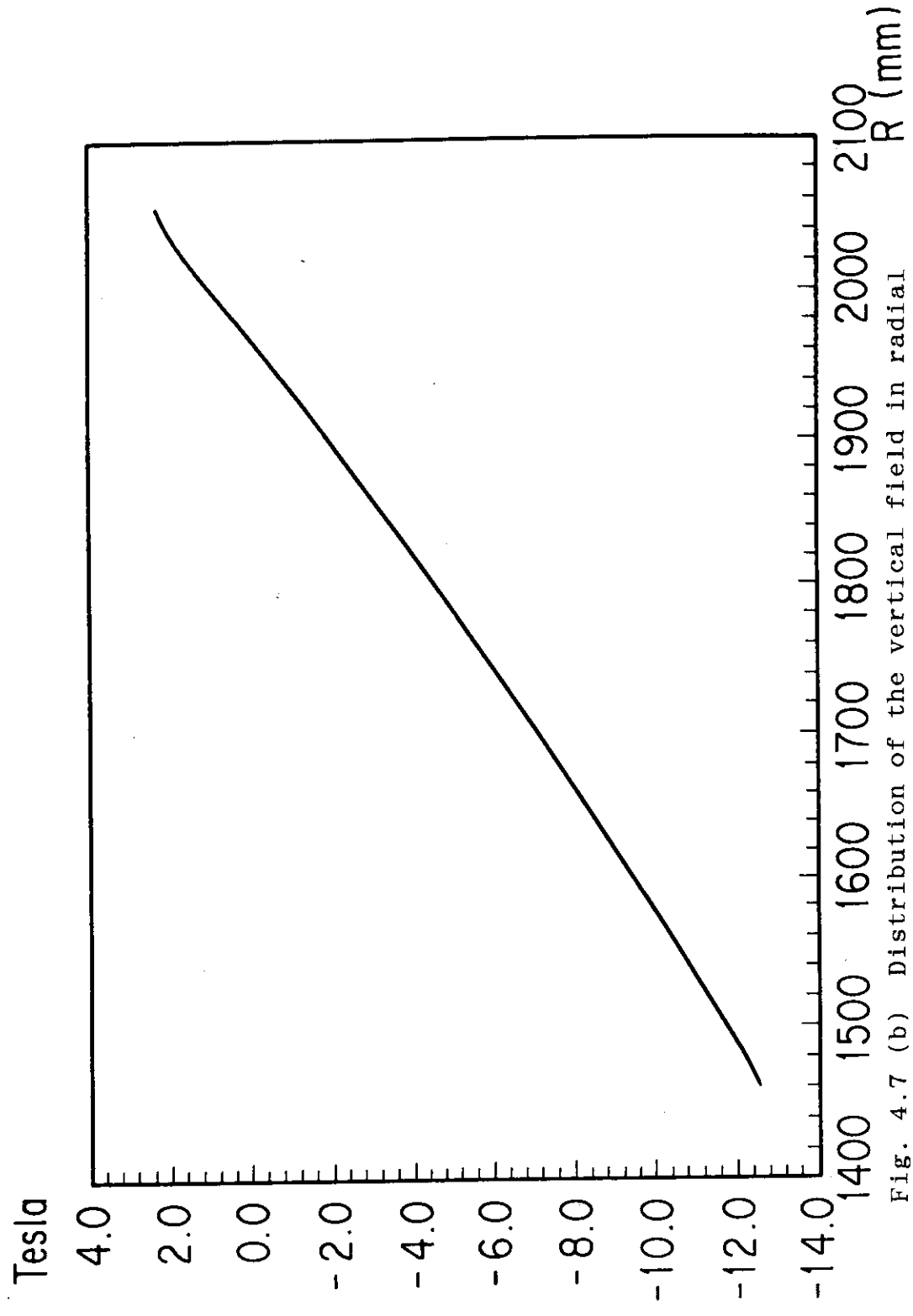

Fig. 4.7 (b) Distribution of the vertical field in radial direction on the horizontal plane at the maximum value point at EOB1.

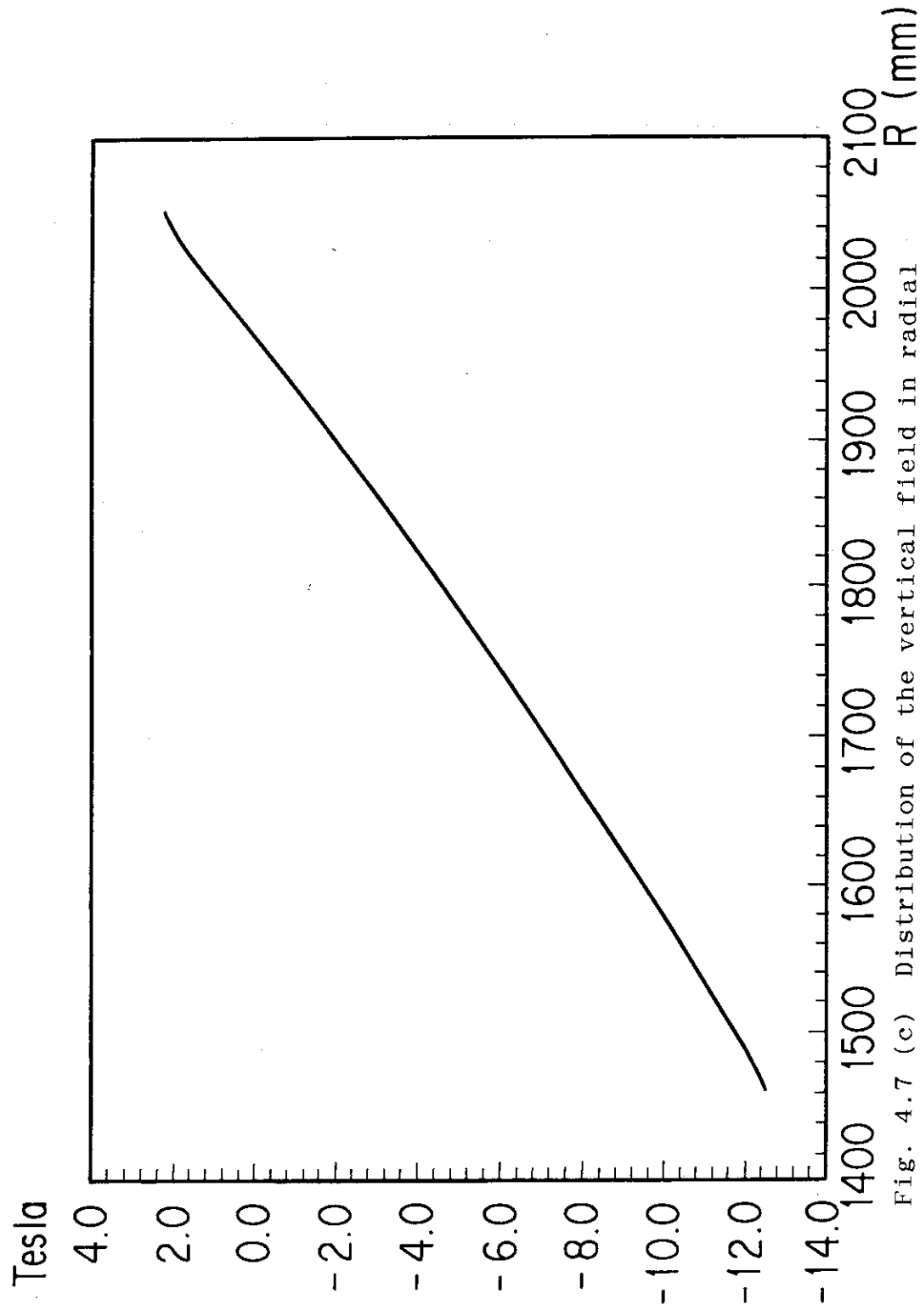

Fig. 4.7 (c) Distribution of the vertical field in radial direction on the horizontal plane at the maximum value point at EOB2.

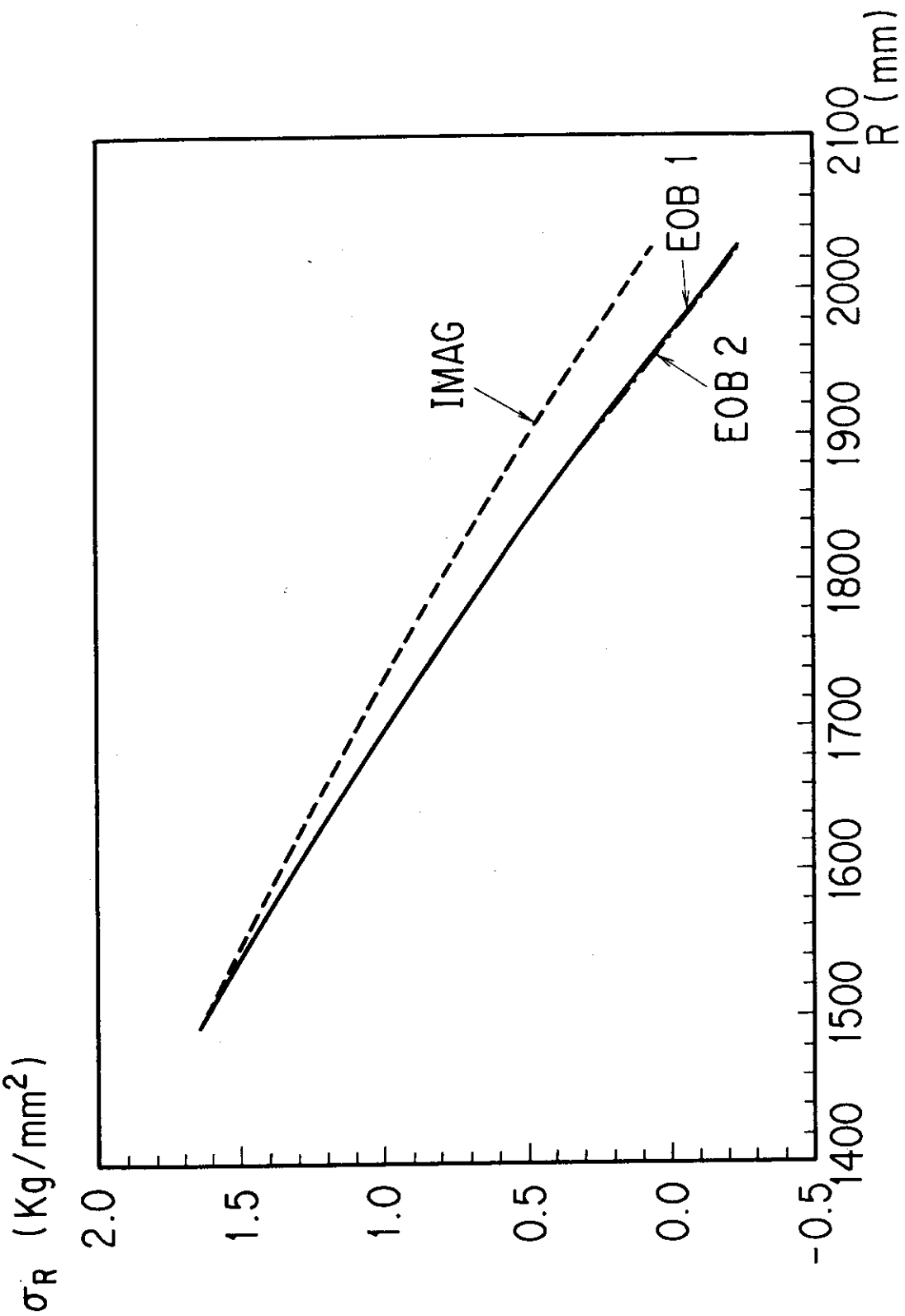

Fig. 4.8 Distribution of the radial pressure inside the conduits.

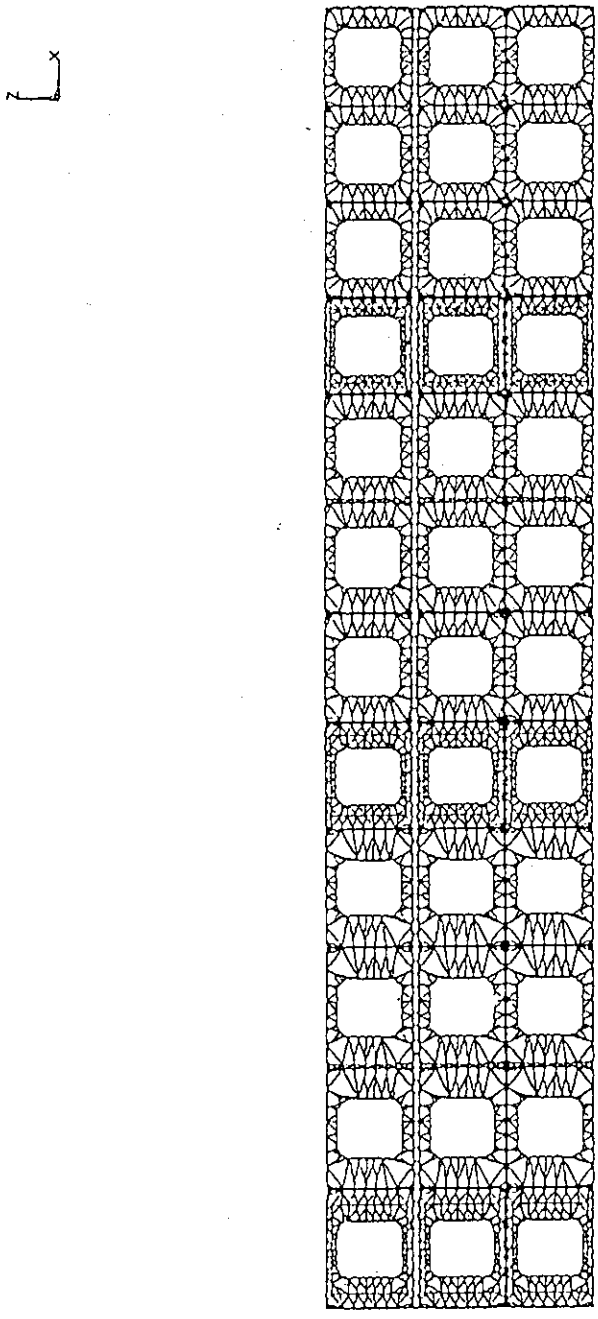

Fig. 4.9 FEM model of three pancakes in ordinary part.

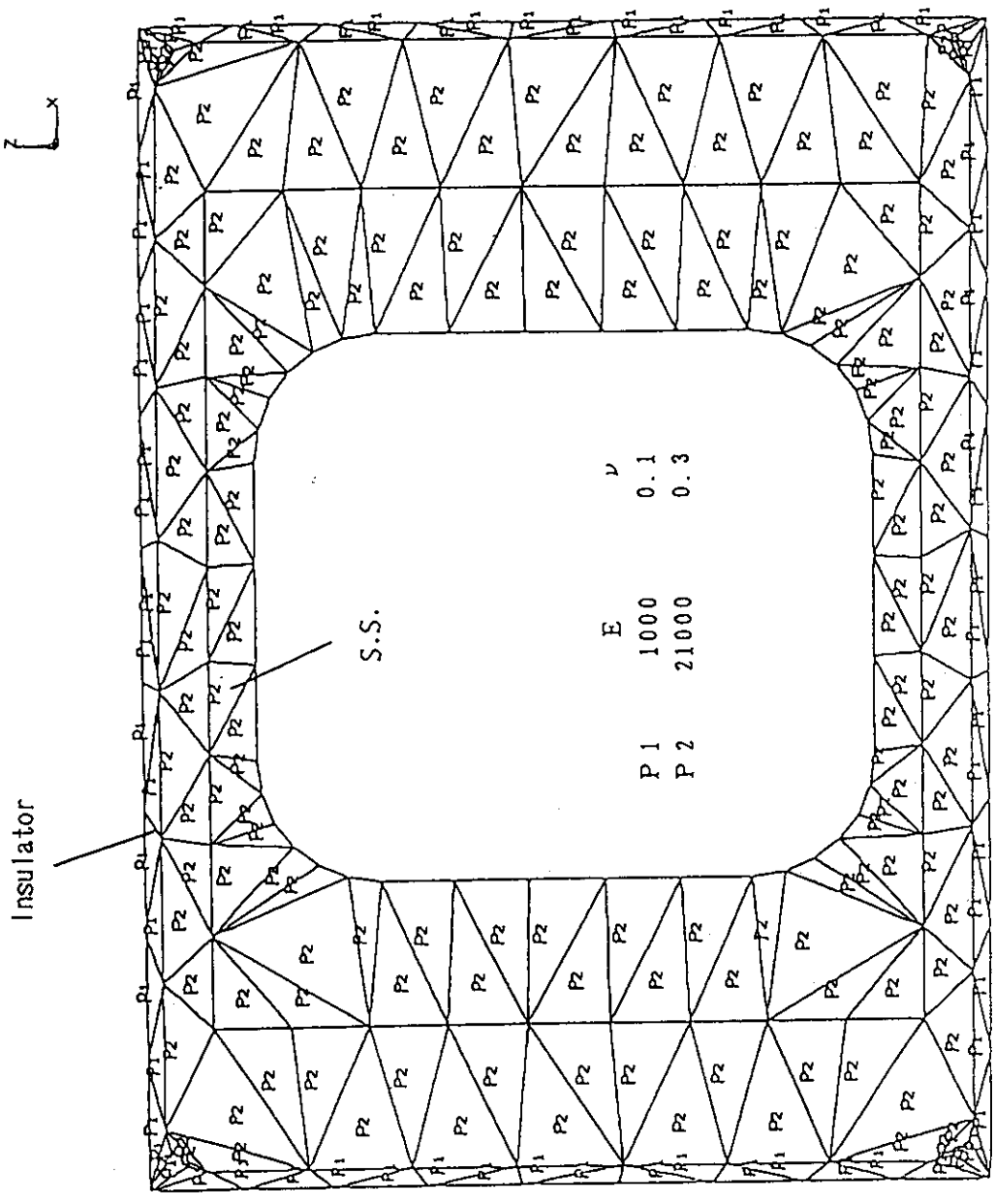

Fig. 4.10 Material properties employed for the analysis.

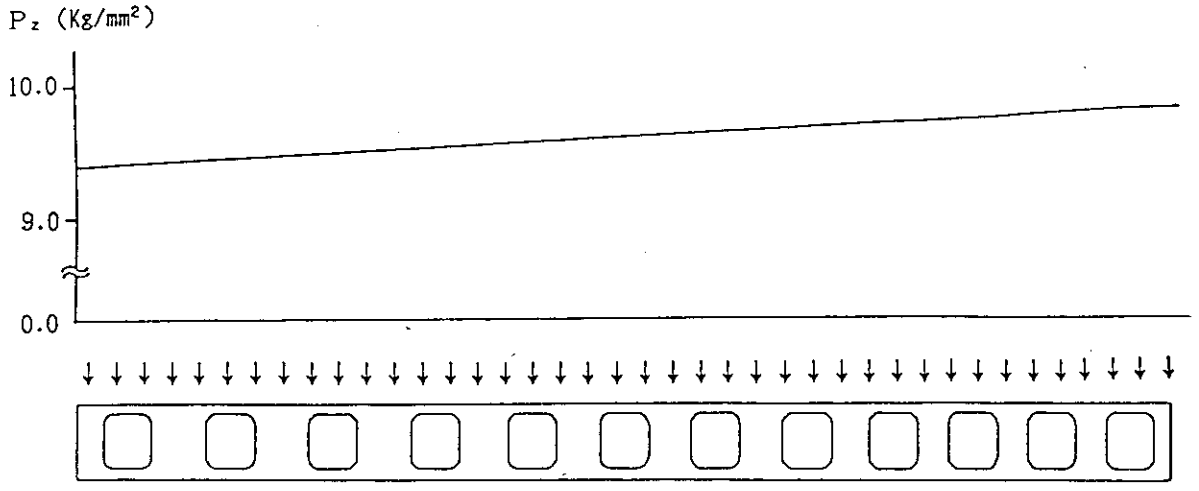

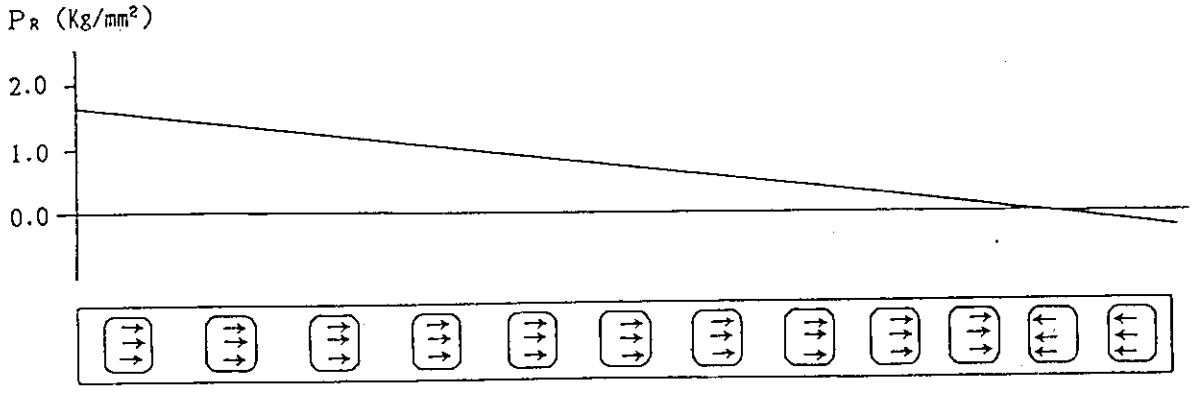

Fig. 4.11 Load condition of the conduits.

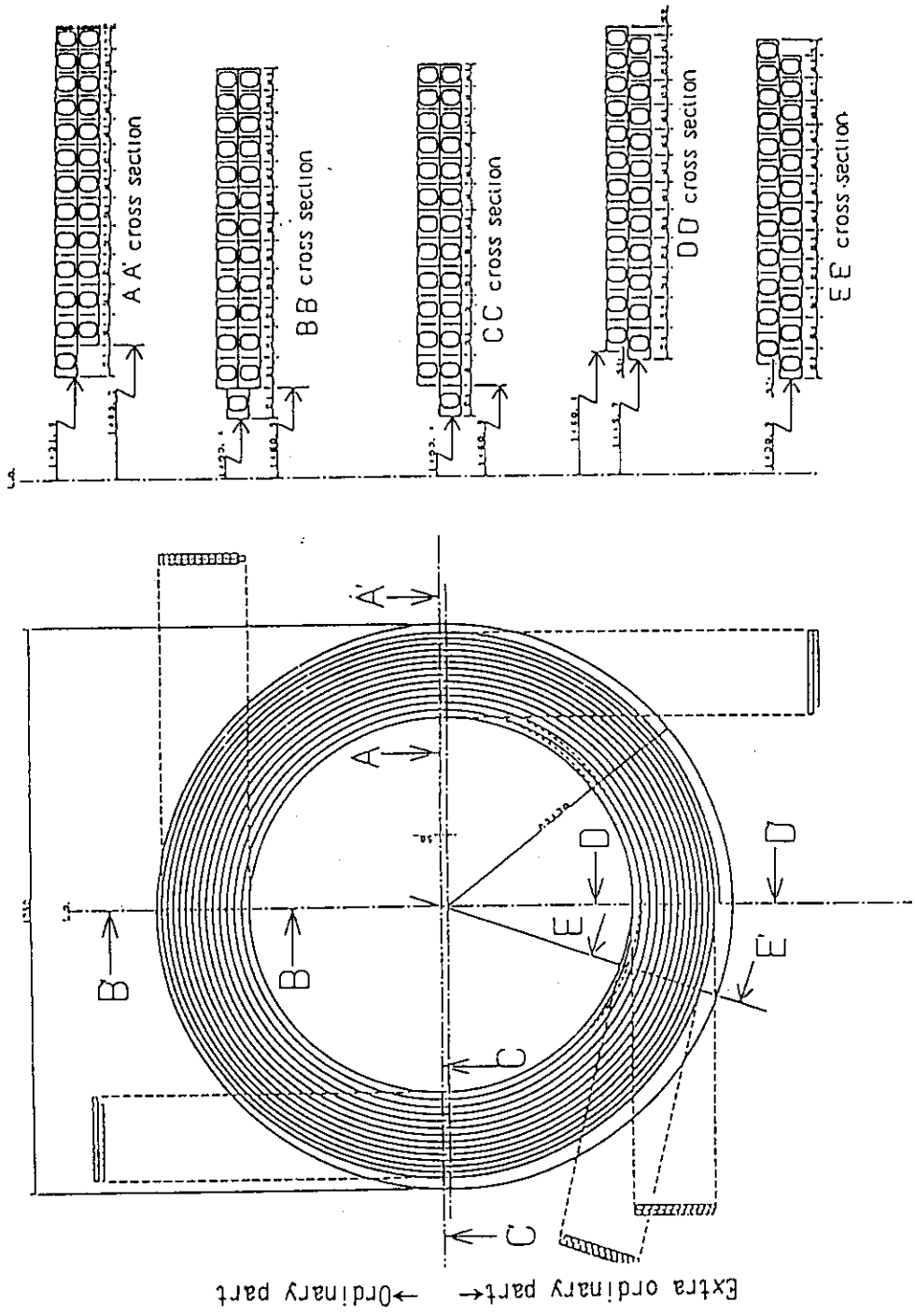

Fig. 4.12 Top view and the cross-section of pancake coil. A-A', B-B',C-C' cross-sections can be considered as an ordinary part and D-D' and E-E' cross sections are considered as an extraordinary part.

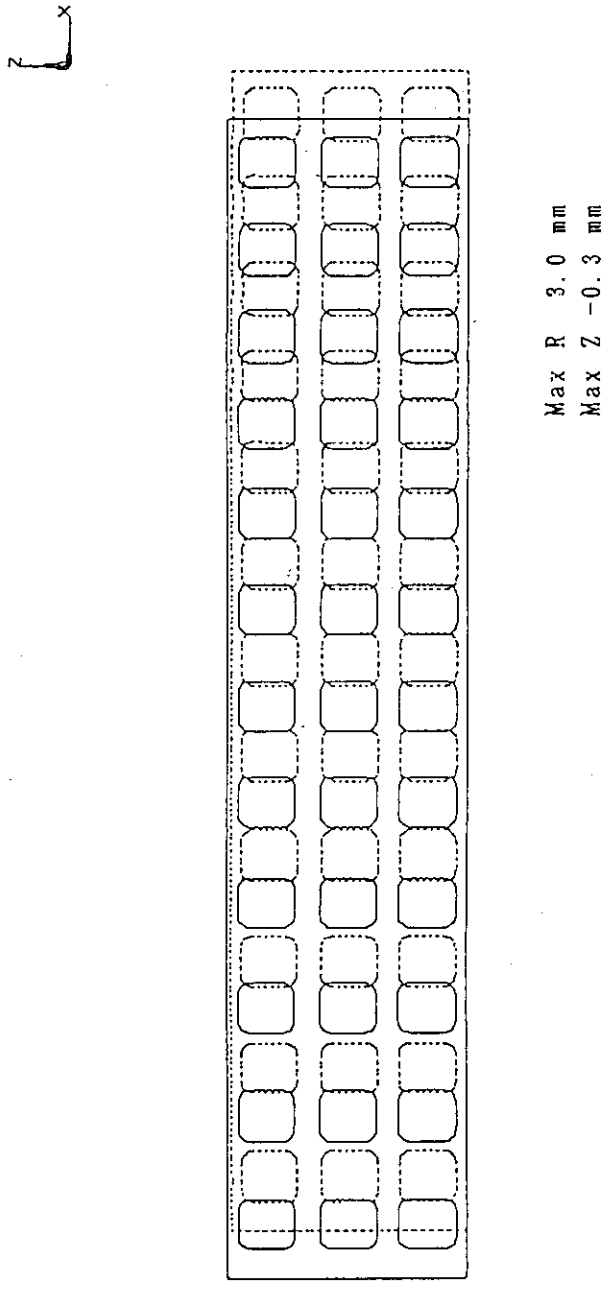

Fig. 4.13 Global displacement of three pancake coils in the ordinary part at EOB1.

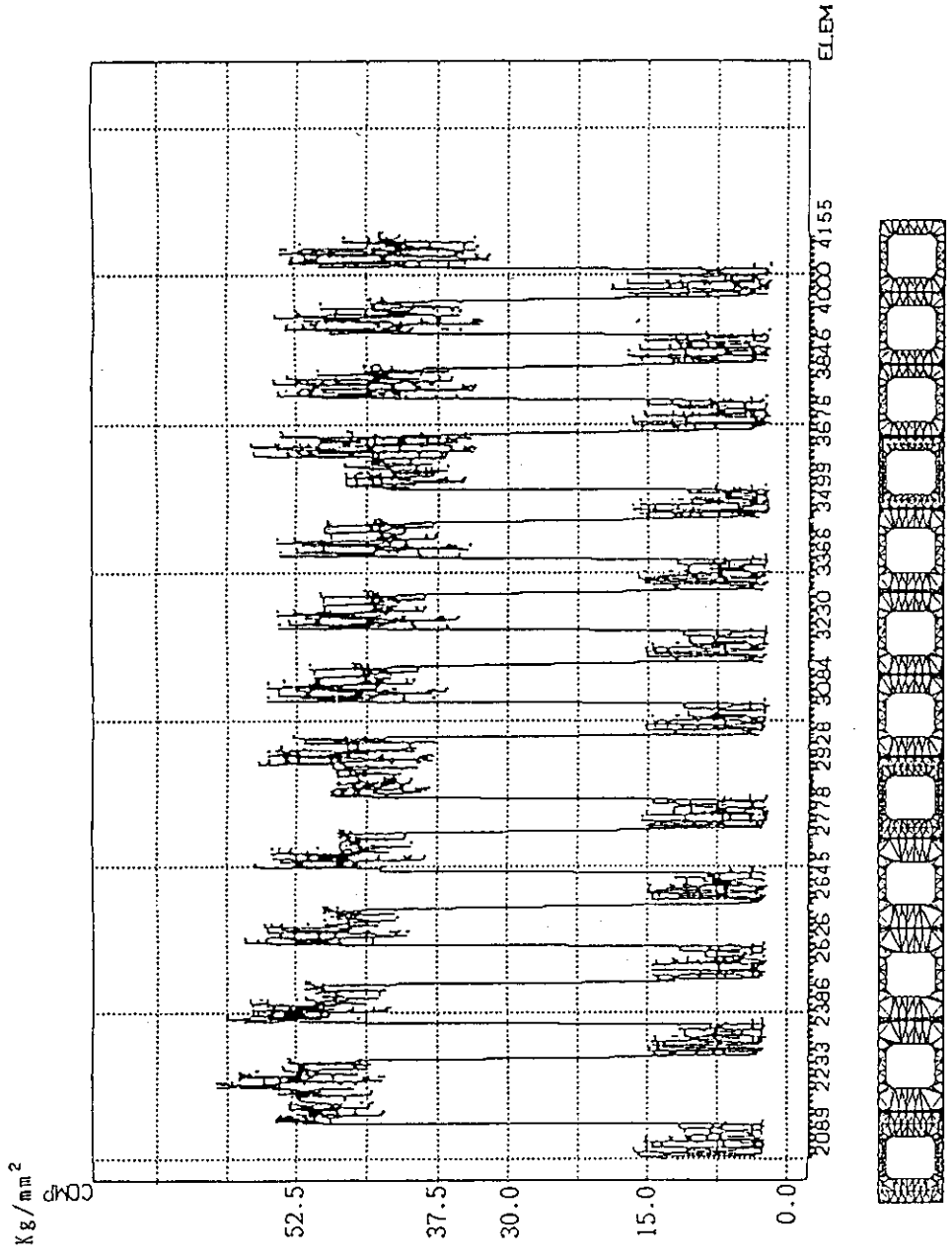

Fig. 4.14 Distribution of the Tresca stress (σ_T) in the middle pancake coil in the ordinary part, the distribution of the element stress along the radial direction at EOB1 is shown in the figure.

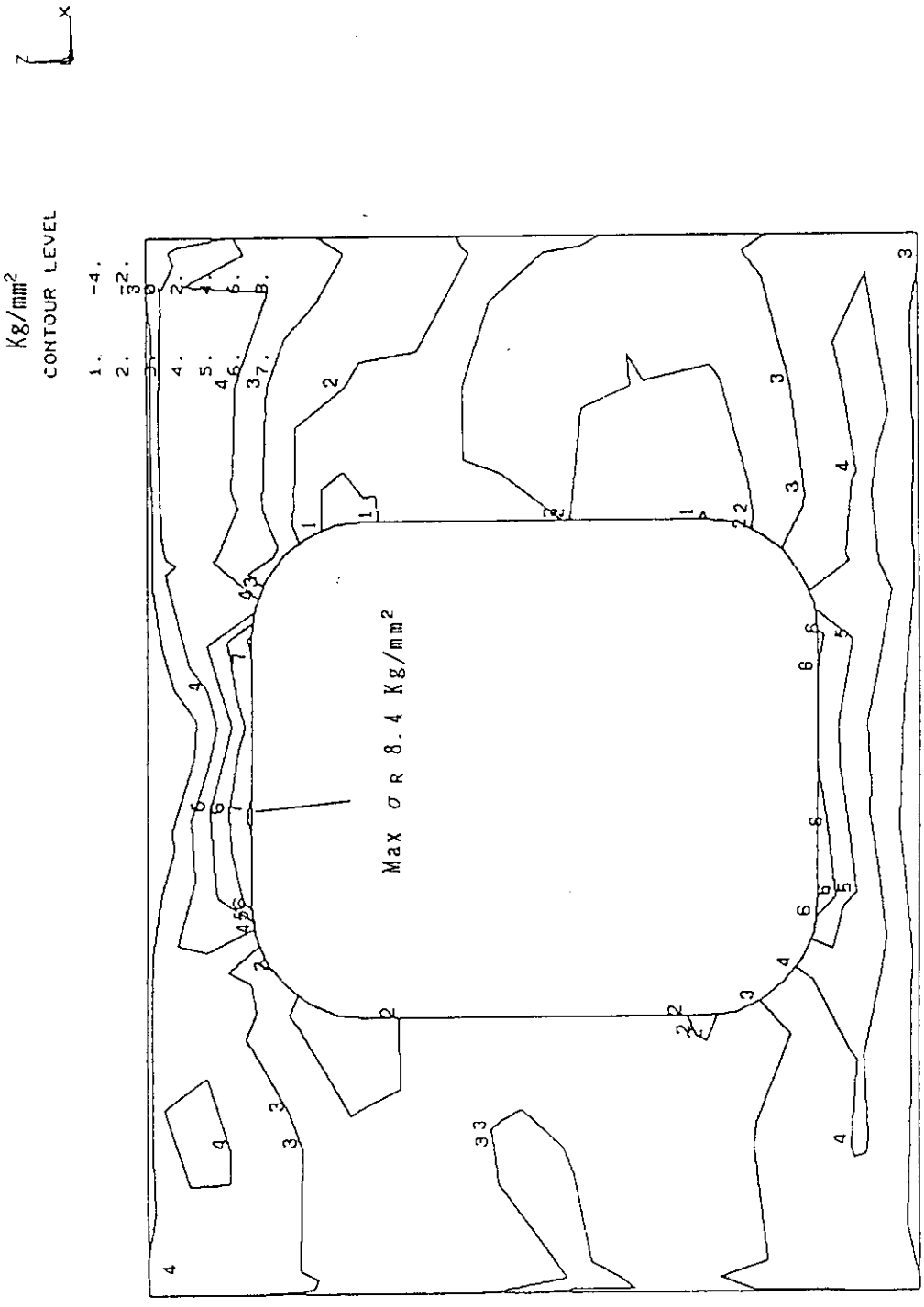

Fig. 4.15 (a) Distribution of the radial stress component (σ_R) in the innermost conduit in the ordinary part at EOB1.

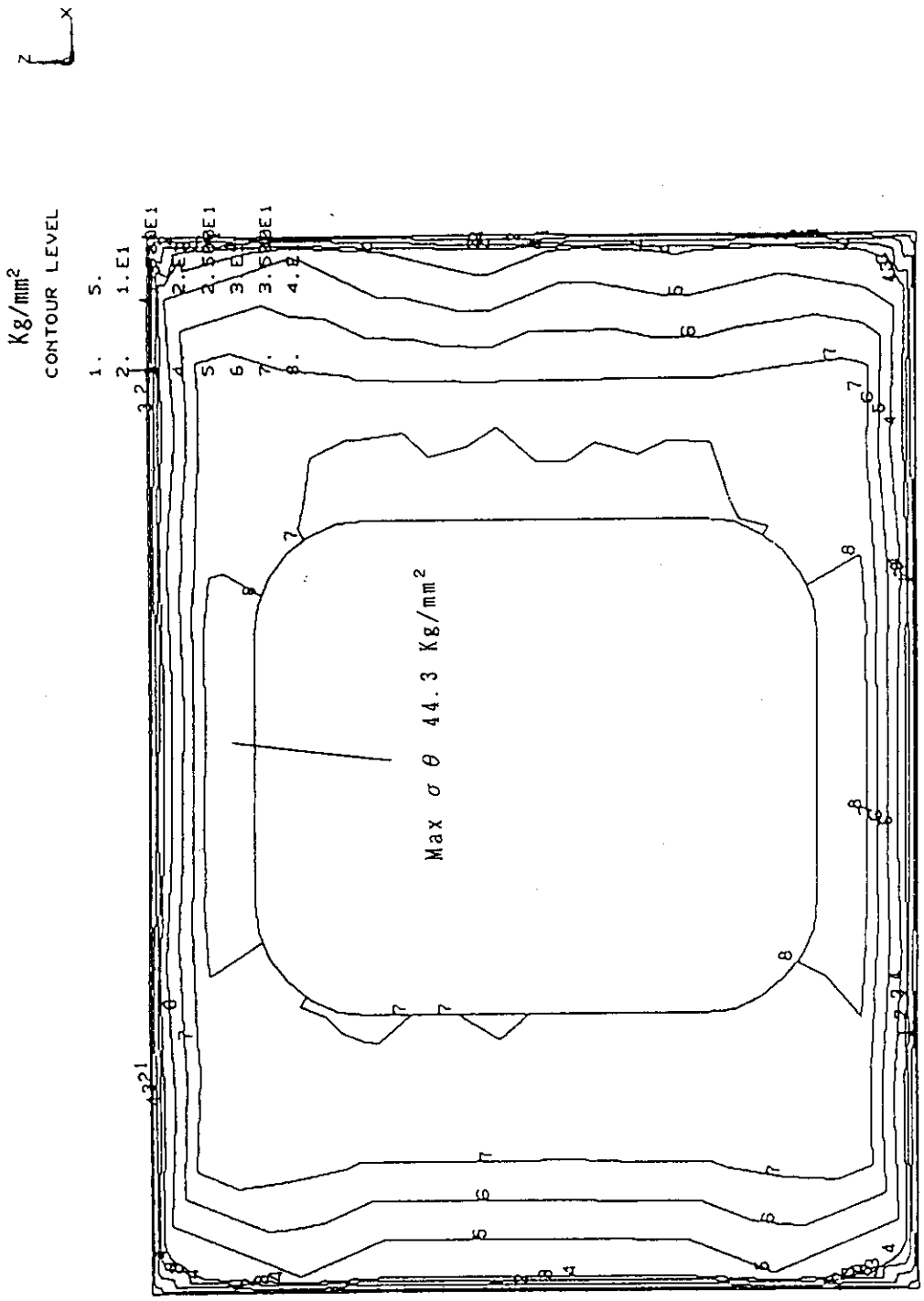

Fig. 4.15 (b) Distribution of the circumferential stress component (σ_θ) in the innermost conduit in the ordinary part at EOB1.

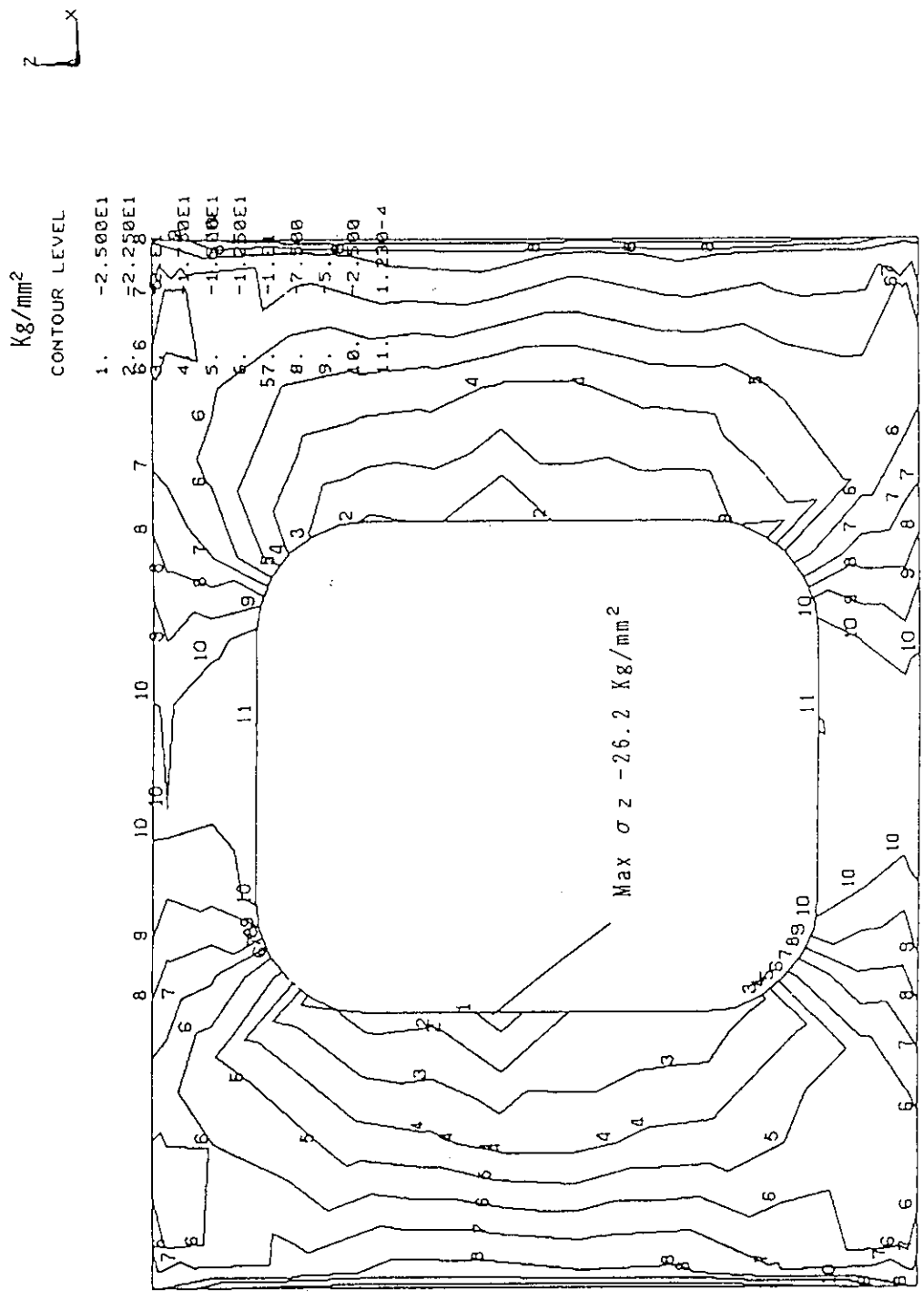

Fig. 4.15 (c) Distribution of the vertical stress component (σ_Z) in the innermost conduit in the ordinary part at EOB1.

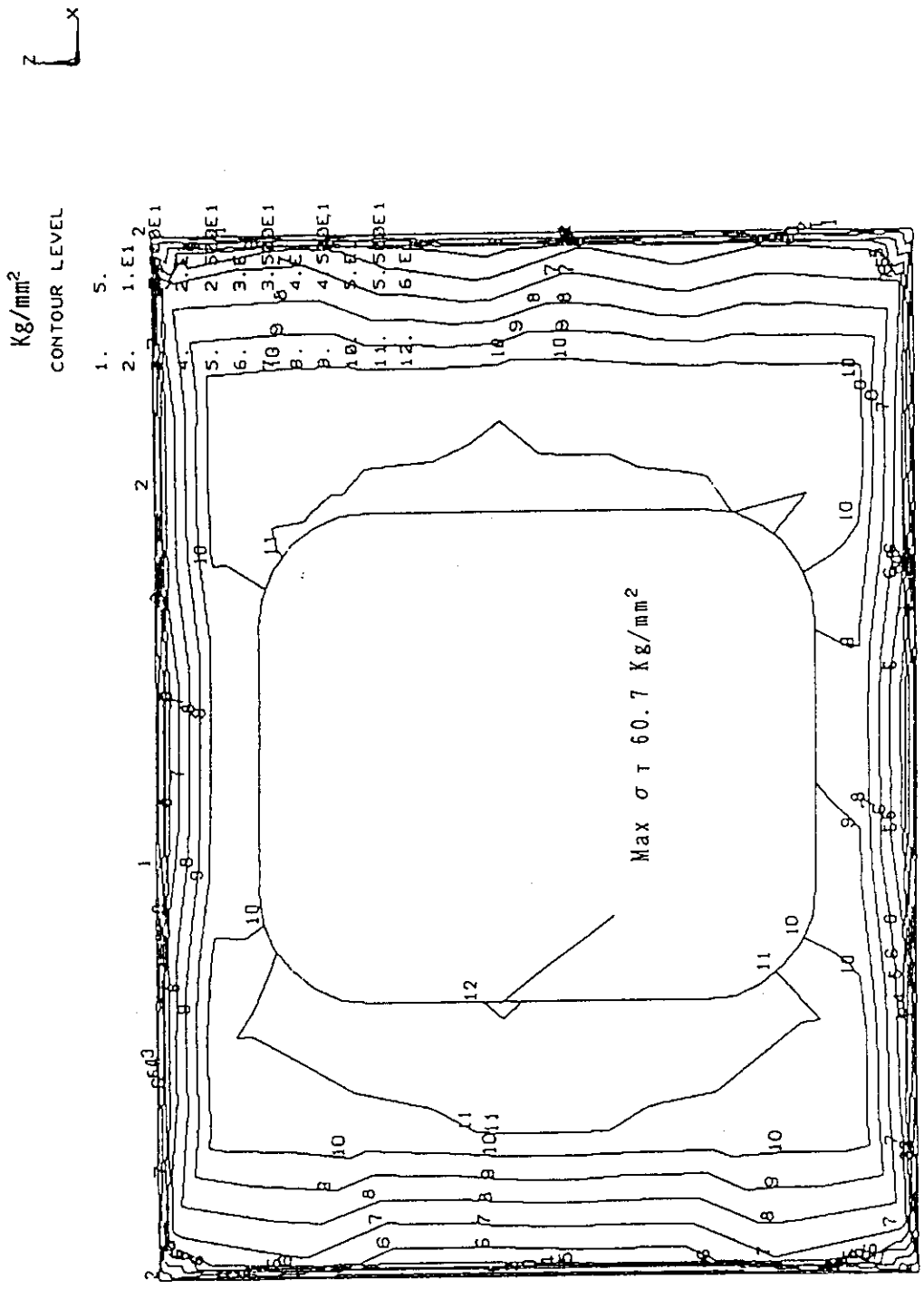

Fig. 4.15 (d) Distribution of Tresca stress (σ_T) in the innermost conduit in the ordinary part at EOB1.

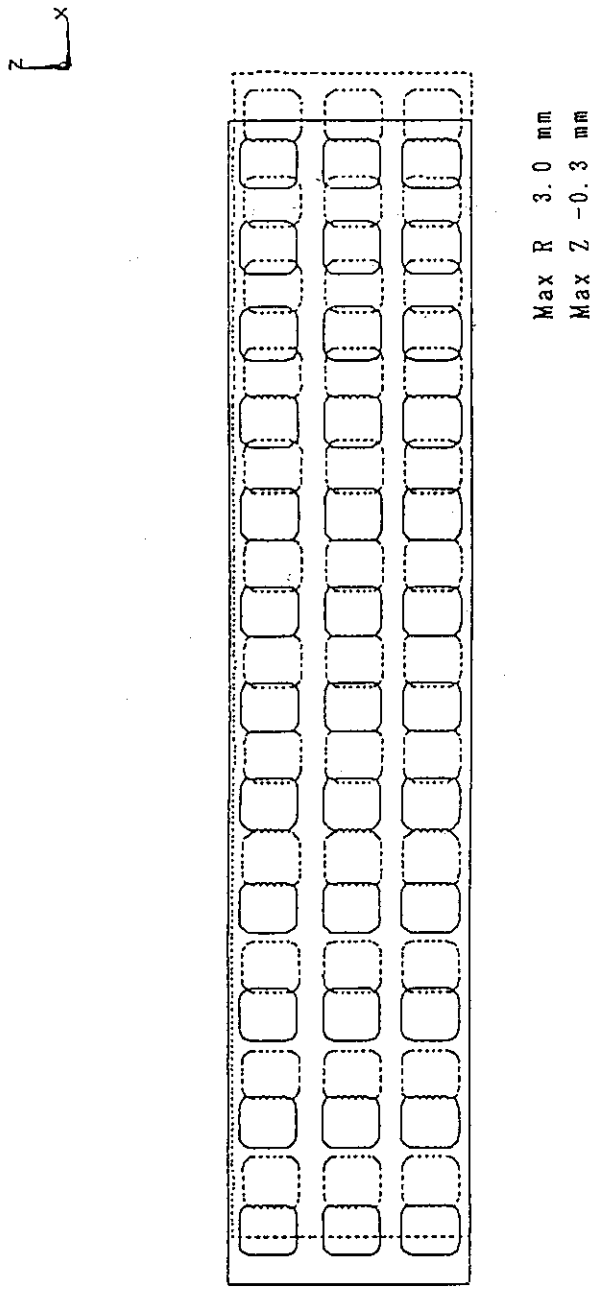

Fig. 4.16 Global displacement of three pancake coils in the ordinary part at EOB2.

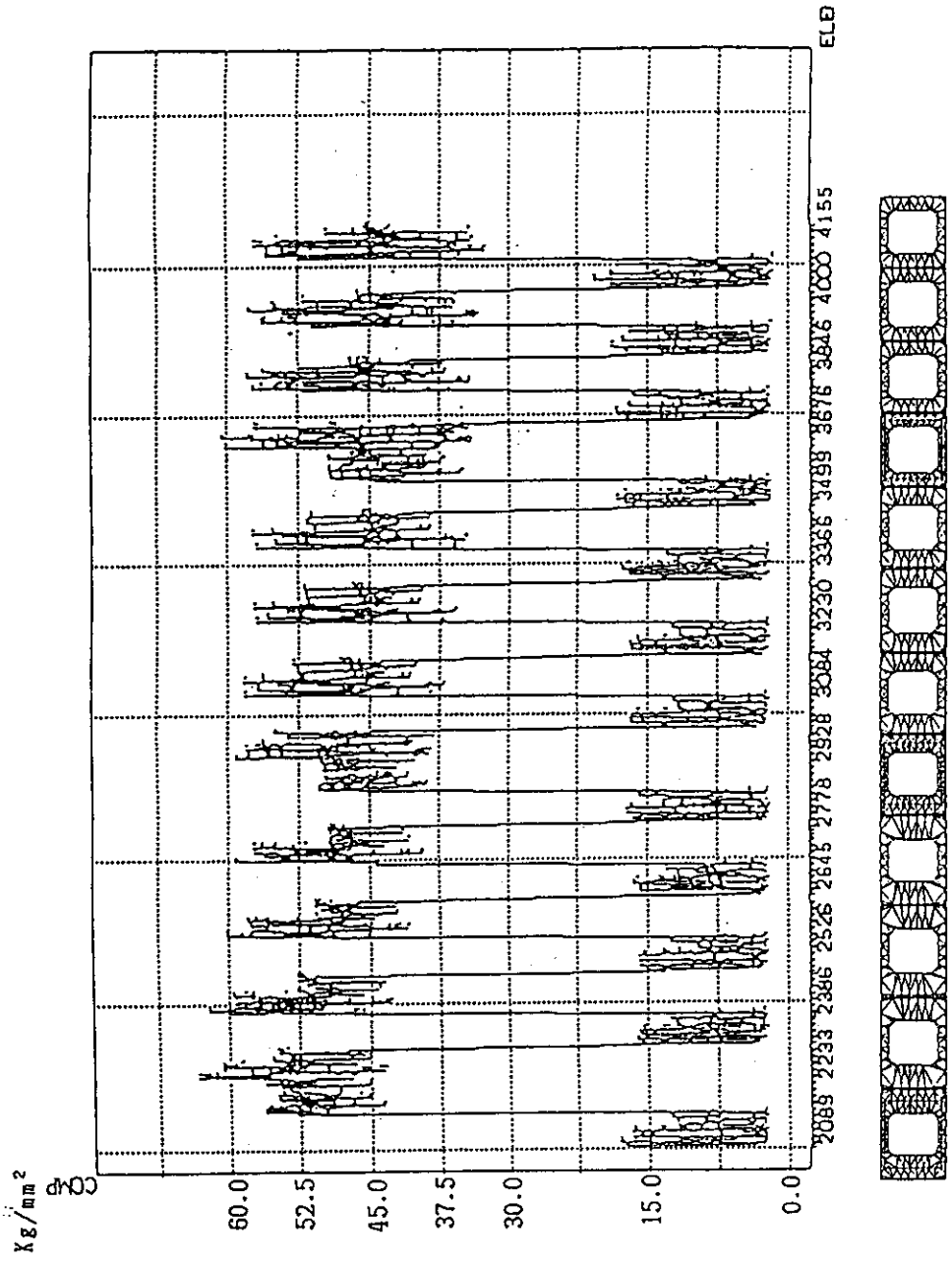

Fig. 4.17 Distribution of the Tresca stress (σ_T) in the middle pancake coil in the ordinary part, the distribution of the element stress along the radial direction at EOB2 is shown in the figure.

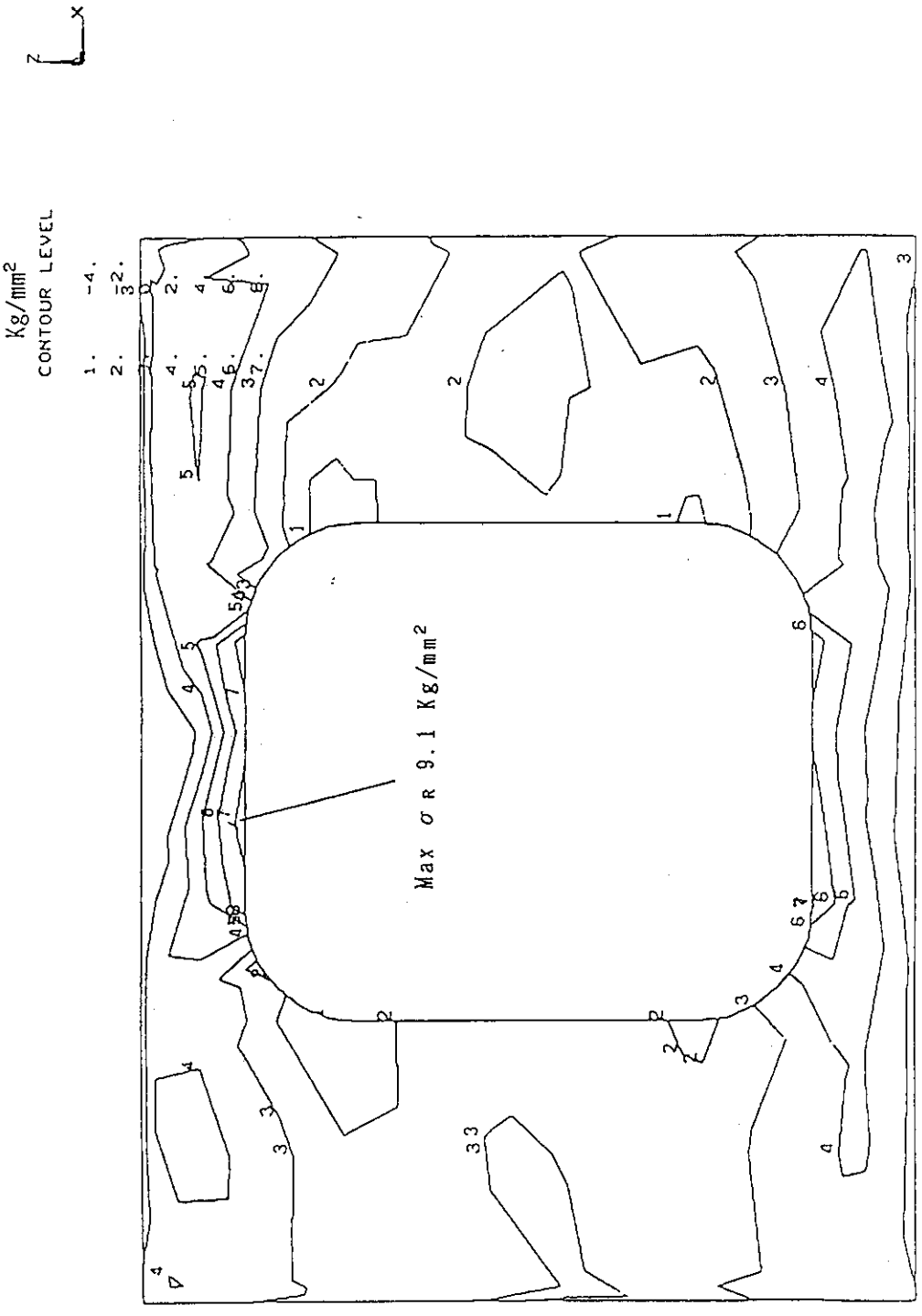

Fig. 4.18 (a) Distribution of the radial stress component (σ_R) in the innermost conduit in the ordinary part at EOB2.

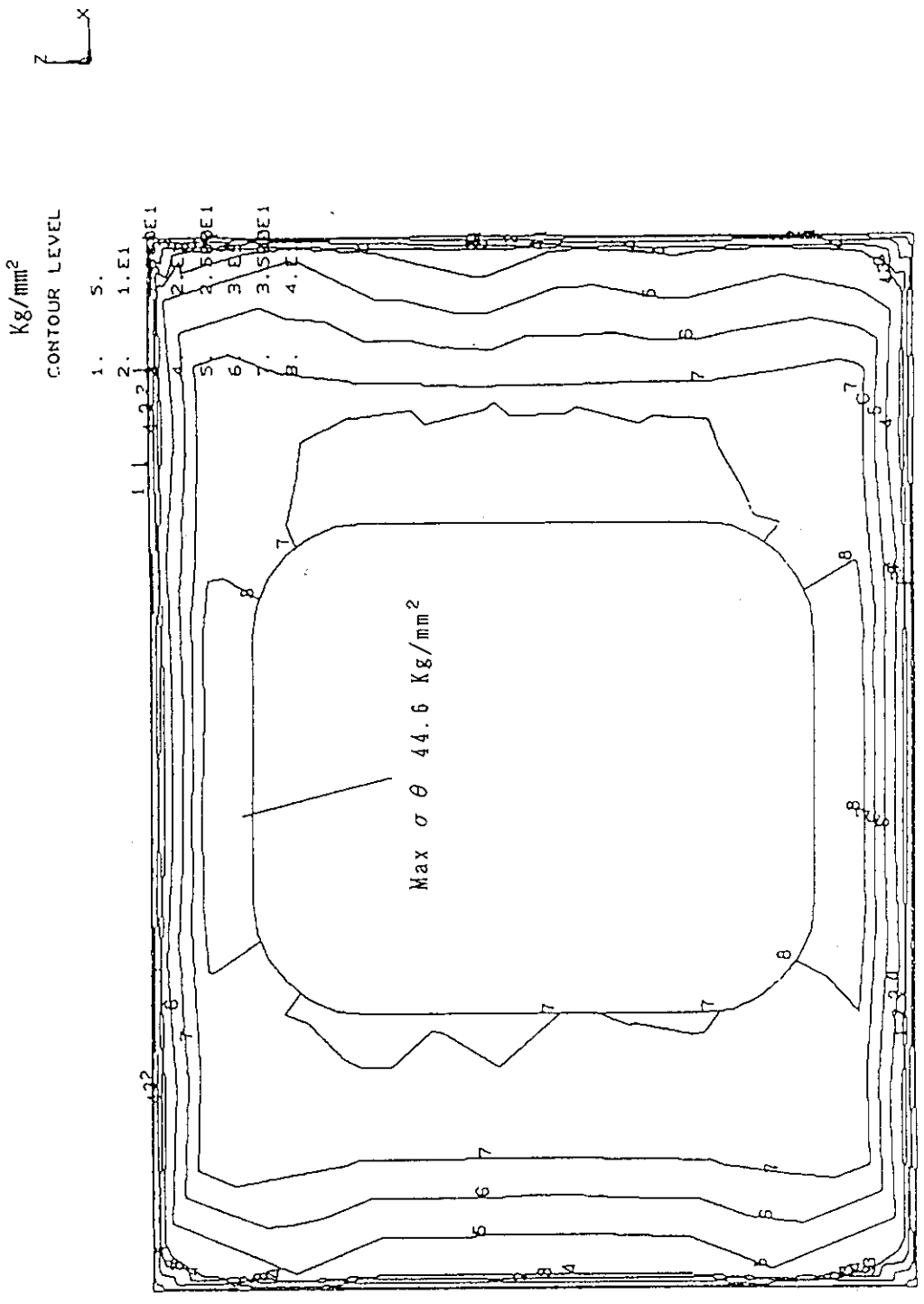

Fig. 4.18 (b) Distribution of the circumferential stress component stress (σ_θ) in the innermost conduit in the ordinary part at EOB2.

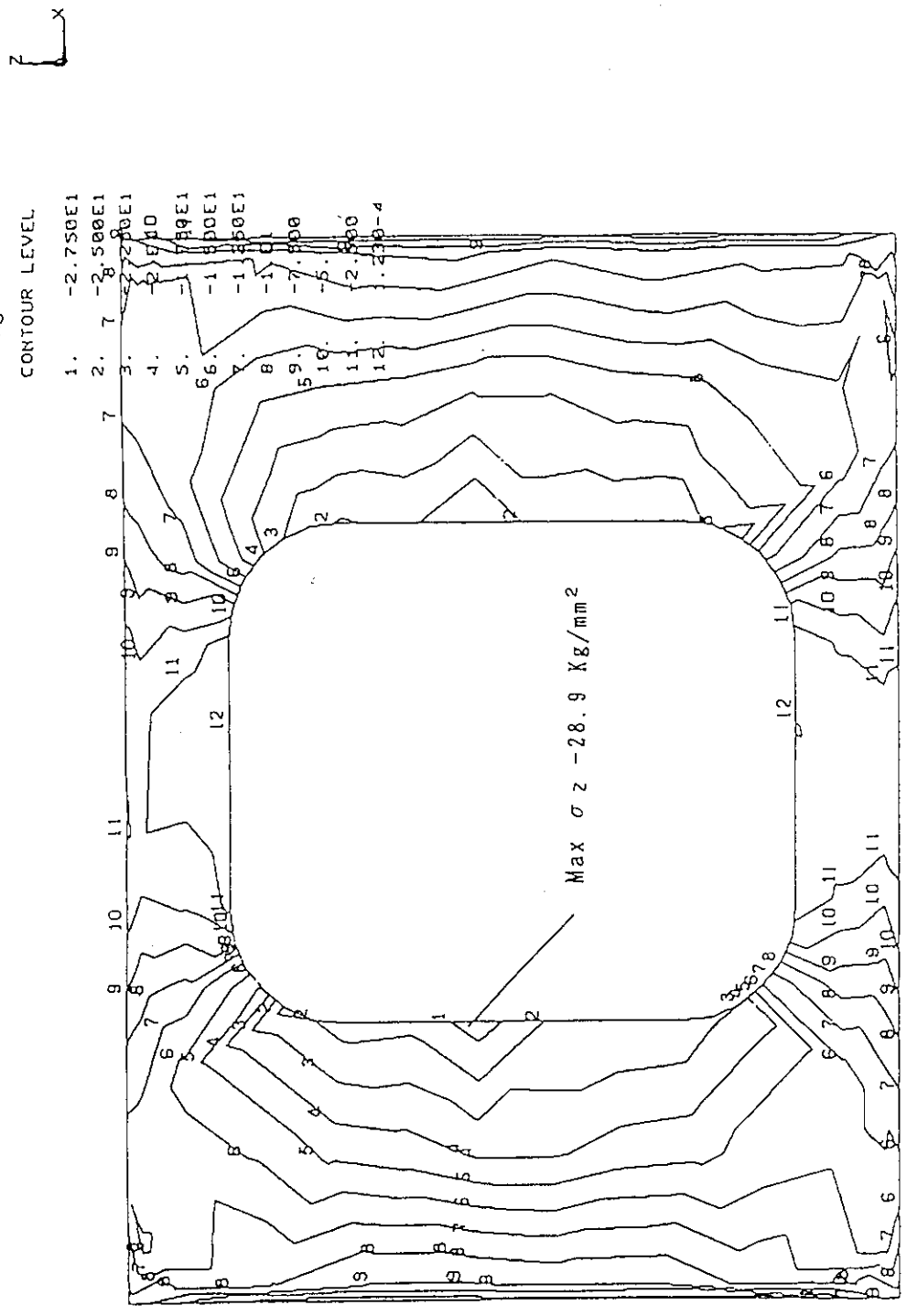

Fig. 4.18 (c) Distribution of the Vertical stress component (σ_Z) in the innermost conduit in the ordinary part at EOB2.

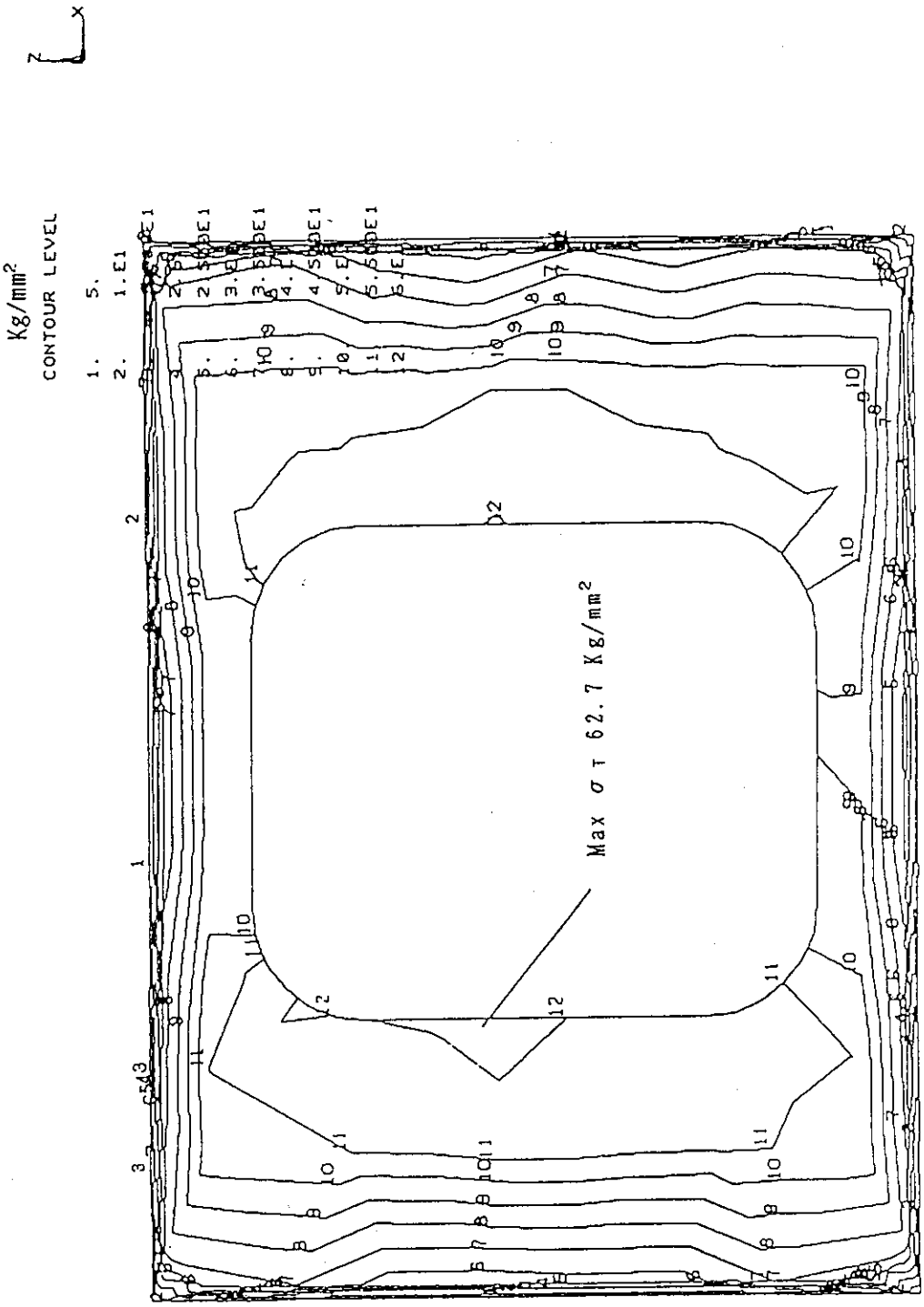

Fig. 4.18 (d) Distribution of the Tresca stress (σ_T) in the innermost conduit in the ordinary part at EOB2.

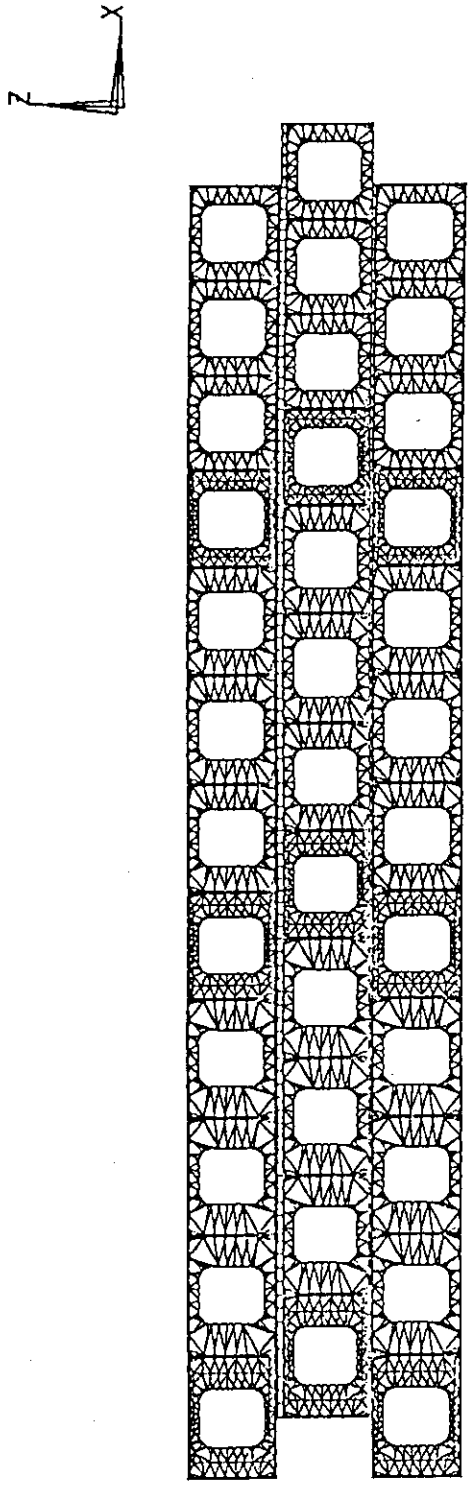

Fig. 4.19 (a) FEM model of the three pancake coils in the extraordinary part, model without the steel filler is shown.

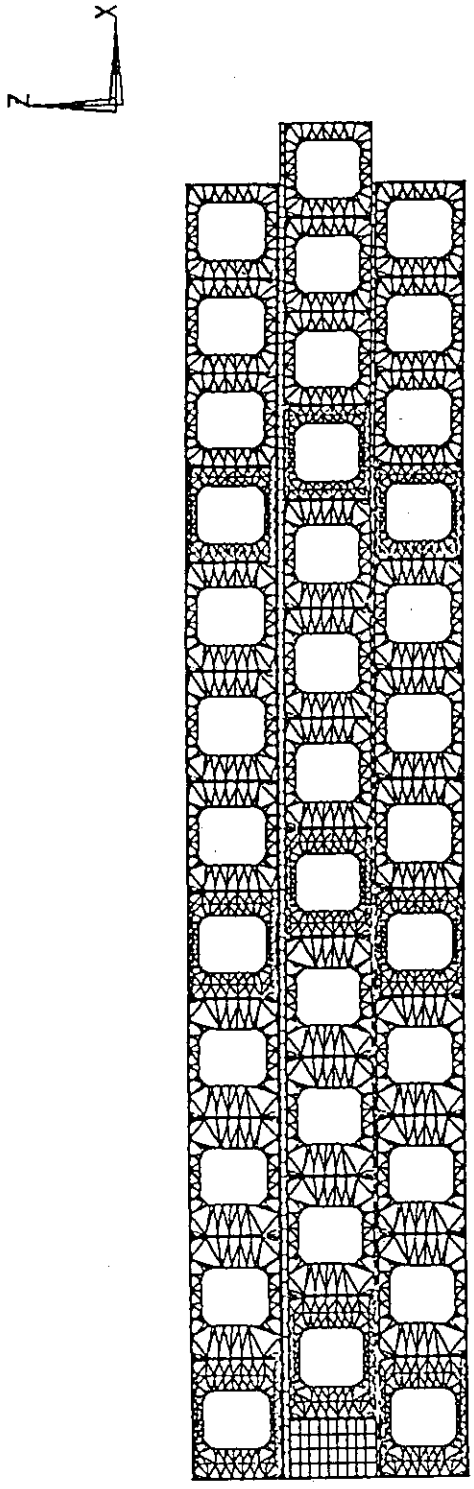

Fig. 4.19 (b) FEM model of the three pancake coils in the extraordinary part, model with the steel filler is shown.

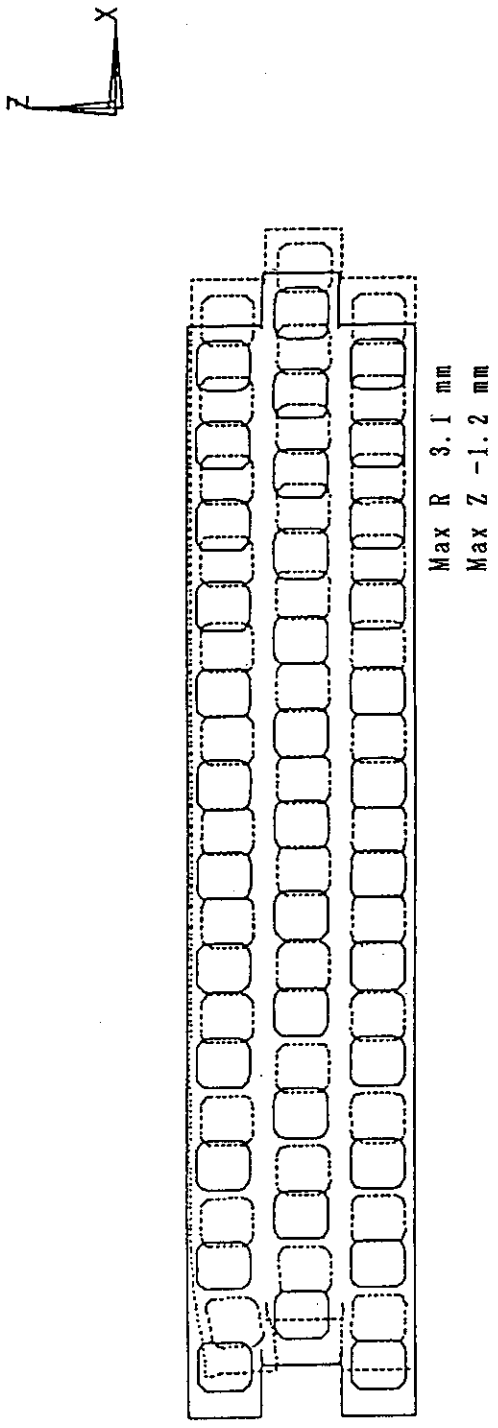

Fig. 4.20 (a) Displacement of the three pancake coils without the steel filler at EOB2.

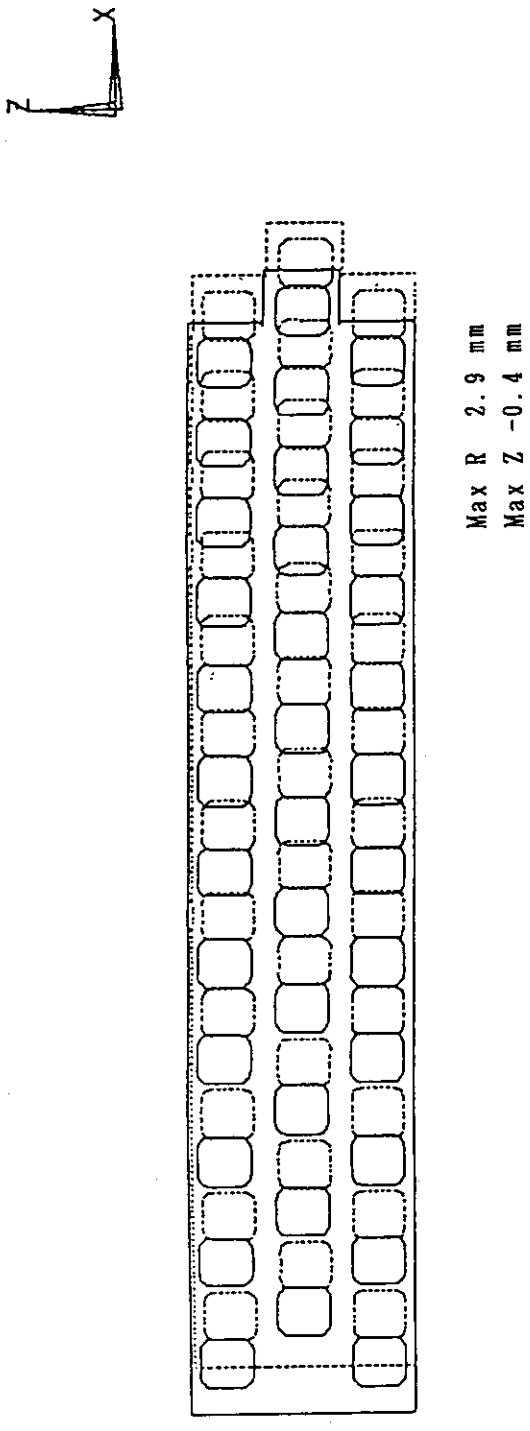

Fig. 4.20 (b) Displacement of the three pancake coils with the steel filler at EOB2.

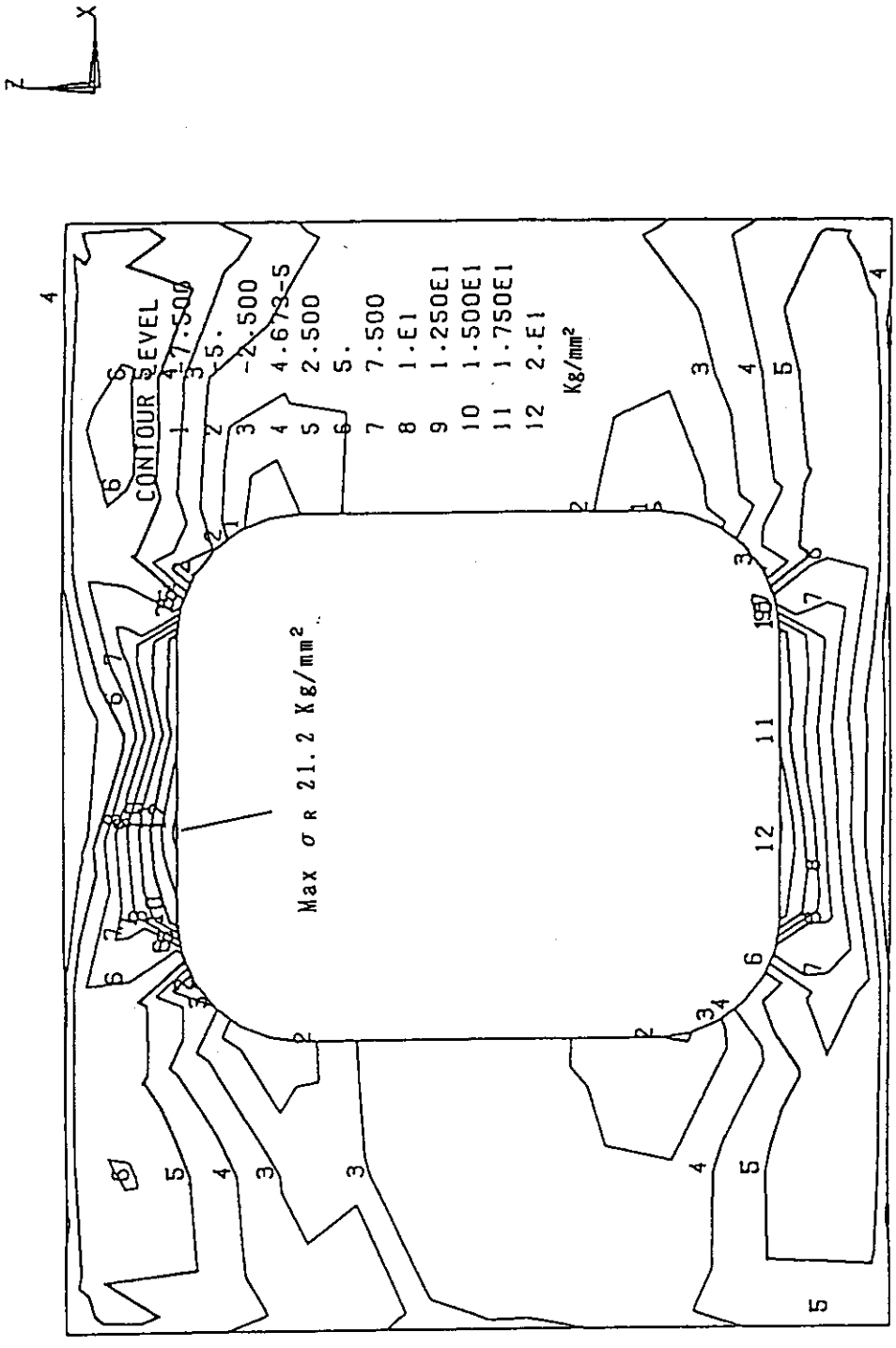

Fig. 4.21 (a) Distribution of the radial stress component (σ_R) in the innermost conduit in the middle pancake in the extraordinary part at EOB2.

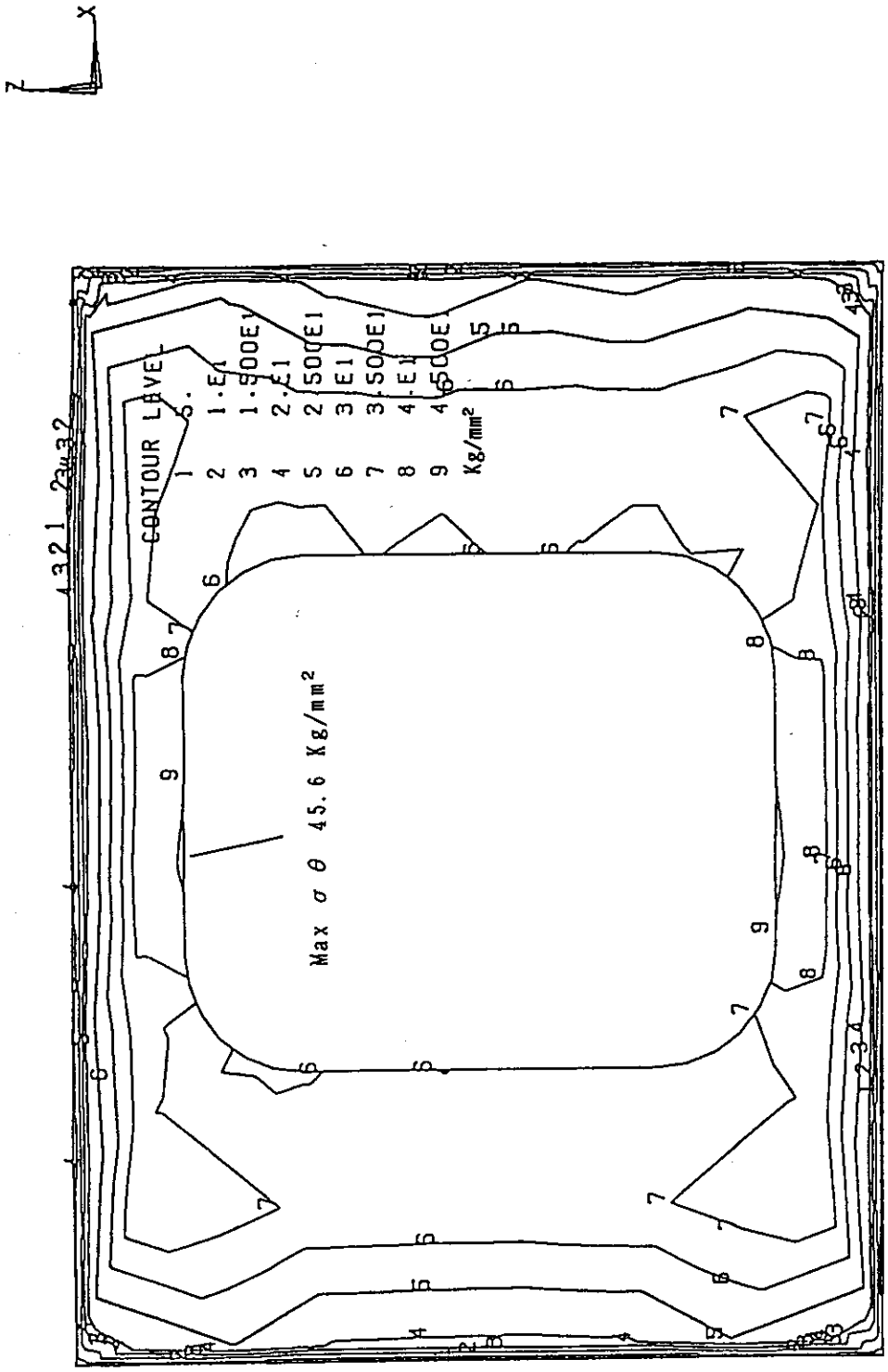

Fig. 4.21 (b) Distribution of the circumferential stress component (σ_θ) in the innermost conduit of the middle pancake in the extraordinary part at EOB2.

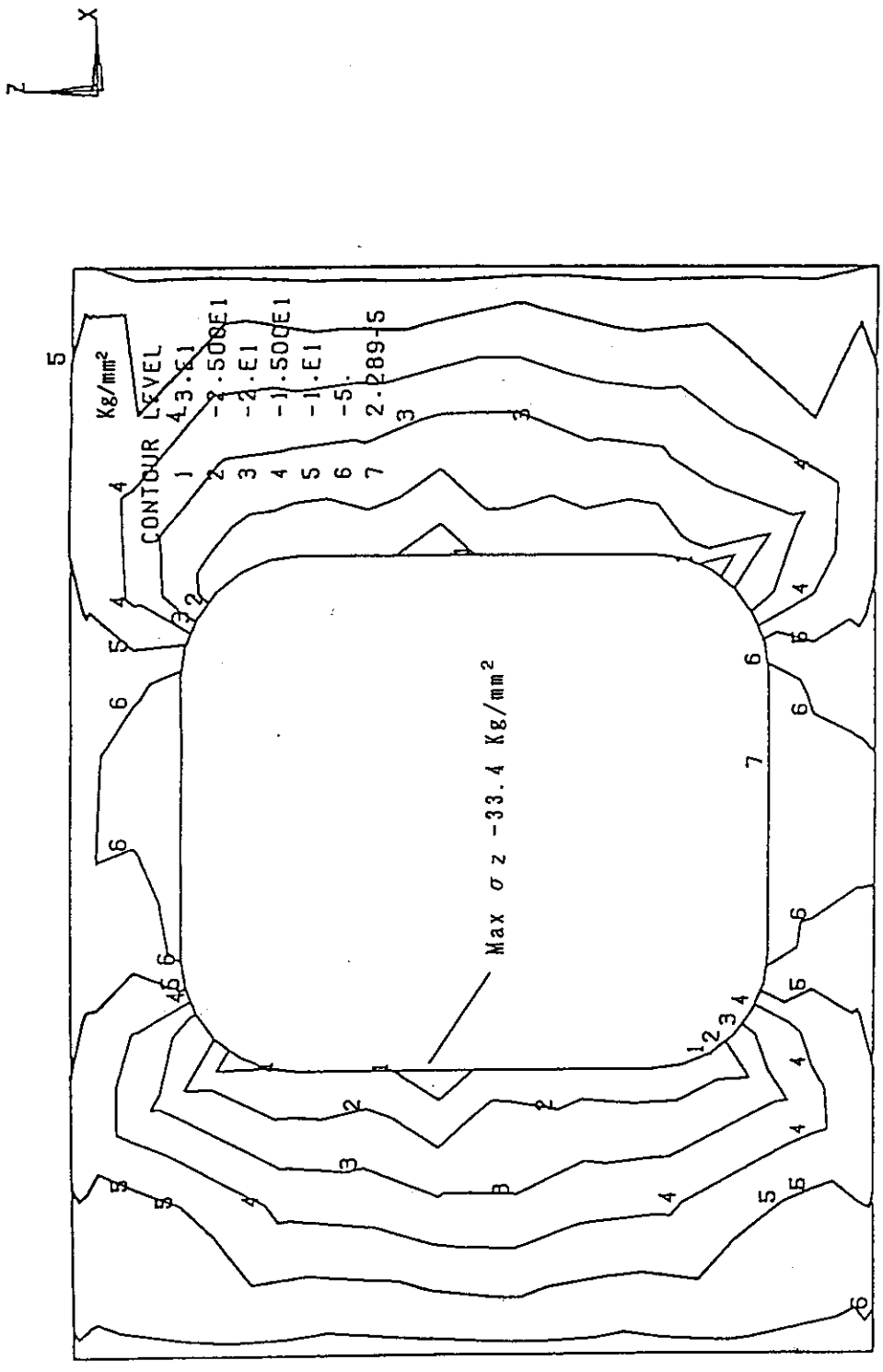

Fig. 4.21 (c) Distribution of the vertical stress component (σ_Z) in the innermost conduit of the middle pancake in the extraordinary part at EOB2.

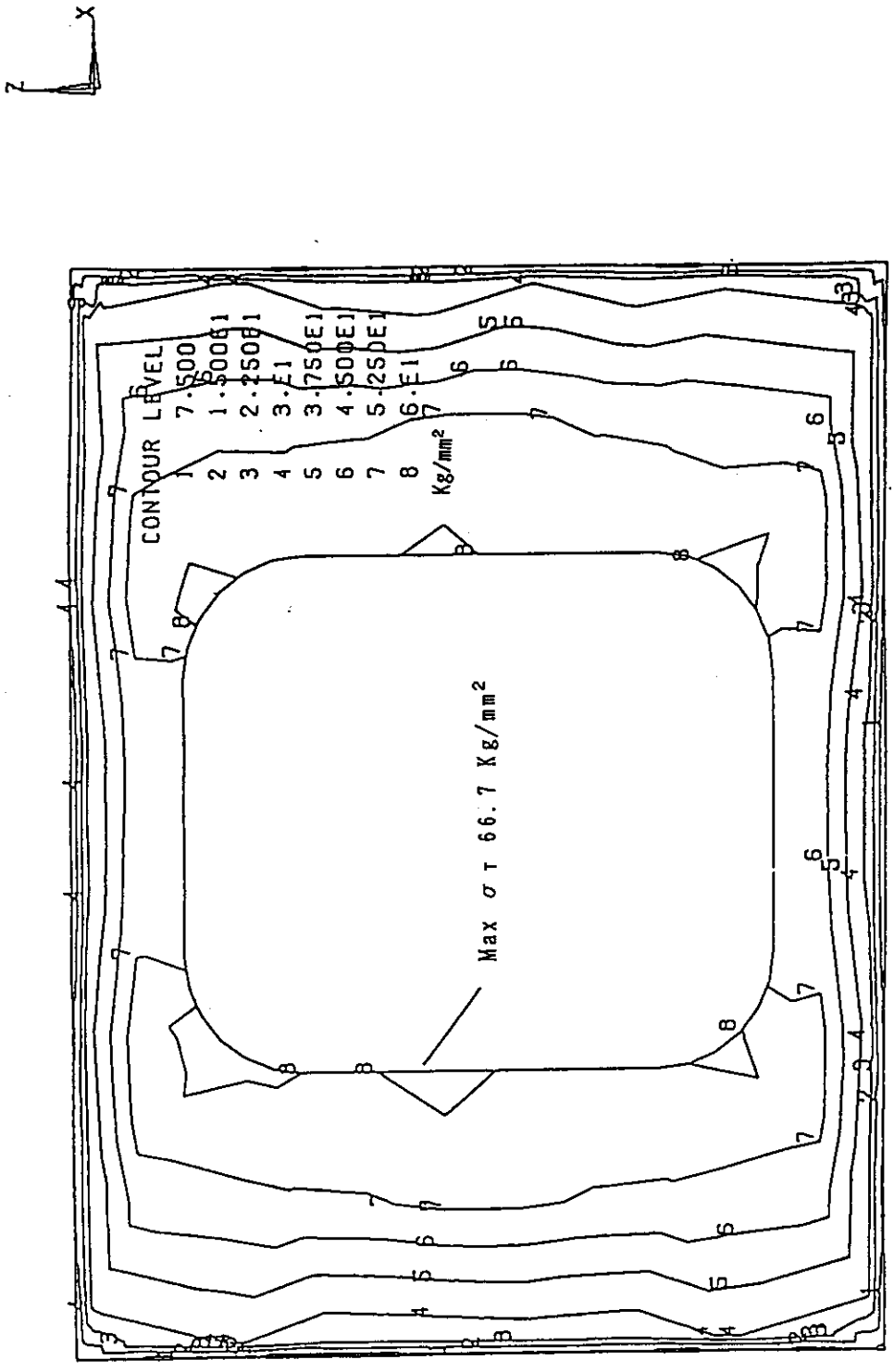

Fig. 4.21 (d) Distribution of the Tresca stress (σ_T) in the innermost conduit of the middle pancake in the extraordinary part at EOB2.

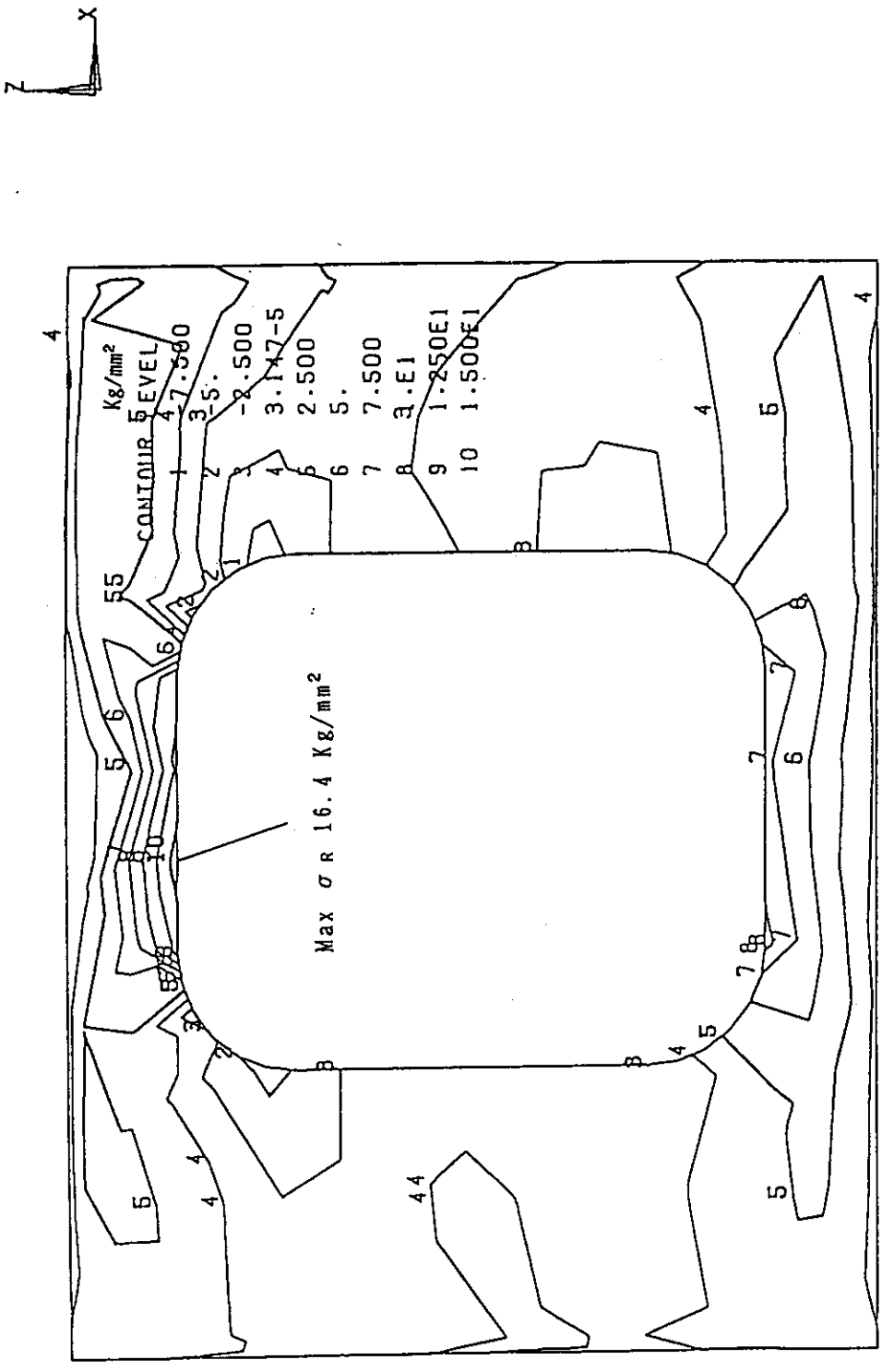

Fig. 4.22 (a) Distribution of the radial stress component (σ_R) in the innermost conduit in the bottom pancake in the extraordinary part at EOB2.

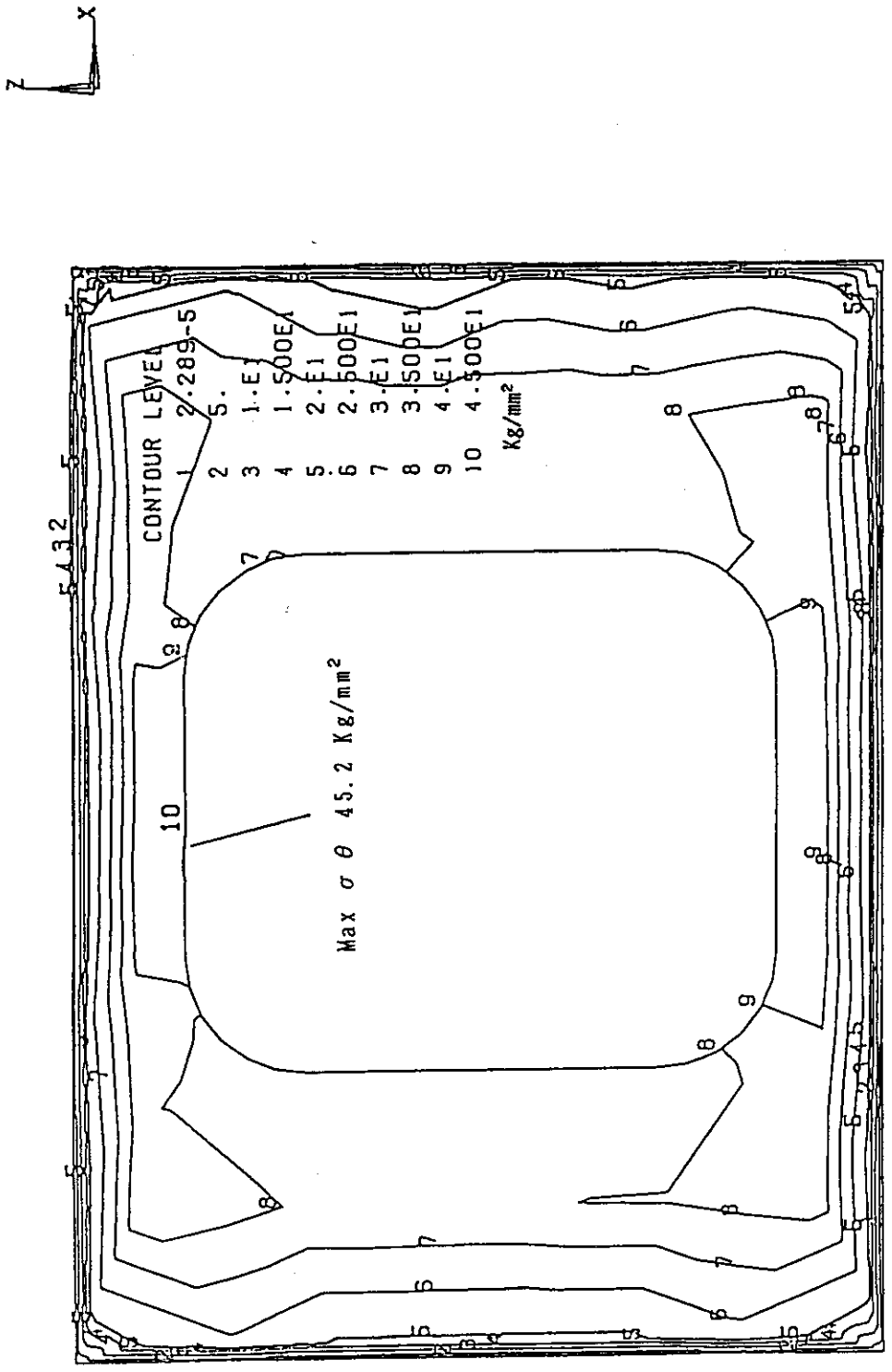

Fig. 4.22 (b) Distribution of the circumferential stress component (σ_θ) in the innermost conduit of the bottom pancake in the extraordinary part at EOB2.

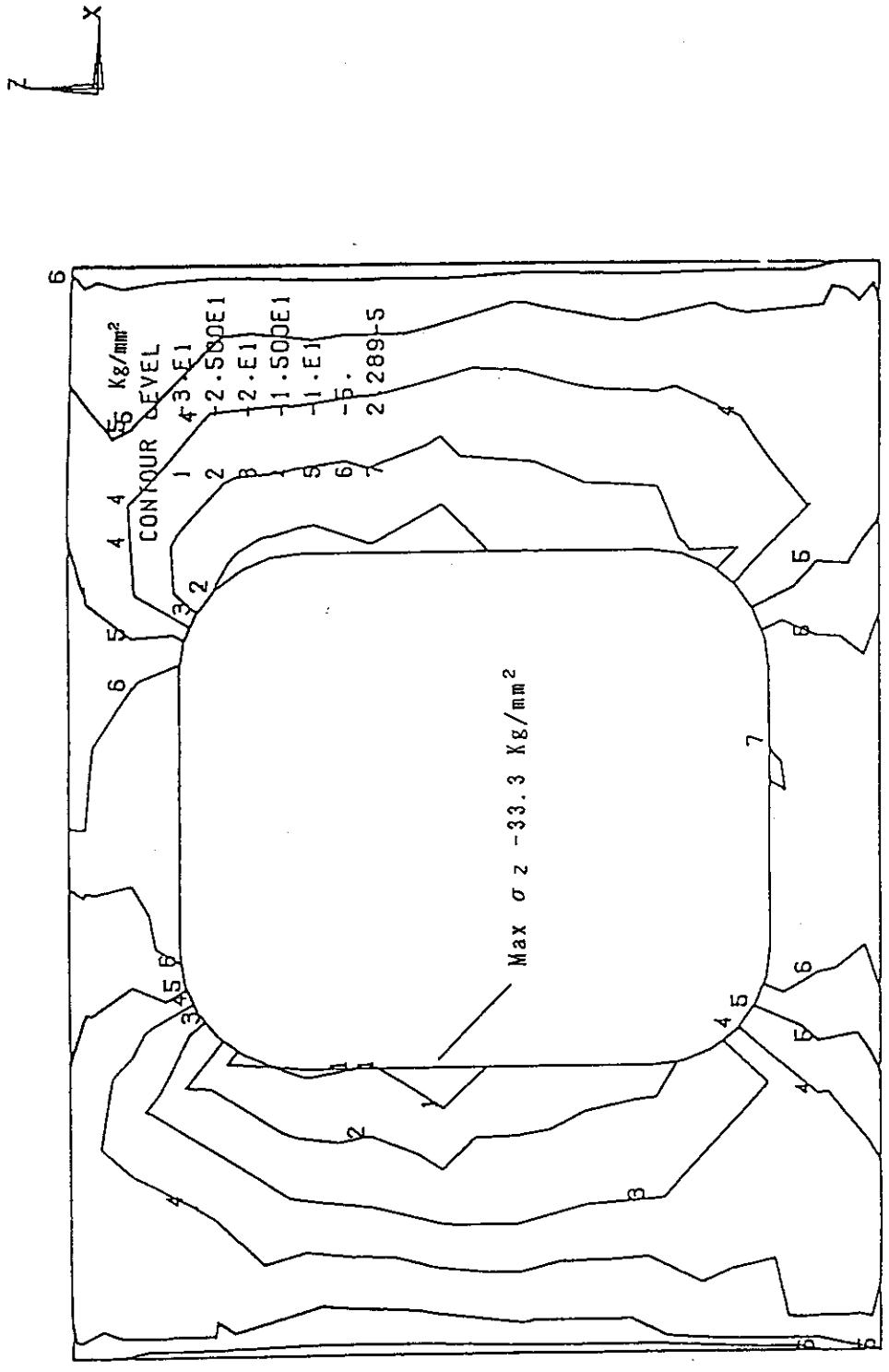

Fig. 4.22 (c) Distribution of the vertical stress component (σ_Z) in the innermost conduit of the bottom pancake in the extraordinary part at EOB2.

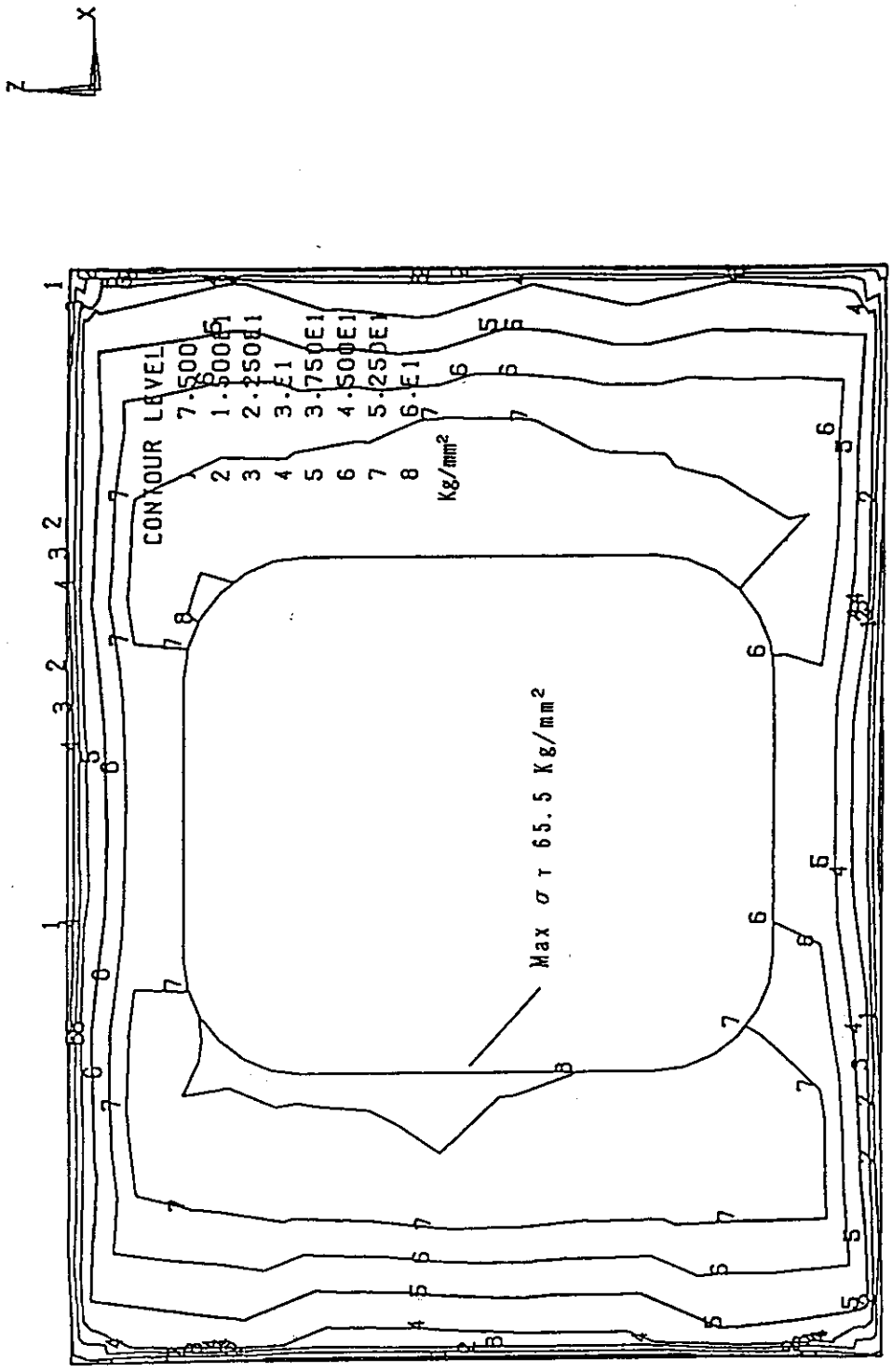

Fig. 4.22 (d) Distribution of the Tresca stress (σ_T) in the innermost conduit of the bottom pancake in the extraordinary part at EOB2.

5. Stress Analysis of PF Coil Support Structure and Outer Ring Coil

5.1 Introduction

The stress analysis of the support structure for the Center Solenoid (CS) coils and the Equilibrium Field (EF) coils were carried out by using FEM models of MSC/NASTRAN. As for the CS coil support structure, if the coils were assembled without initial compression, the repulsive forces acts on the PF-3 and PF-4 coil at 'Start of Flat Top' (SOFT), will make the gap between the PF-2 and the PF-3 coil. At 'End of Burn' (EOB), the repulsive forces change to the compressive forces and the collision between the coils would occur. Since such a collision has a possibility to break the insulator of the coil, the initial compression is required so as not to separate the CS coils. Since the compressive force at EOB is larger than the repulsive force at SOFT, the estimation of the stress due to the initial compression is required. Moreover, since the initial compression should be done at room temperature, the degradation of the mechanical strength at the room temperature should be considered in the stress evaluation.

For the EF coil support structure, the stress analysis is also performed, and the wholesomeness was confirmed.

5.2 Stress analysis of CS coil support structure

5.2.1 Procedure

The procedure to obtain the stresses due to the initial compression is as follows.

(1) Obtain the gap and the stress of support structure between PF-2 and 3 coil at SOFT with the assumption that there is no initial compression .
(2) Determine the force for the initial compression so as not to produce the gap between coils.
(3) Estimate the stress of the support structure due to initial compression by using the result of the first step.

The details of the procedure are as follows.

5.2.2 Stress Analysis with no initial compression

Two operational current patterns of the PF coil system were used for the stress analyses. One is the pattern at SOFT for the reference scenario (l_i=0.65, β_p=0.102) and the other is that also at SOFT for the operation (l_i=0.75, β_p=0.0) in which the largest repulsive force occurs in PF-3 and PF-4. These two operations are named SOFT1 and SOFT2 in this chapter, respectively. The configurations, dimensions, and coil current of each PF coils are shown in Table 5.1. The radial and the axial forces of CS coils calculated at SOFT1 and SOFT2 are shown in Table 5.2. The repulsive forces that act on the support structure were 53.2 MN and 113.5 MN, respectively.

The 2-dimensional FEM model of CS coils and the support structure employed for the analysis is shown in Fig. 5.1 (a). The FEM model is composed of 1482 nodes and 1245 elements. The details of the upper part and lower part is shown in Fig. 5.1 (b) and Fig. 5.1 (c), respectively. The material properties used for the analysis are shown in Fig. 5.2 (a),(b),(c). The equivalent winding stiffness of the PF-3(U,L) and the PF-4(U,L) coil were determined by FEM as described in the chapter 6. The rigidities of PF-1(U,L) and PF-2(U,L) were set equal to 0 Pa, since these coils were compressed by themselves and the gap between PF-2 and PF-3 were produced. As shown in Fig. 5.2(b), the Young's modulus at the top of the upper support structure was set to the half of that in the normal part in order to simulate the reduction of structural material in this part. In the real design, the assembly of radial channels was used for this part.

The deformations of the support structure for SOFT1 and SOFT2 are shown in Fig. 5.3 and Fig. 5.4, respectively. The zoomed up figures for the upper and the lower part for SOFT1 and SOFT2 are shown in Fig. 5.5 (a),(b) and Fig. 5.6 (a),(b), respectively. The Tresca stress distributions for upper and lower part for SOFT1 are shown in Fig. 5.7 (a),(b), respectively. The corresponding figures for SOFT2 are shown in Fig. 5.8 (a),(b). The maximum Tresca stress (σ_T) for the upper and the lower part are summarized in Table 5.3. The

elongations of the distance between the bottom surface of PF-3U coil and the top surface of PF-3L coil for SOFT1 and SOFT2 were 3.2 mm and 6.9 mm, respectively.

5.2.3 Determination of the initial compression

In order to determine the required amount of initial compression, the deformations of PF-1U,L and PF-2U,L coils were calculated by using FEM. The FEM model, the boundary condition, and the material properties are shown in Fig. 5.9. The loading conditions are the same as those for SOFT1 and SOFT2 shown in Table 5.2.

The deformation of PF-1U,L and PF-2U,L coils at SOFT1 and SOFT2 are shown in Fig. 5.10 (a),(b). The amount of the shrinkage were 7.6 mm and 9.0 mm. As a results, the gaps produced without initial compression was calculated to be 10.8 mm (3.2 + 7.6) at SOFT1, and 15.9 mm (6.9 + 9.0) at SOFT2.

In order to determine the amount of the initial compression, we supposed the situation that 15.9 mm width rigid disk block was inserted between the gap at SOFT2. After the removal of the electromagnetic force, the support structure would elongate and the CS coil would shrink. These elongation and the shrinkage can be calculated by using the concept of the equivalent spring constant. The equivalent spring constant for the support structure can be calculated by using the results of the previous section. Since the support structure elongated about 0.68 mm due to the repulsive force of 113.5 MN, the spring constant (k_1) is calculated to be 25.2 MN/mm.
Regarding the CS coil, the spring constant (k_2) can be obtained analytically by using the equivalent Young's modulus (see Fig. 5.2 (a)). The obtained value was 20.9 MN/mm. Using these values, the following equation can be written,

$$F = k_1 y_1 = k_2 y_2$$
$$y_1 + y_2 = 15.9 \text{ mm},$$

where F : Repulsive force, y_1 : Elongation of the support structure and y_2 : Shrinkage of the CS coil.

From the above equation,

$F = 180$ MN
$y_1 = 7.2$ mm
$y_2 = 8.7$ mm.

Consequently, the compression force of 180 MN is required at the initial assembly so as to keep the CS coils together at the of SOFT2. The support structure elongates 7.2 mm and the CS coils shrink 8.6 mm due to the initial compression.

5.2.4 Stress due to initial compression

The stress can be estimated by using the results of stress analysis without the initial compression. Since the maximum Tresca stresses of the upper and the lower part of the support structure were 130.3 MPa and 124.5 MPa with 113.5 MN repulsive force, the corresponding values due to initial compression of 180 MN, are 206 MPa and 197 MPa, respectively. The compressive pressure act on CS coil is about 28 MPa and enough small compared with that at EOB, even if the degradation of the mechanical strength at the room temperature was considered.

At SOFT2 the effect of the initial compression is removed, however, this effect still remain at SOFT1. Since the gap without initial compression was 10.8 mm at SOFT1, if the 15.8 mm disk was installed, the support would extend 2.3 mm, the CS coil would shrink 2.7 mm and the additional repulsive force of 57 MN would be produced and the total repulsive force would become 110 MN.

The list of the maximum Tresca stresses considering the initial compression are shown in Table 5.4.

At Initial magnetization or at End of Burn, the effect of the initial compression also becomes negligibly small, since the CS coils shrink more than or nearly equal to 15.8 mm.

5.3 Stress Analysis of EF Coil Support Structure

5.3.1 Procedure

The stress analyses of the equibrium field (EF) coils and their support structure were performed at two operation conditions. One was that at EOB in the reference scenario (l_i=0.65, β_p=0.102), and the other was that also at EOB for the operation (l_i = 0.6, β_p = 1.0) in which the largest vertical force act on PF-6 coil. These two operating conditions are named EOB1 and EOB3 in this section. The configurations, the dimensions and the current patterns are shown in Table 5.5.

The structure and the boundary conditions of the EF coil and the support structure are shown in Fig. 5.11 (a),(b). The EF coils (PF-6U,L and PF-7U,L) and the support structure, in the part from 11.25 degree to 56.25 degree in circumferential direction, is modeled as shown in Fig. 5.11 (a). The condition of cyclic symmetry was used for the analysis. The plate thickness of the support structure was set to be 50 mm except the top and the bottom plate with the thickness of 100 mm. The dimensions and the structures of PF-6 and PF-7 coil are shown in Fig. 5.12 (a),(b). The rigidities of PF-6 and the PF-7 were obtained by FEM as described in chapter 6. The material properties used for the analysis are summarized in Table 5.6.

The distribution of the radial and the vertical force of the EF coil at EOB1 is shown in Fig. 5.13 (a), (b), along the circumferential direction from 11.25 degree to 56.25 degree. The corresponding figures at EOB3 are also shown in Fig. 5.14 (a), (b). The total radial and vertical forces are shown in Table 5.7.

5.3.2 Results of Analysis

The deformation at EOB3 is shown in Fig. 5.15. The major radius of PF-7L coil becomes 9.0 mm larger.

The maximum Tresca stresses calculated for the EF coil case, insulator, and the support structure are summarized in Table 5.8. The maximum Tresca stress of the support structure was 120 MPa. The Tresca stress distribution of the support

structure at EOB3 is shown in Fig. 5.16. The maximum Tresca stress of the coil case and the insulator were 30 MPa and 22 MPa, respectively. The distribution of Tresca stress in the coil case and insulator of PF-7 coil are shown in Fig. 5.17 and Fig. 5.18, respectively, for example.

The maximum values of the Maximum(σ_1), medium(σ_2), minimum(σ_3) principal and Tresca(σ_T) stresses calculated for the PF-6 and the PF-7 coil are listed in Table 5.9. Since the maximum principal stress can be considered as the tensile stress in the circumferential direction, the maximum tensile stress of the winding is about 100 MPa. Hence, the maximum tensile stress of the conduits of PF-7 coil is about calculated to be 230 Mpa, by using the ratio of equivalent winding stiffness and Young's modulus of steel conduit (2.3). This value is rather small comparing with the value of the CS coil conduit. The distributions of maximum principal and the Tresca stresses are shown in Fig. 5.19 (a), (b). Consequently, since the stresses of the support structure and the winding of EF coils are not so high, the Japanese EF coil and its support structure are wholesomely designed for the mechanical stresses.

5.4 Summary

The stress analysis of the support structure for CS coils and EF coils were performed. Regarding the CS coil support structure, the stress due to the initial compression at room temperature is most severe. The initial compression of 180 MN is required so as not to separate the CS coils. The maximum Tresca stresses of the upper and the lower part of the support structure were 206 MPa and 197 MPa due to initial compression. The stress criteria at room temperature should be applied.

The stress of EF coil support structure was about 120 MPa and the maximum tensile stress of the conduits was about 230 Mpa. They are rather small comparing with those of the CS coil.

Table 5.1 Configuration, dimensions and the coil current of each PF coil at SOFT1 and SOFT2.

	R (mm)	Z (mm)	D_R(mm)	D_Z(mm)	SOFT1 (MA)	SOFT2 (MA)
PF-1U, L	1755	± 950	590	1848	- 16.79	- 17.46
PF-2U, L	1755	± 2850	590	1848	- 16.79	- 17.46
PF-3U, L	1755	± 4750	590	1848	2.85	4.47
PF-4U, L	1755	± 6650	590	1848	0.00	5.25
PF-5U, L	3900	± 9000	900	900	13.60	9.32
PF-6U, L	11500	± 6000	500	1500	- 8.95	- 5.03
PF-7U, L	11500	± 3000	500	900	- 2.72	- 5.09
PLASMA	6000	0	2150	4773	22.00	22.00

Table 5.2 Radial and the axial forces of CS coils at SOFT1 and SOFT2.

	SOFT1		SOFT2	
	F_R (MN)	F_Z (MN)	F_R (MN)	F_Z (MN)
PF－4U	0.0	0.0	73.1	8.4
PF－3U	－ 7.1	53.2	5.8	105.1
PF－2U	410.3	－ 322.0	421.4	－ 382.3
PF－1U	513.6	－ 29.4	551.7	－ 36.9

Table 5.3 Maximum Tresca stress (σ_T) of the upper and the lower part of CS coil support structure without initial compression.

		SOFT1	SOFT2
Repulsive Force (MN)		53.2	114.0
Maximum Tresca Stress (MPa)	Upper Part	63.7	130.0
	Lower Part	55.0	125.0

Table 5.4 Maximum Tresca stress (σ_T) of the upper and the lower part of CS coil support structure with the initial compression.

		Initial Compression	SOFT1	SOFT2
Repulsive Force (MN)		180.0	110.0	114.0
Maximum Tresca Stress (MPa)	Upper Part	206.0	125.0	130.0
	Lower Part	197.0	121.0	125.0

Table 5.5 Configuration, dimensions and the coil current of each PF coil at EOB1 and EOB3.

	R (mm)	Z (mm)	D_R(mm)	D_Z(mm)	EOB1 (MA)	EOB3 (MA)
PF-1U, L	1755	± 950	590	1848	- 22.30	- 21.81
PF-2U, L	1755	± 2850	590	1848	- 22.30	- 21.81
PF-3U, L	1755	± 4750	590	1848	- 9.14	- 13.59
PF-4U, L	1755	± 6650	590	1848	0.00	- 0.01
PF-5U, L	3900	± 9000	900	900	6.25	7.89
PF-6U, L	11500	± 6000	500	1500	- 6.49	- 7.98
PF-7U, L	11500	± 3000	500	900	- 5.25	- 4.99
PLASMA	6000	0	2150	4773	22.00	22.00

Table 5.6 Material properties of EF coils and the support structure.

	Young's Modulus (GPa)			Poisson's Ratio			Shear Modulus (GPa)		
	E_R	$E\theta$	E_Z	$\nu_{R\theta}$	$\nu_{\theta Z}$	ν_{ZR}	G_{ZR}	$G_{R\theta}$	$G_{\theta Z}$
Winding	43.4	92.3	39.3	0.14	0.29	0.22	35.3	35.3	4.8
Insulator	9.8	9.8	9.8	0.10	0.10	0.10	4.9	4.9	4.9
Coil Case	19.6	19.6	19.6	0.20	0.20	0.20	8.2	8.2	8.2
Support Structure	205.8	205.8	205.8	0.30	0.30	0.30	79.4	79.4	79.4

Tbale 5.7 Total Radial and Vertical Force of the EF Coils

	EOB1		EOB3	
	Radial Force	Vertical Force	Radial Force	Vertical Force
PF-6U	222.8	- 175.4	308.8	-213.6
PF-7U	222.2	109.0	222.5	131.8

Unit : MN

Table 5.8 Maximum Tresca stresses(σ_T) of the EF coil case, insulator and the EF coil support structure.

	Maximum Tresca Stress (MPa)	
	EOB1	EOB3
PF-6U Insulator	14.7	21.6
PF-7U Insulator	22.5	22.5
PF-6U Coil Case	18.6	26.5
PF-7U Coil Case	29.4	29.4
Support Structure	121.5	121.5

Table 5.9 Maximum(σ_1), medium(σ_2), minimum(σ_3) principal and Tresca(σ_T) stresses of the PF-6 and the PF-7 coil.

	Maximum Stress Value (MPa)	
	EOB1	EOB3
PF-6U (σ_1)	65.7	79.4
PF-6U (σ_2)	- 5.0	- 7.1
PF-6U (σ_3)	- 9.6	- 13.7
PF-6U (σ_T)	70.6	88.2
PF-7U (σ_1)	92.1	95.1
PF-7U (σ_2)	- 7.4	- 7.3
PF-7U (σ_3)	- 11.8	- 11.8
PF-7U (σ_T)	95.1	99.0

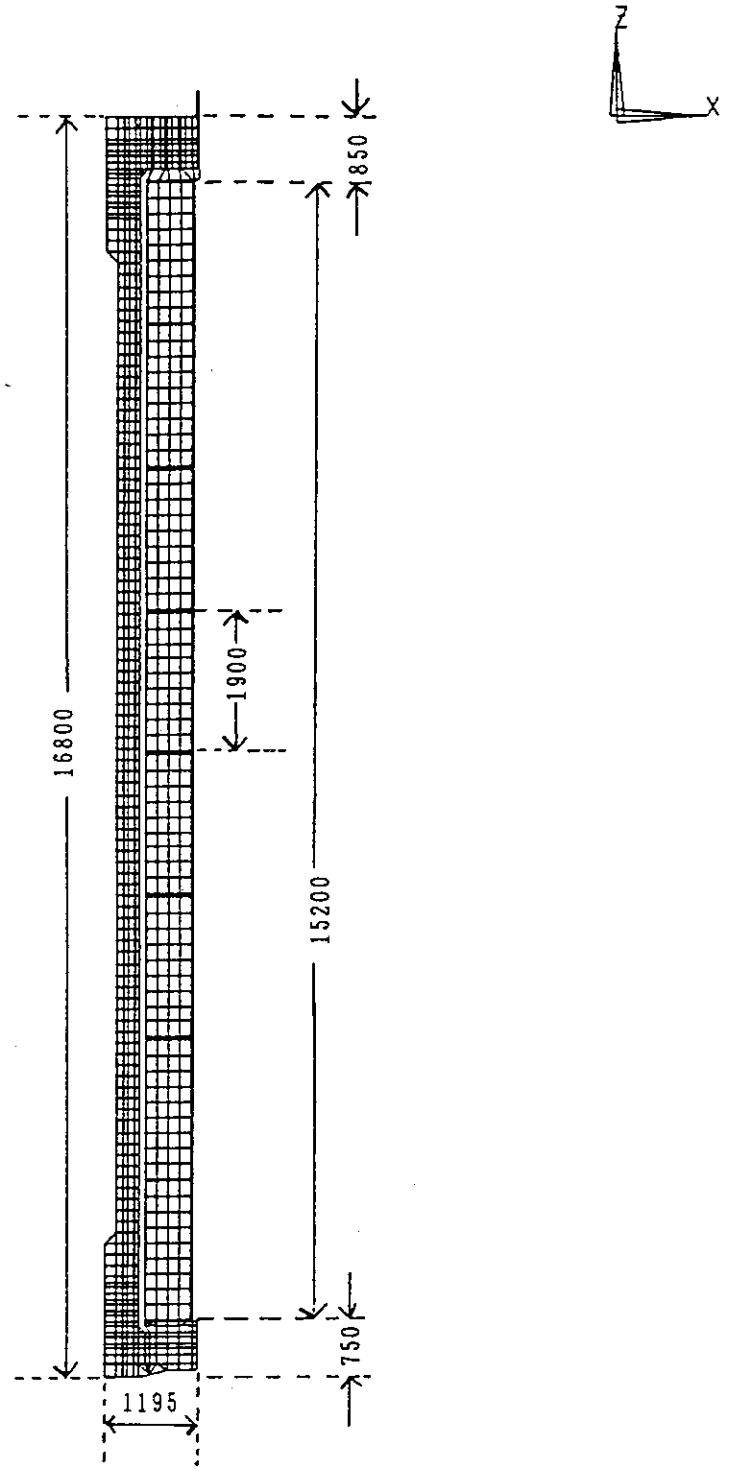

Fig. 5.1 (a) Two dimensional FEM model of the CS coils and the support structure.

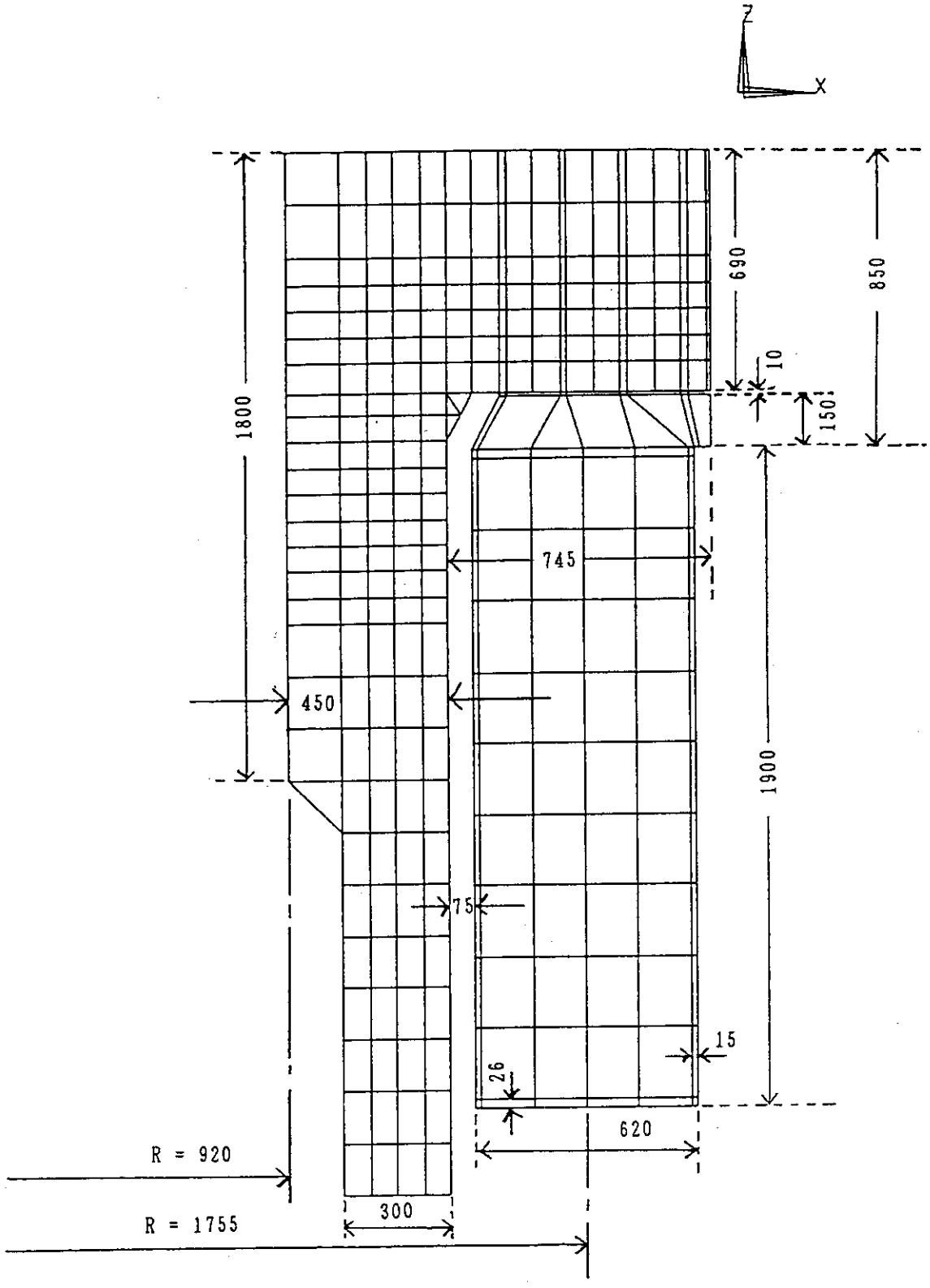

Fig. 5.1 (b) Detailed dimensions and model of the upper part of CS coil support structure.

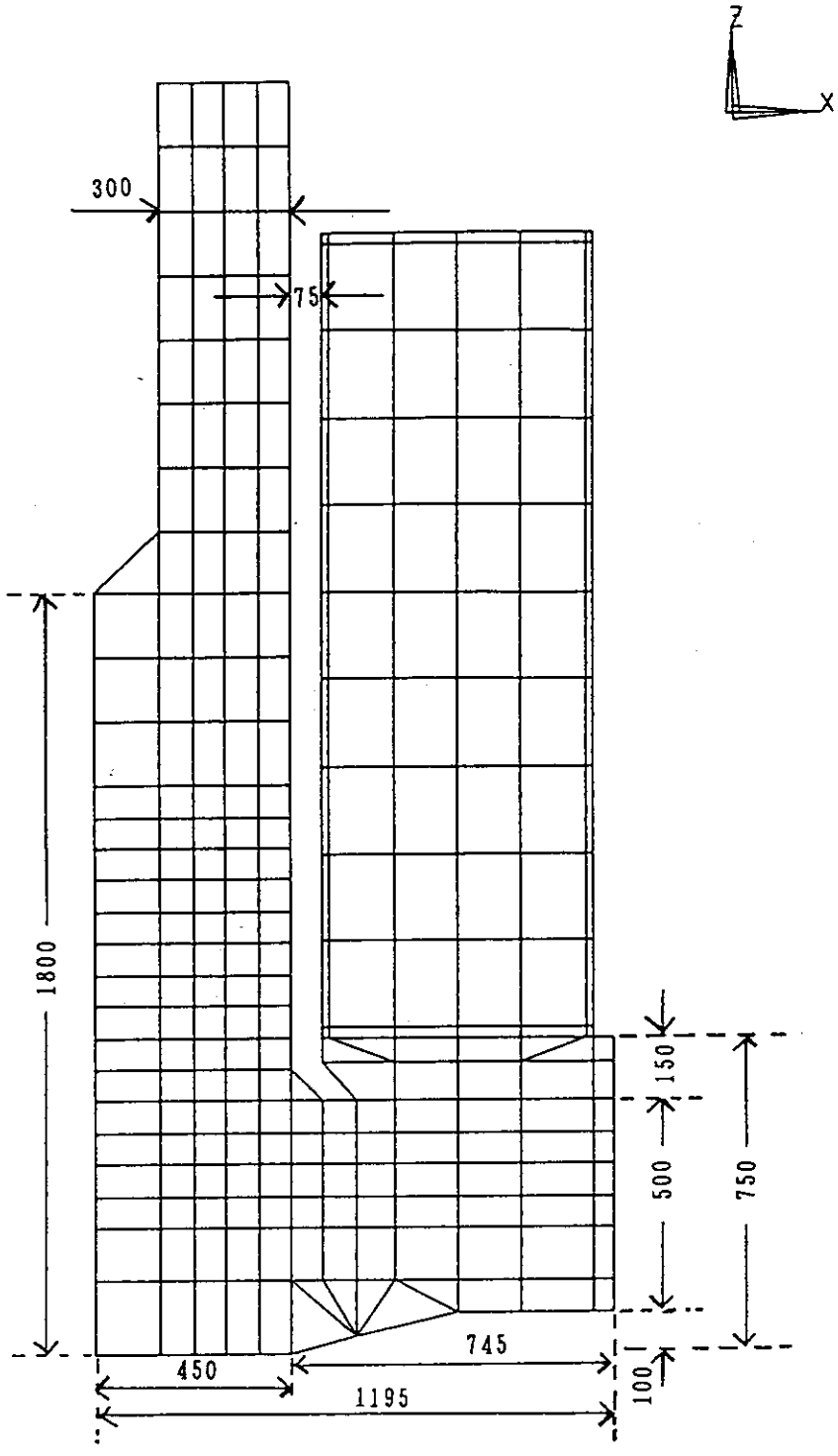

Fig. 5.1 (c) Detailed dimensions and model of the lower part of CS coil support structure.

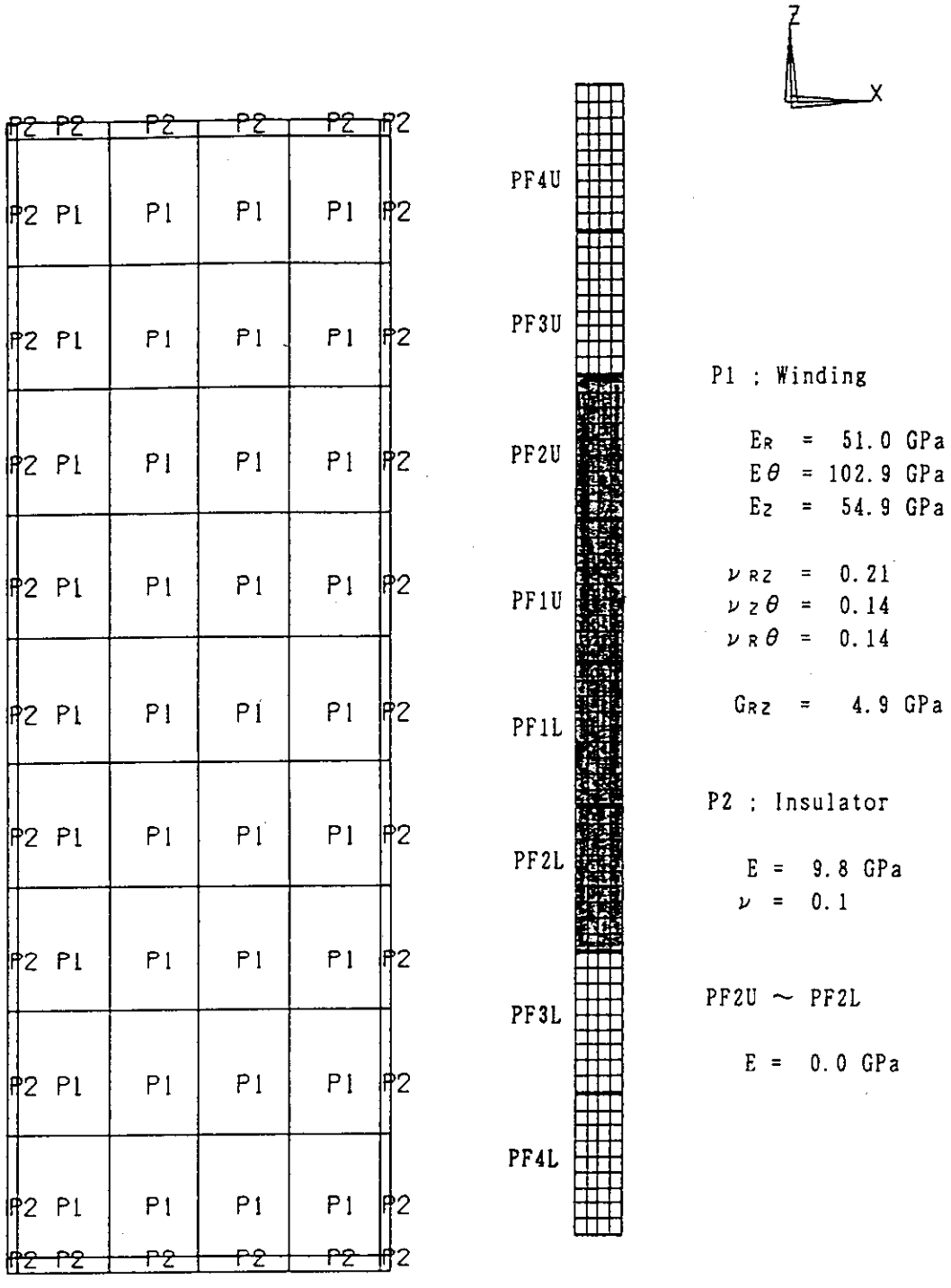

Fig. 5.2 (a) Material properties of the CS coil employed for the FEM analysis.

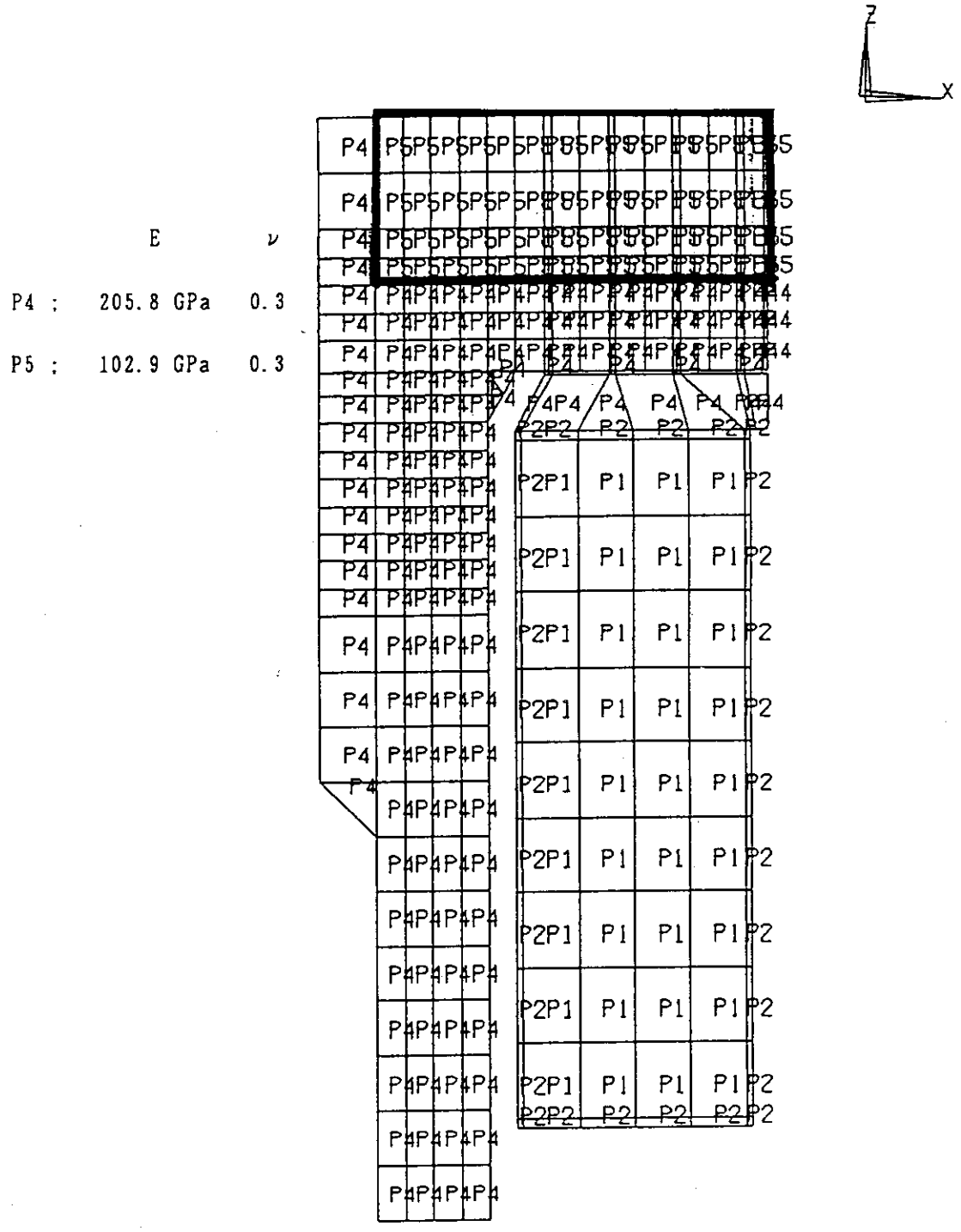

Fig. 5.2 (b) Material properties employed for the upper part of CS coil support structure.

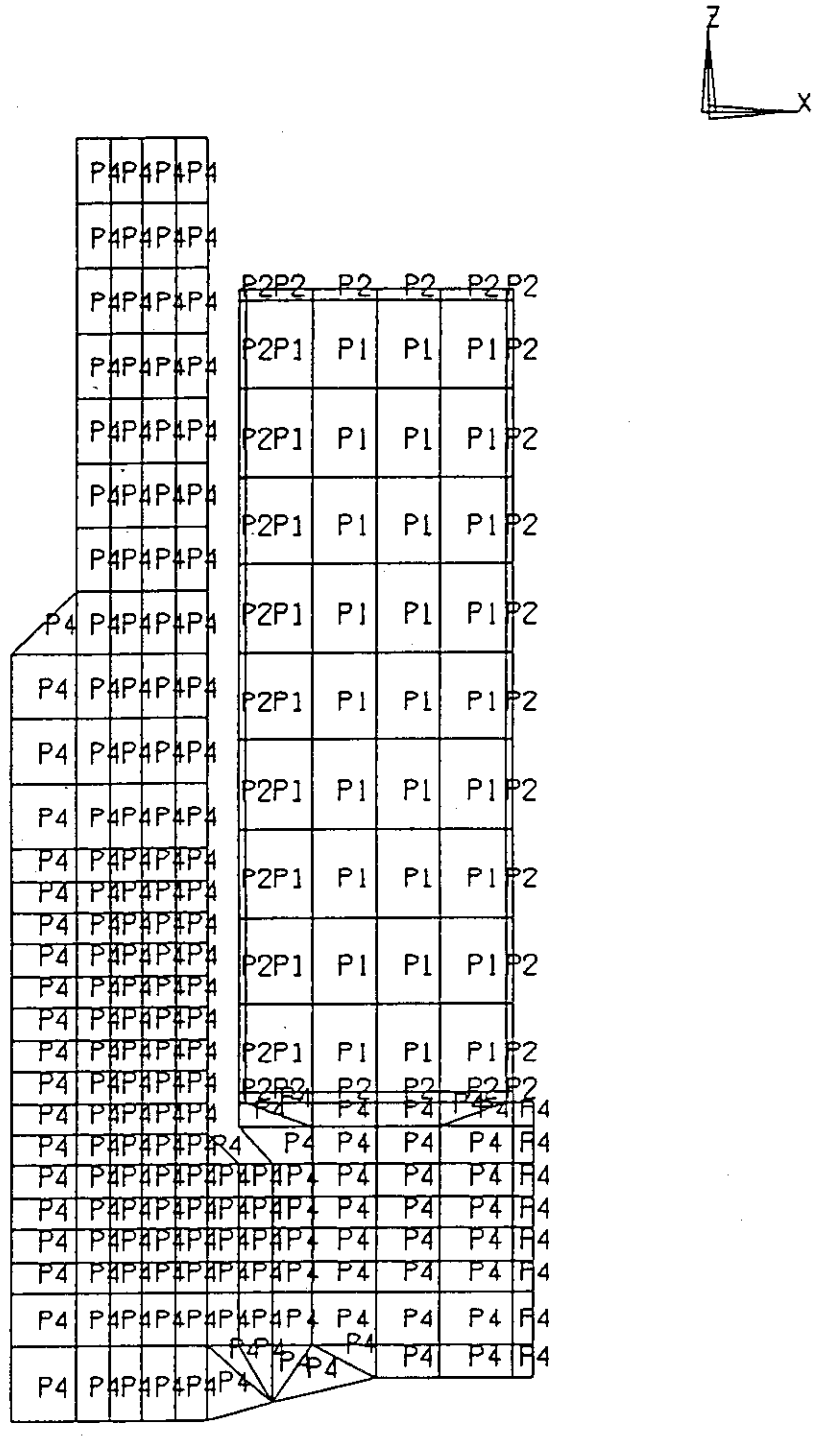

Fig. 5.2 (c) Material properties employed for the lower part of CS coil support structure.

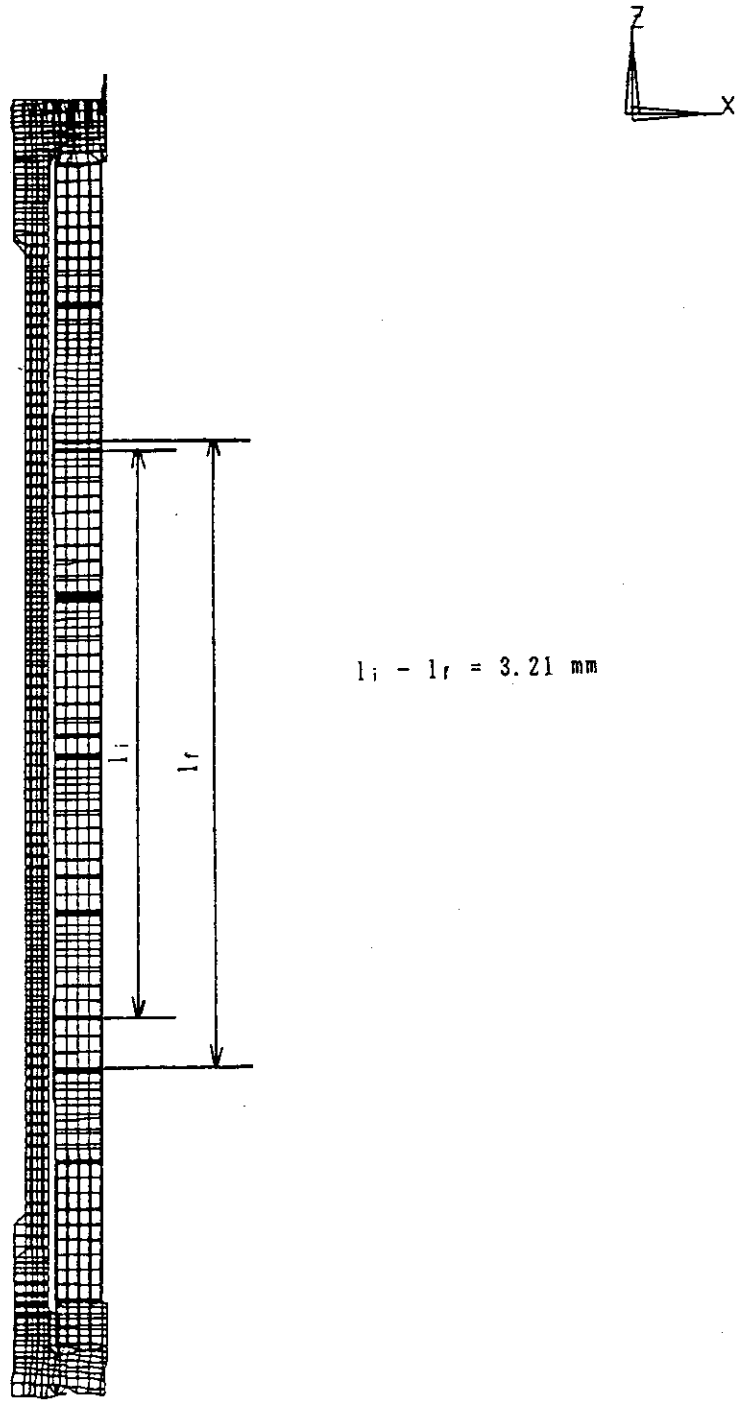

Fig. 5.3 Deformation of the CS coils and support structure at SOFT1. The distances between the bottom surface of PF-3U coil and the top surface of PF-3L coil before and after loading are noted as l_i and l_f, respectively.

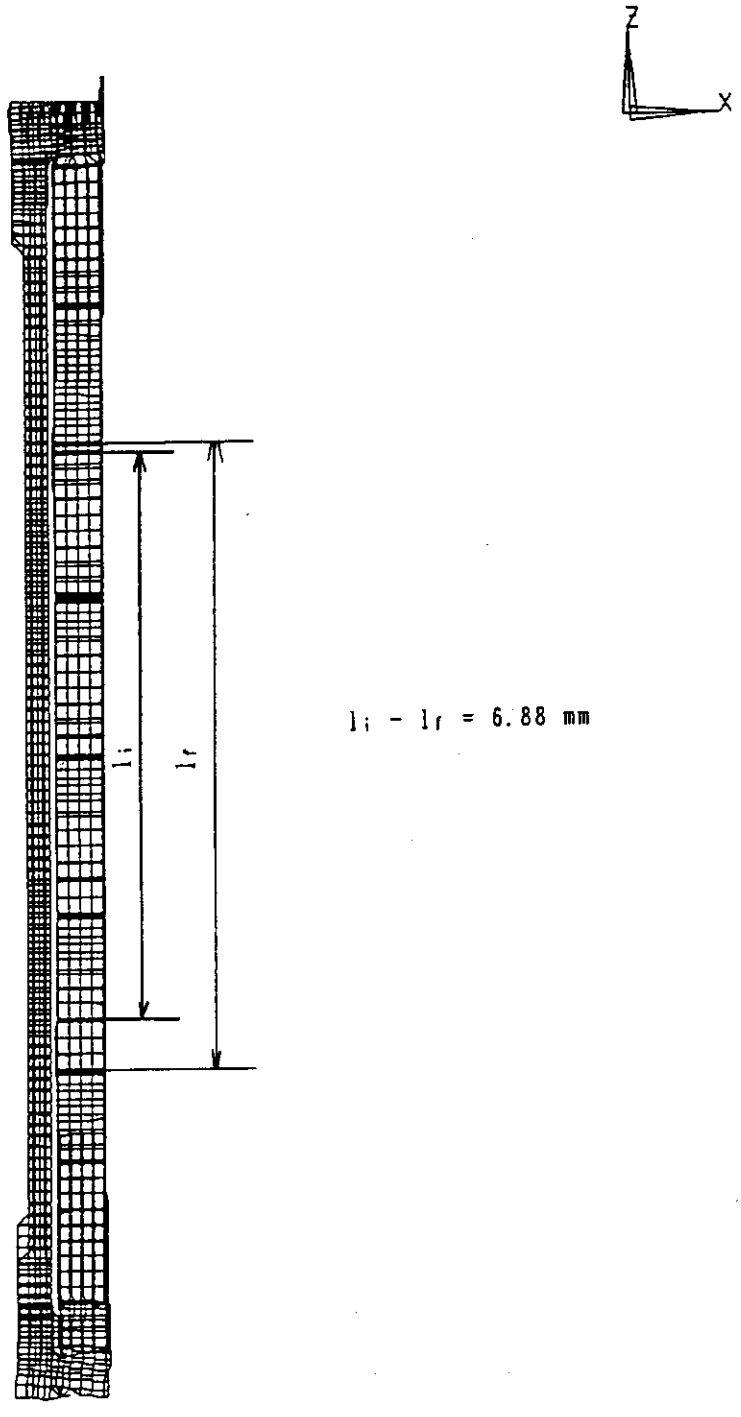

Fig. 5.4 Deformation of the CS coils and support structure at SOFT2. The distances between the bottom surface of PF-3U coil and the top surface of PF-3L coil before and after loading are noted as l_i and l_f, respectively.

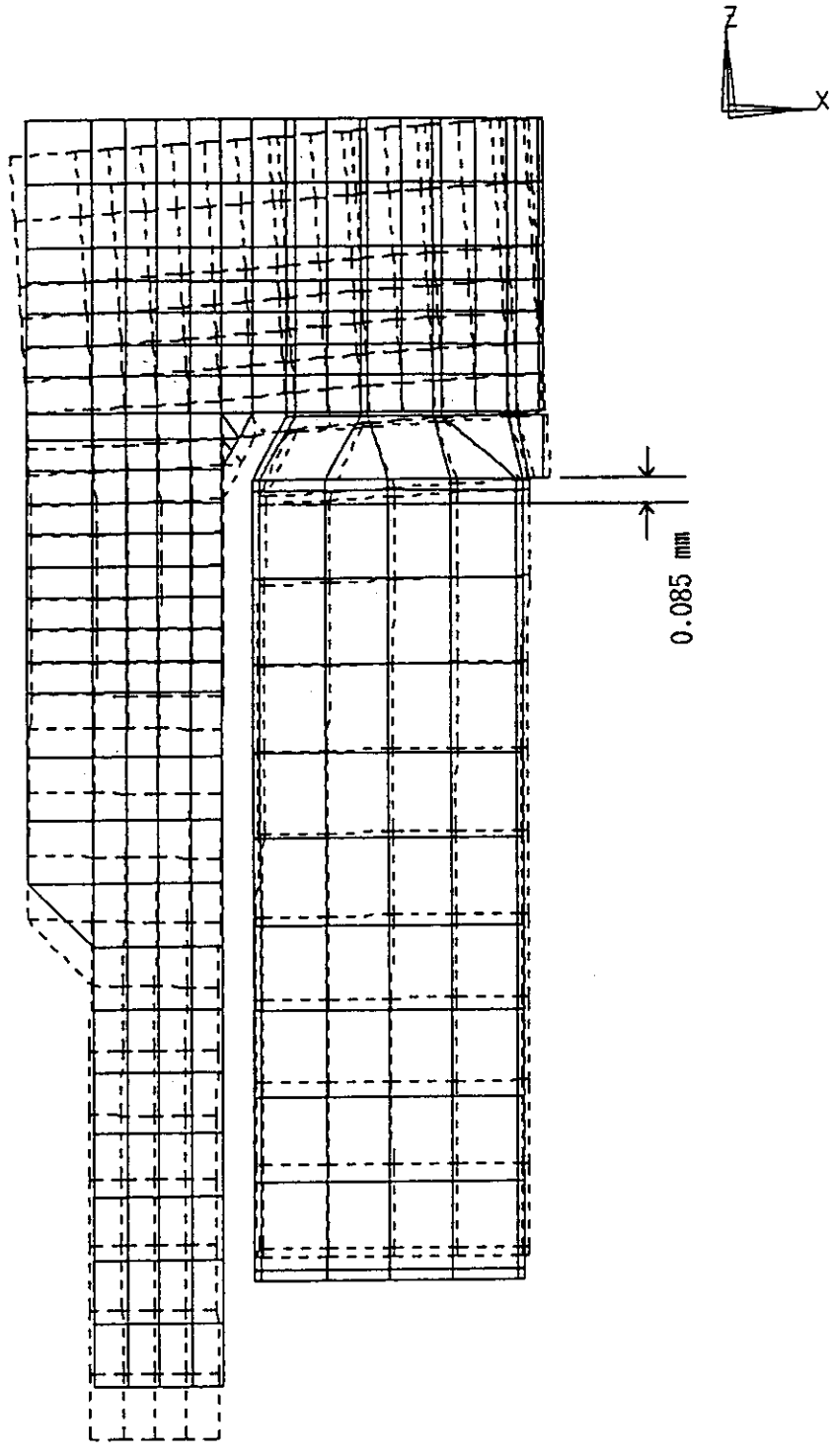

Fig. 5.5 (a) Deformation of the upper part of CS coil support structure at SOFT1 (Zoomed up figure).

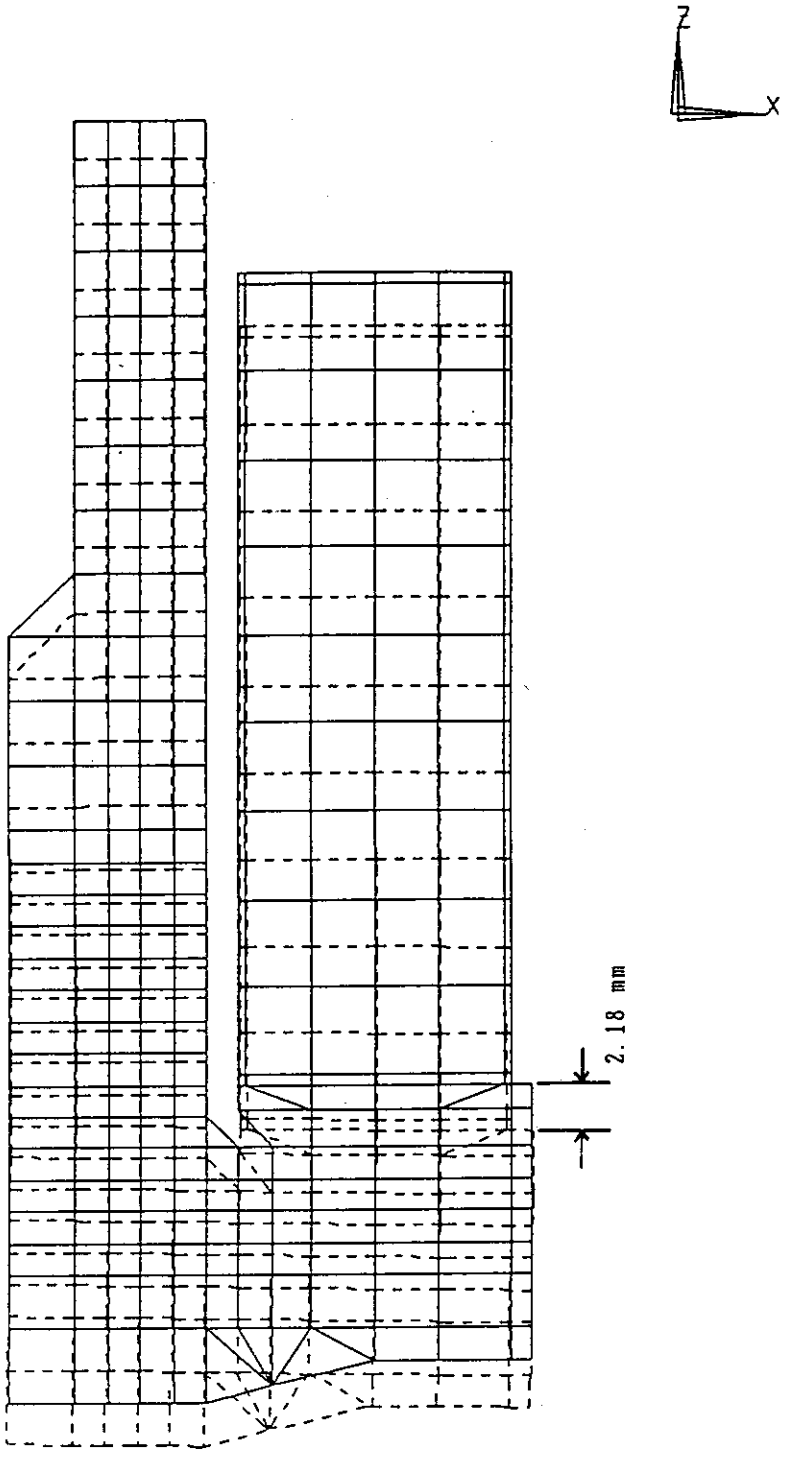

Fig. 5.5 (b) Deformation of the lower part of CS coil support structure at SOFT1 (Zoom up figure).

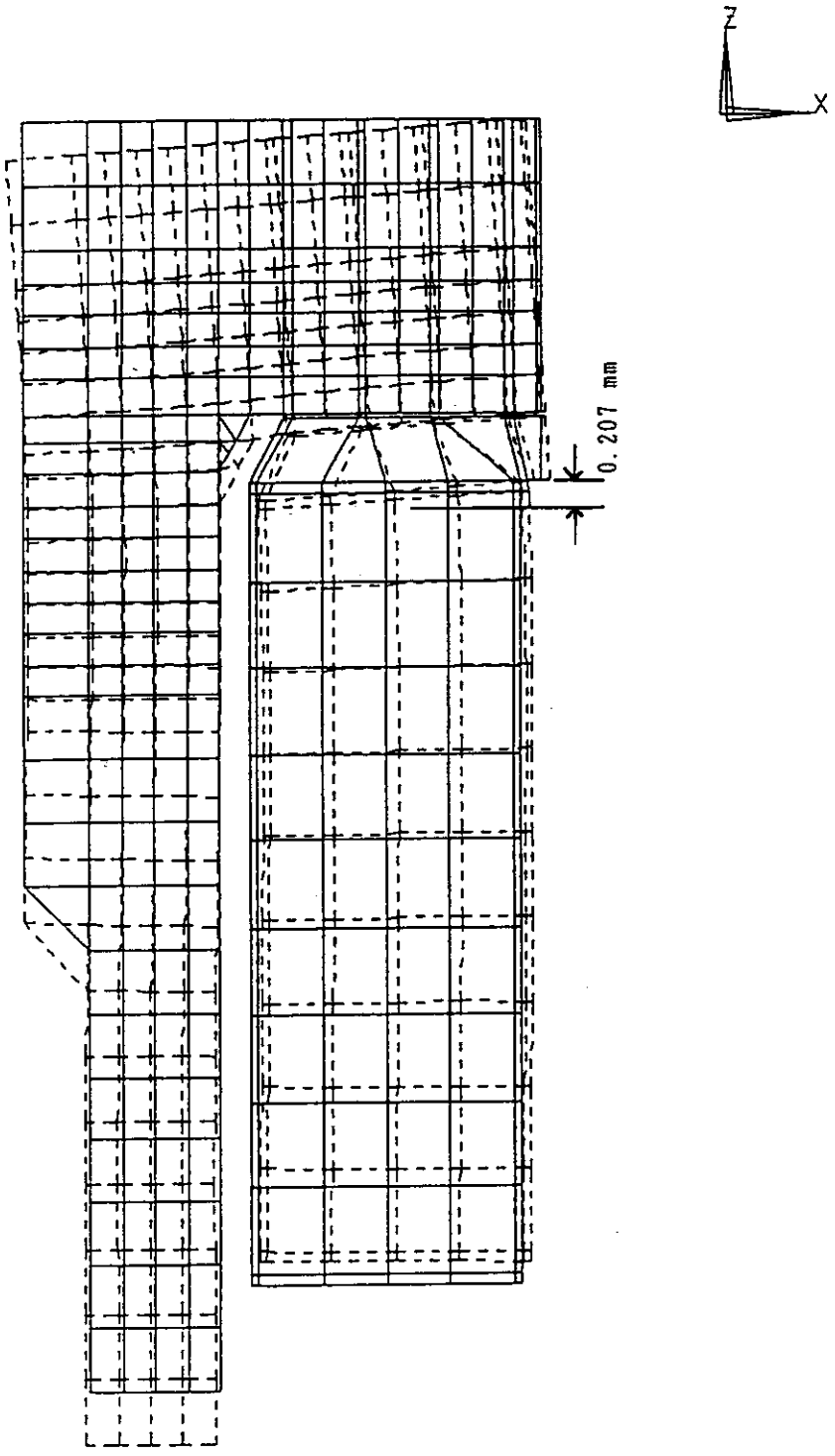

Fig. 5.6 (a) Deformations of the upper part of CS coil support structure at SOFT2 (Zoomed up figure).

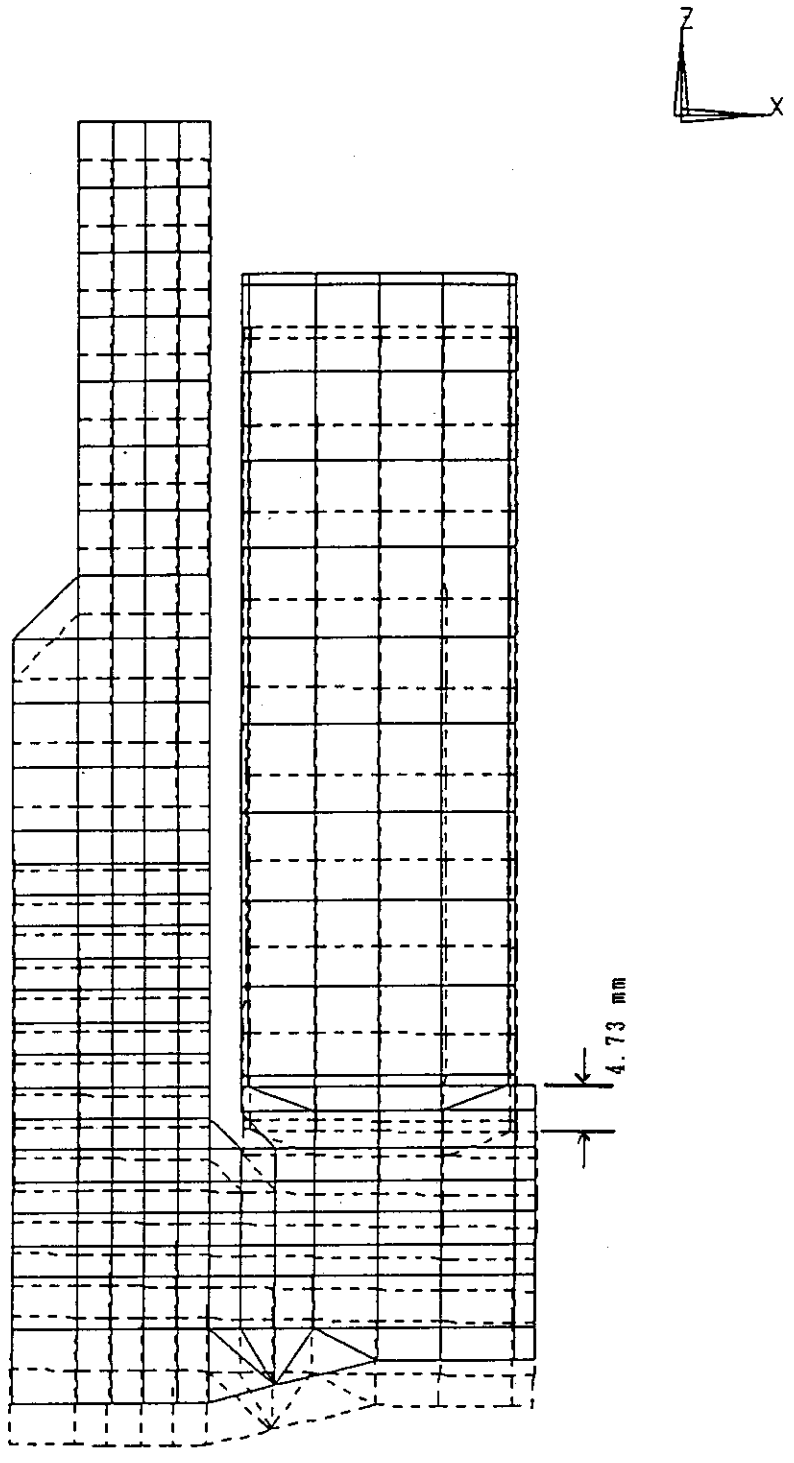

Fig. 5.6 (b) Deformation of the lower part of CS coil support structure at SOFT2 (Zoom up figure).

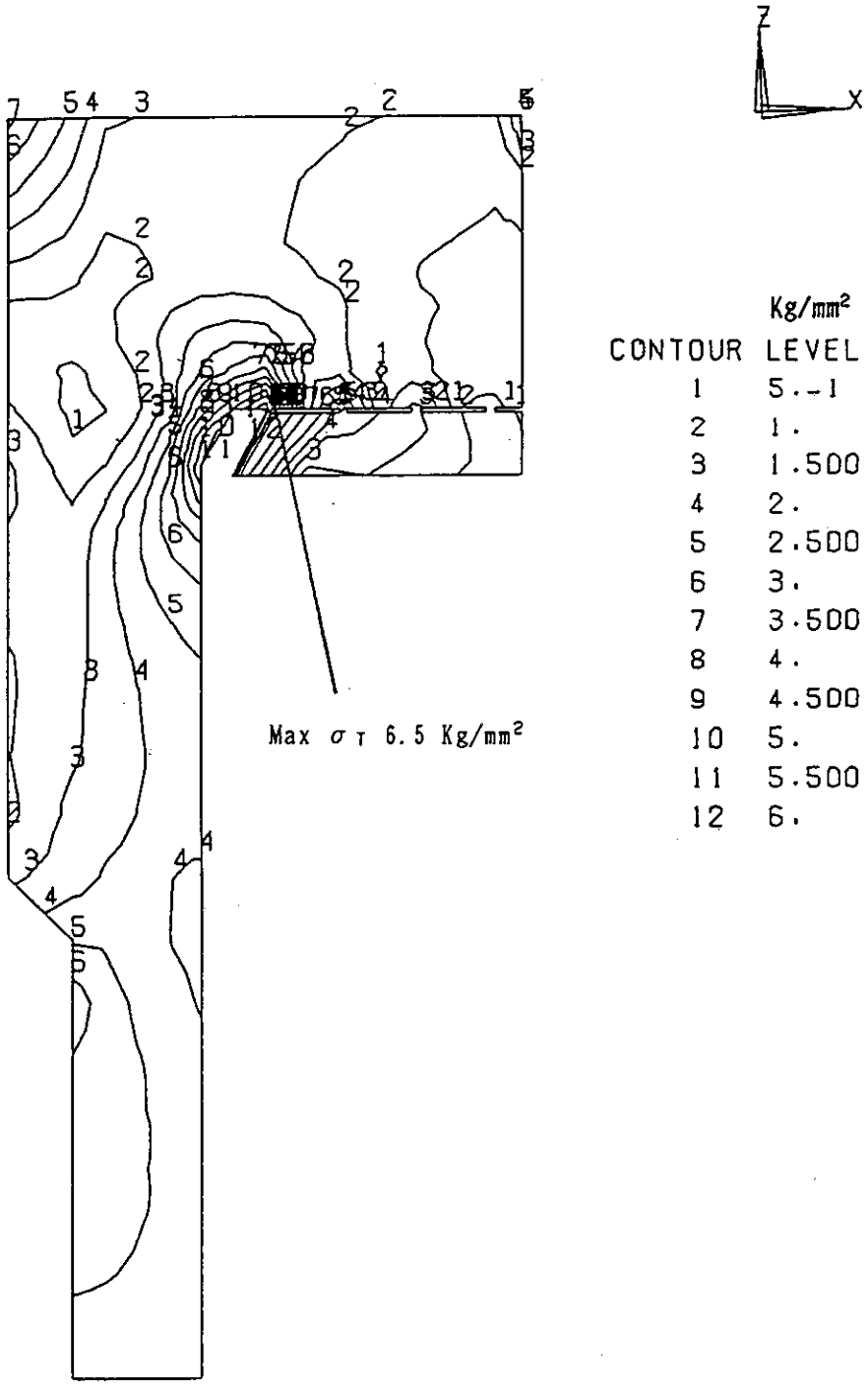

Fig. 5.7 (a) Contour of Tresca stress in the upper part of CS coil support structure at SOFT1.

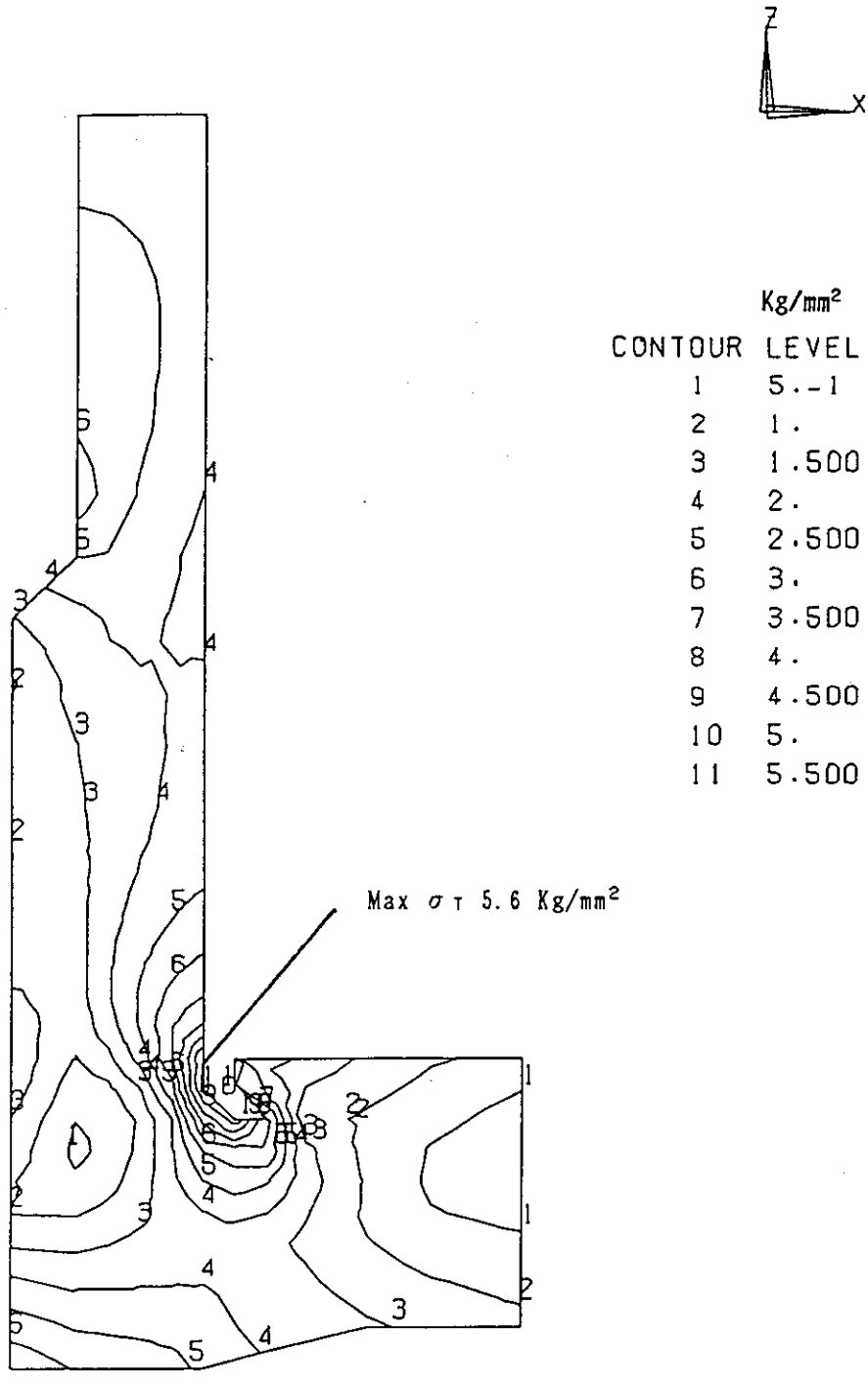

Fig. 5.7 (b) Contour of Tresca stress in the lower part of CS coil support structure at SOFT1.

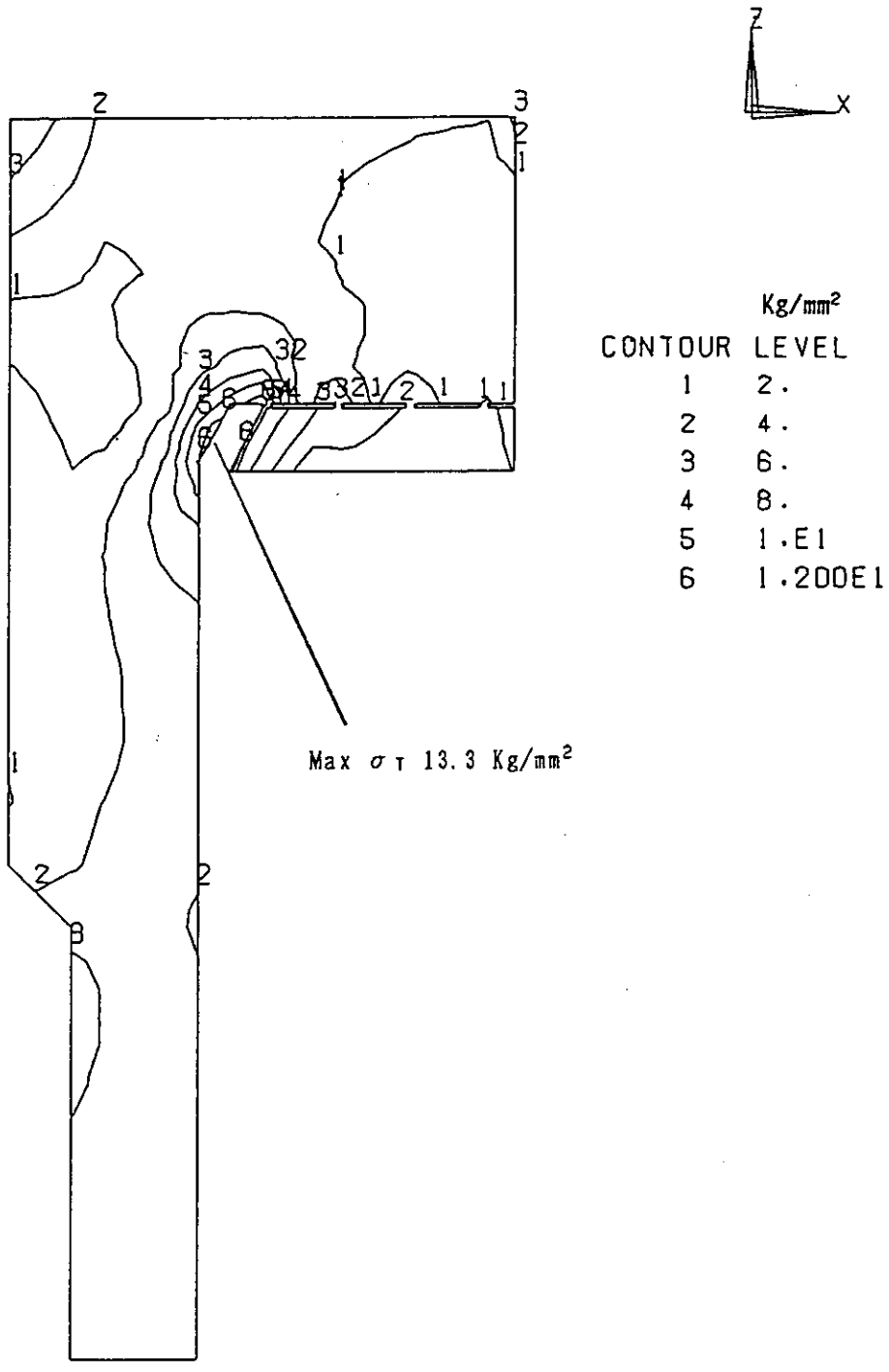

Fig. 5.8 (a) Contour of Tresca stress in the upper part of CS coil support structure at SOFT2

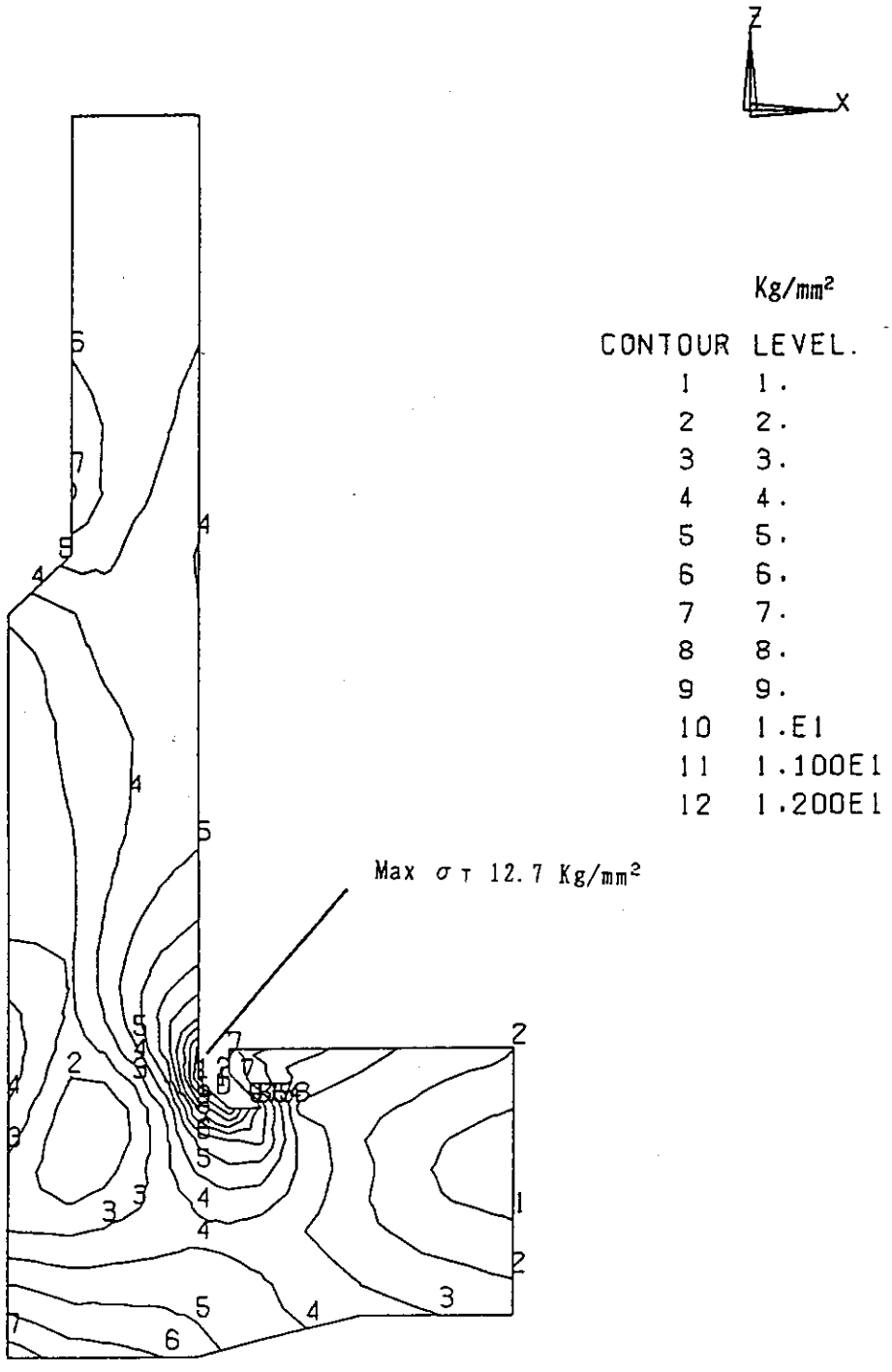

Fig. 5.8 (b) Contour of Tresca stress in the lower part of CS coil support structure at SOFT2.

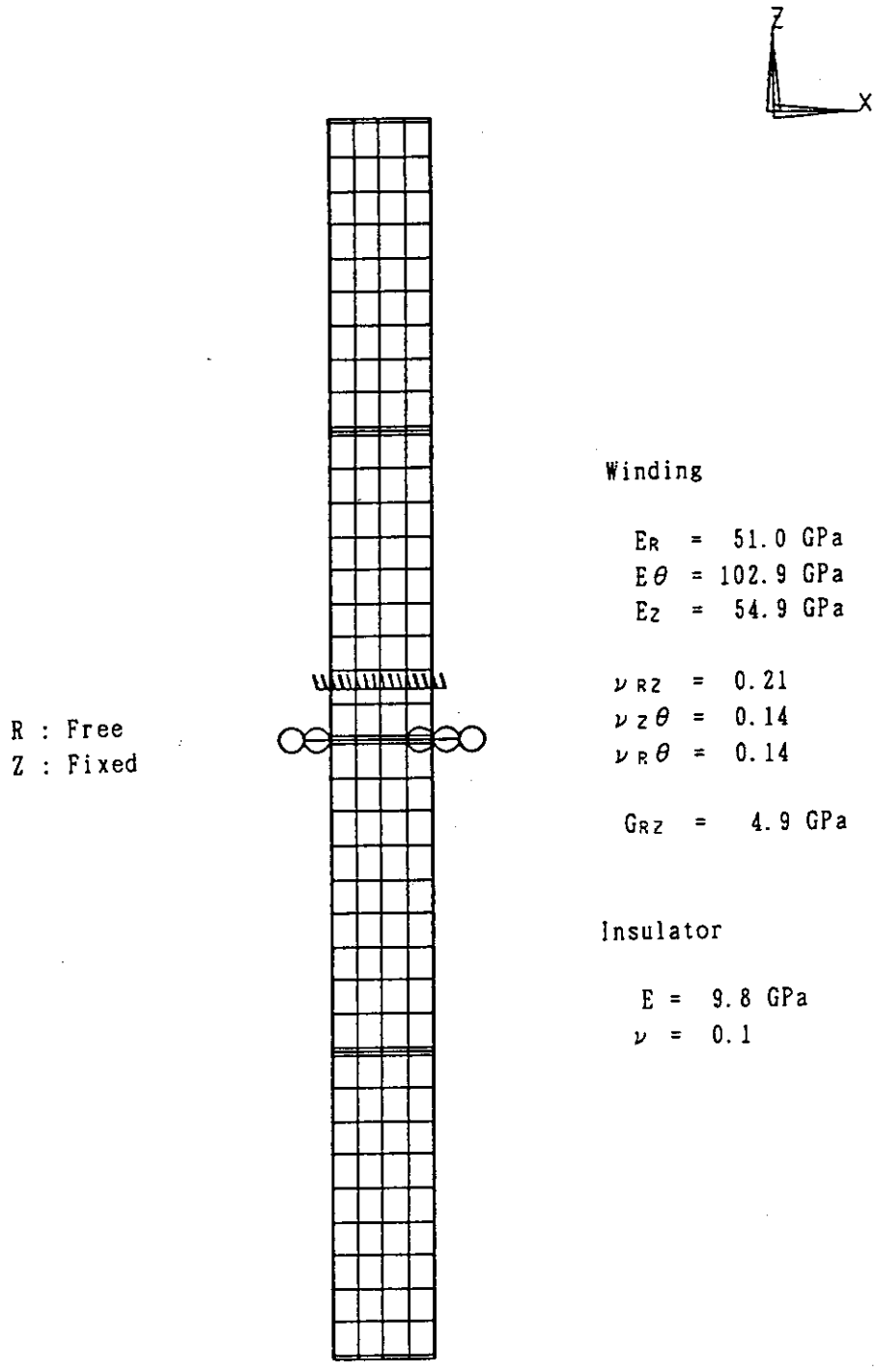

Fig. 5.9 2-dimensional FEM model of PF-1(U,L) and PF-2(U,L), boundary condition and material properties are also shown in the figure.

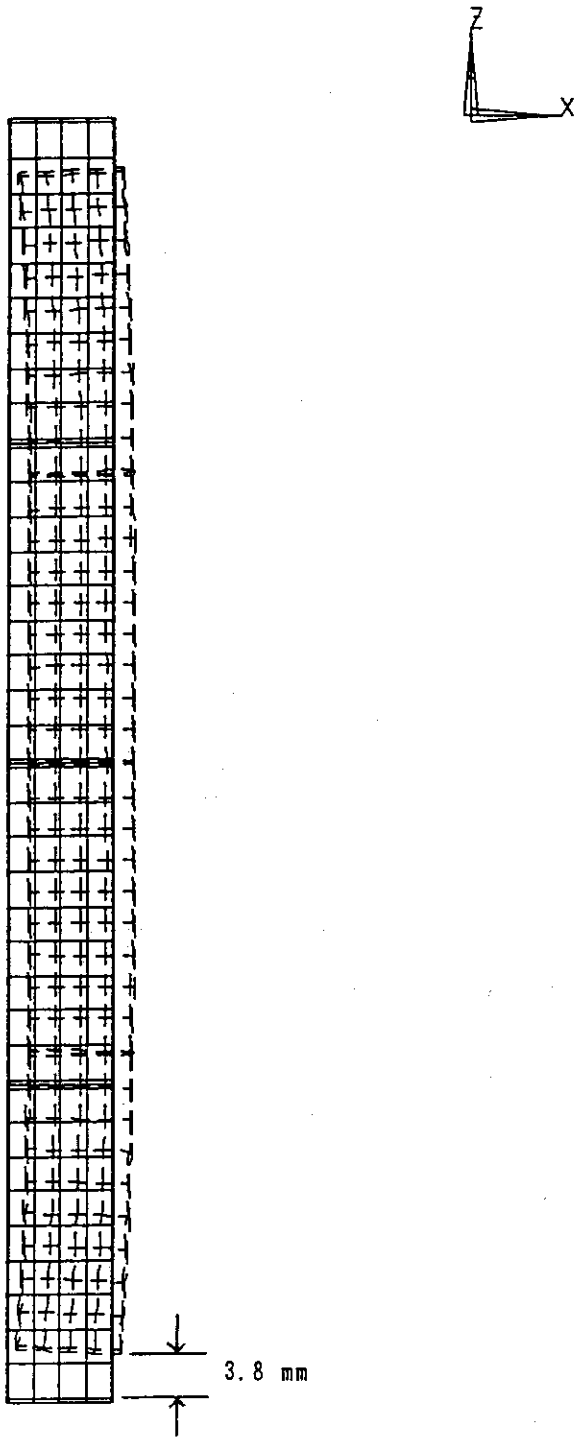

Fig. 5.10 (a) Deformation of PF-1 and PF-2 coils at SOFT1.

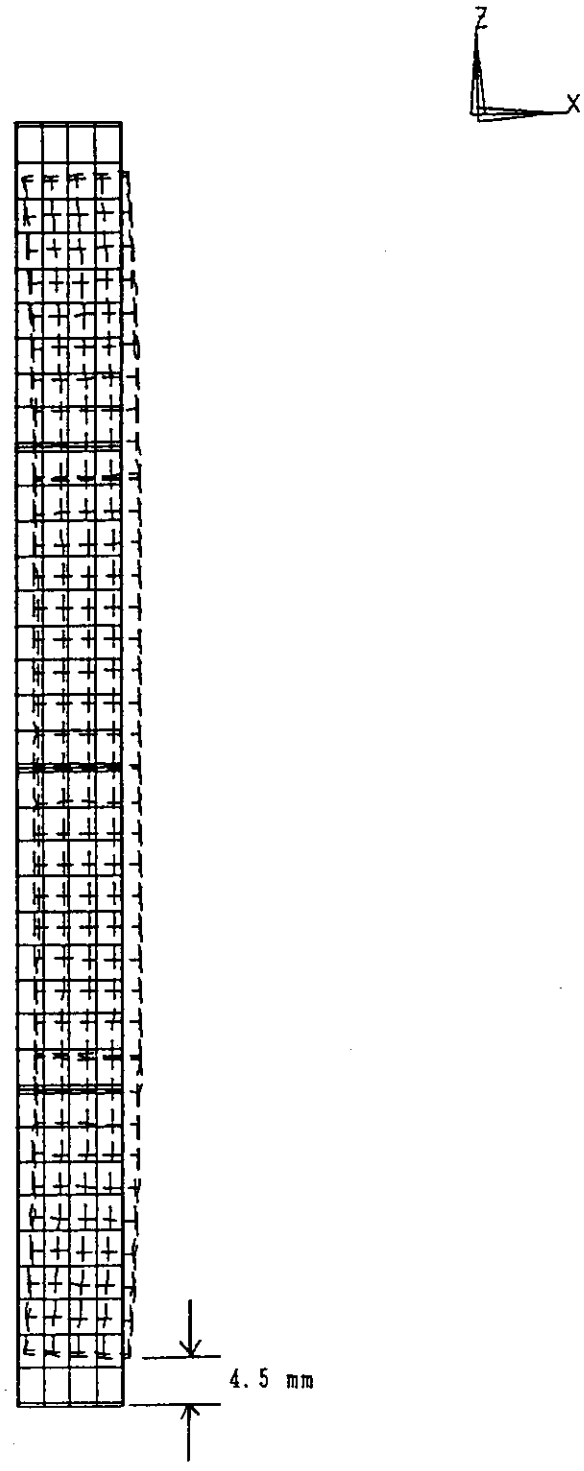

Fig. 5.10 (b) Deformation of PF-1 and PF-2 coils at SOFT2.

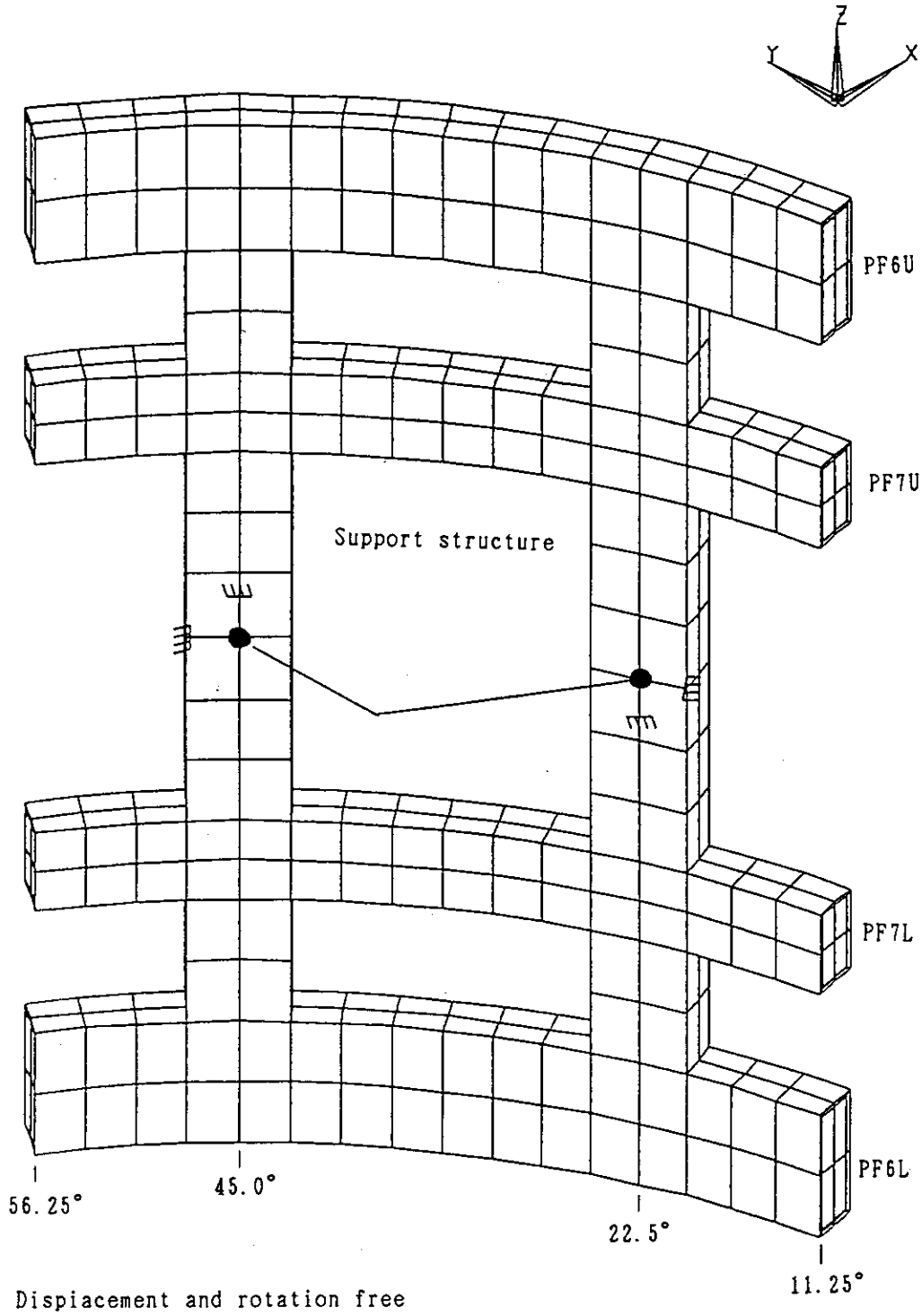

R : Dispiacement and rotation free

θ, Z : Fixed

Fig. 5.11 (a) FEM model of the EF coils and the support structure, boundary conditions are also shown in the figure.

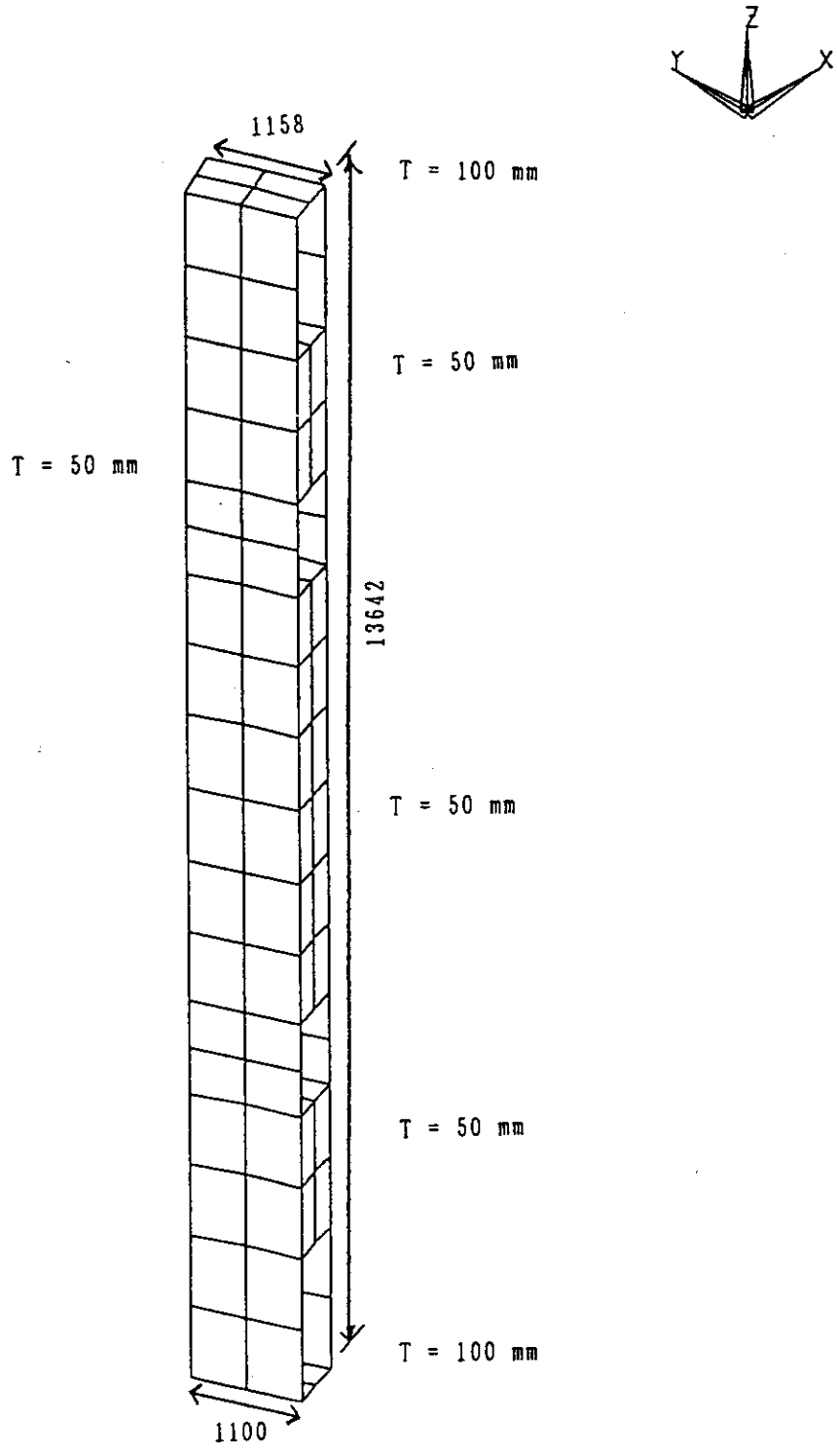

Fig. 5.11 (b) Zoom up of support structure of EF coils.

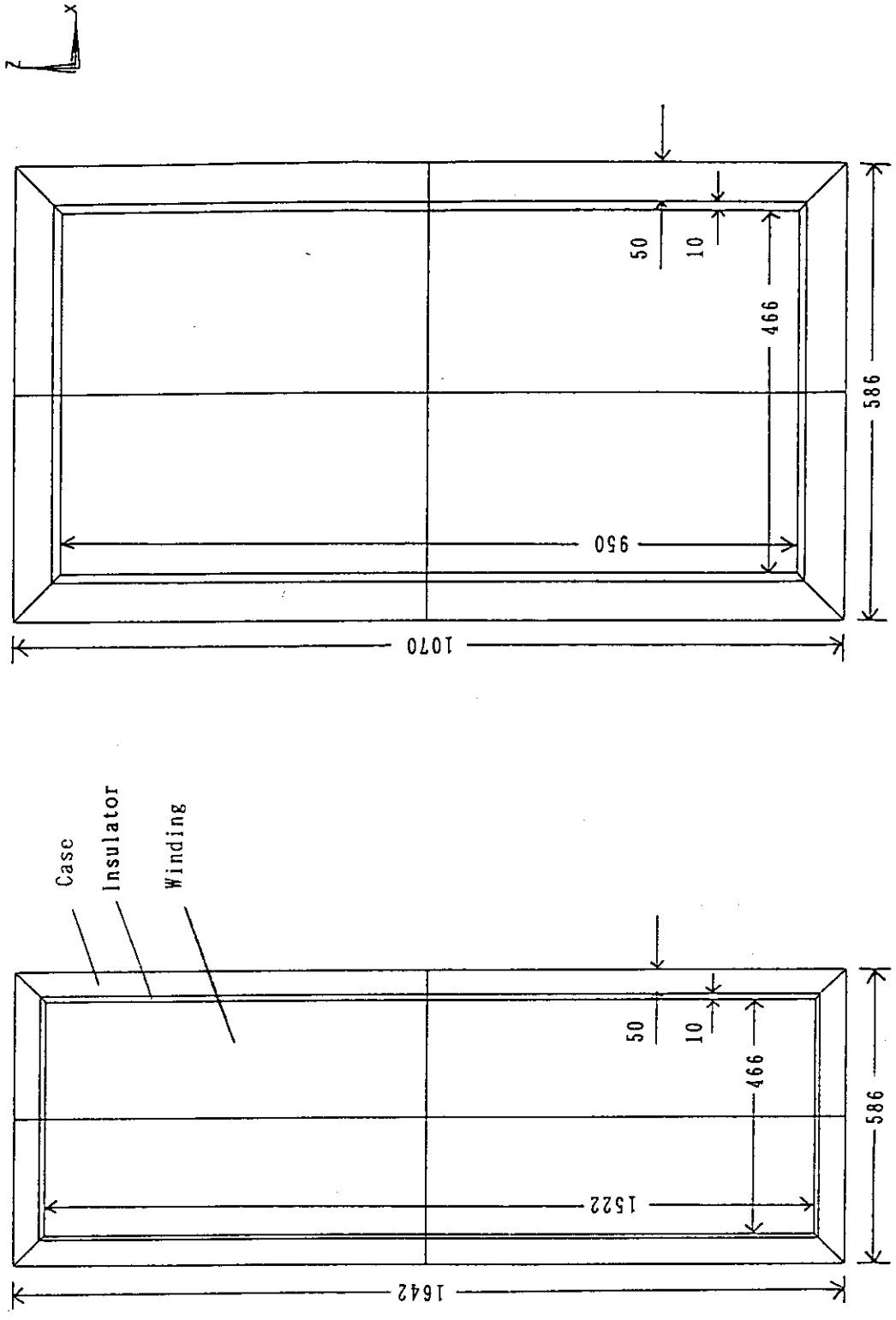

Fig. 5.12 (a) Dimensions of the PF-6 coil. (b) Dimensions of the PF-7 coil.

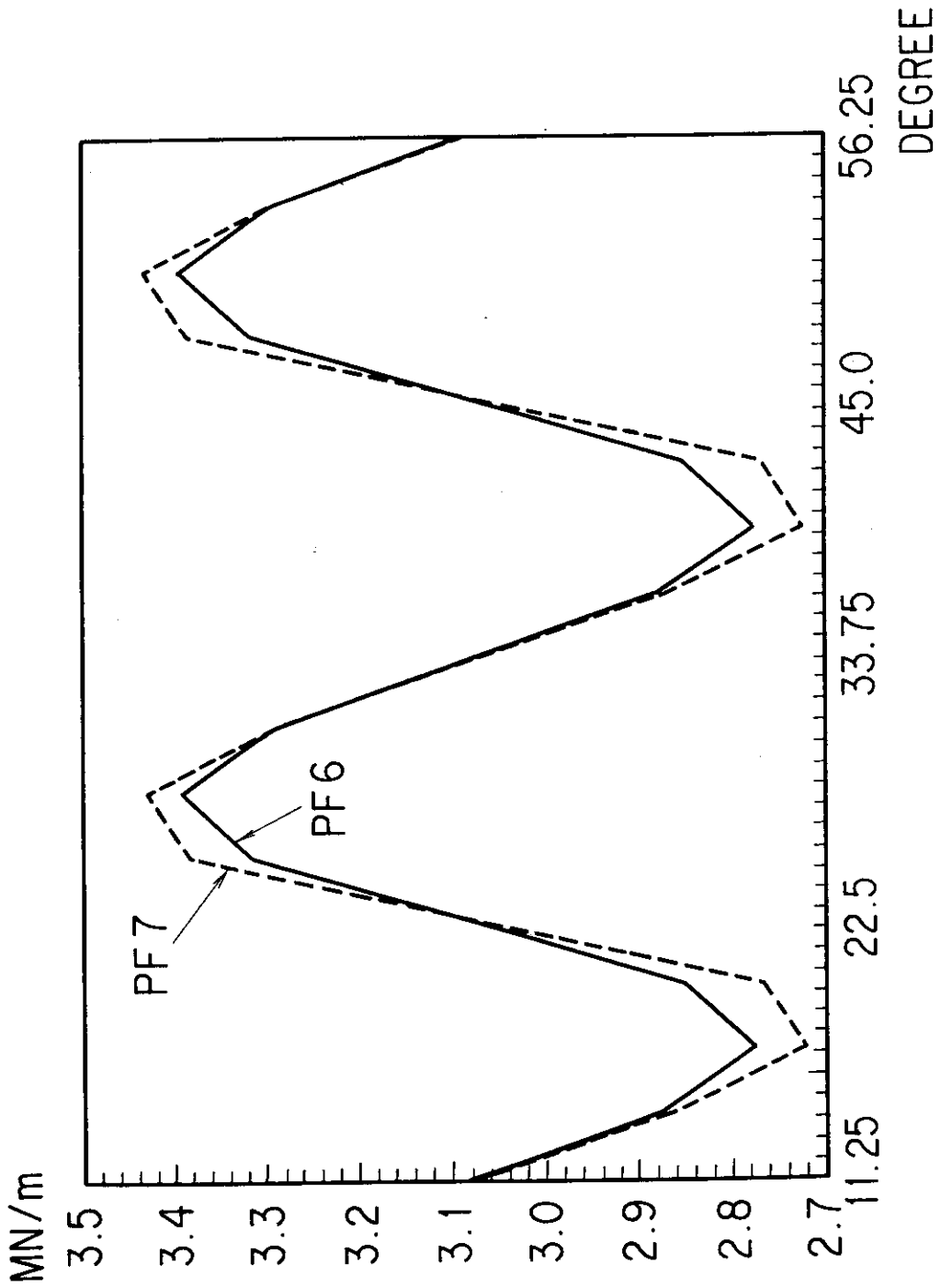

Fig. 5.13 (a) Distributions of radial electromagnetic force of PF-6 and PF-7 coil at EOB1, force between 11.25 degree and 56.25 degree along the circumferential direction is shown.

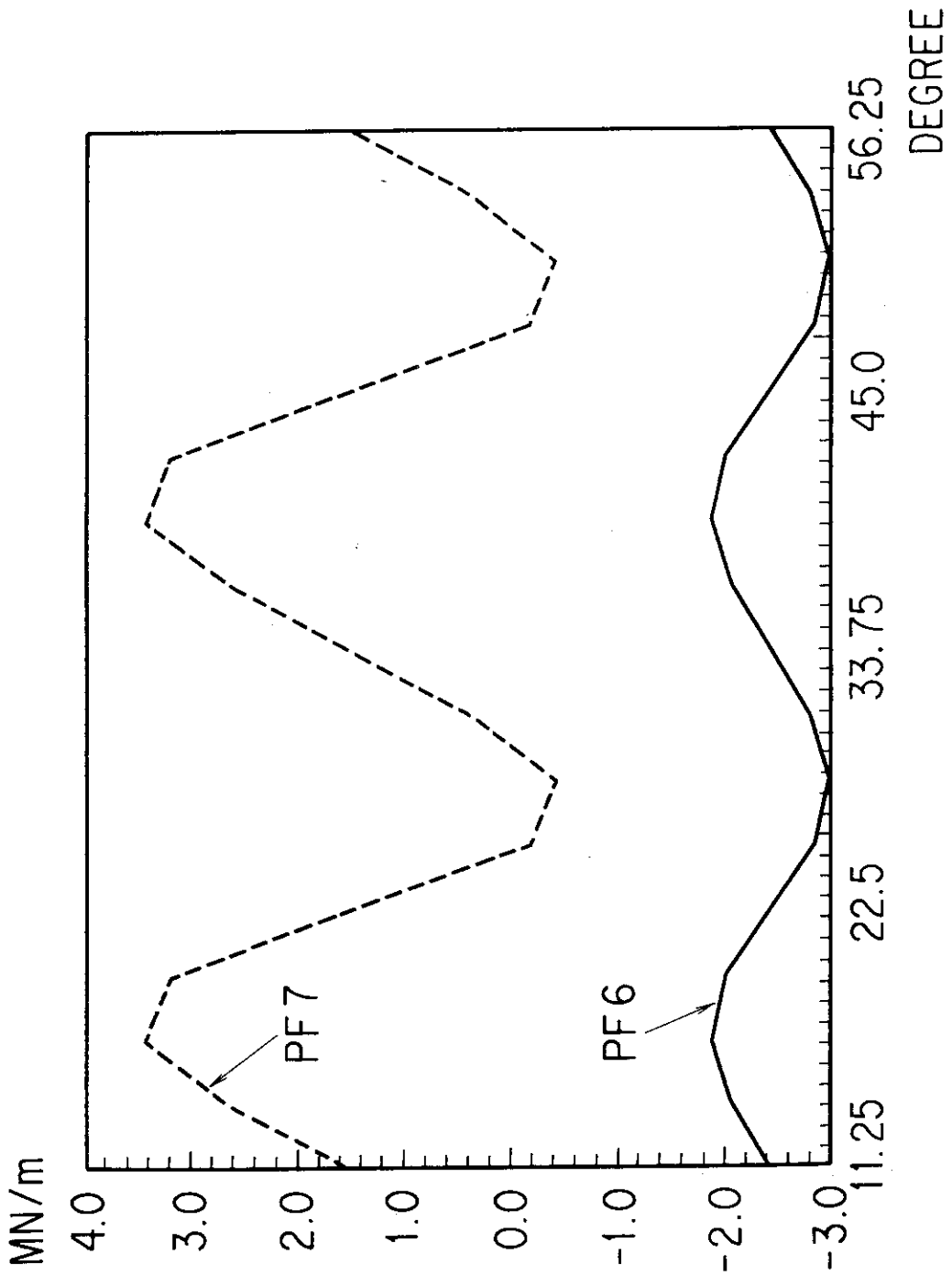

Fig. 5.13 (b) Distributions of vertical electromagnetic force of PF-6 and PF-7 coil at EOB1, force between 11.25 degree and 56.25 degree in the circumferential direction is shown.

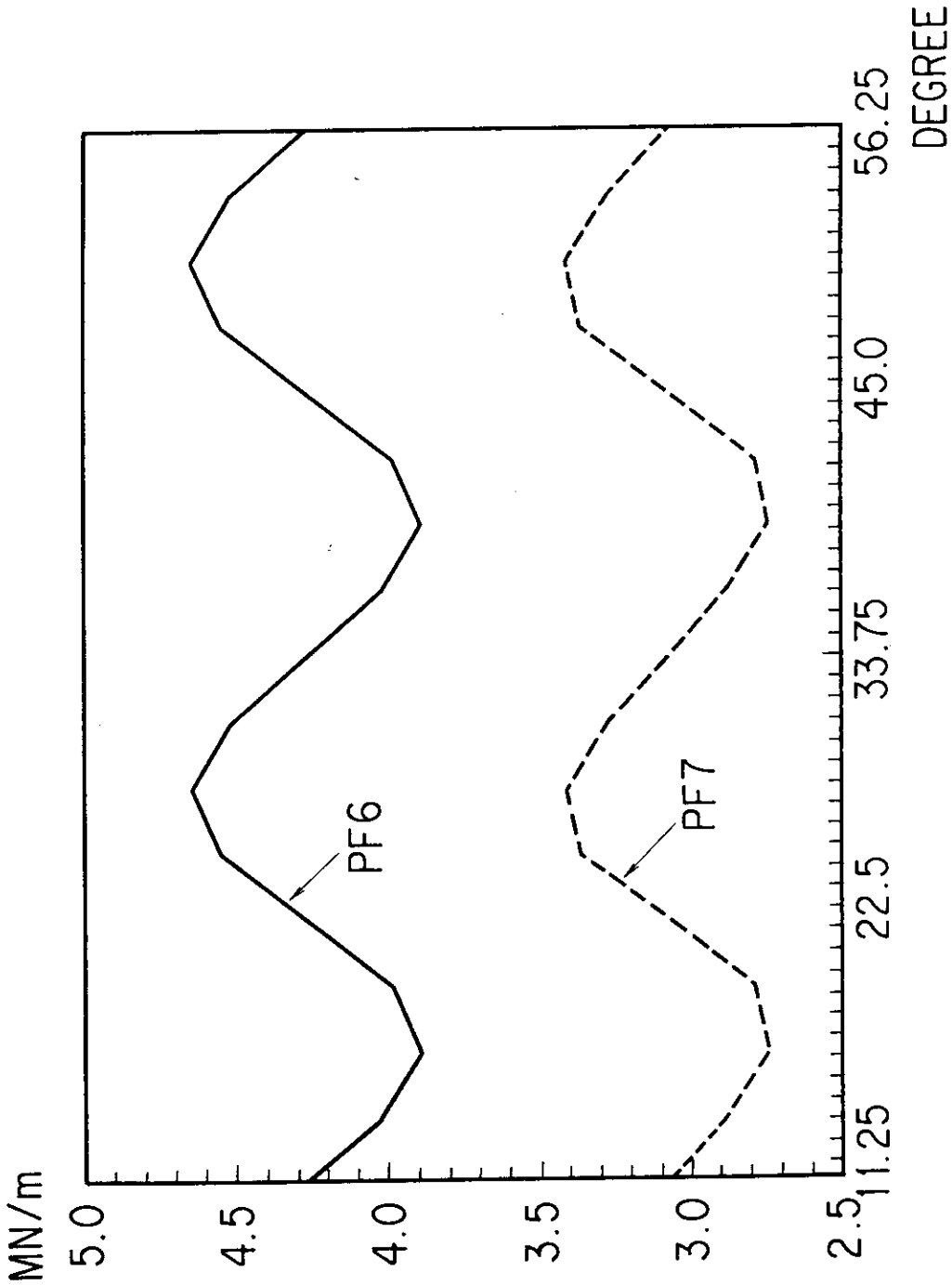

Fig. 5.14 (a) Distributions of radial electromagnetic force of PF-6 and PF-7 coil at EOB3, force between 11.25 degree and 56.25 degree along the circumferential direction of coil is shown.

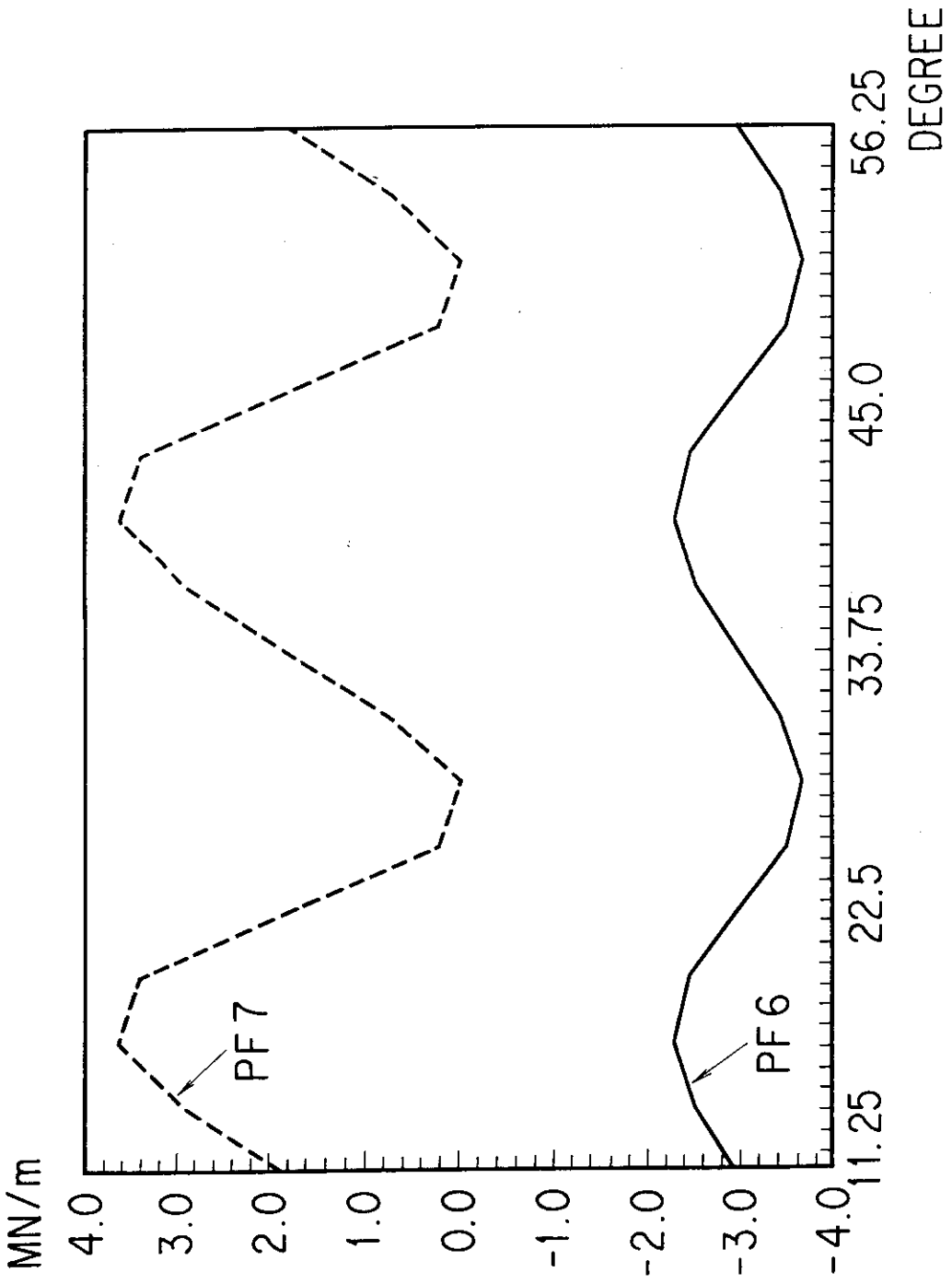

Fig. 5.14 (b) Distributions of vertical electromagnetic force of PF-6 and PF-7 coil at EOB1, force between 11.25 degree and 56.25 degree along the circumferential direction is shown.

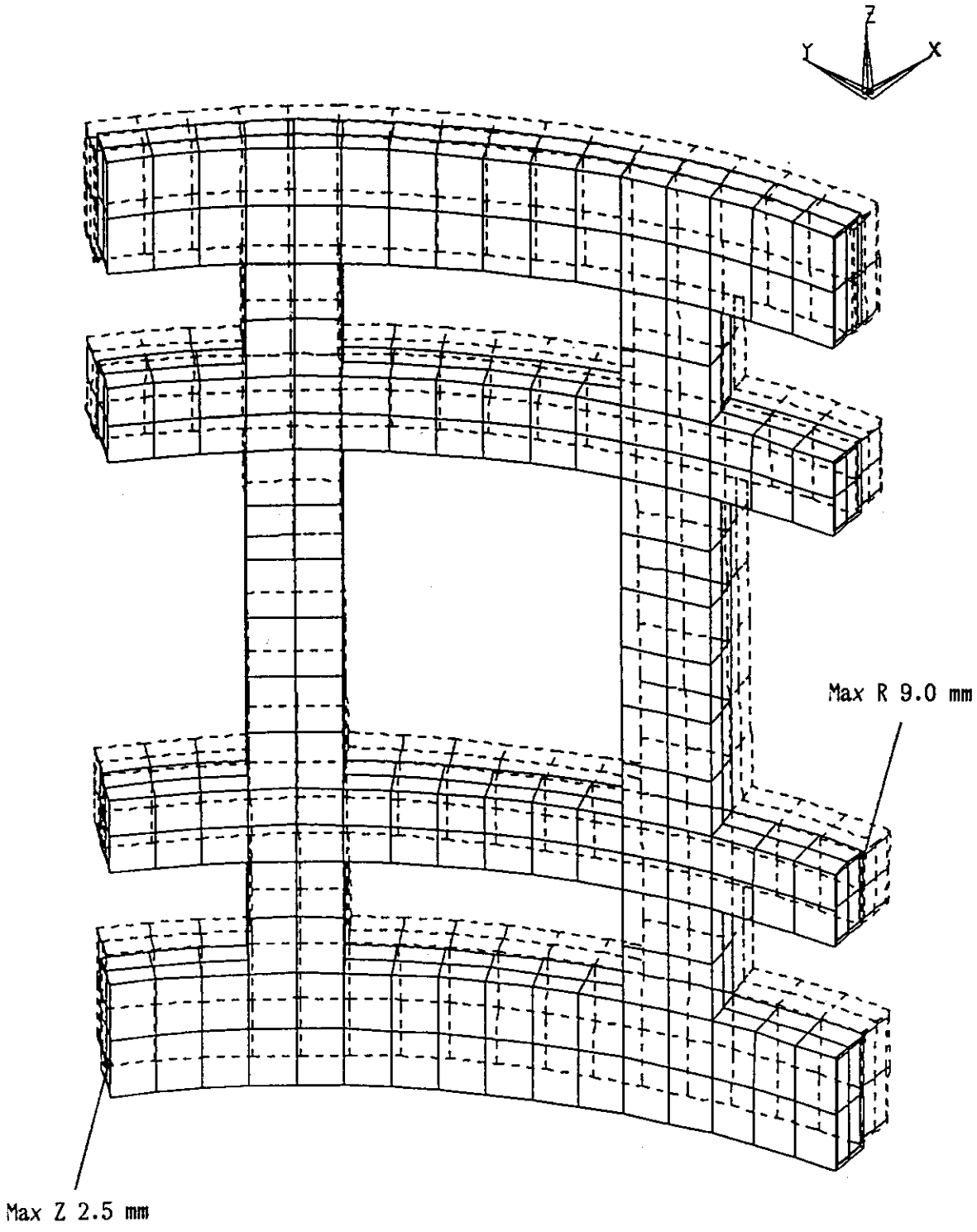

Fig. 5.15 Deformations of EF coil and the support structure at EOB3.

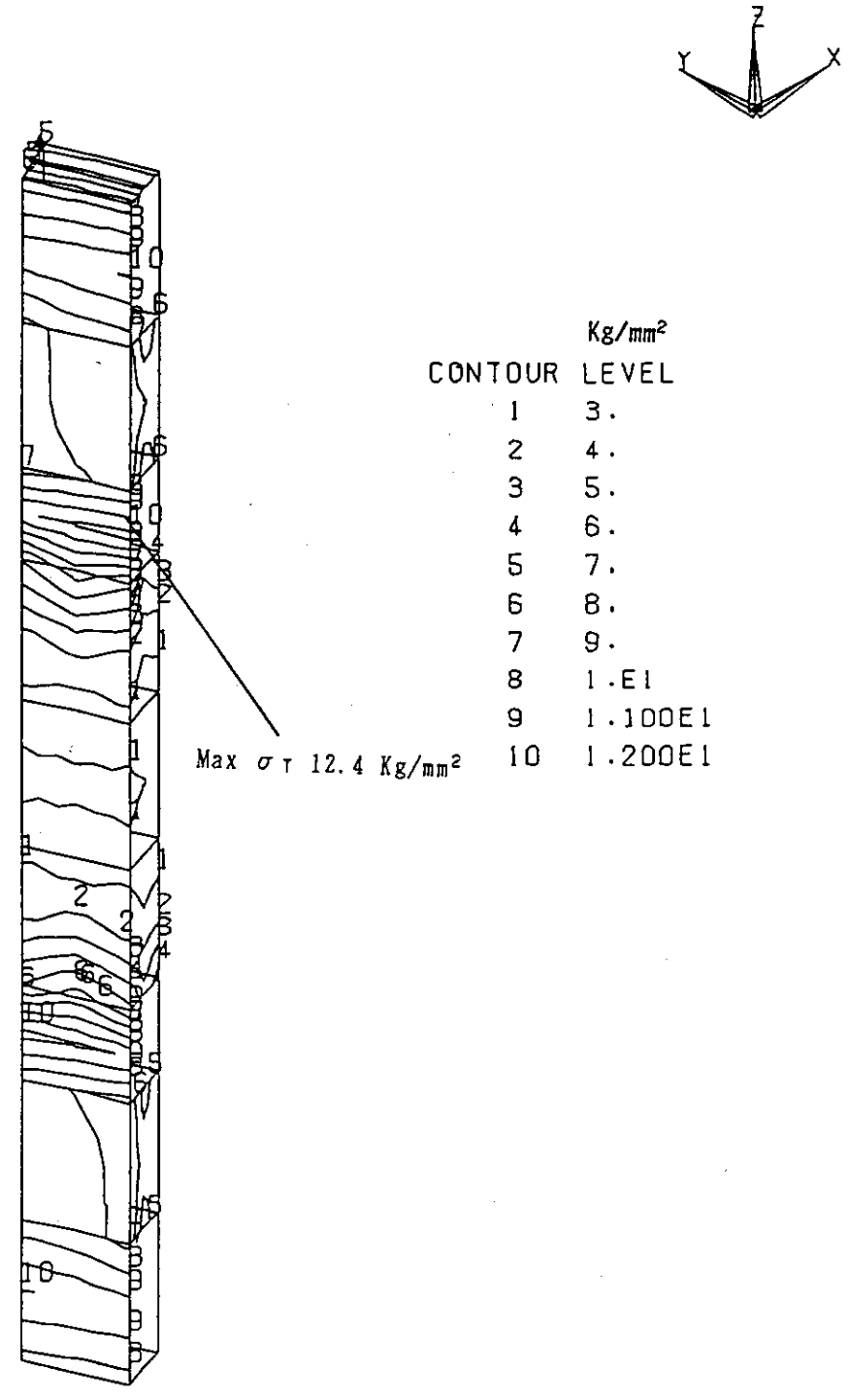

Fig. 5.16 Contour of Tresca stress in the EF coil support structure at EOB3.

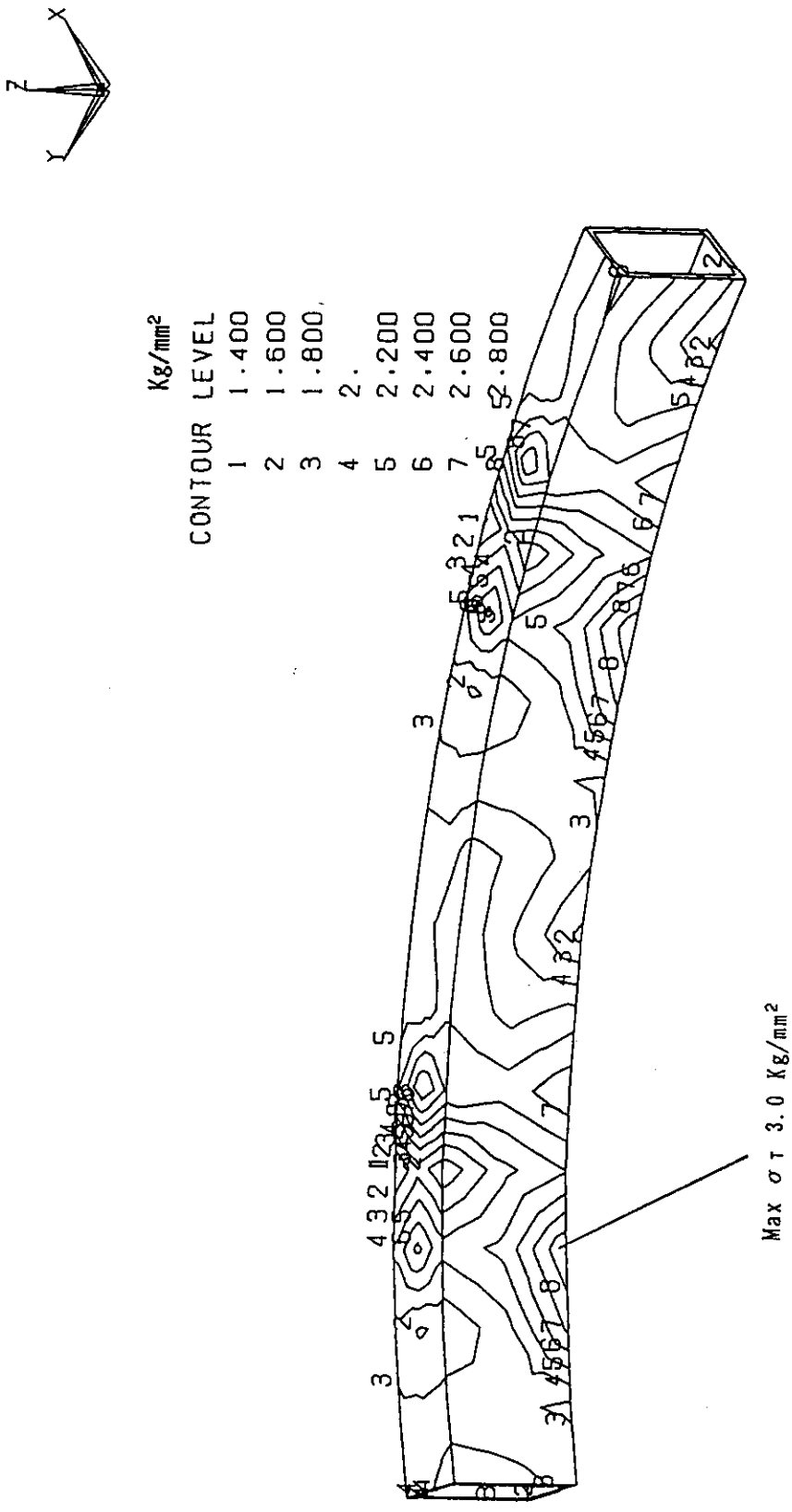

Fig. 5.17 Contour of Tresca stress in the coil case of PF-7 coil at EOB3.

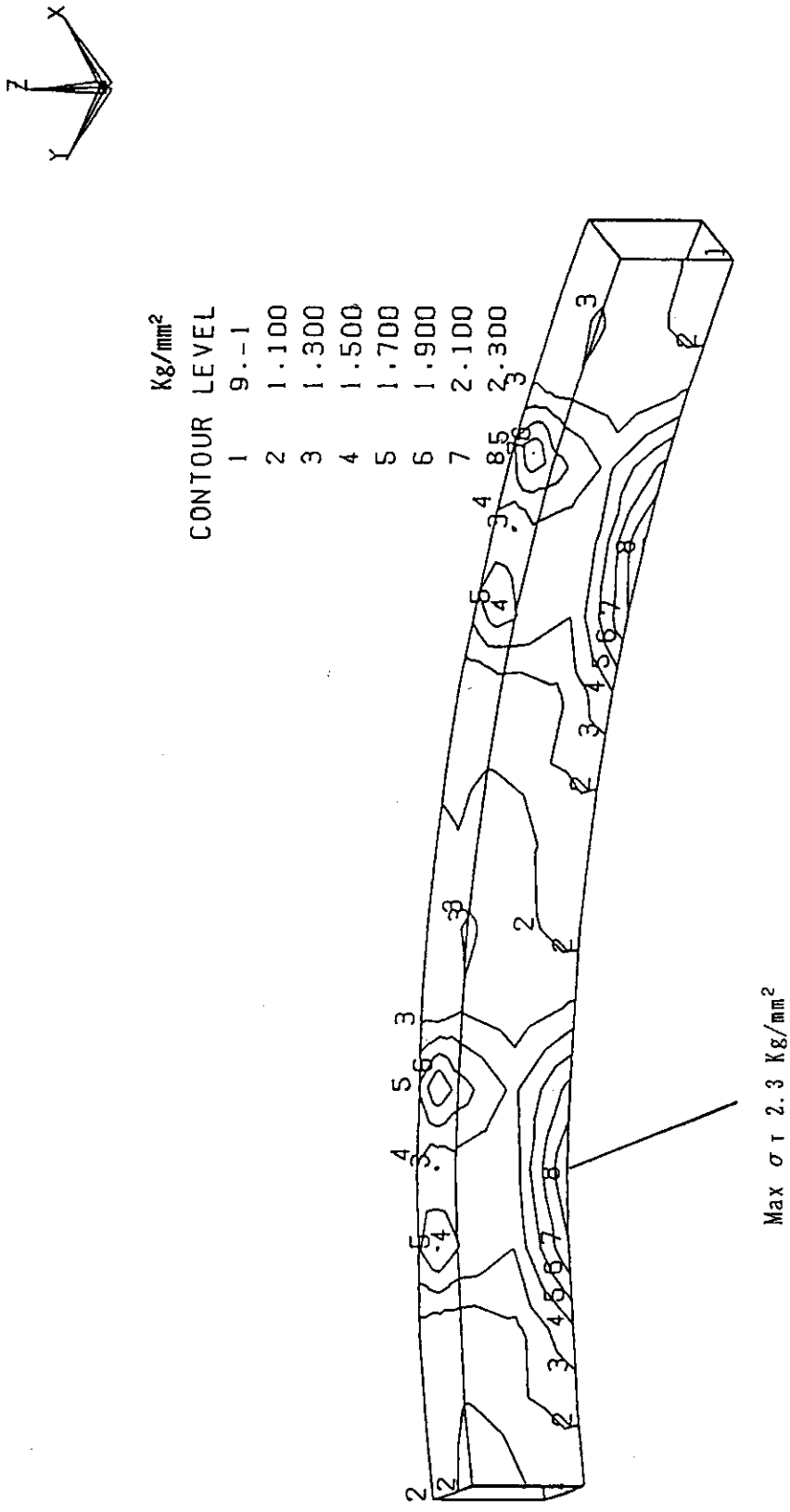

Fig. 5.18 Contour of Tresca stress in the winding insulator of PF-7 coil at EOB3.

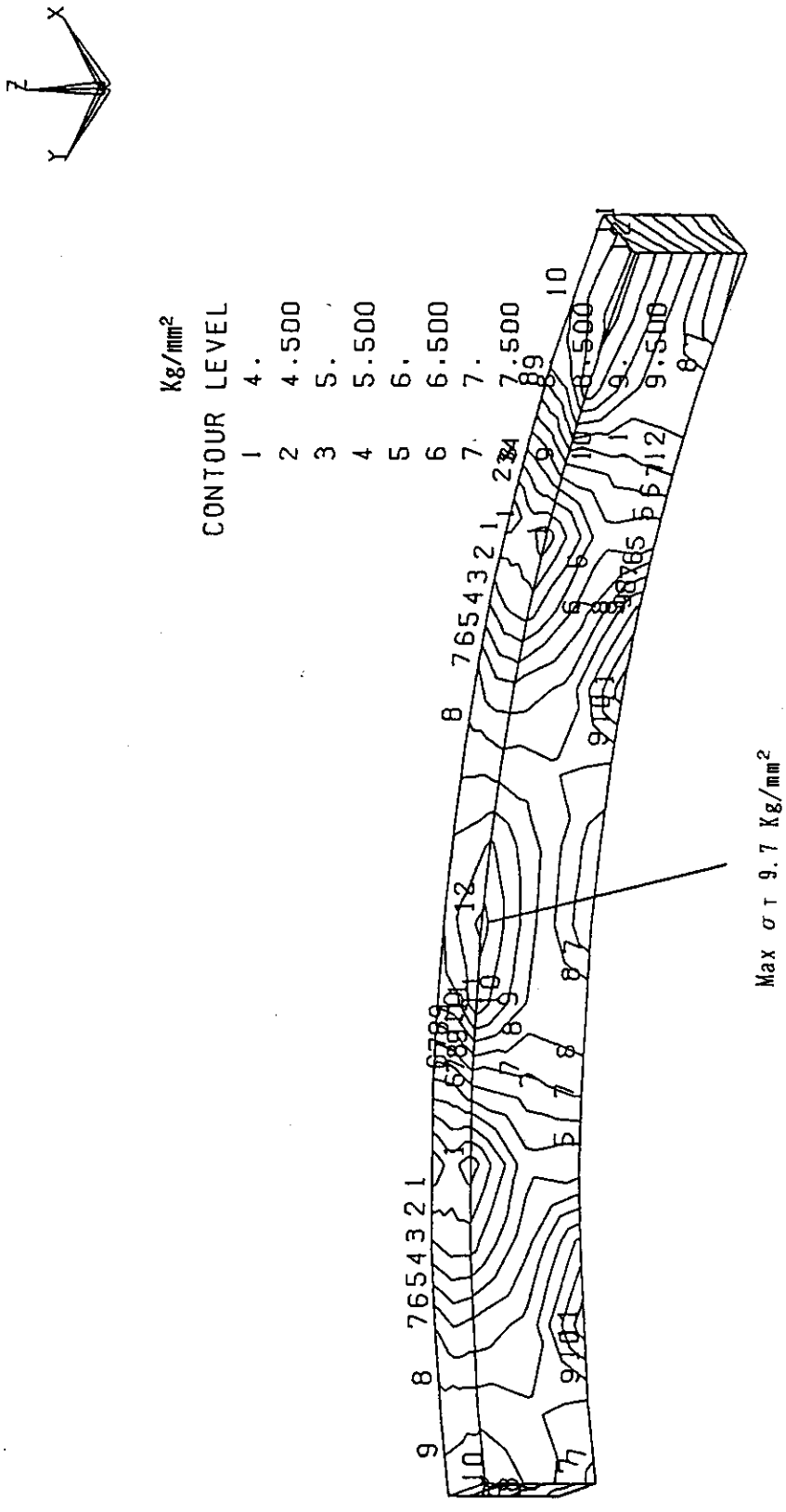

Fig. 5.19 (a) Distribution of the maximum principal stress (σ_1) in the winding of PF-7 coil at EOB3.

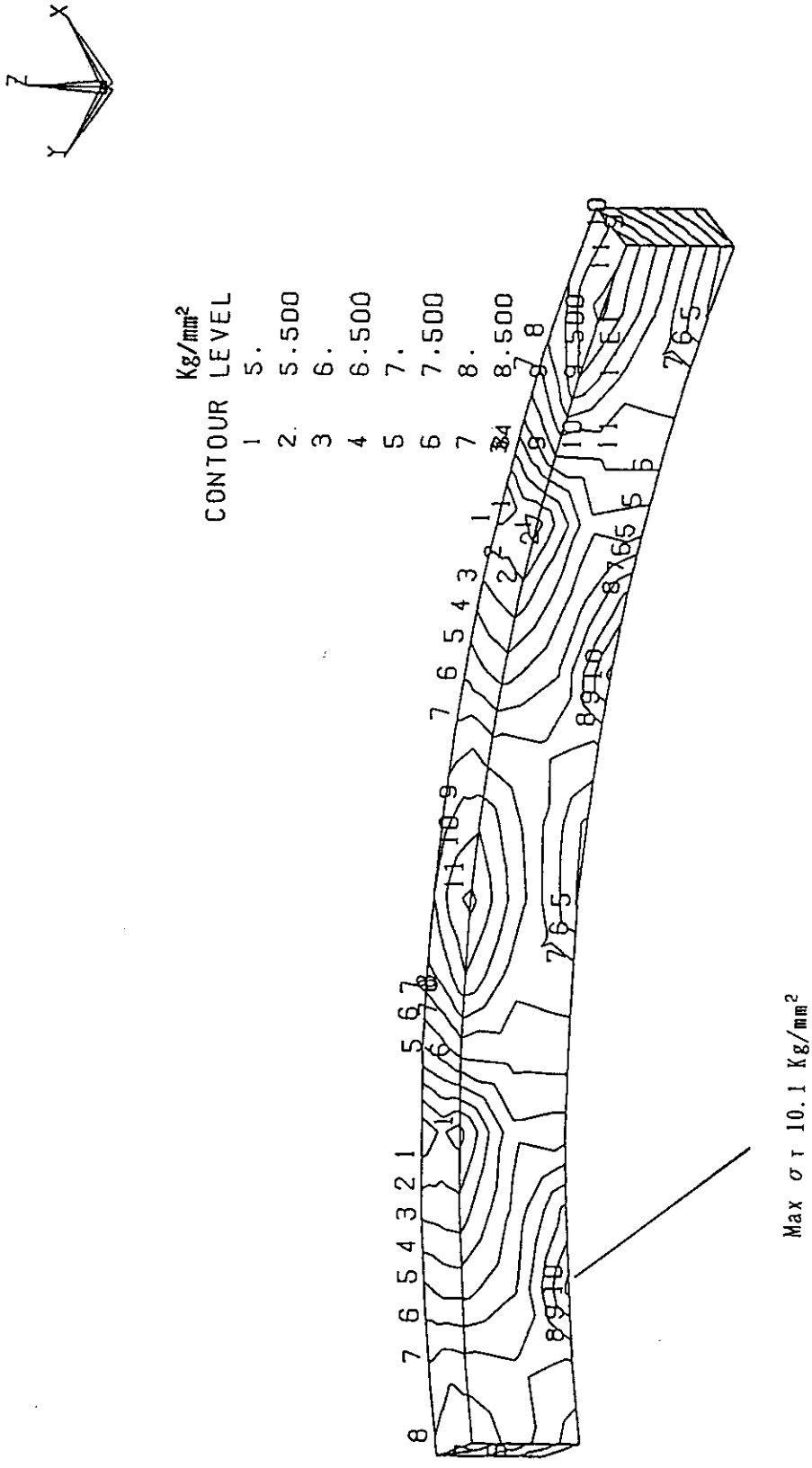

Fig. 5.19 (b) Distribution of Tresca stress.(σ_T) in the winding of PF-7 coil at EOB3.

6. Winding Rigidity Analysis

6.1 Introduction

For the purpose of obtaining the global mechanical behavior of winding, it is useful to use the equivalent Young's modulus. Moreover, in order to analyze the mechanical behavior of surrounding support structure using a finite element method, it is often required to replace the wound coil to uniform matter with the equivalent Young's and shear moduli due to the constraint of total nodes number and element numbers.

From this point of view the equivalent Young's moduli and the shear moduli of the Japanese designed coils for ITER were estimated.

In order to confirm the validity of the procedure and the obtained results described in this chapter, the comparison between the computed data and the experimentally obtained data is also discussed in last section.

6.2 Procedure

The finite element method (FEM) using MSC/NASTRAN was used for the analysis. The two dimensional axial symmetrical FEM model was made for 5 x 5 conductors. The major radius was set extremely larger than the width of conduits so as to simulate the straight coil. The reason why two dimensional axial symmetrical model was used is that it is more convenient compared with 3 dimensional model. Another reason is that the poison's ratio of $\nu_{\theta z}$ (θ : circumferential direction, z : vertical direction) can be obtained simultaneously by using an average radial displacement.

The deformation of middle 3 x 3 conduits was used for obtaining equivalent rigidity, since the peripheral conduits suffer the effects of boundary condition and produce the local deformation.

Since the major radius is very large, the orthotropic relation between stress and strain can be used and the fundamental equations are,

$$\varepsilon_R = \sigma_R/E_R - \nu_{\theta R}\sigma_\theta/E_\theta - \nu_{ZR}\sigma_Z/E_Z,$$

$$\varepsilon_\theta = \sigma_\theta/E_\theta - \nu_{R\theta}\sigma_R/E_R - \nu_{Z\theta}\sigma_Z/E_Z,$$

$$\varepsilon_Z = \sigma_Z/E_Z - \nu_{\theta Z}\sigma_\theta/E_\theta - \nu_{RZ}\sigma_R/E_R.$$

In addition the following symmetry relation must hold,

$$\nu_{\theta R}/E_\theta = \nu_{R\theta}/E_R,$$

$$\nu_{\theta Z}/E_\theta = \nu_{Z\theta}/E_Z,$$

$$\nu_{ZR}/E_Z = \nu_{RZ}/E_R.$$

The general procedure to obtain the each component is as follows.

6.2.1 Young's Modulus E_Z, Poisson's ratio ν_{ZR} and $\nu_{Z\theta}$

For the purpose of obtaining E_Z, ν_{ZR} and $\nu_{Z\theta}$, the uniform vertical pressure(P_Z) was loaded on the top surface of 5 x 5 conduits FEM model. The vertical displacement on the bottom surface was constrained, however, in the radial direction, there is no constraint. Since $\sigma_Z >> \sigma_R$, σ_θ in this case, the fundamental equations can be reduced to,

$$\varepsilon_R = -\nu_{ZR}\sigma_Z/E_Z.$$

$$\varepsilon_\theta = -\nu_{Z\theta}\sigma_Z/E_Z.$$

$$\varepsilon_Z = \sigma_Z/E_Z.$$

By using the computed value of ε_Z, ε_R, and ε_θ and the relation $P_Z = \sigma_Z$, the values of E_Z, ν_{ZR}, and $\nu_{Z\theta}$ can be obtained.

6.2.2 Young's Modulus E_R, Poisson's ratio ν_{RZ}

The uniform radial pressure (P_R) was loaded inner lateral surface. The outer lateral surface was constrained. Since $\sigma_\theta E_R/\sigma_R E_\theta \sim W_R/R << 1$ (W_R : Width of the model in the radial direction, R : Major radius) and $\sigma_R >> \sigma_Z$ in this case, the fundamental equations are reduced to,

$$\varepsilon_R = \sigma_R/E_R,$$

$$\varepsilon_\theta = \sigma_\theta/E_\theta - \nu_{R\theta}\sigma_R/E_R,$$

$$\varepsilon_Z = -\nu_{RZ}\sigma_R/E_R.$$

By using the computed value of ε_R, ε_Z and the relation $P_R = \sigma_R$, the values of E_R, ν_{RZ} can be obtained.

6.2.3 Young's Modulus E_θ

Young's modulus of E_θ was obtained analytically. By using material Young's Moduli(E_i) and the area ratios $g_i=S_i/S_{total}$, (S_i : Area for i-th material in the conductor, S_{total} : Conductor area) E_θ is given by

$$E_\theta = \Sigma\ g_i E_i.$$

6.2.4 Shear Modulus G_{RZ}

Shear Modulus G_{RZ} is also computed using the same 2 dimensional FEM model. The bottom surface was completely constrained and the transverse load (F) were distributed uniformly on the top surface. Shear Modulus G_{RZ} can be obtained by using the following relation,

$$F/A = G_{R\theta}\gamma_{R\theta},$$

where A is an area of the top surface and γ is a shear strain of middle 3 x 3 conduits.

6.2.5 Shear Modulus $G_{\theta Z}$, $G_{\theta R}$

Shear Modulus $G_{\theta Z}$, $G_{\theta R}$ were obtained only for EF coil conductor, since in other cases these parameters do not affect the analysis.

In this calculation, 3 dimensional FEM model of solid elements was employed only for three conduits (1 x 3). The procedure is same as that for obtaining G_{RZ}.

6.3. Results

The equivalent Young's moduli, Poisson's ratios and shear moduli calculated for the Japanese designed conductors for ITER, which are shown in Fig. 6.1, are summarized in Table 6.1. The details of the computation are described in the following sections.

6.3.1 Conductor for TF Coils (TMC-FF)

TMC-FF conductor is one of the monolithic type conductors. A monolithic type superconductor is composed of stainless steel conduit, insulator, and superconducting part which consists of the stabilizing copper and superconducting material. The material properties of each component are shown in Fig. 6.2. The material properties of the superconducting part was set to the material properties of copper stabilizer.

The typical deformation of the TMC-FF conductors due to vertical and radial pressures are shown in Fig. 6.3 (a) and (b), respectively.

6.3.2 Conductor for CS Coils (PF-CS40)

PF-CS40 conductor for the CS coil is one of the bundle type conductor. A bundle type superconductor is composed of stainless steel conduit, insulator and superconducting strands. The FEM model and the material properties of each component are shown in Fig. 6.4. The superconducting strands were not considered as a structural member for transverse loading, since

the void for helium flow exist between the strands. Consequently, the strands inside of the conduit are not included in the FEM model. On the other hand, for the longitudinal loading, the DPC experiment in JAERI [1] shows that the strands have mechanical effect on the longitudinal rigidity. However, in the stress analysis of the ITER bundle type conductor, the rigidity of the strands in the longitudinal direction was neglected, because the width of the stainless steel conduits is so thick that its rigidity is much greater than that of the strands.

The typical deformations of PF-CS40 conductors due to the vertical and the radial pressure and the sharing force are shown in Fig. 6.5 (a),(b) and (c),respectively. These figures show that the local deformations occurs in the part of peripheral conduits as mentioned previously.

6.3.3 Conductor for PF-6 and PF-7 coils (Sub Channel CICC : EF-40)

Sub Channel CICC : EF-40 conductor is also the bundle type conductor. The FEM model of the conductors and the material properties of each component are shown in Fig. 6.6.

The typical deformation of the conduits due to the vertical and radial pressure and the sharing force are shown in Fig. 6.7 (a),(b) and (c),respectively.

In order to obtain the shear modulus $G_{\theta Z}$, the solid model which consists of three conduits was built as shown in Fig. 6.8. The deformations due to the shearing force is shown in Fig. 6.9.

6.4 Comparison with the experimental data

Since there is a possibility that the assumptions that were employed for the calculation are not valid, for example the fillers inserted between corners of conduits are assumed to be fully packed, it is required to confirm the validity of the calculation experimentally.

From this point of view the equivalent Young's modulus of

DPC coil was computed and compared with the actually obtained data in DPC experiments [1]. The cross section of the conduits of DPC-U1, U2 coil is shown in Fig. 6.10.

The two dimensional axial symmetrical FEM model of DPC-U1, U2 winding, which was made for 5 x 5 conductors, is shown in Fig. 6.11. The major radius of the FEM model was set extremely larger than the width of conduits so as to simulate the straight coil as mentioned previously.

Since the stiffness of the fillers which were inserted between the corners, is estimated to be in the range of 5-20 GPa, the analyses was performed changing the Young's modulus of the filler as 5 GPa, 10 GPa and 20 GPa. In order to make clear the effect of the filler, the case of the Young's modulus equal to 0 Pa is also examined.

The transverse uniform pressure was loaded vertically and the deformation was computed. The deformation of middle 3 x 3 conduits was used for obtaining equivalent Young's modulus E_Z. The deformation of conduits is shown in Fig. 6.12. This figure clearly shows that the local deformations occurs in the peripheral conduits.

The results of the equivalent Young's modulus are summarized in Table 6.2. The equivalent Young's modulus is in the range from 12.4 GPa to 16.2 GPa for the case that Young's modulus of the filler is in the region of 5 GPa to 20 GPa. However, in the case that the fillers have no mechanical effects, i.e. the Young's modulus of the filler is equal to 0 GPa, the equivalent Young's modulus is down to 4.6 GPa.

Since the experimentally obtained value is about 30 GPa and has a region 10 ~ 30 GPa, it can be said that the experimental data of DPC-U1,2 Coils can be deduced considering the mechanical effect of the filler.

Therefore, it can be concluded that the estimation method of the equivalent Young's modulus is valid and applicable to the design of the superconducting coils of ITER.

6.5. Summary

The equivalent stiffness of the coil windings which were

used for the Japanese design of ITER was estimated using Finite Element Method. The validity of the calculating procedure and the results were checked by using the obtained data in the DPC U1, U2 experiments.

References

[1] H. Nakajima, K. Okuno, H. Tsuji et al., Mechanical characteristic in the experiment of the Nb-Ti Demo Poloidal Coils (DPC-U1,U2). MT-11 Conference, 1989 in Tsukuba.

Table 6.1 Equivalent Young's moduli and shear moduli of the Japanese designed conductors for ITER.

Conductor	Young's Modulus (GPa)			Poisson's Ratio			Shear Modulus (GPa)		
	E_R	$E\theta$	E_Z	$\nu_{R\theta}$	$\nu_{\theta Z}$	ν_{ZR}	G_{ZR}	$G_{R\theta}$	$G_{\theta Z}$
TMC-FF	73	105	84	0.15	0.21	0.17	---	---	---
PF-CS40	51	55	103	0.14	0.26	0.23	---	---	4.0
CICC EF-40	43	105	40	0.13	0.11	0.21	35	35	4.7

Table 6.2 Dependence of the Equivalent Young's modulus E_Z on the Young's Modulus of the filler.

	Young's Modulus of Filler (GPa)	Equivalent Young's Modulus E_Z of the Winding (GPa)
Case 1	0.0	4.6
Case 2	5.0	12.4
Case 3	10.0	14.4
Case 4	20.0	16.2

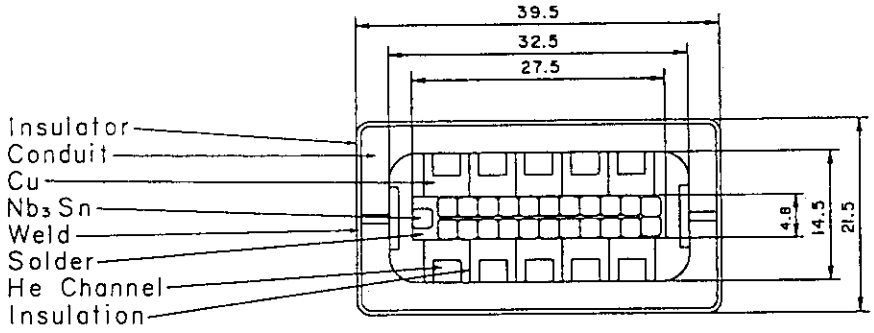

12T−30kA Conductor for TF Coils
(TMC−FF)

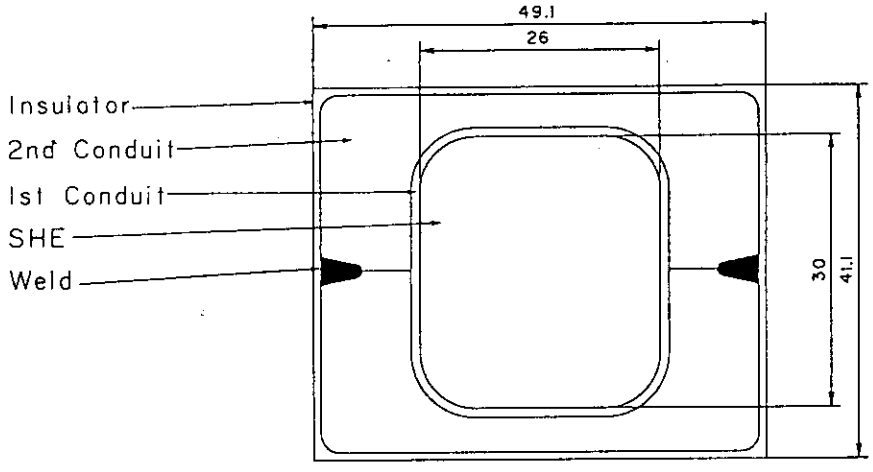

13T−40kA Conductor for CS Coils
(PF−CS40)

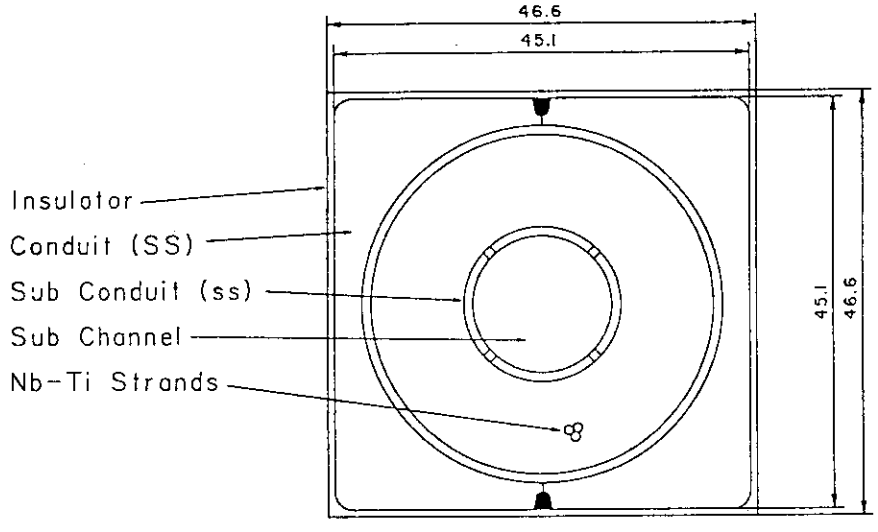

5.5T−43kA Conductor for EF Coils
(Sub Channel CICC: EF−40)

Fig. 6.1 Structure and dimensions of the Japanese designed conductors for ITER.

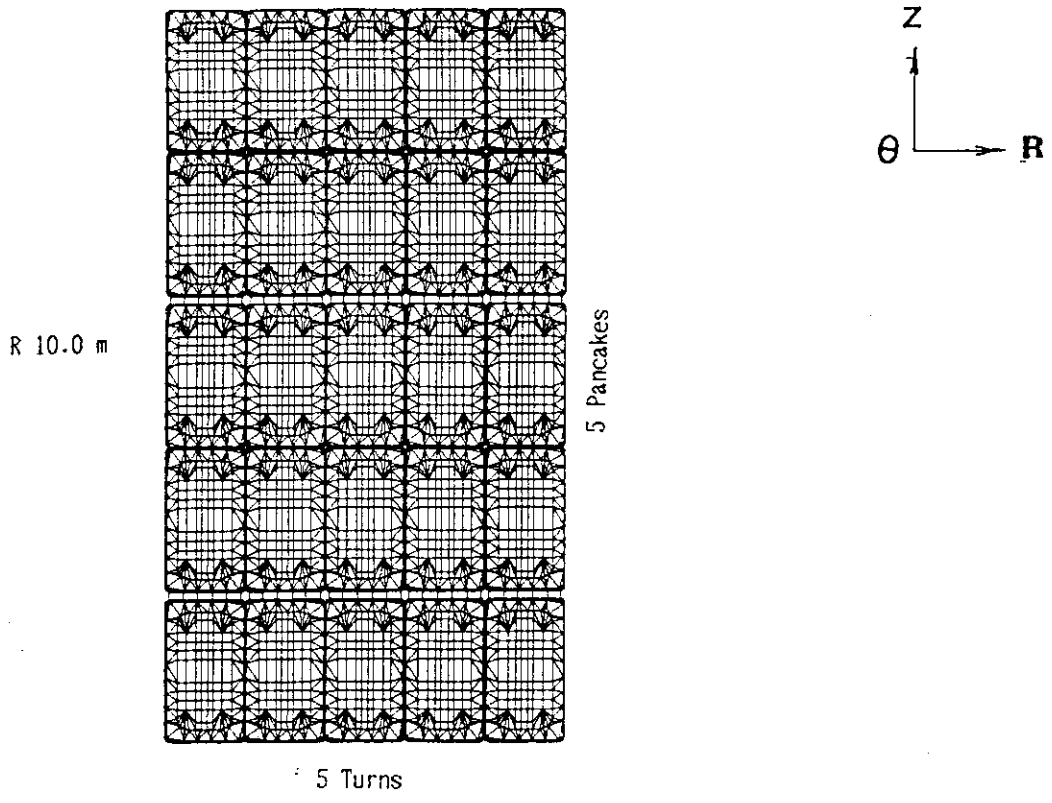

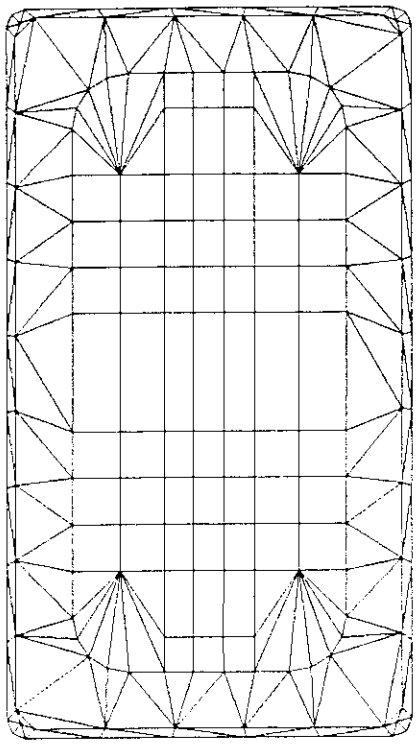

Insulator (E = 9.8 GPa , ν = 0.1)

Superconductor (E = 137.2 GPa , ν = 0.275)

Conduit(s.s.) (E = 205.8 GPa , ν = 0.3)

Cooling Channel (E = 0.0 GPa , ν = 0.0)

Cu (E = 137.2 GPa , ν = 0.275)

Fig. 6.2 FEM model for the calculation of equivalent Young's modulus of the TMC-FF conductor, material properties of each components are shown in the figure.

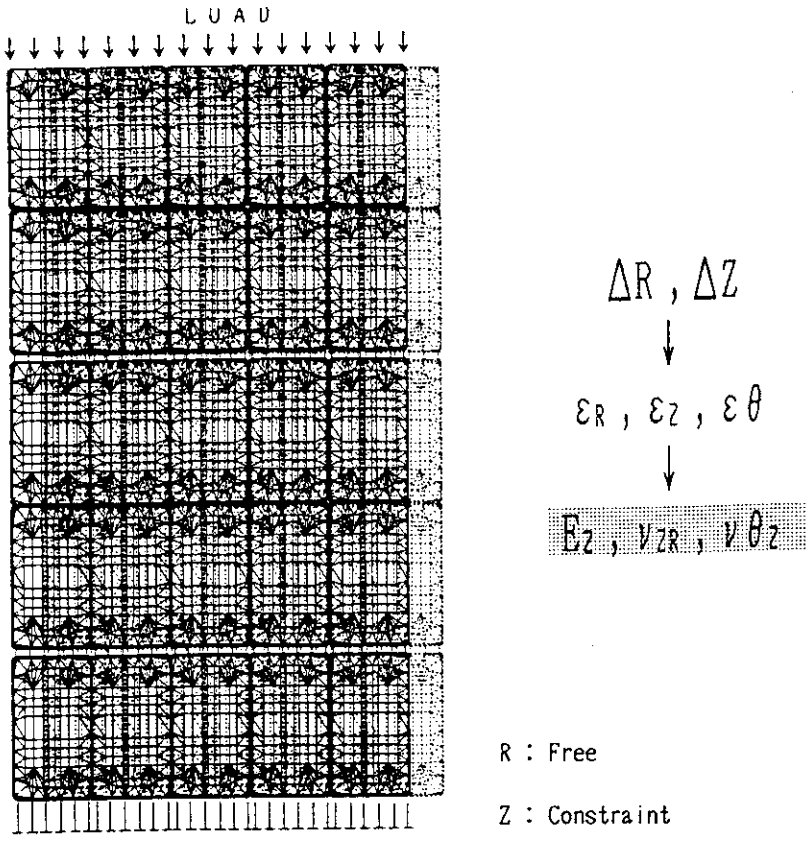

Fig. 6.3 (a) Deformation of the winding of TMC-FF conductor due to vertical uniform pressure.

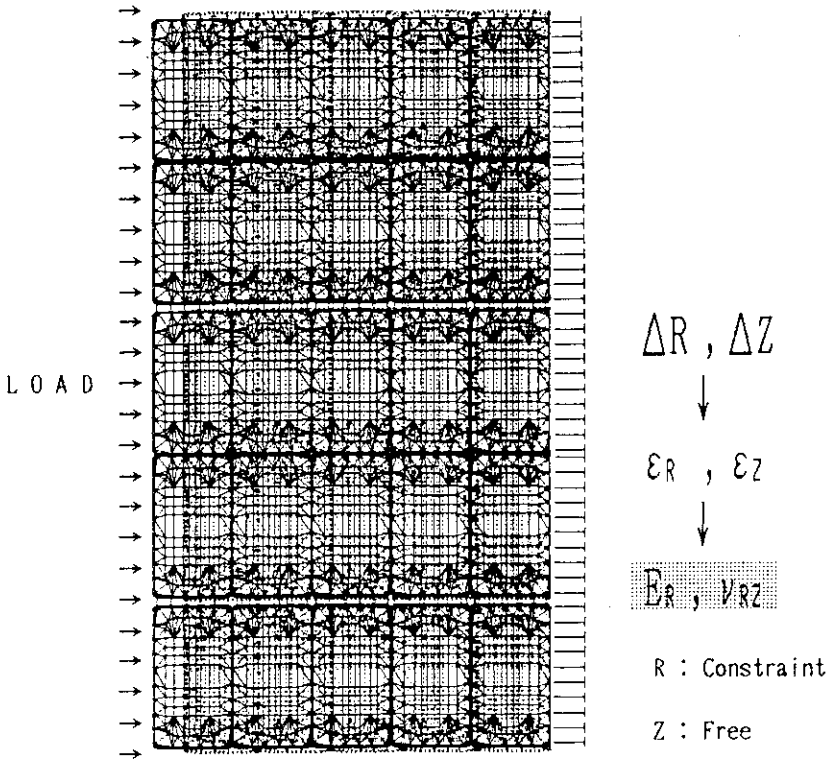

Fig. 6.3 (b) Deformation of the winding of TMC-FF conductor due to radial uniform pressure.

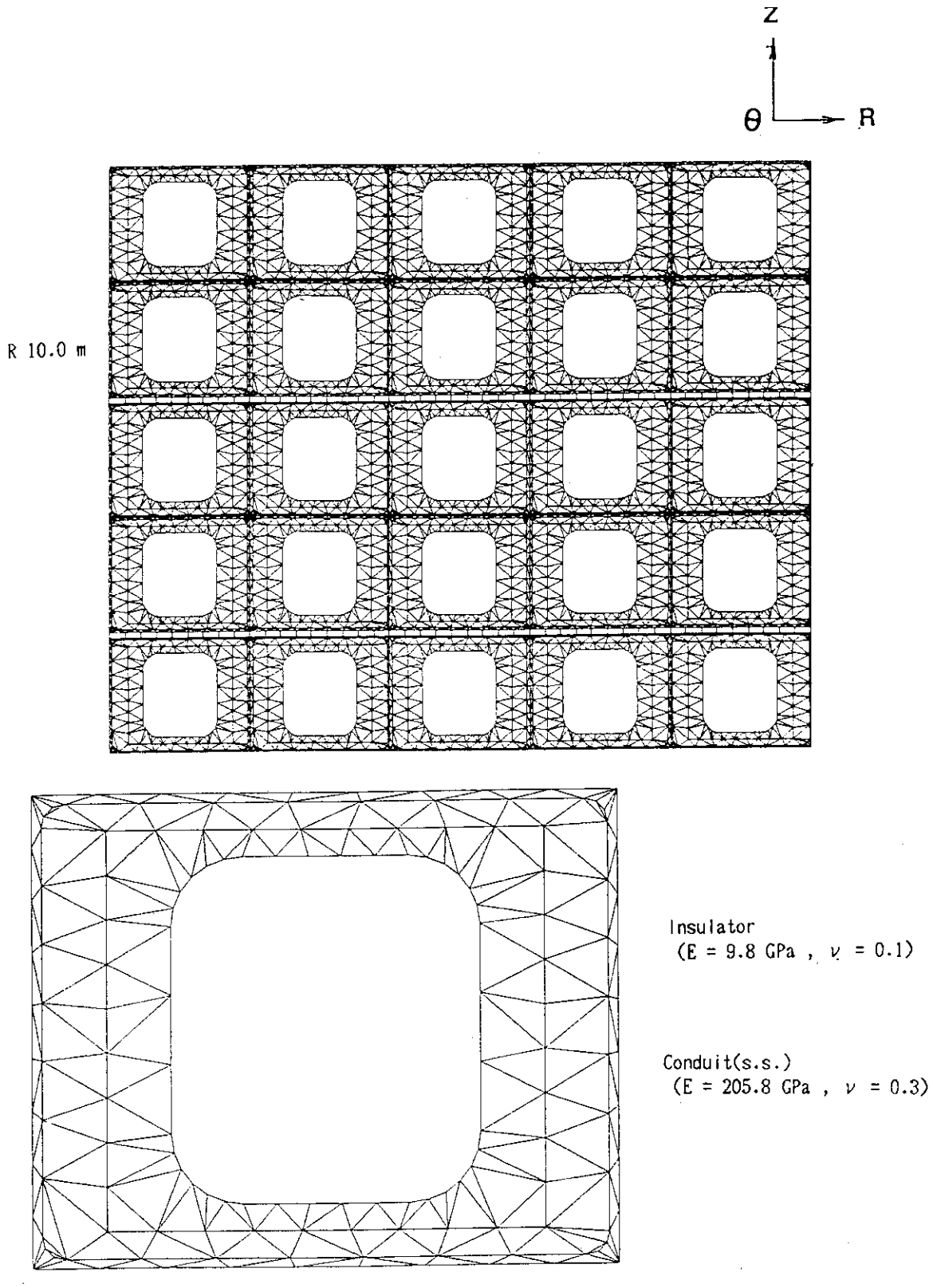

Fig. 6.4 FEM model for the calculation of equivalent Young's modulus of the PF-CS40 conductor, material properties of each components are shown in the figure.

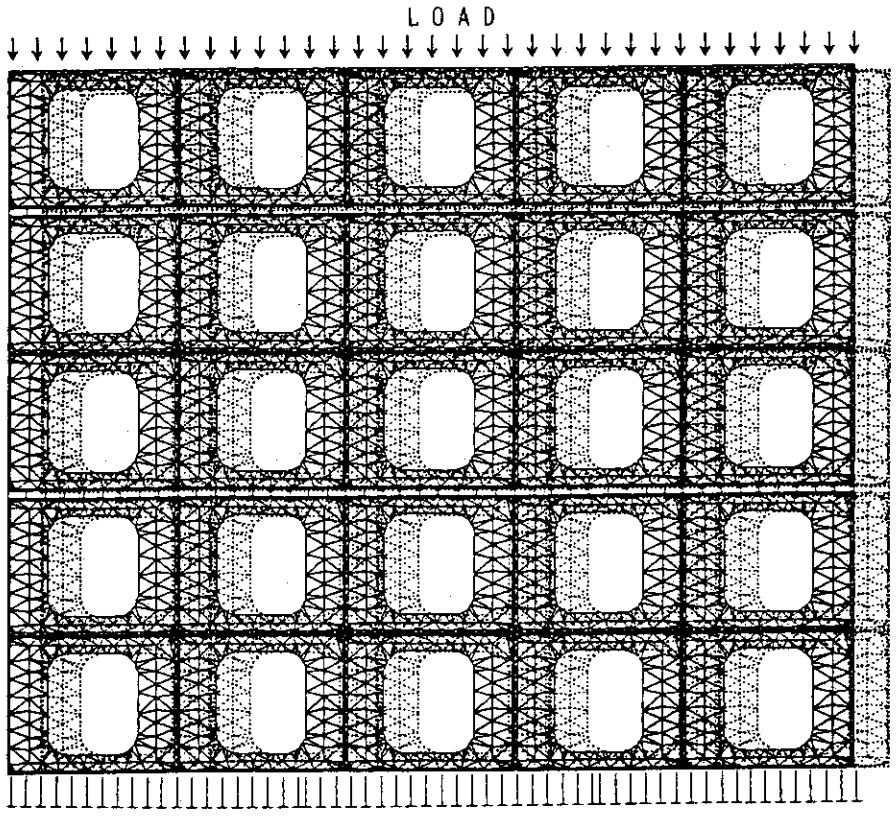

Fig. 6.5 (a) Deformation of the winding of PF-CS40 conductor due to vertical uniform pressure.

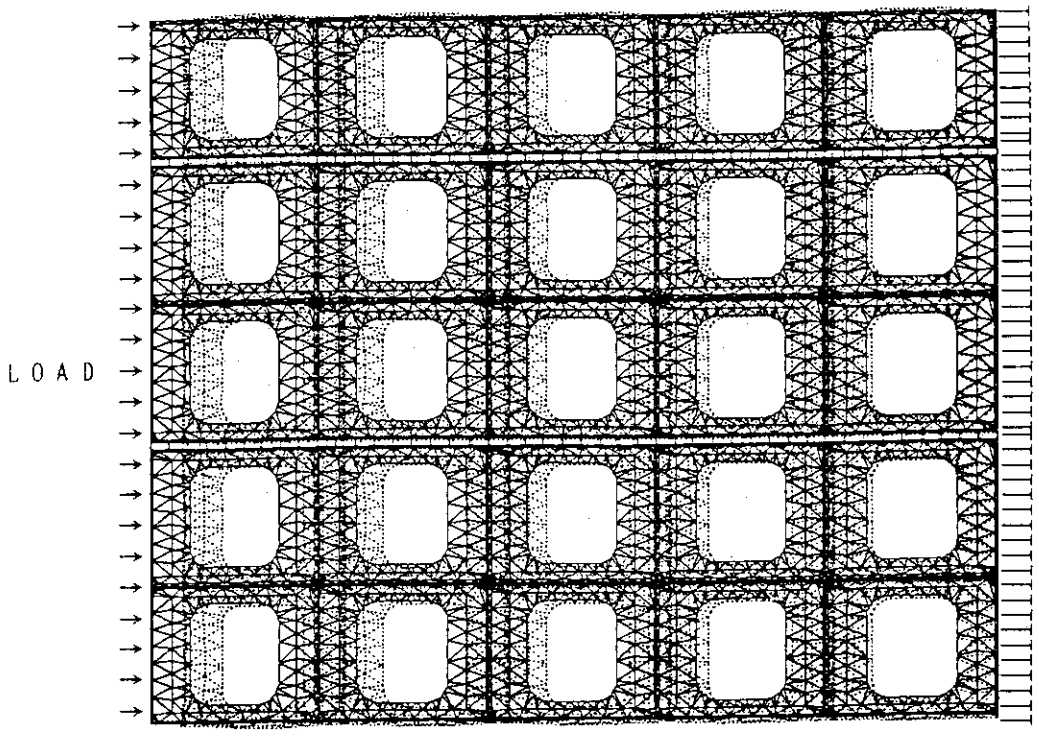

Fig. 6.5 (b) Deformation of the winding of PF-CS40 conductor due to radial uniform pressure.

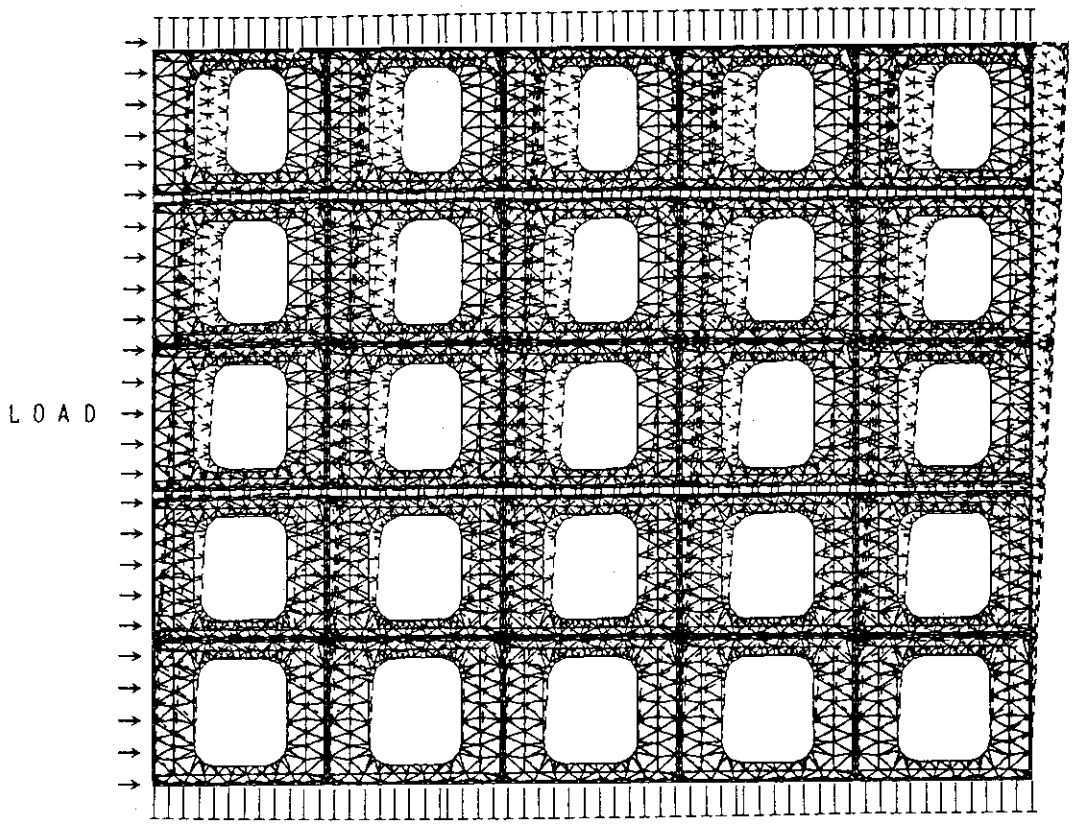

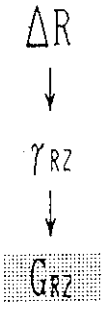

Fig. 6.5 (c) Deformation of the winding of PF-CS40 conductor due to radial shearing force.

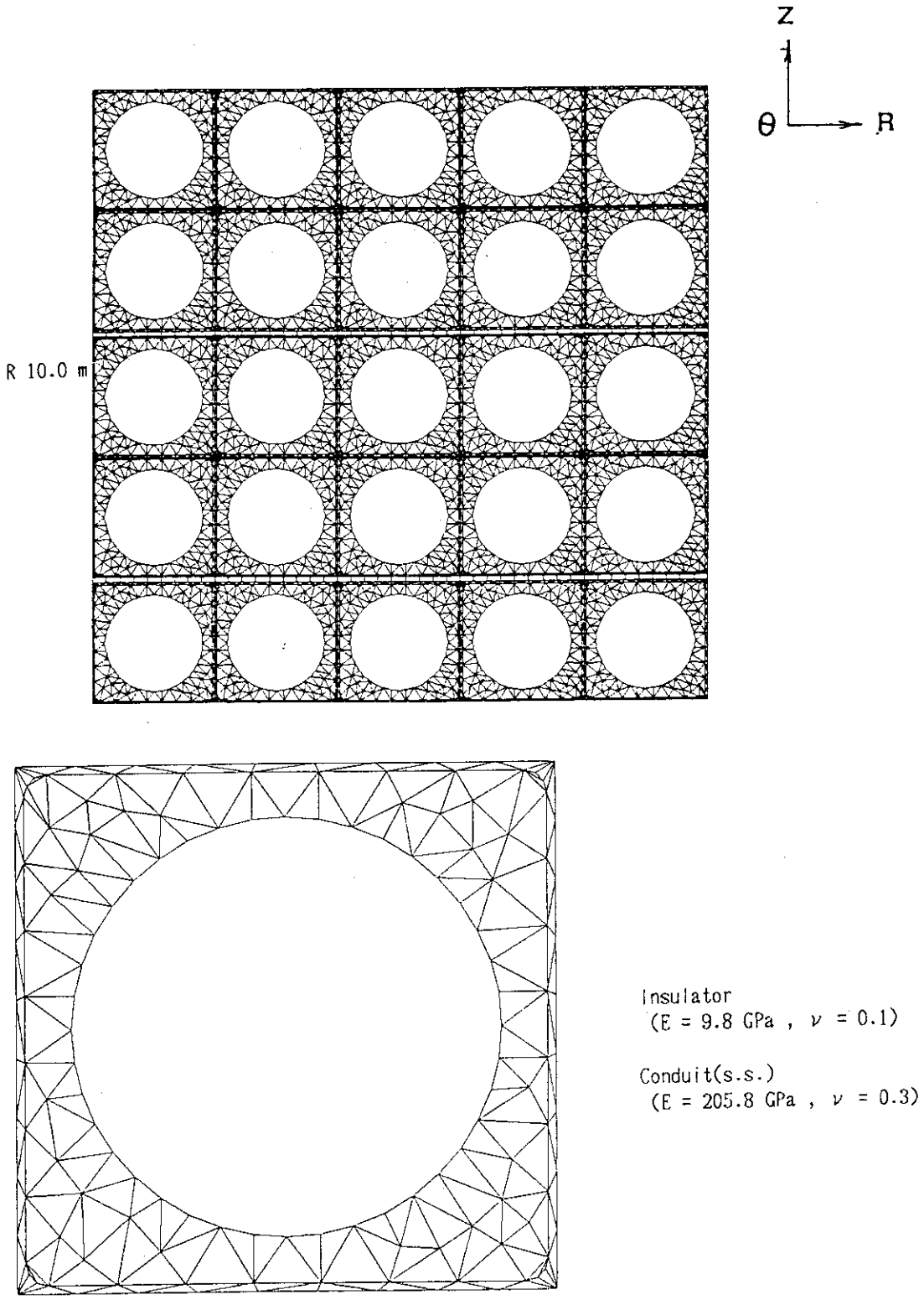

Fig. 6.6 FEM model for the calculation of equivalent Young's modulus of the CICC:EF-CS40 conductor, material properties of each components are shown in the figure.

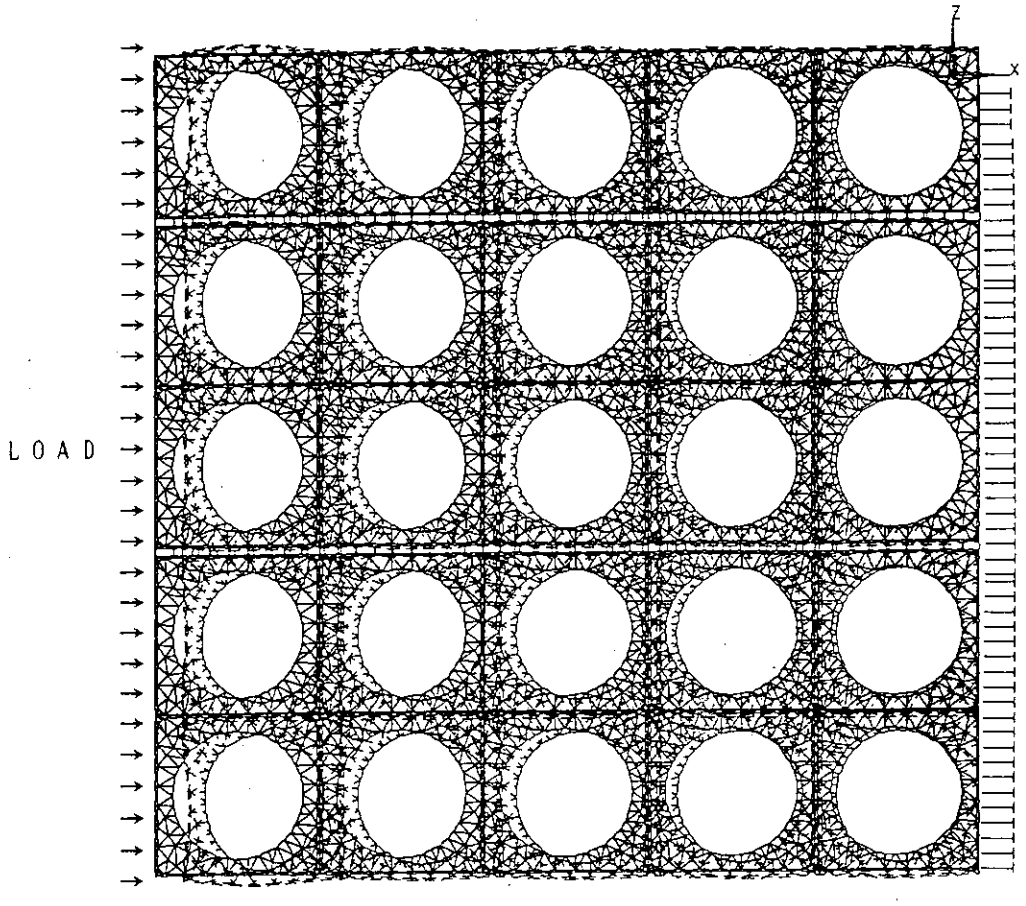

Fig. 6.7 (a) Deformation of winding of CICC:EF-40 conductor due to vertical uniform pressure.

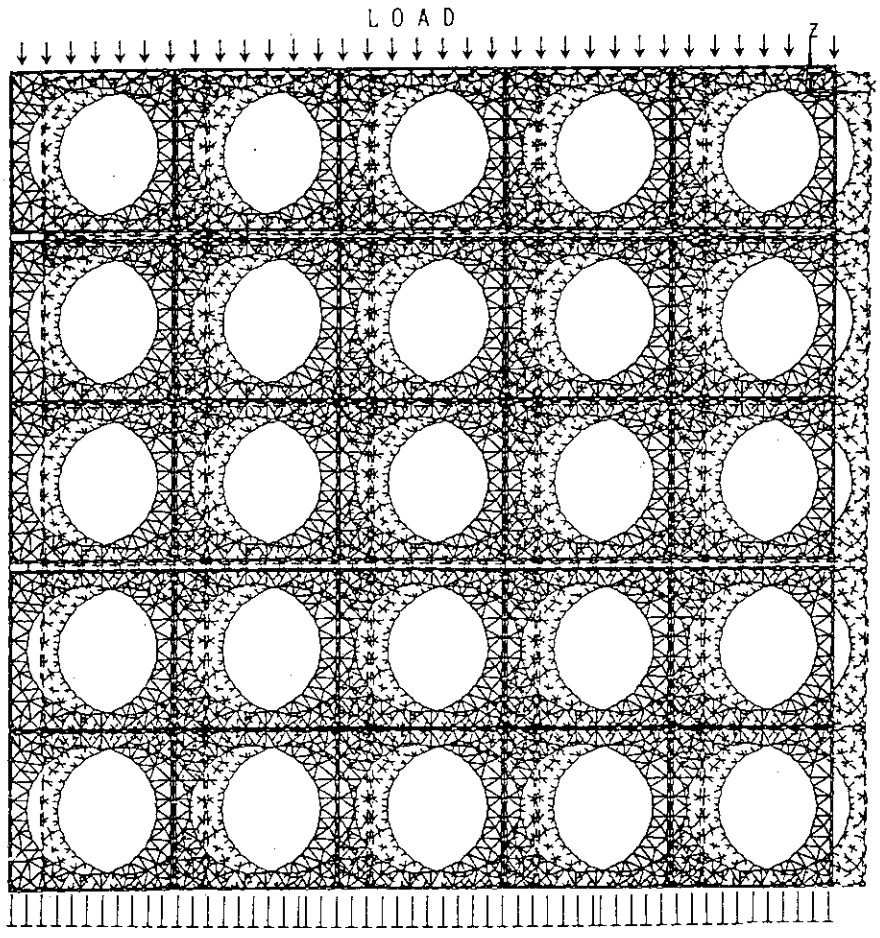

Fig. 6.7 (b) Deformation of winding of CICC:EF-40 conductor due to radial uniform pressure.

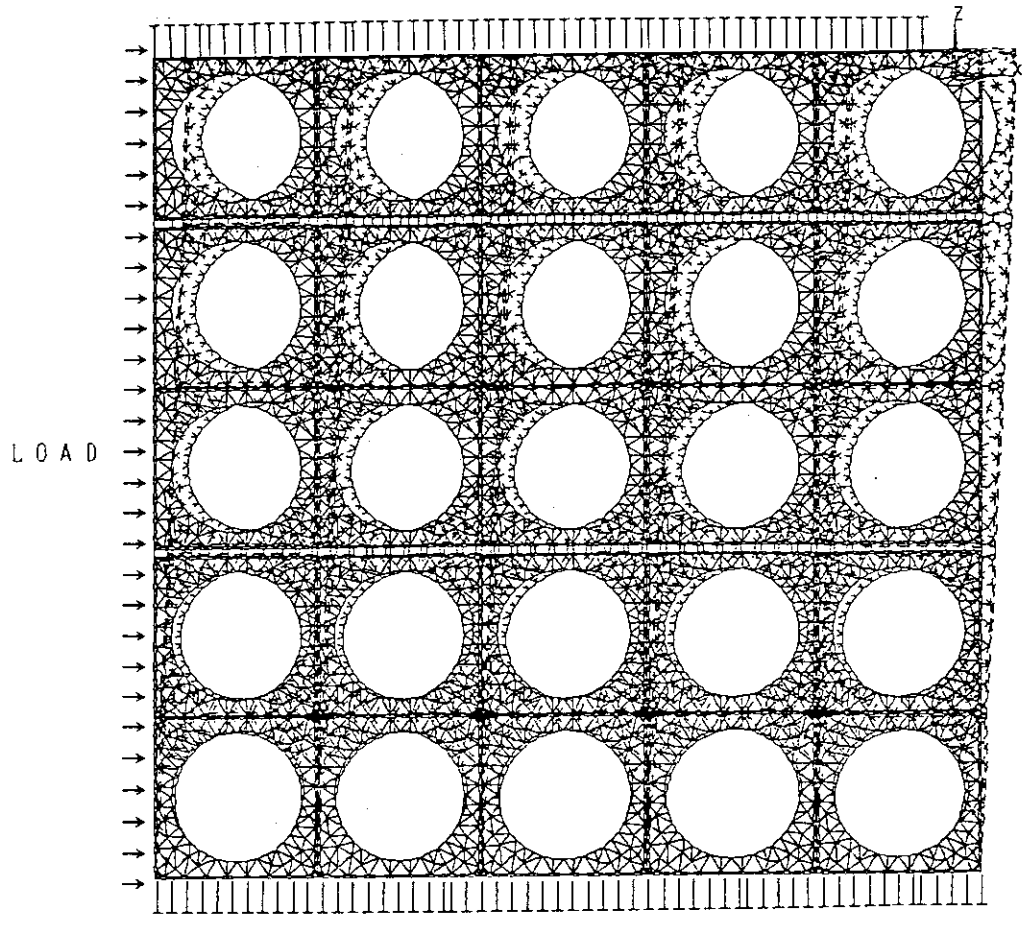

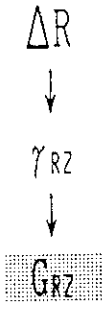

Fig. 6.7 (c) Deformation of winding of CICC:EF-40 conductor due to radial shearing force.

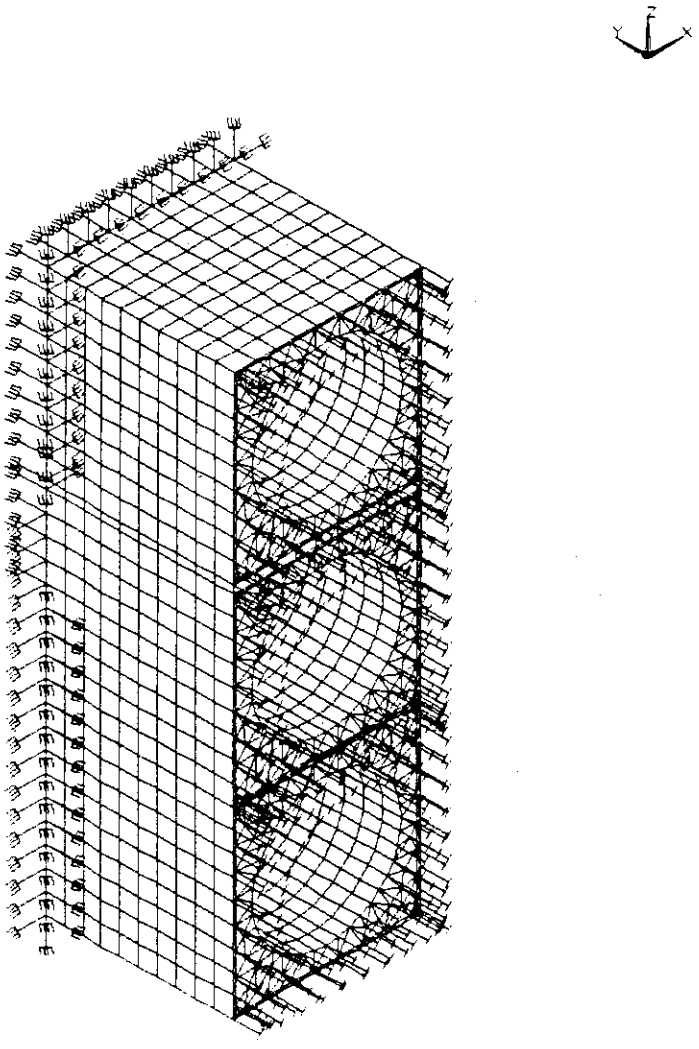

Fig. 6.8 Solid model of CICC:EF-40 for the calculation of the shear modulus $G_{\theta Z}$.

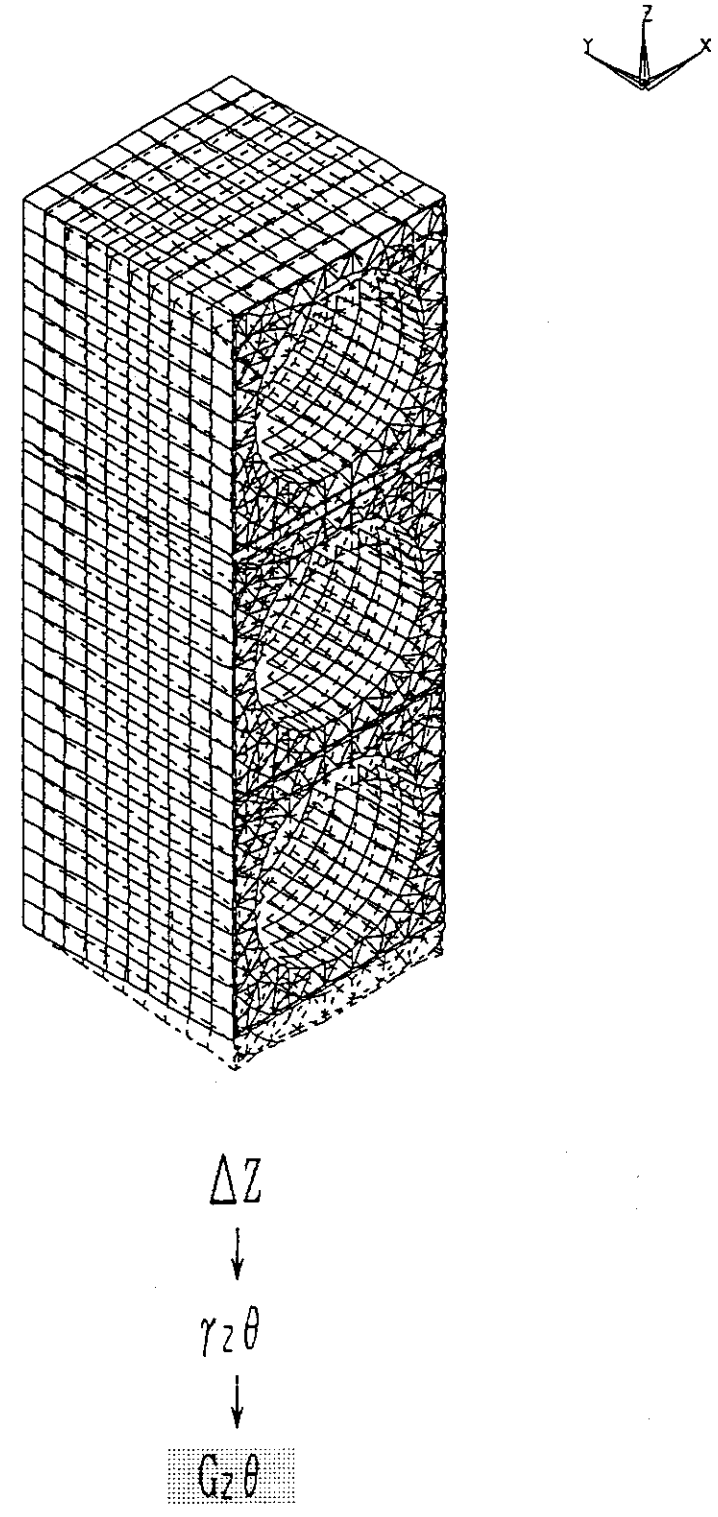

Fig. 6.9 Deformation of the winding of CICC:EF-40 conductor due to the shearing force.

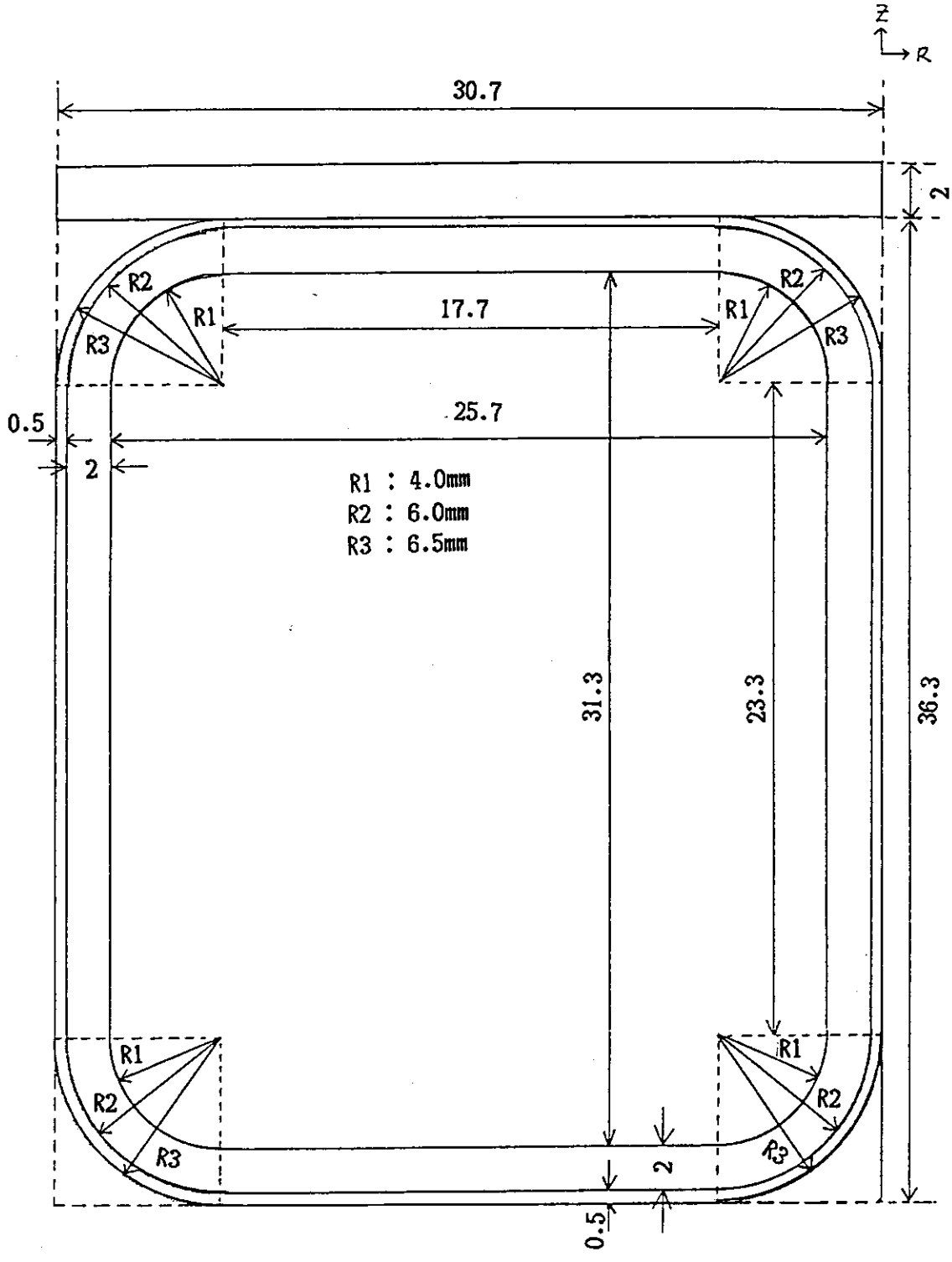

Fig. 6.10 Cross section of the conductor for DPC-U1, U2 coil.

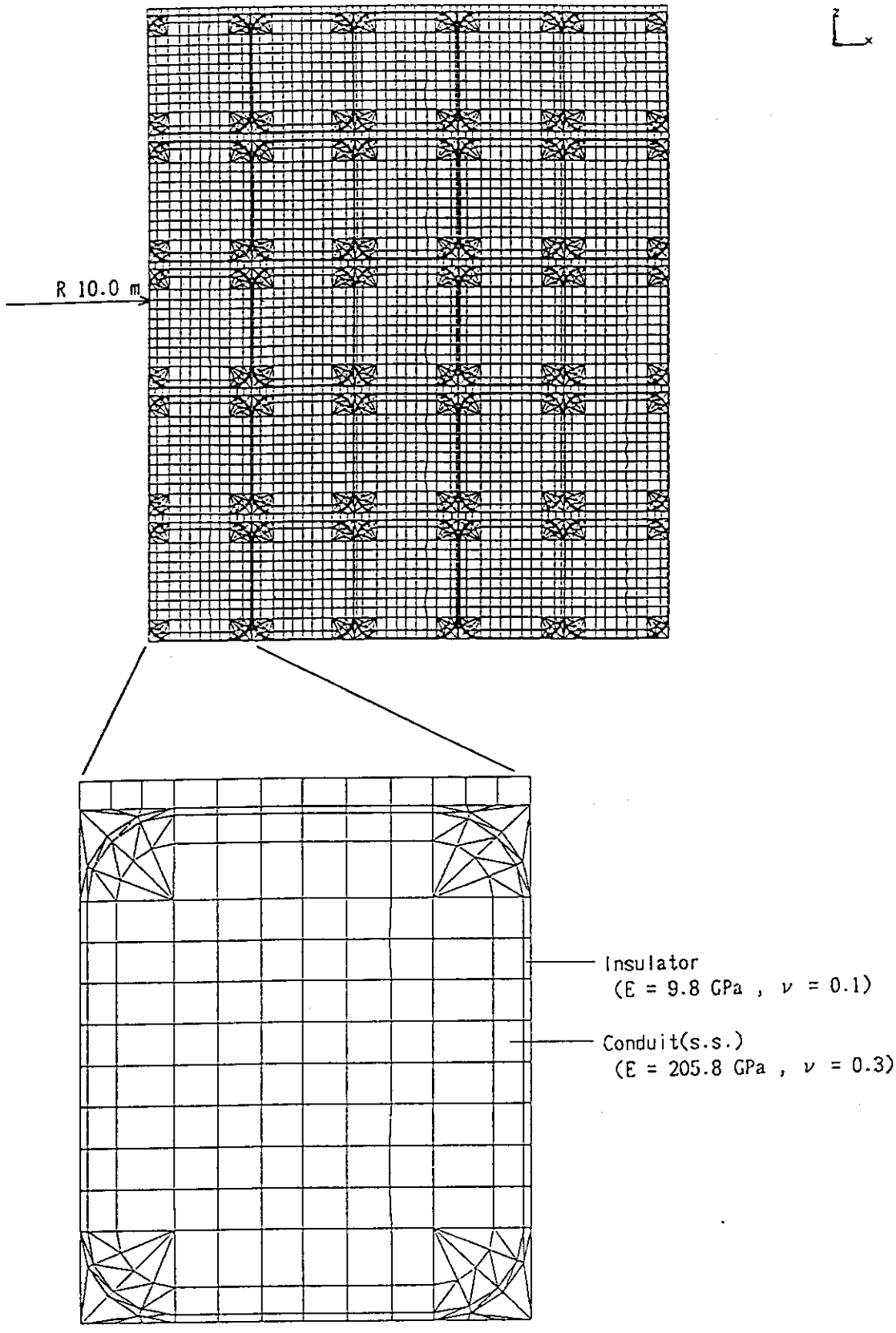

Fig. 6.11 FEM model for the calculation of equivalent Young's modulus of the DPC-U1, U2 coil, material properties of each components are shown in the figure.

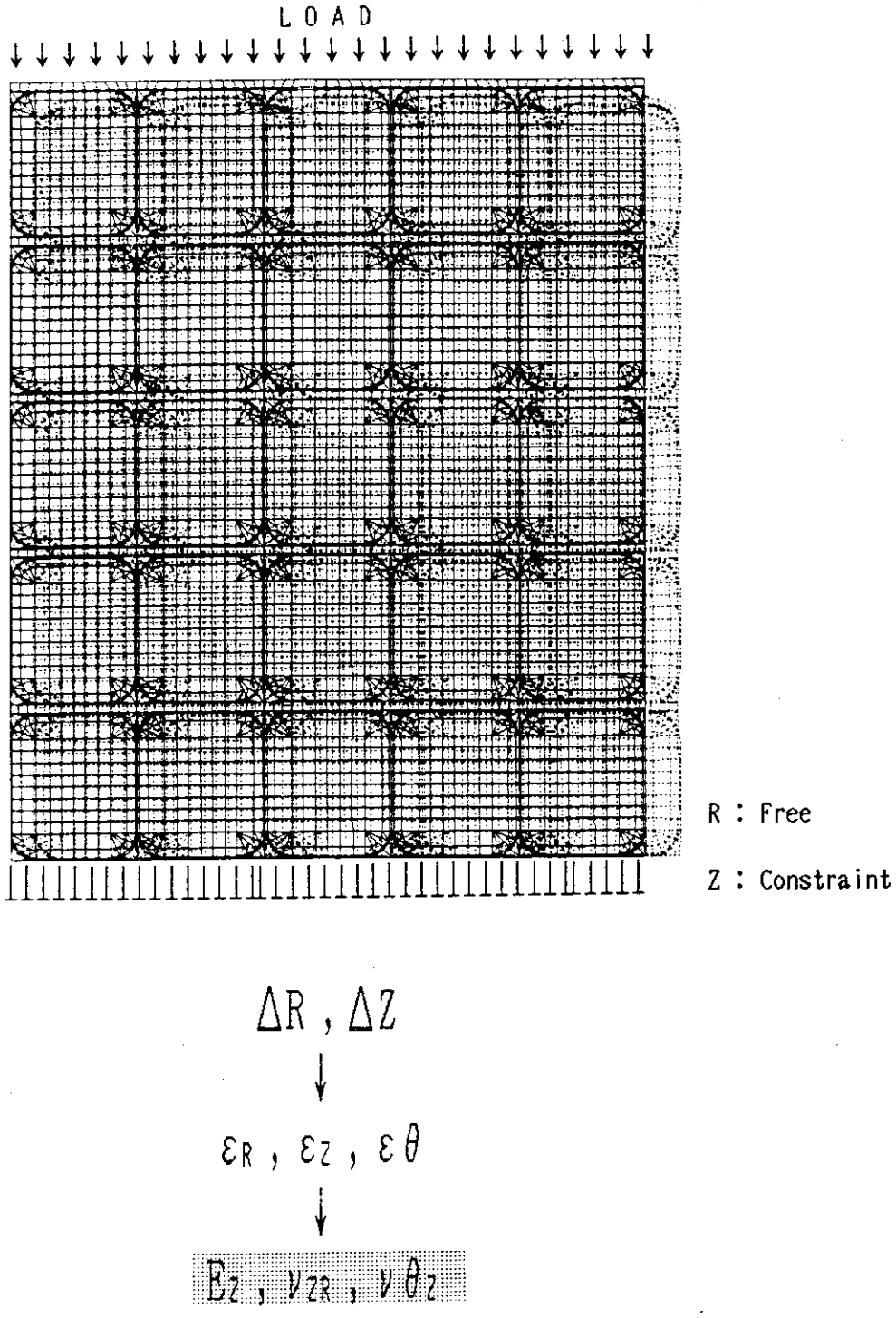

Fig. 6.12 Deformation of the winding of DPC-U1, U2 conductor due to vertical uniform pressure.

7. Summary

Based on the Japanese coil design, the mechanical behaviors of the ITER TF coils, CS coils, EF coils and their support structures were analyzed by using FEM models of MSC/NASTRAN. The maximum Tresca stresses calculated for each coil and support structures were compared with the allowable limit of 800 MPa for static loading and 600 MPa for cyclic loading.
The major results obtained by a series of analysis and stress evaluations are summarized as follows ;

(1) The mechanical behaviors of TF coil under normal loading condition at EOB were analyzed by using idealized boundary conditions of cyclic symmetry. The Tresca stresses of the coil case were within the allowable limit of 600 MPa except the most thin section at the inner leg. The maximum Tresca stress of 655 MPa at this part should be reexamined by detailed analysis to specify the mechanical safety margin of TF coil.

(2) The mechanical behaviors of the TF coil system under 4 fault loading conditions were also calculated by FEM model. The imbalance of the centering load and out-of-plane load, caused by the "Short Circuit" and "Open Circuit", has the possibility to generate the high stress of more than 750 MPa in the coil case. Since the mechanical behaviors of the coil system largely depend on the mechanical reliability of the interfaces among coils, such as the wedging and outer intercoil structure, more careful analysis and the investigation should be required. Also the results must be confirmed with the final power supply configuration since the design of power supply and coil protection system may prevent some of fault conditions.

(3) The structural grading for the CS coil is feasible to flatten the stress distribution. In the ordinary part of the winding, in which the conduits are piled up regularly in the vertical direction, the maximum Tresca stress in the

innermost conduit is 615 MPa. In the extraordinary part, where the empty space is required to adjust the conductor splice, the maximum stress reaches 650 MPa under the most severe operation which consider the operational flexibility. The filler of stainless steel which is packed into the empty space is required to reduce the stress level.

(4) The initial compression of 180 MN is required to prevent the separation or interaction of CS coils. This initial compression at room temperature cause the most severe stress of 197 - 206 Mpa in the CS coil support structure. Compared with the results on the CS coil support structure, the maximum stress in the EF coil support structure is rather low level, 120 MPa. The maximum tensile stress of 230 MPa estimated for the EF coil is also within the allowable level with much margin.

(5) The procedure to obtain the equivalent winging stiffness employed for the FEM analysis was developed. The validity of the calculating procedure and the results were confirmed by the data obtained in the DPC-U1, U2 experiments.

ACKNOWLEDGEMENTS

The authors would like to thank Dr. S. Shimamoto and Dr. S. Mastuda for their strong support and kind encouragement of our design activities during the past three years. Also, the authors wish to thank the staff of the Superconducting Laboratory and the Fusion Experimental Reactor Design Team for their consultation. And authors would also like to thank Mr. T. Shimizu, Mr. Y. Nakane, Mr. H. Shimane, Mr. T. Nishino, and Mr. E. Yaguti from Kanazawa Computer Service Co Ltd for their computer analysis. Also thanks to Miss Y. Iida, Miss Y. Hasegawa, Mr. K.Hirano, and Miss H.Nagahori for the CAD operations, and Miss A. Miwa of Gensiryoku Shiryo Service Co Ltd for the publishing.

innermost conduit is 615 MPa. In the extraordinary part, where the empty space is required to adjust the conductor splice, the maximum stress reaches 650 MPa under the most severe operation which consider the operational flexibility. The filler of stainless steel which is packed into the empty space is required to reduce the stress level.

(4) The initial compression of 180 MN is required to prevent the separation or interaction of CS coils. This initial compression at room temperature cause the most severe stress of 197 - 206 Mpa in the CS coil support structure. Compared with the results on the CS coil support structure, the maximum stress in the EF coil support structure is rather low level, 120 MPa. The maximum tensile stress of 230 MPa estimated for the EF coil is also within the allowable level with much margin.

(5) The procedure to obtain the equivalent winging stiffness employed for the FEM analysis was developed. The validity of the calculating procedure and the results were confirmed by the data obtained in the DPC-U1, U2 experiments.

ACKNOWLEDGEMENTS

The authors would like to thank Dr. S. Shimamoto and Dr. S. Mastuda for their strong support and kind encouragement of our design activities during the past three years. Also, the authors wish to thank the staff of the Superconducting Laboratory and the Fusion Experimental Reactor Design Team for their consultation. And authors would also like to thank Mr. T. Shimizu, Mr. Y. Nakane, Mr. H. Shimane, Mr. T. Nishino, and Mr. E. Yaguti from Kanazawa Computer Service Co Ltd for their computer analysis. Also thanks to Miss Y. Iida, Miss Y. Hasegawa, Mr. K.Hirano, and Miss H.Nagahori for the CAD operations, and Miss A. Miwa of Gensiryoku Shiryo Service Co Ltd for the publishing.